Variability modeling and numerical biomarkers design in cardiac electrophysiology

THÈSE DE DOCTORAT

Présentée par

Eliott Tixier

pour obtenir le grade de

DOCTEUR DE
L' UNIVERSITÉ PIERRE ET MARIE CURIE - Paris VI

Spécialité : Mathématiques Appliquées

Soutenue publiquement le 18/12/2017 devant le jury composé de :

Jean-Frédéric Gerbeau	Directeur de thèse
Olivier Le Maître	Rapporteur
Damiano Lombardi	Directeur de thèse
Yvon Maday	Président
Bertrand Maury	Rapporteur
Clémentine Prieur	Examinatrice

Après avis favorables des rapporteurs : Olivier Le Maître et Bertrand Maury

Thèse préparée au sein de l'équipe-projet REO
Laboratoire Jacques-Louis Lions
Université Pierre et Marie Curie - Paris 6
et **Centre de Recherche Inria de Paris**
2 rue Simone Iff
75589 Paris Cedex 12

Remerciements

Je remercie les rapporteurs de ma thèse Olivier Le Maître et Bertrand Maury pour le temps qu'ils ont consacré à évaluer mon manuscrit, pour leurs rapports détaillés ainsi que pour leur participation au jury. Je remercie également Yvon Maday et Clémentine Prieur d'avoir accepté de faire partie de ce même jury. Je souhaite remercier chalheureusement mes directeurs de thèse Jean-Frédéric Gerbeau et Damiano Lombardi. Je vous remercie de m'avoir proposé ce sujet passionnant, de m'avoir accompagné et encadré pendant ces trois années et d'avoir été très disponibles, encourageants et toujours prompts à me donner de bons conseils. Votre soutien et votre bienveillance m'ont permis de mener ce projet avec sérénité et confiance. Ces trois années ont été riches d'enseignements et m'ont beaucoup apporté. Les cadres matériel et humain dont j'ai bénéficié à l'Inria m'ont permis de mener ce doctorat dans des conditions idéales. Je pense pouvoir dire sans me tromper que ce fut l'expérience la plus formatrice de mon parcours.

Je remercie mes collègues des équipes REO, ALPINES, ANGE et MAMBA et plus généralement les occupants du mythique pavillon 16 de Rocquencourt et du 3ème étage du bâtiment A pour nos nombreux échanges et discussions. Nos interactions et petits moments du quotidien ont fait de ces trois années une formidable expérience humaine. Je remercie Marc, Céline, Muriel, Laurent, Irène, Miguel, Jacques, Martin et Bernard pour leur présence bienveillante et leurs conseils avisés. Je remercie Marina pour les voyages en char d'assaut pour rejoindre la piscine du Chesnay et les débats constructifs sur la place de la voiture en ville, Jean-Frédéric pour sa gentillesse, sa pédagogie et les nombreux footings en forêt, Damiano pour son enthousiasme sans faille même dans l'adversité et particulièrement face aux *reviewers* "raisonnables". Je remercie Matteo pour les *master class* de *scacchi*, de C++ et de décomposition de domaine *é che mi ha insegnato un po di italiano ma che non mi corregerà si scrivo qualcosa*, Chloé pour son altruisme, sa sa gentillesse et sa contribution certaine à la vie sociale du labo, Nicolas pour sa sempiternelle bonne humeur et son émerveillement constant devant les petites choses de la vie, Fabien pour notre bataille commune pour repousser les limites de notre connaissance en modélisation de l'électrophysiologie, ses blagues et jeux de mots douteux en comparaison desquels les miens deviennent presque drôles, sa bonne humeur et une cohabitation fructueuse à tous égards, Léa pour son érudition et sa patience, Noémie pour sa gentillesse, ses récits d'aventures et ses gâteaux, Gaëtan pour son énergie de la jeunesse et sa bonhomie, Gautier dont la défense de la firme à la pomme contre vents et marées impose le respect, Lara pour ses critiques constructives de la société française, Alberto pour son ingénuité, Ludovic pour sa résurrection de l'intégration continue, Yi pour sa gentillesse et ses bonnes adresses du 13ème, j'aurais bien écrit quelques mots en mandarin mais je n'ai pas trouvé le *package* LaTeXidoine, Olivier pour ses origamis à l'aérodynamisme médiocre, Hussam pour m'avoir appris que Nadia El Mansour n'a pas du tout l'accent syrien et enfin Alexandre, Paul, Axel, Sébastien et tous les autres qui ont partagé nos déjeuners et pauses détente.

Je voudrais remercier ceux avec qui je n'ai partagé que l'expérience bucolique roc-

quencourtoise : Benoît pour sa gentillesse et sa force tranquille, Faisal pour ses analyses pertinentes et objectives de la société américaine, Mikel pour les longues conversations dans la mythique navette, Sanjay pour ses nombreux conseils en Python et son expérience de manière générale, Vivien pour son éclairage sur l'univers de *Game of Thrones* et enfin Elisa et Annabelle que j'ai peu cotoyées mais dont les manuscrits de thèse m'ont été très utiles.

Je remercie ma famille et mes amis de m'avoir soutenu et toi, Lucie, d'avoir cru en moi et de partager ma vie.

Variability modeling and numerical biomarkers design in cardiac electrophysiology

Abstract:

This PhD thesis is dedicated to the study of the variability observed in cardiac electrophysiology (*i.e.* the electrical activity of biological tissues) measurements and to the design of numerical biomarkers extracted from these measurements. The potential applications are numerous, ranging from a better understanding of existing electrophysiology models to the assessment of adverse effects of drugs or the diagnosis of cardiac pathologies. The cardiac electrophysiology models considered in the present work are either ODEs or PDEs depending on whether we focus on the cell scale or the tissue scale. In both cases, these models are highly non-linear and computationally intensive. We proceed as follows: first we develop numerical tools that address general issues and that are applicable beyond the scope of cardiac electrophysiology. Then, we apply those tools to synthetic electrophysiology measurements in various realistic scenarios and, when available, to real experimental data.

In the first part of this thesis, we present a general method for estimating the probability density function (PDF) of uncertain parameters of models based on ordinary differential equations (ODEs) or partial differential equations (PDEs). The method is non-instrusive and relies on offline evaluations of the forward model, making it computationally cheap in practice compared to more sophisticated approaches. The method is illustrated with generic PDE and ODE models. It is then applied to synthetic and experimental electrophysiology measurements.

In the second part of this thesis, we present a method to extract and select biomarkers from models outputs in view of performing classication tasks or solving parameter identification problems. The method relies on the resolution of a sparse optimization problem. The method is illustrated with simple models and then applied to synthetic measurements, including electrocardiogram recordings, and to experimental data obtained from micro-electrode array measurements.

Keywords: cardiac electrophysiology, statistical inverse problems, moment matching, maximum entropy, bidomain equations, micro-electrode array, classification, feature selection

Modélisation de la variabilité et conception de biomarqueurs numériques en électrophysiologie cardiaque

Résumé:

Cette thèse de doctorat est consacrée à l'étude de la variabilité observée dans les mesures d'électrophysiologie (*i.e.* l'activité électrique des tissus biologiques) cardiaque et à la conception de biomarqueurs numériques extraits de ces mesures. Les applications potentielles sont nombreuses, pouvant aller d'une meilleure compréhension des modèles électrophysiologiques existants à l'évaluations des effets nocifs de médicaments en passant par le diagnostic de pathologies cardiaques. Les modèles d'électrophysiologie cardiaque présentés dans ce travail sont, soit des équations différentielles ordinaires (EDOs), soit des équations aux dérivées partielles (EDPs), selon qu'ils concernent l'échelle cellulaire ou l'échelle du tissu. Dans les deux cas, ces modèles sont hautement non linéaires et nécessitent d'intenses ressources computationnelles. Nous adoptons l'approche suivante : de prime abord, nous développons des outils numériques afin de répondre à des problèmes généraux, au-delà de l'électrophysiologie. Puis, nous appliquons ces outils à des mesures synthétiques d'électrophysiologie dans différents scénarios réalistes et, lorsque cela est possible, à des mesures expérimentales.

Dans la première partie de cette thèse, nous présentons une méthode générale pour estimer la densité de probabilité de paramètres incertains de modèles basés sur des EDOs ou des EDPs. La méthode est non intrusive et repose sur des évaluations "hors-ligne" du modèle direct, ce qui la rend en pratique computationellement moins dispendieuse que d'autres approches plus sophistiquées. La méthode est illustrée avec des mesures synthétiques et expérimentales d'électrophysiologie.

Dans la seconde partie de cette thèse, nous présentons une méthode de sélection de biomarqueurs à partir des sorties de modèles en vue d'effectuer des tâches de classification ou de résoudre des problèmes d'estimation de paramètres. La méthode repose sur la résolution d'un problème d'optimisation creux. La méthode est illustrée avec des modèles simples et ensuite appliquée à des mesures synthétiques, incluant des enregistrements d'électrocardiogramme, et à des données expérimentales obtenues à partir de mesures de matrices de microélectrodes.

Mots-clés : électrophysiologie cardiaque, problèmes inverses statistiques, matching des moments, maximum d'entropie, équations bidomaine, matrice de microélectrode, classification, sélection des caractéristiques

Contents

1 Introduction **1**
- 1.1 Scientific and industrial context . . . 3
- 1.2 Scientific contributions . . . 4
- 1.3 Contents and manuscript organization . . . 5
- 1.4 Scientific dissemination . . . 6

2 A Moment-Matching Method to Study the Variability of Phenomena Described by Partial Differential Equations **9**
- 2.1 Introduction . . . 11
- 2.2 Methodology . . . 12
- 2.3 Comparison with existing techniques for an ODE model . . . 30
- 2.4 Numerical illustrations . . . 39
- 2.5 Limitations and Discussion . . . 46
- 2.6 Concluding remarks . . . 47
- 2.7 Appendix . . . 49

3 Modeling Variability in Cardiac Electrophysiology: A Moment Matching Approach **55**
- 3.1 Introduction . . . 57
- 3.2 Methods . . . 58
- 3.3 Results . . . 66
- 3.4 Discussion . . . 76
- 3.5 Supplementary Material . . . 83

4 How to Choose Biomarkers in View of Parameter Estimation **91**
- 4.1 Introduction . . . 93
- 4.2 Numerical Method . . . 95
- 4.3 Numerical Experiments . . . 101
- 4.4 Application to electrophysiology and hemodynamics . . . 106
- 4.5 Conclusions and Perspectives . . . 116

5 Optimal Biomarkers Design for Drug Safety Evaluation Using Microelectrode Array Measurements **119**
- 5.1 Introduction . . . 121
- 5.2 Methods . . . 122
- 5.3 Results . . . 130
- 5.4 Discussion . . . 132
- 5.5 Tables and Figures . . . 135

5.6 Supplementary Material 142

6 Computing Numerical Biomarkers for Electrocardiograms 147
6.1 Introduction 149
6.2 Methods 149
6.3 Results 156
6.4 Conclusions and perspectives 162
6.5 Appendix 163

Conclusions and Perspectives 170

Bibliography 173

Chapter 1

Introduction

Contents

1.1 Scientific and industrial context 3
1.2 Scientific contributions 4
1.3 Contents and manuscript organization 5
1.4 Scientific dissemination 6
1.4.1 Publications 6
1.4.2 Conferences 7
1.4.3 Implementation 7

1.1 Scientific and industrial context

Akin to many other industries (aeronautics, car manufacturing, finance, ...) which saw their practices disrupted by the use of mathematical modeling and numerical simulations, the pharmaceutical industry is following suit by incorporating *in silico* models in the development process of new drugs. Safety pharmacology (SP) is a relatively new discipline whose aim is to assess undesirable effects of drugs in their early development phase. The present work focuses on cardiac safety pharmacology (CSP), a branch of SP focusing on the effects of drugs onto the cardiomyocytes (heart muscle cells). More precisely, we concentrate on cardiac electrophysiology: the study of heart cells electrical properties. The use of numerical simulations in CSP has recently triggered much interest from both the academic and industrial communities. From an industrial perspective, the potential gains are immense. Indeed, replacing part of the real experimentations on animals with computer simulations would be very beneficial both financially and ethically. From an academic perspective, it raises important challenges both in terms of modeling and numerical methods. In order to reliably assess the effects of new drugs, the mathematical models of cardiomyocytes electrophysiology must be able to replicate both healthy and abnormal known behaviors but also to predict previously unknown responses. Furthermore, efficient numerical methods need to be developed to produce reliable simulations at reasonable computational costs, ideally in real-time. Apart from these technical aspects, a "cultural" change needs to be initiated in the pharmaceutical industry. Since computer simulations are generally seen as less reliable than experimentation, it is crucial to build trustworthy numerical frameworks and ultimately to demonstrate that the proposed approaches are scientifically valid and robust. Convincing experimentalists of the complementarity of numerical simulations and regulatory agencies (FDA[1], EMA[1], ...) of the necessity to modify their guidelines is not an easy task.

Parallel to this new appetite for *in silico* assistance, some hardware innovations may also induce radical changes in CSP practices. The Micro-Electrode Array (MEA, see Figure 1.1) enables high-throughput electrophysiology measurements that are less labour-intensive than the state-of-the-art patch-clamp technique[2]. On the biological side, the use of human-induced pluripotent stem cells (hiPSC) is thriving [MBGF04] and their recent large-scale production makes them a viable human model replacement [CGB+16]. This thesis was initiated within the scope of the CardioXcomp project whose aim is to simulate electrophysiology measurements in an environment combining these two technologies: MEA and hiPSC. More precisely, the purpose of the present work is to model the variability observed in the experimental measurements in electrophysiology. Investigating this variability has several motivations. It can be used to predict the response of cardiomyocytes to certain

[1] FDA: US Food and Drug Administration. EMA: European Medicines Agency.

[2] The patch clamp technique is used to measure electrical currents in a single cell by perforating its membrane. It is a long and delicate procedure which requires much expertise from the experimentalist. To learn more about it, see [HMN+81].

drugs. It can also provide insight into cell modifications at the origin of common heart diseases such as atrial fibrillation for instance. Like in most biological systems, the observed variability is the consequence of many different sources of randomness. We choose to restrict our analysis to ionic channel maximal current densities and we formulate the goal to estimate the probability density function (PDF) of these parameters given a certain set of measurements. To that end, specific numerical methods have been developed and tested on both synthetic and experimental measurements.

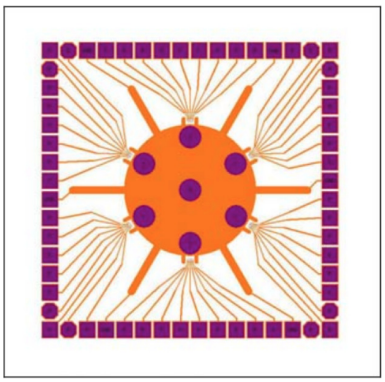

(a) 6-well MEA. Approximative size: 5cm x 5cm.

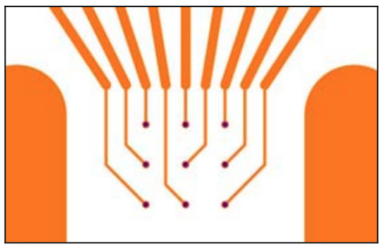

(b) Zoom on one well. Each of the 9 dots corresponds to an electrode. The lateral and bottom (not visible) sides are electrical grounds. The area in white is covered with a tissue of hiPSC cells.

Figure 1.1: Schematic of a Multichannel Systems Micro-Electrode Array (MEA). Reproduced from [Sys].

1.2 Scientific contributions

A general method for estimating the PDF of the uncertain parameters of a given model (ODE or PDE models for instance) is developed. Numerous strategies developed to address such a problem may be found in the literature, such as a stochastic approximation of the expectation maximization method [KL05, GLV14] or a least squares minimization of the moments discrepancy [ZG08]. The key features of our method are its non-parametric and non-intrusive nature and the fact that it only uses offline computations of the forward model. In that regard, it is in practice computationally less expensive than other methods that require multiple forward evaluations at each iteration of the procedure. The proposed method infers the PDF of the parameters from the matching of the statistical moments of observable degrees of freedom (DOFs, also referred to as physical DOFs in the following) of the model. It builds on the Maximum Entropy principle [Jay57, MP84] which has previously been applied successfully in many different contexts [SZ06, VdSB08, MLKDC10, GS13]. In our case, the PDF is sought so that it maximizes the Shannon entropy [Sha48] while satisfying the aforementioned moments constraints. This is translated into an

optimization problem for which we propose algorithms to find the solution. This method is called observable moment matching in the following.

This inverse procedure is improved by incorporating an algorithm that selects a subset of the model DOFs that both reduces its computational cost and increases its robustness. The selection relies on the approximation of a sensitivity Gram matrix [Rus10, CDW14] and on a clustering of the DOFs. The DOFs are selected so that the maximum information on the sensitivities is conserved. This algorithm uses the pre-computed model outputs to build an approximation of the local sensitivities and therefore does not require additional evaluations of the forward model.

After having illustrated the approach with generic PDE and ODE models, it is applied to electrophysiology measurements. This is part of a global and recent effort towards the modeling and understanding of the variability in electrophysiology measurements [BBOVA+13, SBOW+14, GBRQ14, JCB+15, PDB+16]. First, we focus on measurements at the cell scale which are modeled by non-linear coupled sets of ODEs. Different models are presented which vary in terms of complexity (from 3 to 29 ODEs) and in terms of modeled cell types (canine, human, ventricular, atrial, etc.). The MEA measurements are modeled using the bidomain model [Tun78] which is a set of non-linear reaction diffusion PDEs where the reaction term corresponds to the single cell models described above.

Our next contribution is related to inverse problems and classification problems. Regardless of the method used to solve these problems, one key aspect is the choice of quantities of interest: quantities to be fitted for the inverse problem or features in a classification context. In electrophysiology, such quantities are called biomarkers. Biomarkers are usually proposed by the community, based on physical intuition and experimental observations. They are often relevant in qualitatively describing the hidden quantities. However, in most practical applications, although the biomarkers exhibit a good correlation with respect to the hidden quantity they are designed to monitor, they have a non-negligible correlation with respect to others, making them less robust or of difficult interpretation. We propose an algorithm that automatically selects optimal biomarkers, referred to as numerical biomarkers, in the sense that they are maximally correlated with their associated parameter and minimally correlated with all the others.

Finally, the previous tools are applied to the classification of drug from MEA measurements. The measurements are either experimental or synthetic. Synthetic measurements are generated using the forward PDE model (bidomain equations) adapted to the MEA. The classification of drugs is carried out using state-of-the-art Machine Learning tools. We also present an application to electrocardiogram measurements using a 3-D full-body electrophysiology model [BCF+10].

1.3 Contents and manuscript organization

The manuscript is organized as follows.

In Chapter 2, the statistical inverse problem framework is presented. The observ-

able moment matching method is presented along with the physical DOF selection algorithm. Some analysis of the PDF estimation error is provided and the hyper-parameters of the method are studied on an ODE test case. The approach is then illustrated with PDE and ODE models.

In Chapter 3, the observable moment matching is specifically applied to electrophysiology problems. The biological context is explained and the approach is illustrated with synthetic measurements. Then, the approach is applied to experimental measurements from which the PDF of some key parameters are estimated.

In Chapter 4, the feature selection algorithm is presented. The corresponding optimization problem is described. The approach is applied to simple test cases and then to electrophysiology and hemodynamics models.

In Chapter 5, a drug classification problem is proposed. Experimental measurements of MEA-hiPSC potentials are available with different drugs. The classification is carried out using Machine Learning algorithms. The classification is improved by incorporating synthetic MEA measurements generated using the bidomain equations.

In Chapter 6, the variability of human electrocardiograms (ECGs) is studied. A full-body, 3-D electrophysiology model is described and synthetic ECGs are generated using the FeLiScE finite element library. Some parameters of the model are varied to generate a synthetic population of ECGs in healthy and in pathological conditions. Numerical biomarkers are computed in order to monitor some key parameters of the heart and, eventually, solve parameter estimation problems.

1.4 Scientific dissemination

1.4.1 Publications

The presentation of the statistical inverse problem framework, the description of the observable moment matching method and its application to ODE and PDE models led to the following paper and its extended version on HAL:

- Jean-Frédéric Gerbeau, Damiano Lombardi, Eliott Tixier
  A moment-matching method to study the variability of phenomena described by partial differential equations.
  In Review.

- Extended version: `https://hal.archives-ouvertes.fr/hal-01391254`

The application of the observable moment matching method to electrophysiology data and in particular to experimental measurements led to the following paper:

- Eliott Tixier, Damiano Lombardi, Blanca Rodriguez, Jean-Frédéric Gerbeau
  Modeling variability in cardiac electrophysiology: a moment matching approach.
  Journal of the Royal Society Interface, 14(133), 2017.

- Also on HAL: https://hal.archives-ouvertes.fr/hal-01570828

The feature selection algorithm and its application to realistic biological scenarios led to the following paper:

- Jean-Frédéric Gerbeau, Damiano Lombardi, Eliott Tixier
  How to choose biomarkers in view of parameter estimation.
  Submitted.

The automatic classification of drugs from MEA measurements led to the following paper:

- Eliott Tixier, Fabien Raphel, Damiano Lombardi, Jean-Frédéric Gerbeau
  Optimal biomarkers design for drug safety evaluation using microelectrode array measurements.
  Submitted.

- Also on HAL: https://hal.archives-ouvertes.fr/hal-01570819

1.4.2 Conferences

- QUIET 2017 Workshop - Quantification of Uncertainty: Improving Efficiency and Technology, July 18-21, 2017, Trieste, Italy. *Poster presentation*

- SIAM Conference on Uncertainty Quantification, Apr 5-8, 2016, Lausanne, Switzerland. *Minisymposium talk*

- 4th International Conference on Computational & Mathematical Biomedical Engineering (CMBE 2015), June 29 - July 1, 2015, Cachan, France. *Minisymposium talk*

- 1st International Conference on Uncertainty Quantification in Computational Sciences (UNCECOMP 2015), May 25-27, 2015, Hersonissos, Greece. *Minisymposium talk*

- Lions-Magenes Days Scientific Meeting, April 13-14, 2015, Pavia, Italy. *Invited speaker*

1.4.3 Implementation

The algorithms described in this work were implemented in cardioXcomp, an in-house C++ project dedicated to the simulation of cardiac electrophysiology measurements and their analysis. I also contributed to the development of the C++ Finite Element library FeLiScE by implementing a Robin-Robin coupling between heart and torso for electrophysiology simulations.
To better spread our work and allow other people to use the tools we developed, three GitHub projects were set up.

- https://github.com/eltix/omm_jrsi: Implementations of the observable moment matching algorithm and the physical DOF selection algorithm. This project also contains the data required to replicate the results of Chapter 3.
- https://github.com/eltix/numbio: Implementation of the feature (numerical biomarker) selection algorithm and toy model data to demonstrate the method presented in Chapter 4.
- https://github.com/eltix/seqomm: Implementation of the coupling of the observable moment matching algorithm and the physical DOF selection as described in Chapter 2

Chapter 2

A Moment-Matching Method to Study the Variability of Phenomena Described by Partial Differential Equations

---

This chapter is based on [GLT16]

Many phenomena are modeled by deterministic differential equations, whereas the observation of these phenomena, in particular in life sciences, exhibits an important variability. This chapter addresses the following question: how can the model be adapted to reflect the observed variability?

Given an adequate model, it is possible to account for this variability by allowing some parameters to adopt a stochastic behavior. Finding the parameters probability density function that explains the observed variability is a difficult stochastic inverse problem, especially when the computational cost of the forward problem is high. In this paper, a non-parametric and non-intrusive procedure based on offline computations of the forward model is proposed. It infers the probability density function of the uncertain parameters from the matching of the statistical moments of observable degrees of freedom (DOFs) of the model. This inverse procedure is improved by incorporating an algorithm that selects a subset of the model DOFs that both reduces its computational cost and increases its robustness. This algorithm uses the pre-computed model outputs to build an approximation of the local sensitivities. The DOFs are selected so that the maximum information on the sensitivities is conserved. The method is studied and validated with a nonlinear ODE and the strategy is compared with two existing ones. Then, the proposed approach is illustrated with elliptic and parabolic PDEs.

Contents

2.1 Introduction 11
2.2 Methodology 12
2.2.1 Notation 12
2.2.2 Handling the noise 13
2.2.3 Overview of the strategy 14
2.2.4 Inverse problem: observable moment matching (OMM) . . . 14
2.2.5 Physical DOFs reduction: clustered sensitivities (CS) algorithm 24
2.2.6 Visualization and interpretation of the results 27
2.2.7 Main algorithm 28
2.3 Comparison with existing techniques for an ODE model . . 30
2.3.1 The MV model 30
2.3.2 Reference test case 31
2.3.3 Comparison with existing techniques 35
2.4 Numerical illustrations 39
2.4.1 Application to an elliptic PDE: the Darcy equations 39
2.4.2 Application to a parabolic PDE: the FKPP equation 43
2.5 Limitations and Discussion 46
2.6 Concluding remarks 47
2.7 Appendix 49
2.7.1 Calculus of variations 49
2.7.2 Illustration of the analysis hypotheses 50
2.7.3 Illustration with an unidentifiable model 51

2.1 Introduction

The context of this work is the following: a collection of experimental measurements is available, which exhibit variability, caused for instance by an heterogeneity in the physical settings [CDE06, SZ06]. We assume that the observable quantities correspond to the degrees of freedom (DOFs) of a model that depends on fixed and uncertain parameters. The model is typically a system of ordinary differential equations (ODE) or partial differential equations (PDE).

The aim of this paper is twofold. First, we propose a non-parametric and non-intrusive method to estimate the uncertain parameters probability density function (PDF) by exploiting the observable variability. Second, we propose a method to make this estimation "parsimonious", *i.e.* requiring as few model evaluations as possible and as few observables (or DOFs) as possible.

To tackle the first problem, two different strategies may be envisioned. First, one could estimate the model parameters associated with each experimental sample using classical inverse problem tools such as Bayesian approaches [WZ04, Kou09] or genetic algorithms [HNGK09]. These strategies would yield a collection of parameters values from which the PDF would be computed by using histograms or more sophisticated PDF estimation techniques [AA13]. As straightforward as this approach is, it becomes computationally intensive as the number of experimental samples grows larger. Second, one may see the experimental data set as a whole, which has the advantage of being both computationally cheaper and more robust to noise and low-quality measurements. In this paper, we focus on the second strategy and present an adaptation of the well-known problem of moments [ST43]. The problem of moments consists in finding the PDF of the parameters such that its statistical moments have a prescribed set of values. It has been used as an inverse problem tool with success in various contexts [GNSG11, SZ06, PS09]. A popular regularization of the problem of moments is the maximum entropy principle, which is rooted in information theory and is justified by practical mathematical considerations [Jay57, MP84]. In most cases however, parameters of a model are not directly observable. Therefore, one needs a technique that takes into account the observable variability. In this context, we introduce an "observable moment matching" method which consists in maximizing the PDF entropy under the constraints of matching the moments of the observable itself (not of the parameters). This is a two-step method. First, the model is evaluated for a fixed number of parameters samples and the corresponding outputs, i.e. the simulated observables, are stored. Second, the PDF is found by an iterative process that maximizes its entropy under the constraints of matching the moments of the experimental and simulated observables.

To address the second problem, we propose an algorithm that selects the DOFs in the physical domain where the moments are to be matched in order to alleviate the cost of the inverse problem – which is crucial for complex models such as PDEs – and to improve its conditioning. This algorithm exploits the sensitivity information provided by the pre-computed model evaluations. The sensitivity Gram matrix, computed for every DOF, reveals active subspaces [Con15, CELI15] of the parameter

space. The DOFs are selected by clustering the active subspaces and choosing their best representatives. This strategy allows for a reduction of the number of DOFs by several orders of magnitude and therefore proves to drastically reduce the computational cost of the inverse problem without requiring any additional evaluation of the model.

This paper is organized as follows. The whole methodology is detailed in Section 2.2. First, we introduce the observable moment matching algorithm and we formulate the associated inverse problem in terms of an optimization problem. Then, the clustered sensitivities algorithm is introduced and the reduction of the number of DOFs is explained. In Section 2.3, our approach is illustrated with a set of ODEs modeling the transient action potential of a heart cell. We compare its performance with two existing statistical inverse problem techniques: one proposed by N. Zabaras and B. Ganapathysubramanian [ZG08], the other one proposed by E. Kuhn and M. Lavielle [KL05]. In Section 2.4, our algorithm is applied to the Darcy equations. The PDF of five coefficients that parametrize an inner field is recovered using measurements on the domain boundaries. Then, we consider a nonlinear parabolic PDE model, namely the FKPP equation. Under certain conditions, this model exhibits a wave propagation whose shape depends on the location of the source term and on certain parameters. The PDFs of the source term and the reaction parameters are recovered using measurements at different times and locations.

Finally, we present some concluding remarks in Section 2.6.

2.2 Methodology

2.2.1 Notation

Let us consider a data set that exhibits variability and a physical model assumed to accurately depict the observations. Let $\mathcal{D} \subseteq \mathbb{R}^d$ be an open subset, the physical domain (space, time or space-time), in which the governing equations are written. Let $(\Theta, \mathcal{A}, \mathcal{P})$ be a complete probability space, Θ being the set of outcomes, $\mathcal{A}$ a σ–algebra and $\mathcal{P}$ a probability measure. The model can be written in a compact notation as:

$$\mathcal{L}(u(\mathbf{x}, \boldsymbol{\theta})) = \mathbf{0}, \tag{2.1}$$

where $\mathcal{L}$ denotes a generic nonlinear differential operator.
The vector $\boldsymbol{\theta} = \left(\theta_1, \ldots, \theta_{n_p}\right) \in \Theta$ denotes the uncertain parameters of the model and Θ is a bounded subset of $\mathbb{R}^{n_p}$, sometimes referred to as the stochastic domain [ZG08]. A set of measurements $\{\mathbf{y}_1, \ldots, \mathbf{y}_N\}$ is available. Each measurement $\mathbf{y}_i$ is assumed to take the following form:

$$\mathbf{y} = g\left(u(\mathbf{x}, \boldsymbol{\theta})\right) + \varepsilon, \tag{2.2}$$

where g is a function describing the measurement process and ε is the noise, assumed to be additive and independent. For practical reasons, g is normalized to take values in $[0, 1]$. Let $\mathbb{E}$ be the expectation operator. We make the hypothesis that the random fields associated with the observables are p-integrable, that is:

$\int_{\mathcal{D}} |\mathbb{E}(y^p)| \, \mathrm{d}\mathbf{x} < M$, where the exponent p is the highest available moment. The variability in the observations is due to two main contributions: the variability in the parameters and the noise in the measurement process. In a classical forward Uncertainty Quantification (UQ) context, given the probability density function (PDF) of the parameters ρ, the moments of the observables are computed. In the present work, an inverse problem is solved which consists in finding the PDF of the parameters that generates the observed variability in a set of available data. Let us introduce the m^{th} order empirical moment of the measurements:

$$\mu_m(\mathbf{x}) = \frac{1}{N} \sum_{i=1}^{N} y_i(\mathbf{x})^m \approx \mathbb{E}((g+\varepsilon)^m), \tag{2.3}$$

and the m^{th} order moment of the simulations:

$$\mu_m^\rho(\mathbf{x}) = \int_{\boldsymbol{\theta}\in\Theta} (y_{sim}(\boldsymbol{\theta}))^m \, \rho(\boldsymbol{\theta}) \mathrm{d}\boldsymbol{\theta} = \mathbb{E}(y_{sim}^m), \tag{2.4}$$

where y_{sim} are the observations of the simulated system.

2.2.2 Handling the noise

Under the assumption that the noise is additive, independent and with a known structure, it is straightforward to account for its influence on the measurements moments. Using the linearity of the expectation operator and the independence of the noise, it follows from definition (2.2) that:

$$\mathbb{E}\left[y^m\right] = \sum_{k=0}^{m} \binom{m}{k} \mathbb{E}\left[g^m\right] \mathbb{E}\left[\varepsilon^{m-k}\right].$$

As an example, consider the case where the noise follows a zero-mean normal distribution with a known variance τ^2: $\varepsilon \sim \mathcal{N}(0, \tau^2)$. Then, the following corrections may be applied to the first three empirical moments defined in Eq. (2.3):

$$\begin{aligned}
\tilde{\mu}_1(\mathbf{x}) &= \mu_1(\mathbf{x}), \\
\tilde{\mu}_2(\mathbf{x}) &= \mu_2(\mathbf{x}) - \tau^2, \\
\tilde{\mu}_3(\mathbf{x}) &= \mu_3(\mathbf{x}) - 3\tau^2 \mu_1(\mathbf{x}).
\end{aligned}$$

In the numerical experiments, the noise is assumed to be gaussian and its level is defined as the ratio $4\tau/A$ where A is the signal amplitude. In Section 2.3, the effect of τ^2 on the PDF estimation is investigated.

Only Gaussian noises are considered here. However, the same procedure may be applied to any noise whose power moments are known. If the noise structure is completely unknown, a strategy can be set up to estimate it but it is not investigated in the present work.

2.2.3 Overview of the strategy

The overall algorithm aims at estimating the PDF ρ of the uncertain parameters $\boldsymbol{\theta}$, given the empirical moments of the observables. The Jaynes principle of maximum entropy is applied (see [Jay57]): the PDF is sought so that it has the maximum entropy under the constraints that the experimental and simulated moments be equal. Two additional constraints correspond to the positivity and the PDF normalization. This leads to the following optimization problem:

$$\begin{cases} \textbf{Minimize:} & \int_\Theta \rho \log(\rho) & \\ \textbf{Subject to:} & \tilde{\mu}_m(\mathbf{x}) - \mu_m^\rho(\mathbf{x}) = 0, & \forall \mathbf{x} \in \mathcal{D}, 1 \leq m \leq N_m, \\ & \rho(\boldsymbol{\theta}) \geq 0, & \forall \boldsymbol{\theta} \in \Theta, \\ & \int_\Theta \rho = 1. & \end{cases} \tag{2.5}$$

In what follows, this is referred to as the Observable Moment Matching (OMM) problem. In Section 2.2.4 the optimality conditions for the OMM problem are derived and a dual formulation is introduced. The latter leads to a nonlinear problem which is, in general, ill-conditioned. Moreover, its computational cost is prohibitive when models described by PDEs are at hand. To overcome these difficulties a reduction approach is introduced, based on a sensitivity analysis. As a consequence, the OMM procedure is only applied to a subset $\mathcal{S}$ of the DOFs of the model variables discretized in the physical domain $\mathcal{D}$. More precisely, the eigendecomposition of an approximation of the following matrix is computed:

$$\mathbf{C}(\mathbf{x}) = \int_\Theta \left[\nabla_{\boldsymbol{\theta}} g(\mathbf{x}, \boldsymbol{\theta})\right] \left[\nabla_{\boldsymbol{\theta}} g(\mathbf{x}, \boldsymbol{\theta})\right]^T \rho(\boldsymbol{\theta}) \mathrm{d}\boldsymbol{\theta}, \tag{2.6}$$

referred to as the exact sensitivity Gram matrix (SGM).The study of the SGM eigenvalues allows us to identify active subspaces [Con15] in the parameter space associated with each DOF. The subspaces are clustered based on a similarity function and the "best" DOFs are then picked based on a criterion defined in Section 2.2.5 to form the selected subset $\mathcal{S}$. This selection method will be later referred to as the Clustered Sensitivities (CS) procedure.

2.2.4 Inverse problem: observable moment matching (OMM)

The classical problem of moments consists in finding a PDF ρ of the parameters θ_k from the knowledge of a finite number N_m of its power moments $\mu_{m,k}$, $m = 1, \ldots, N_m$, $k = 1, \ldots, n_p$:

$$\mathbb{E}_\rho\left[\theta_k^m\right] = \mu_{m,k}, \qquad m = 1, \ldots, N_m, \ k = 1, \ldots, n_p,$$

where $\mathbb{E}_\rho(\cdot)$ denotes the expectation operator given a density function ρ. This problem has been extensively discussed in the literature and has been addressed by adopting a wide range of strategies. When only a finite number of moments are known, which is often the case in practice, the problem becomes under-determined.

Indeed, there exists an infinite number of densities that have the same N_m moments. Therefore, one needs to introduce a regularization in order to obtain a unique distribution function among all the feasible solutions. Several approaches exist, such as minimizing the mean squared error $\varepsilon(\rho) = \sum_{m,k} \left(\mathbb{E}_\rho\left[\theta_k^m\right] - \mu_{m,k}\right)^2$ with the constraint that ρ be a finite expansion of polynomials [HLM14] or Padé approximants [WG69].

This problem has been successfully used in situations where the moments of the model parameters are directly measurable, for instance in the context of microstructure reconstruction [GNSG11, SZ06, PS09]. In general however, the moments of the model parameters are not observable. Therefore, we propose to apply the moment matching constraints not on the parameters but on the observable itself.

To regularize the problem, the maximum entropy principle is used: find the PDF that maximizes the entropy under the constraint of matching the first N_m moments, where the Shannon definition [Sha48] of the PDF entropy reads: $S(\rho) = -\int_\Theta \rho \log(\rho)$. There are three main reasons why this choice of regularization is well suited to the present case. First, from an information theory point of view, the maximum entropy PDF is considered the best choice when a limited amount of information is available (here, only a finite number of moments are known). This principle was first introduced by Jaynes [Jay57] and was successfully applied to numerous practical cases [MP84, SZ06, MLKDC10, VdSB08]. Second, $-S(\rho)$ is a convex cost function which enables the use of efficient optimization tools. Last, ρ can be written as an exponential term (see below), which dispenses the addition of an inequality constraint ensuring its positivity.
A set of constraint functions is introduced, expressing the mismatch between the moments of the measured observable and the moment of the simulated observable. They read:

$$c_m(\mathbf{x}) = \mu_m^\rho(\mathbf{x}) - \tilde{\mu}_m(\mathbf{x}) = \int_\Theta g^m(\mathbf{x}, \boldsymbol{\theta}) \rho(\boldsymbol{\theta}) \, \mathrm{d}\boldsymbol{\theta} - \tilde{\mu}_m(\mathbf{x}), \quad m = 1, \dots, N_m. \tag{2.7}$$

Introducing the Lagrange multipliers $\lambda(\mathbf{x}) = (\lambda_m(\mathbf{x}))_{m=1\dots N_m}$, λ_0 and $\nu(\boldsymbol{\theta})$, the initial optimization problem (2.5) is recast in the following saddle-point problem:

$$\inf_\rho \sup_{\lambda, \lambda_0, \nu \geq 0} \mathcal{L}\left(\rho, \lambda, \lambda_0, \nu\right), \tag{2.8a}$$

with

$$\mathcal{L}\left(\rho, \lambda, \nu\right) = \int_\Theta \rho \log(\rho) - \sum_{m=1}^{N_m} \int_\mathcal{D} \lambda_m(\mathbf{x}) c_m(\mathbf{x}) \, \mathrm{d}\mathbf{x} - \lambda_0 \left(\int_\Theta \rho - 1 \right) - \int_\Theta \rho \nu. \tag{2.8b}$$

The Euler-Lagrange equations are derived from the calculus of variations (see Appendix 2.7.1). The necessary conditions for optimality are derived by cancelling out

$\partial\mathcal{L}/\partial\rho$ in (2.52) and $\partial\mathcal{L}/\partial\lambda$ in (2.54):

$$\rho = \exp(\nu + \lambda_0 - 1) \exp\left(\sum_{m=1}^{N_m} \int_{\mathcal{D}} g^m \lambda_m \, \mathrm{d}\mathbf{x}\right), \tag{2.9}$$

$$\int_{\Theta} g^m \exp(\lambda_0 - 1) \exp\left(\sum_{h=1}^{N_m} \int_{\mathcal{D}} g^h \lambda_h \, dx\right) \, \mathrm{d}\boldsymbol{\theta} - \tilde{\mu}_m = 0, \; m = 1, \ldots, N_m \tag{2.10}$$

In the present case, by virtue of the entropy regularization, the primal variable ρ can be expressed in an analytic form as a function of the dual variable and the positivity constraint is automatically satisfied (Eq.(2.9)). Hence, the solution of the system can be reduced to the solution of a nonlinear problem for the dual variable (Eq.(2.10)).

In the following, we suppose the problem is well-posed in the sense that the solution exists and is unique. It is shown in Appendix B of [GS13] that it is the case when the constraints are algebraically independent. The algebraic independence of the constraints, as formulated in [GS13], is equivalent to saying that there exists a non-zero measure subset $\tilde{\Theta}$ of Θ such that, for any nonzero vector $v^{(m)}$, $m = 1, \ldots, N_m$ in $L^2(\mathcal{D})$, one has:

$$\mathcal{A}_{\tilde{\Theta}} := \int_{\tilde{\Theta}} \left(\sum_{m=1}^{N_m} \left\langle v^{(m)}, g^m \right\rangle_{L^2(\mathcal{D})} \right)^2 \mathrm{d}\boldsymbol{\theta} > 0. \tag{2.11}$$

The error in the density can be evaluated by means of the Kullback-Leibler divergence. In the following Lemma, it is shown that it is bounded by the error in the dual variable. Let the distribution that maximizes the entropy under the moment constraints be denoted by ρ^* and let its actual approximation be ρ. The true dual variable being λ^* and its approximation being λ, the error in the dual variable is defined as: $\delta\lambda := \lambda^* - \lambda$. The following result holds.

Lemma 2.1
The Kullback-Leibler (KL) divergence between ρ^* and ρ, denoted by $\phi(\rho^*|\rho)$, is bounded by the error in the dual variable as follows:

$$|\phi(\rho^*|\rho)| \leq |\delta\lambda_0| + \mathrm{meas}(\mathcal{D})^{1/2} \sum_{m=1}^{N_m} \|\delta\lambda_m\|_{\mathbf{x},2}. \tag{2.12}$$

Proof. The KL divergence reads:

$$\phi(\rho^*|\rho) := \int_{\Theta} \log\left(\frac{\rho^*}{\rho}\right) \, \rho^* \mathrm{d}\boldsymbol{\theta}. \tag{2.13}$$

We deduce from the optimality conditions:

$$\frac{\rho^*}{\rho} = \exp(\delta\lambda_0) \exp\left(\sum_{m=1}^{N_m} \langle g^m, \delta\lambda_m \rangle_{\mathbf{x}}\right), \tag{2.14}$$

so that the expression of the KL divergence can be rewritten as:

$$\phi(\rho^*|\rho) = \delta\lambda_0 + \sum_{m=1}^{N_m} \int_\Theta \langle g^m, \delta\lambda_m \rangle_{\mathbf{x}} \ \rho^* \mathrm{d}\boldsymbol{\theta}. \tag{2.15}$$

The Cauchy-Schwarz inequality is applied to the scalar product in the physical space:

$$|\phi(\rho^*|\rho)| \leq |\delta\lambda_0| + \sum_{m=1}^{N_m} \|\delta\lambda_m\|_{\mathbf{x},2} \int_\Theta \|g^m\|_{\mathbf{x},2}(\boldsymbol{\theta}) \ \rho^* \mathrm{d}\boldsymbol{\theta}. \tag{2.16}$$

Hence the result since the observable is bounded by 1. ■

2.2.4.1 Discretization of the inverse problem

The discretization of the nonlinear system Eq.(2.10) is addressed in this section. The observable, as well as the Lagrange multipliers λ_m, are discretized in space (or space-time) by means of standard methods and the total number of DOFs is denoted by $N_{\mathbf{x}}$. The integrals in the stochastic space are approximated by a quasi-Monte Carlo method. The stochastic domain Θ is discretized using the Sobol sequence [Sob76]. These quasi-random samples have a low-discrepancy, and are competitive compared to random uniform samples [Lem09]. When integrating functions featuring a certain regularity, sparse grid methods, which are often used in uncertainty propagation (see [GZ07]), can outperform quasi-Monte Carlo ones [BG04]. In the present context, however, a reason to prefer a quasi-Monte Carlo discretization of the stochastic domain is that the probability density distribution is the unknown of the problem, and it is not known in advance. Roughly speaking, since sparse grids have strong preferential directions, the risk of "missing" the area of interest in the stochastic domain is non-negligible, making evenly distributed points a more suitable discretization. Figure 2.1 shows how a two-dimensional domain is discretized using each of the three options described above. It illustrates how the Sobol sequence both performs a more even coverage of the domain than uniform pseudo-random samples and does not favor specific directions such as in sparse grids. Let us denote

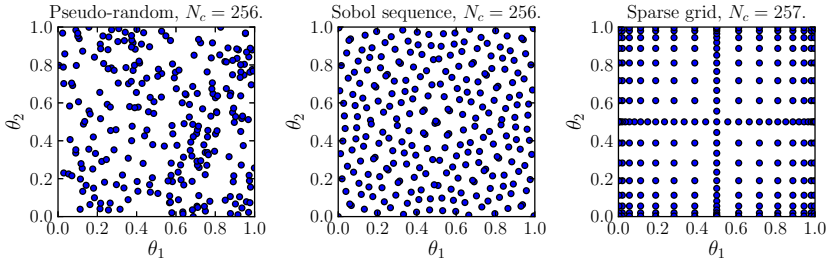

Figure 2.1: Different discretizations of the parameter space: random uniform (left), Sobol sequence (center), sparse grid (right).

by N_c the number of sample points in Θ and $|\Theta|$ the stochastic domain volume.

To compute the integrals approximations in (2.10), the model is evaluated for each sample $\boldsymbol{\theta}_i$. The corresponding set $\{y_{sim}(\boldsymbol{\theta}_i, \mathbf{x}_j), i = 1, \dots, N_c,\ j = 1, \dots, N_{\mathbf{x}}\} \in \mathbb{R}^{N_c \times N_{\mathbf{x}}}$ will later be referred to as the *simulation set*. Assuming a subset $\mathcal{S}$ of $\mathcal{D}$ has been selected, the number of DOFs in $\mathcal{S}$ is denoted by N_k. For the sake of clarity, the following notation is now used:

$$\rho_i = \rho(\boldsymbol{\theta}_i), \quad g_{i,j} = y_{sim}(\boldsymbol{\theta}_i, \mathbf{x}_j), \quad \lambda_{j,m} = \lambda_m(\mathbf{x}_j), \quad \mu_{j,m} = \mu_m(\mathbf{x}_j), \quad \beta = \frac{|\Theta|}{N_c}$$
$$\text{for} \quad i = 1, \dots, N_c, \quad j = 1, \dots, N_k, \quad m = 1, \dots, N_m.$$

The discretization of Eq.(2.9) reads:

$$\rho_i = \exp(\lambda_0 - 1) \exp\left(\sum_{j=1}^{N_k} \sum_{m=1}^{N_m} \omega_j \lambda_{j,m} g_{i,j}^m \right), \quad i = 1, \dots, N_c, \tag{2.17}$$

where the ω_j are quadrature weights for the physical domain discretization.

Before discretizing Eq.(2.10), a vector form is introduced. Let $\boldsymbol{\omega} = \begin{bmatrix} \omega_1 & \dots & \omega_{N_k} \end{bmatrix}$, $\boldsymbol{\lambda} = \begin{bmatrix} \lambda_{1,1} & \dots & \lambda_{N_k,N_m} & \lambda_0 - 1 \end{bmatrix}^T$, $\boldsymbol{\mu} = \begin{bmatrix} \tilde{\mu}_{1,1} & \dots & \tilde{\mu}_{N_k,N_m} & 1 \end{bmatrix}^T$ and $\mathbf{G} = \begin{bmatrix} \mathbf{G}^{(1)} & \dots & \mathbf{G}^{(N_m)} & \mathbf{1} \end{bmatrix}^T$ with $G_{i,j}^{(k)} = g_{i,j}^k$, $k = 1, \dots, N_m$, $i = 1, \dots, N_c$, $j = 1, \dots, N_k$. Note that $\mathbf{G} \in \mathbb{R}^{N_G \times N_c}$ where $N_G = N_k N_m + 1$. It has an extra column of ones to take into account the normalization constraint. Finally, let $\boldsymbol{\Delta} = \operatorname{diag}(\underbrace{\boldsymbol{\omega}, \boldsymbol{\omega}, \dots, \boldsymbol{\omega}}_{N_m \text{ times}}, 1)$.

The density can be written as: $\boldsymbol{\rho} = \exp\left(\mathbf{G}^T \boldsymbol{\Delta} \boldsymbol{\lambda}\right)$. The discretization of Eq.(2.10) reads:

$$\beta \mathbf{G} \boldsymbol{\rho} - \boldsymbol{\mu} = \beta \mathbf{G} \exp\left(\mathbf{G}^T \boldsymbol{\Delta} \boldsymbol{\lambda}\right) - \boldsymbol{\mu} = 0. \tag{2.18}$$

A Newton method is used to solve this step. However, since the Hessian is ill-conditioned in practical cases, a regularization is proposed. Let $\mathbf{U}, \mathbf{S}, \mathbf{V}$ be the SVD decomposition of $\mathbf{G}$, done with respect to the scalar product induced by $\boldsymbol{\Delta}$, *i.e.* $\mathbf{U}^T \boldsymbol{\Delta} \mathbf{U} = I$. The residual now reads:

$$\mathbf{r} = \beta \mathbf{U} \mathbf{S} \mathbf{V}^T \exp\left[\mathbf{V} \mathbf{S} \mathbf{U}^T \boldsymbol{\Delta} \boldsymbol{\lambda}\right] - \boldsymbol{\mu}. \tag{2.19}$$

Instead of making $\mathbf{r}$ vanish, we propose to solve for $\hat{\mathbf{r}} = \hat{\mathbf{U}}^T \boldsymbol{\Delta} \mathbf{r} = 0$. This is equivalent to taking a low-rank approximation $\hat{\mathbf{G}}$ of $\mathbf{G}$ by replacing the matrix of singular values $\mathbf{S}$ with its truncation $\hat{\mathbf{S}}$. $\hat{\mathbf{S}}$ is defined so that it shares the first n_σ singular values with $\mathbf{S}$ and the following are set to zero. The low-rank approximation $\hat{\mathbf{U}}$ (resp. $\hat{\mathbf{V}}$) of $\mathbf{U}$ (resp. $\mathbf{V}$) is obtained by setting its last $n_G - n_\sigma$ columns to zero. Replacing $\mathbf{G}$ by $\hat{\mathbf{G}} = \hat{\mathbf{U}} \hat{\mathbf{S}} \hat{\mathbf{V}}^T$ in (2.19) and left-multiplying by $\hat{\mathbf{U}}^T \boldsymbol{\Delta}$, one obtains:

$$\hat{\mathbf{r}} = \beta \hat{\mathbf{S}} \hat{\mathbf{V}}^T \exp\left[\hat{\mathbf{V}} \hat{\mathbf{S}} \hat{\mathbf{U}}^T \boldsymbol{\Delta} \boldsymbol{\lambda}\right] - \hat{\mathbf{U}}^T \boldsymbol{\Delta} \boldsymbol{\mu}. \tag{2.20}$$

Proceeding to the change of variables $\boldsymbol{\lambda} = \hat{\mathbf{U}}\boldsymbol{\phi}$, the residual now reads:

$$\hat{\mathbf{r}} = \beta\hat{\mathbf{S}}\hat{\mathbf{V}}^T\boldsymbol{\rho} - \hat{\mathbf{U}}^T\boldsymbol{\Delta}\boldsymbol{\mu}, \tag{2.21a}$$

$$\text{where} \quad \boldsymbol{\rho} = \exp\left[\hat{\mathbf{V}}\hat{\mathbf{S}}\boldsymbol{\phi}\right]. \tag{2.21b}$$

Note that the residual is no longer a function of the vector of experimental moments $\boldsymbol{\mu}$ but rather its projection $\hat{\mathbf{U}}^T\boldsymbol{\Delta}\boldsymbol{\mu}$. Therefore, the number of non-truncated singular values n_σ is chosen so that the representation error $\| \left(\mathbf{I} - \hat{\mathbf{U}}\hat{\mathbf{U}}^T\boldsymbol{\Delta}\right)\boldsymbol{\mu}\|$ is smaller than a user-defined tolerance parameter α. The Hessian matrix of the problem now reads:

$$\mathbf{H} = \frac{\partial\hat{\mathbf{r}}}{\partial\boldsymbol{\phi}} = \beta\hat{\mathbf{S}}\hat{\mathbf{V}}\text{diag}(\boldsymbol{\rho})\hat{\mathbf{V}}^T\hat{\mathbf{S}}, \tag{2.22}$$

which is symmetric, positive semi-definite of rank n_σ. Its Moore-Penrose pseudo-inverse $\mathbf{P}$ is computed and the Newton actualization step reads:

$$\boldsymbol{\phi}^{(n+1)} = \boldsymbol{\phi}^{(n)} - \mathbf{P}\hat{\mathbf{r}}. \tag{2.23}$$

The components of $\boldsymbol{\phi}$ are initialized to zero, which is equivalent to taking a uniform PDF as the initial guess for $\boldsymbol{\rho}$ or, more precisely, a uniform mass on the discrete ρ_i. The overall OMM inverse procedure in summarized in Algorithm 1.

Remark that the problem of computing the PDF value at each collocation point

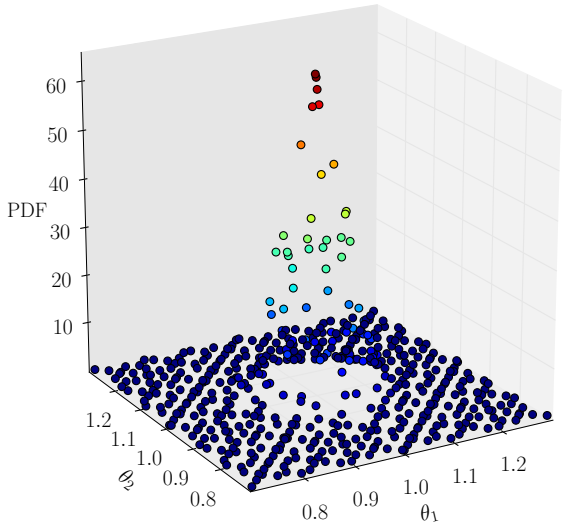

Figure 2.2: Solution of the moment-matching method: joint PDF of two parameters.

$\rho_i, i = 1, \ldots, N_c$ has been transformed into a problem of computing the unknown Lagrange multipliers λ_0, $\lambda_{1,1}, \ldots, \lambda_{N_k,N_m}$. In other words, the size of the problem is now that of the physical domain subset ($\mathcal{S}$) times the number of moments instead

Algorithm 1: Observable moment matching algorithm.

Input:

- $\mathcal{S} = \{\mathbf{x}_1, \ldots, \mathbf{x}_{N_k}\}$ subset of $\mathcal{D}$ selected using CS algorithm.
- $\tilde{\mu}_{j,m}$, $j = 1, \ldots, N_k$, $m = 1, \ldots, N_m$: corrected experimental moments.
- $g_{i,j}$, $i = 1, \ldots, N_c$, $j = 1, \ldots, N_k$: simulation subset.
- A tolerance $\alpha > 0$.
- A stopping criterion for the Newton iterations $\varepsilon_{\text{Newton}} > 0$.

Initialization:

- Assemble $\mathbf{G} = \begin{bmatrix}((g_{i,j})) & \ldots & ((g_{i,j}))^{N_m} & \mathbf{1}\end{bmatrix}$ and $\boldsymbol{\mu} = \begin{bmatrix}((\tilde{\mu}_{j,k})) & 1\end{bmatrix}$.
- Compute SVD decomposition of $\mathbf{G}$: $\mathbf{U}, \mathbf{S}, \mathbf{V}$
- Number of singular values $n_\sigma = \text{Card}\left\{\sigma \mid \| \left(\mathbf{I} - \hat{\mathbf{U}}\hat{\mathbf{U}}^T\right) \boldsymbol{\mu}\| \leq \alpha\right\}$.
- $\boldsymbol{\phi}^{(0)} = \mathbf{0}$ (*i.e.* $\boldsymbol{\rho}^{(0)}$ uniform over Θ).

$n = 1$;
while $\|\hat{\mathbf{r}}^{(n-1)}\| > \varepsilon_{Newton}$ **do**
  Compute $\boldsymbol{\rho}^{(n)}$ using (2.21b);
  Compute residual $\hat{\mathbf{r}}^{(n)}$ = using (2.21a);
  Assemble Hessian matrix $\mathbf{H}^{(n)}$ using (2.22);
  Update Lagrange multipliers using (2.23);
  $n \leftarrow n + 1$;
end

Output: ρ_i, $i = 1, \ldots, N_c$: the PDF estimate.

of that of the stochastic domain. This is therefore computationally cheaper as long as the physical subset size remains sufficiently small, an issue that is addressed in the next section.

2.2.4.2 Analysis of the regularization error

In this section, we propose to justify some aspects of the proposed strategy. The true measure on the stochastic domain is $\mathcal{P}_e$, absolutely continuous with respect to Lebesgue measure. The associated probability density is ρ_e. The density which maximizes the entropy under the moment constraints is denoted by ρ^* and the actual approximation is ρ. There are two main contributions to the error: the first one is related to the entropic regularization, and the second one is due to the approximation of the constrained optimization problem. The latter is controlled by the norm of the error in the dual variable approximation, as shown in Lemma 2.1. In what follows, the regularization error is studied.

The hypotheses under which this analysis is performed are the following: the observable is $g(\mathbf{x}, \boldsymbol{\theta}) \in H^1(\mathcal{D} \times \Theta) \cap L^\infty(\mathcal{D} \times \Theta)$. We remind that we assume that g takes values in $[0, 1]$. The standard $L^2(\mathcal{D} \times \Theta)$ scalar product is denoted by $\langle u, v \rangle$, and the norms are defined accordingly. The scalar product in the physical and in the stochastic space will be denoted by $\langle u, v \rangle_{\mathbf{x}}$ and $\langle u, v \rangle_{\boldsymbol{\theta}}$ respectively.

The regularization error is studied in the case where an infinite number of moments exists. A first Lemma is presented to prove under which condition the total residual on the moments is L^2 summable, and then an identifiability condition for the inverse problem is derived.

LEMMA 2.2
Let $\|v\|_{L^p(\mathcal{D}\times\Theta),\rho_e} = \left(\int_{\mathcal{D}} \int_{\Theta} v^p \mathrm{d}\mathbf{x}\rho_e \mathrm{d}\boldsymbol{\theta}\right)^{1/p}$ *be the* L^p *norm. If there exist* $C, \delta > 0$ *such that* $\|g\|_{L^p(\mathcal{D}\times\Theta),\rho_e} \leq \left(\frac{C}{p^{1+\delta}}\right)^{1/p}$, *then* $\sum_{m=1}^{\infty} \|\mu_m^{\rho_e}\|^2_{L^2(\mathcal{D})} < +\infty$.

Proof. The Jensen inequality gives:

$$\|\mu_m^{\rho_e}\|^2_{L^2(\mathcal{D})} = \int_{\mathcal{D}} \left(\int_{\Theta} g^m \rho_e \, d\boldsymbol{\theta} \right)^2 d\mathbf{x} \leq \|g^m\|^2_{L^2(\mathcal{D}\times\Theta),\rho_e}. \tag{2.24}$$

The norm can be rewritten as follows:

$$\|g^m\|^2_{L^2(\mathcal{D}\times\Theta),\rho_e} = \int_{\mathcal{D}} \int_{\Theta} g^{2m} \, d\mathbf{x} \, \rho_e \mathrm{d}\boldsymbol{\theta} = \|g\|^{2m}_{L^{2m}(\mathcal{D}\times\Theta),\rho_e} \leq \frac{C}{(2m)^{1+\delta}}, \tag{2.25}$$

and thus:

$$\sum_{m=1}^{\infty} \|\mu_m^{\rho_e}\|^2_{L^2(\mathcal{D})} \leq \sum_{m=1}^{\infty} \frac{C}{(2m)^{1+\delta}} < +\infty. \tag{2.26}$$

■

The hypotheses of Lemma 2.2 are difficult to verify in practice with complex PDE models such as those studied in the present work. It is however possible to show that they are verified in some simpler cases as described in Section 1 of the Supplementary Material.
Let us assume that both the exact density ρ_e and the entropic regularization ρ^* satisfy the hypotheses of Lemma 2.2. Upper and lower bounds for the L^2 error $\varepsilon := \rho_e - \rho^*$ can be found. Consider that, by linearity: $\int_{\mathcal{D}} g^m \varepsilon = \mu_m^{\rho_e} - \mu_m^{\rho^*} = \delta\mu_m$. The result is summarized in the following proposition.

Proposition 1
Let ρ_e, ρ^* satisfy the hypotheses of Lemma 2.2.

Let $\gamma = \inf_{\|v\|_{L^2(\mathcal{D}\times\Theta)}=1} \left[\sum_{m=1}^{\infty} \langle g^m, v\rangle^2\right]$; let $\beta = \sum_{m=1}^{\infty} \|g^m\|^2_{L^2(\mathcal{D}\times\Theta)}$. Then, assuming $\beta, \gamma > 0$:

$$\frac{\sum_{m=1}^{\infty} \|\delta\mu_m\|^2_{L^2(\mathcal{D})}}{\beta} \leq \|\varepsilon\|^2_{L^2(\Theta)} \leq \frac{\sum_{m=1}^{\infty} \|\delta\mu_m\|^2_{L^2(\mathcal{D})}}{\gamma}. \tag{2.27}$$

Proof. The Cauchy-Schwarz inequality implies:

$$\sum_{m=1}^{\infty} \|\delta\mu_m\|^2_{L^2(\mathcal{D})} = \sum_{m=1}^{\infty} \int_{\mathcal{D}} \left(\int_{\Theta} g^m \varepsilon \, d\boldsymbol{\theta}\right)^2 \mathrm{d}\mathbf{x} \leq \sum_{m=1}^{\infty} \int_{\mathcal{D}} \int_{\Theta} \|g^m\|^2_{L^2(\Theta)} \|\varepsilon\|^2_{L^2(\Theta)} \mathrm{d}\mathbf{x}, \tag{2.28}$$

The error norm does not depend on the physical space coordinates and thus:

$$\sum_{m=1}^{\infty} \int_{\mathcal{D}} \int_{\Theta} \|g^m\|^2_{L^2(\Theta)} \|\varepsilon\|^2_{L^2(\Theta)} \mathrm{d}\mathbf{x} \leq \left(\sum_{m=1}^{\infty} \|g^m\|^2_{L^2(\mathcal{D}\times\Theta)}\right) \|\varepsilon\|^2_{L^2(\Theta)} = \beta \|\varepsilon\|^2_{L^2(\Theta)}. \tag{2.29}$$

Then, the upper bound for the error is proved:

$$\sum_{m=1}^{\infty} \|\delta\mu_m\|^2_{L^2(\mathcal{D})} = \sum_{m=1}^{\infty} \int_{\mathcal{D}} \left(\int_{\Theta} g^m \varepsilon \mathrm{d}\boldsymbol{\theta}\right)^2 \mathrm{d}\mathbf{x}, \tag{2.30}$$

$$\geq \sum_{m=1}^{\infty} \inf_{\|v\|_{L^2(\mathcal{D}\times\Theta)}=1} \left[\langle g^m, v\rangle^2\right] \|\varepsilon\|^2_{L^2(\theta)}, \tag{2.31}$$

that can be deduced by considering that g^m can be expressed on a dense tensorized complete orthonormal basis of $L^2(\mathcal{D}) \otimes L^2(\Theta)$. Indeed, let $\{r_1(\mathbf{x})s_1(\boldsymbol{\theta}), r_2(\mathbf{x})s_2(\boldsymbol{\theta}), \ldots\}$ be such as basis. One has in particular $\langle r_j, r_k\rangle_{L^2(\mathcal{D})} = \delta_{j,k}$ and $\langle s_j, s_k\rangle_{L^2(\Theta)} = \delta_{j,k}$. For a given m, by considering the decomposition of g^m

onto this basis, $g_m = \sum_{j=1}^{\infty} \langle g^m, r_j s_j \rangle \, r_j s_j$ and defining $b_j^m := \langle g^m, r_j s_j \rangle$, one has:

$$\int_{\mathcal{D}} \left(\int_{\Theta} g^m \varepsilon \mathrm{d}\boldsymbol{\theta} \right)^2 \mathrm{d}\mathbf{x} = \int_{\mathcal{D}} \left(\int_{\Theta} \sum_{j=1}^{\infty} b_j^m r_j s_j \varepsilon \right)^2 \mathrm{d}\mathbf{x}, \tag{2.32}$$

$$= \int_{\mathcal{D}} \left(\sum_{j=1}^{\infty} b_j^m \hat{\varepsilon}_j r_j \right)^2 \mathrm{d}\mathbf{x}, \quad \text{where } \hat{\varepsilon}_j := \langle \varepsilon, s_j \rangle_{L^2(\Theta)} \tag{2.33}$$

$$= \sum_{j=1}^{\infty} \langle g^m, r_j s_j \rangle^2 \, \hat{\varepsilon}_j^2, \tag{2.34}$$

$$\geq \inf_{\|v\|_{L^2(\mathcal{D}\times\Theta)}=1} \langle g^m, v \rangle^2 \, \|\varepsilon\|_{L_2(\Theta)}^2 \tag{2.35}$$

■

The condition for the error to be bounded, namely $\gamma > 0$, can be seen also as an identifiability condition for the problem and it is verified when the set of function g^m is a complete basis of the space. The result of the following Lemma shows a meaningful case in which the density is not identifiable and the error is unbounded.

LEMMA 2.3
Let the stochastic domain be the box $\Theta = \Theta_1 \times \dots \Theta_d$. Let $\mathcal{D}_1 \subseteq \mathcal{D}$ an open subset of the physical domain where the observable does not depend on θ_i, i.e. for which $\partial_{\theta_i} g = 0$. Then $\gamma = 0$.

Proof. The proof is done in a constructive way, by building a function v which is of unitary norm, making the scalar product with all the g^m vanish. Let $v = f_1(\theta_i) f_2(\theta_{j\neq i}) f_3(\mathbf{x})$ such that $\int_{\Theta} f_1 \mathrm{d}\boldsymbol{\theta} = 0$ and $f_3(\mathbf{x}) = 0$ *on* $\mathcal{D}/\mathcal{D}_1$. For all h,

$$\int_{\mathcal{D}} \int_{\Theta} g^m v \; \mathrm{d}\boldsymbol{\theta} \; \mathrm{d}\mathbf{x} = \int_{\mathcal{D}_1} \int_{\Theta} g^m f_1 f_2 \mathrm{d}\boldsymbol{\theta} f_3(\mathbf{x}) \; \mathrm{d}\mathbf{x}, \tag{2.36}$$

since f_3 vanishes outside $\mathcal{D}_1$. Then, since the observable g does not depend on θ_i,

$$\int_{\mathcal{D}_1} \int_{\Theta} g^m f_1 f_2 \mathrm{d}\boldsymbol{\theta} f_3(\mathbf{x}) \mathrm{d}\mathbf{x} = \int_{\mathcal{D}_1} \left(\int_{\Theta_i} f_1 \mathrm{d}\theta_i \right) \left(\int_{\Theta/\Theta_i} g^m f_2(\theta_{j\neq i}) \mathrm{d}\theta_j \right) f_3(\mathbf{x}) \mathrm{d}\mathbf{x} = 0. \tag{2.37}$$

■

The result of this Lemma sheds some light onto the identifiability of the inverse problem. In particular, the problem is ill-posed whenever there are regions in the physical space in which the observable does not depend on one or more parameters. A way to overcome this is to reduce the physical domain by excluding the regions (*i.e.* the DOFs) where the observable is not sensitive to the parameters.

2.2.5 Physical DOFs reduction: clustered sensitivities (CS) algorithm

As explained before, the dual variable formulation of the optimization problem transfers the resolution effort onto the solution of a system whose size is the number of DOFs in the physical domain times the number of moments. However, in many practical applications, as for instance when models are described by PDEs, the number of DOFs used to discretize the solution in the physical domain is large, making the Hessian matrix inversion computationally intensive. Aside from the sheer computational cost of linear algebra operations, dealing with many large simulations – say thousands of simulations counting millions of DOFs – poses undeniable issues in terms of storage capacity and Input/Output computer operations. The main idea to reduce the computational cost is to retain only the subsets of the physical domain in which the observable conveys more information about the variability of the parameters. Consider for instance a region in which the observable does not vary, or its variation amplitude is lower than the noise level: then, matching the moments in this region will certainly not convey any meaningful information about the parameters. Even worse, it may increase the Hessian condition number and degrade the overall accuracy of the method. It may also happen that part of the data is redundant, meaning that the observable exhibits the same variations with respect to the parameters in two different DOFs. In this section, we propose an algorithm that selects a subset $\mathcal{S}$ of the full set of DOFs $\mathcal{D}$. This subset is then used in the OMM inverse procedure described before. Notice that we are not interested in building a low-dimensional surrogate model with fewer outputs. On the contrary, we aim at developing a non-intrusive approach where we only choose to discard some outputs of the high fidelity model. To do that, we propose the following gradient-based algorithm which is rooted in the global sensitivity analysis of the model.

2.2.5.1 The SGM matrix

For each $\mathbf{x}_j$, we consider an approximation of the exact SGM matrix (defined in (2.6)) as follows:

$$\mathbf{C}^j \simeq \beta \sum_{i=1}^{N_c} \left[\nabla_{\boldsymbol{\theta}} g(\mathbf{x}_j, \boldsymbol{\theta}_i)\right] \left[\nabla_{\boldsymbol{\theta}} g(\mathbf{x}_j, \boldsymbol{\theta}_i)\right]^T \rho_i,$$

where $\nabla_{\boldsymbol{\theta}} g(\mathbf{x}_j, \boldsymbol{\theta}_i)$ is a vector of size n_p whose components are the derivatives of g with respect to each parameter at a given $\mathbf{x}_j$ and a given parameter sample $\boldsymbol{\theta}_i$. $\mathbf{C}^j$ is a n_p-by-n_p matrix containing the sensitivity information of the observable with respect to the input parameters at $\mathbf{x}_j$. It may also be seen as the uncentered covariance matrix of the gradient of the observable with respect to the uncertain parameters.
In this work, the gradient $\nabla_{\boldsymbol{\theta}} g$ is approximated by using local polynomial approx-

imations. Other well-known methods exist, such as adjoint equations [CLPS03] or automatic differentiation [GW08], but they will not be discussed here. For each sample $\boldsymbol{\theta}_i$ in the stochastic space, its K nearest neighbors are found and their indices are denoted by i_k, $k = 1, \ldots, K$. An implementation of the `k-NN` algorithm (using k-d trees) from the Scikit-learn library [PVG+11] was used for an efficient search of the nearest neighbors. The method consists in fitting a polynomial model to the K values of the observable $g_{i_k,j}$, $k = 1, \ldots, K$. Given a set of linearly independent polynomials $\{P_l(\boldsymbol{\theta})\}_{l=1,\ldots,n_l}$, the collocation matrix Φ_i reads:

$$\Phi_i = \begin{pmatrix} P_1(\boldsymbol{\theta}_{i_1}) & \cdots & P_{n_l}(\boldsymbol{\theta}_{i_1}) \\ \vdots & \ddots & \vdots \\ P_1(\boldsymbol{\theta}_{i_K}) & \cdots & P_{n_l}(\boldsymbol{\theta}_{i_K}) \end{pmatrix}.$$

The local polynomial model is obtained by solving the following linear system:

$$\boldsymbol{\Phi}_i \mathbf{q} = \mathbf{y}_{i,j},$$

where $\mathbf{y}_{i,j} = \begin{pmatrix} g_{i_1,j} & \cdots & g_{i_K,j} \end{pmatrix}^T$ and $\mathbf{q}$ is the vector of unknowns of size n_l. For stability reasons, K must be greater than n_l and so the system is solved in the least-squares sense. In practice, we used a basis of local multivariate quadratic monomials so that $n_l = \frac{n_p^2+3n_p+2}{2}$. The number of nearest neighbors is set to $K = n_l + 2$. Once $\mathbf{q}$ is computed, one obtains the following approximation of the gradient:

$$\nabla_{\boldsymbol{\theta}} g(\mathbf{x}_j, \boldsymbol{\theta}_i) \simeq \sum_{l=1}^{n_l} q_l \nabla_{\boldsymbol{\theta}} P_l(\boldsymbol{\theta}_i). \tag{2.38}$$

In what follows, this approximation of $\nabla_{\boldsymbol{\theta}} g(\mathbf{x}_j, \boldsymbol{\theta}_i)$ is denoted by $\mathbf{d}_{i,j}$. We now have an easily computable approximation $\hat{\mathbf{C}}^j$ of the SGM:

$$\hat{\mathbf{C}}^j = \beta \sum_{i=1}^{N_c} \mathbf{d}_{i,j} \mathbf{d}_{i,j}^T \rho_i, \tag{2.39}$$

which is symmetric and positive semidefinite so its eigenvalues are real and non-negative. Note that the approximation in (2.39) is computed using the Sobol sequence quadrature rule and the same simulation set $\{g_{i,j}\}$ as previously computed. This means that no additional model evaluation is required.

2.2.5.2 Parameter space dominant directions

The eigenvalues of the SGM play an important role in the classification of the DOFs.

For a given $\mathbf{x}_j$ the eigenvalues are denoted by $\lambda_1^j, \ldots, \lambda_{n_p}^j$, in descending order. The corresponding eigenvectors, denoted by $\mathbf{e}_1^j, \ldots, \mathbf{e}_{n_p}^j$, form an orthonormal basis of the parameter space. The vector $\mathbf{e}_1^j$ corresponds to the direction (in the parame-

ter space) of maximum variation, on average, of g at $\mathbf{x}_j$. Its associated eigenvalue η_1^j corresponds to the mean-squared directional derivative of the observable along the direction $\mathbf{e}_1^j$ [Con15, Lemma 3.1]. For instance, if there are two input parameters θ_1 and θ_2, then $\mathbf{e}_1^j = (1, 0)$ means that the observable variation of g at $\mathbf{x}_j$ is mostly due, on average, to variations of θ_1. Each $\mathbf{x}_j$ is therefore associated with a dominant direction in the parameter space $\mathbf{e}_1^j$ and its corresponding eigenvalue η_1^j. We are now able to address the initial problem: on the one hand, the DOFs where the variation of the observable is not significant are characterized by a low first eigenvalue. A threshold on η_1^j may be applied to remove the DOFs where the observable variation amplitude is lower than the noise level. On the other hand, the DOFs that are redundant from the observable point of view are characterized by "similar" dominant directions. This notion of similarity will be introduced hereafter. Knowing this, we propose to divide the set of $N_{\mathbf{x}}$ dominant directions into N_k clusters using an agglomerative hierarchical clustering algorithm. This algorithm consists in clustering vectors according to a given similarity function. First, each vector is associated with its own cluster and pairs of similar clusters are iteratively merged. We refer to [LW67] for an overview of such algorithms. In the present work, we used the Scikit-learn library [PVG+11] which provides a Python implementation of an agglomerative hierarchical algorithm that accepts user-defined similarity functions. The similarity function between two (unit-norm) vectors is defined as follows:

$$s(\mathbf{u}, \mathbf{v}) = |\mathbf{u} \cdot \mathbf{v}| \,,$$

i.e. the absolute value of the cosine of the angle between $\mathbf{u}$ and $\mathbf{v}$. Once the $N_{\mathbf{x}}$ DOFs of the full physical set are divided into N_k clusters, the ones with maximum trace of $\hat{\mathbf{C}}^j$ are chosen as their cluster representatives. The subset $\mathcal{S}$ is then formed by the N_k representatives.

Remark 1

The agglomerative clustering guarantees that the sequence of selected subsets is nested. This means that if $\mathcal{S}^{(n)}$ and $\mathcal{S}^{(n+1)}$ respectively count n and $n+1$ elements, then they have n elements in common. From a practical viewpoint, the full sequence of clusters can be computed once so that there is no additional cost linked to the clustering when N_k increases. Furthermore, in our simulations, we noticed that the residual had a smoother behavior as N_k increases compared to other clustering techniques.

The output of the CS algorithm is a nested sequence of subsets $\mathcal{S}^{(1)} \subset \ldots \subset \mathcal{S}^{(N_{\mathbf{x}})}$ and we denote by N_k the cardinality of a given subset $\mathcal{S}$.

Remark 2

In the works by Constantine [CDW14] and Russi [Rus10], where the term "active subspace" was introduced, the matrix $\mathbf{C}$ is used to reduce the parameter space dimension. It is particularly efficient when dealing with complex models counting a

very large number of parameters while only a few directions in the parameter space are responsible for the observed variability [CELI15]. In our case it is used to reduce the number of DOFs in the discretized physical domain. However, the interpretation of the SGM eigenvalues and eigenvectors in terms of the sensitivity of the model is the same. In the papers by Streif et al. [SFB06] and Himpe & Ohlberger [HO14], a similar Gramian matrix is used to assess the observability and controllability of linear and nonlinear systems. Though quite different from the CS analysis, their approach is another illustration of the interpretation of Gramian matrices in terms of sensitivity analysis.

Algorithm 2: Clustered Sensitivities algorithm.

Input:

- $g_{i,j}$, $i = 1, \ldots, N_c$, $j = 1, \ldots, N_{\mathbf{x}}$: simulation subset.
- ρ: PDF estimate.

for $j = 1$ **to** $N_{\mathbf{x}}$ **do**
  for $i = 1$ **to** N_c **do**
    Compute $\mathbf{d}_{ij}$ using (2.38)
  end
  Compute $\hat{C}^{(j)}$ using (2.39);
  Compute first eigenvector $\mathbf{e}_1^j$ and eigenvalues trace $t(\mathbf{x}_j) = \sum_k \eta_k^j$;
end

Compute sequence of clusters for $j = 1, \ldots, N_{\mathbf{x}}$ using similarity function s;
for $N_k = 1$ **to** $N_{\mathbf{x}}$ **do**
  $\mathcal{S}^{(N_k)} = \{\}$;
  for $k = 1$ **to** N_k **do**
    Select representative $\mathbf{x}_k$ of cluster C_k as: $\arg\max_{\mathbf{x} \in C_k} \{t(\mathbf{x})\}$;
    Append $\mathbf{x}_k$ to $\mathcal{S}^{(N_k)}$;
  end
end

Output: Subset sequence: $S^{(1)} \subset \ldots \subset \mathcal{S}^{(N_{\mathbf{x}})}$.

2.2.6 Visualization and interpretation of the results

The output of the proposed algorithm is the estimated PDF values at the collocation points: $\rho(\boldsymbol{\theta}_i), i = 1, \ldots, N_c$. Although a direct visualization of the PDF is possible (see Fig. 2.2), it becomes irrelevant if the number of parameters is greater than two. Therefore it may be convenient to consider the marginal density of the k^{th} parameter, defined as follows:

$$z_k(x) = \int_{\theta_l, l \neq k} \cdots \int \rho(\theta_1, \ldots, x, \ldots, \theta_{n_p}) \prod_{l \neq k} \mathrm{d}\theta_l. \tag{2.40}$$

An approximation of Eq.(2.40) may be computed using the discrete PDF values and the corresponding quadrature rule.
In the numerical tests we illustrate the proposed algorithm with synthetic data, meaning the true PDF ρ^* of the parameters is known. There are several ways to compare the estimated and true PDFs such as the 2–norm of their difference. However, for density functions, it is more natural to consider the Kullback-Leibler (KL) divergence, introduced in Lemma 2.1. Here we use a discrete approximation of the symmetric KL divergence, defined as follows:

$$KL(\rho|\rho^*) = \frac{1}{2}\left(\varphi(\rho,\rho^*) + \varphi(\rho^*,\rho)\right),$$
$$\text{where} \quad \varphi(u,v) = \beta \sum_{i=1}^{N_c} u_i \log(u_i/v_i).$$

It is also possible to compute the parameters moments with the estimated PDF and compare them with their true values.

2.2.7 Main algorithm

The proposed inverse procedure consists in combining the OMM and CS algorithms (see Alg. (3)). To assess the convergence of the procedure, we use the *global* moment residual $\mathbf{R} \in \mathbb{R}^{N_\mathbf{x} \times N_m}$ defined as follows:

$$R_{j,m} = \beta \sum_{i=1}^{N_c} g_{i,j}^m \rho_i - \tilde{\mu}_{j,m}, \;\; j = 1,\dots,N_\mathbf{x}, \;\; m = 1,\dots,N_m.$$

Note that while the OMM algorithm is designed to cancel out the residual $\mathbf{r}$ defined on a subset $\mathcal{S}$ of $\mathcal{D}$, $\mathbf{R}$ is defined on the full DOFs set $\mathcal{D}$.
One iteration of the main algorithm consists in progressively adding DOFs to the subset $\mathcal{S}$ using the CS algorithm and applying the OMM algorithm for each $\mathcal{S}$ until stagnation of the $\|\mathbf{R}\|_2$. Then, the SGM is updated with the new PDF estimate and another iteration is done. The main algorithm stops when no improvement of $\|\mathbf{R}\|_2$ is observed. The total number of iterations is later referred to as n_{iter}.
Figure 2.5 shows an example of the dependence between the global residual norm $\|\mathbf{R}\|_2$ and the cardinality of the subset $\mathcal{S}$.
Table 2.1 presents an overview of the computational cost of the whole procedure. In practice, this cost is strongly dominated by the construction of the simulation set (step one), each model evaluation having a high cost C_{forward}. However, this step is embarrassingly parallelizable with respect to N_c. Step two is embarrassingly parallelizable both with respect to N_c and $N_\mathbf{x}$. In our implementation, the SGM computations are only parallelized with respect to $N_\mathbf{x}$. Step three is dominated by the cost of the Hessian pseudo-inverse computation. As it scales with $(N_m N_k)^3$, the need to reduce the number of DOFs in the physical space becomes obvious. The pseudo-inverse computation could also be parallelized but this was not done in our implementation. The cost of the pseudo-inverse is multiplied by n_{Newton}, the

Algorithm 3: Main algorithm.

Input:

- Corrected experimental moments: $\tilde{\mu}_{j,m}$, $j = 1, \ldots, N_{\mathbf{x}}$, $m = 1, \ldots, N_m$;
- Number of stochastic samples: N_c;
- Tolerance parameters : α, $\varepsilon_{\text{Newton}}$;

Step 1:

- Build the simulation set $\{g_{i,j}\}$;

Initial guess $\rho^{(0,0)}$: uniform distribution over Θ ;
$j = 1$, $N_k = 0$;
while $\|\mathbf{R}^{(j-1,N_k)}\|_2$ *not converged* **do**
  Apply CS procedure with $\rho^{(j-1,0)}$ (**Step 2**);
    $\rightarrow$ nested subsets sequence $\mathcal{S}^{(j,1)} \subset \ldots \subset \mathcal{S}^{(j,N_{\mathbf{x}})}$;
  $n = 1$;
  while $\|\mathbf{R}^{(j-1,n)}\|_2$ *not converged* **do**
    Apply OMM procedure with $\mathcal{S}^{(j,n)}$ (**Step 3**);
      $\rightarrow \rho^{(j,n+1)}$;
    $n \leftarrow n + 1$;
  end
  $j \leftarrow j + 1$;
  $N_k \leftarrow n$;
end
$n_{\text{iter}} = j$.

number of Newton iterations.

Table 2.1: Complexity of the inverse procedure. C_{forward} denotes the cost of one model evaluation.

Step	Complexity	Parallelizable
1. Simulation Set	$\mathcal{O}\left(N_c \times C_{\text{forward}}\right)$	massively w.r.t. N_c
2. Clustured Sensitivities	$\mathcal{O}\left(N_{\mathbf{x}} \times N_c \times n_p^3\right)$	massively w.r.t. N_c and $N_{\mathbf{x}}$
3. Observable Moment Matching	$\mathcal{O}\left(n_{\text{Newton}} \times (N_k \times N_m)^3\right)$	possible

2.3 Comparison with existing techniques for an ODE model

In this section, a nonlinear ODE model is introduced. It serves as a simple reference test case to both illustrate the method and compare its accuracy and cost with different existing techniques.

2.3.1 The MV model

The proposed numerical method is applied to an ODE model counting four state variables g, u, v, w which satisfy

$$\left\{\begin{array}{rcl} \partial_t g &=& -J_1(g,u) - J_2(g,\theta_1,\theta_2) - J_3(g,v,w) \\ \partial_t u &=& f_1(g,u) \\ \partial_t v &=& f_2(g,v) \\ \partial_t w &=& f_3(g,w) \end{array}\right. \tag{2.41a}$$

along with the initial conditions

$$g(0) = 0, \quad u(0) = 0, \quad v(0) = 1, \quad w(0) = 1. \tag{2.41b}$$

The J_i and f_i are nonlinear functions of the variables and of the input parameters. The proposed model was designed to replicate the electrical activity of a heart muscle cell. It is known as the Minimum Ventricular model and will be referred to as the MV model in what follows. For the sake of simplicity, it is not fully transcribed here but we refer the reader to the original paper by Bueno-Orovio *et al.* [BOCF08] for the detailed equations. Out of the numerous input parameters of the MV model, θ_1 and θ_2 were picked for the illustration of the method. In the original paper, these two parameters are respectively denoted by k_{so} and τ_{so1}. All remaining parameters are fixed to reference values found in [BOCF08]. Our observable is the state variable $g(t)$ which corresponds to the cell membrane potential. Note that the relationship between the observable and the input parameters is nonlinear.

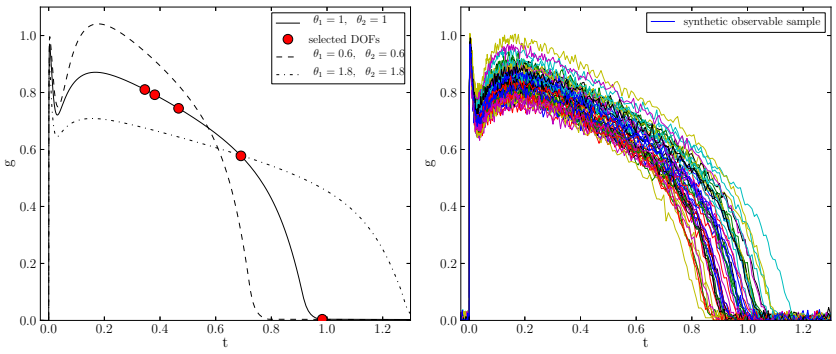

Figure 2.3: Solution of the ODE model for different values of the input parameters (left) and synthetic measurements (right). 5 time steps selected by the CS algorithm are indicated as red circles.

2.3.2 Reference test case

Numerical settings The ODE is solved using a BDF3 scheme with adaptive time steps. The number of DOFs $N_{\mathbf{x}} = 334$ corresponds in this case to the number of steps used in the time integration. The synthetic data set is generated by evaluating the model in (2.41) for $N = 10^3$ samples of $\boldsymbol{\theta} = (\theta_1, \theta_2)$. The samples are drawn from an uncorrelated bivariate normal distribution of mean $\boldsymbol{\mu} = [1.1, 1.1]$ and covariance matrix $\boldsymbol{\Sigma} = 0.1^2 \times \mathbf{I}_2$.
First, the noise level is set to 5% for the comparison study but its influence is investigated later in this section. The first N_m order moments are computed using (2.3) and stored for the inverse problem. Our strategy is applied to the joint PDF estimation of the synthetic population θ_1 and θ_2. The stochastic domain $\Theta = [0.6, 1.8]^2$ is discretized using $N_c = 1024$ quadrature points from the Sobol sequence. It should be noted that the width of the stochastic domain is equal to 12σ and is not centered on μ. Taking a domain which is wide enough with respect to the exact PDF support, and not centered on the exact mean, is important if one wants to assess the accuracy of the method without any "favorable bias" induced by the choice of the stochastic domain bounds. Indeed, in practical cases, one does not have a precise knowledge on the exact means and standard deviations of the parameters distributions.

To investigate the effect of several hyper-parameters of the procedure, the number of global iterations in temporarily set to $n_{iter} = 1$. The CS procedure is applied with the initial guess $\rho^{(0,0)}$ being a uniform distribution over Θ. Figure 2.4 shows the SGM eigenvectors $\mathbf{e}_j = (e_1, e_2)_j$, $j = 1, \ldots, N_{\mathbf{x}}$. The size of the markers is proportional to the logarithm of the associated eigenvalues η_j. Since the eigenvectors are normalized, the points are scattered over the unitary circle. Each cluster is featured with a different color (here $N_k = 5$ so the points are divided into 5 clusters).

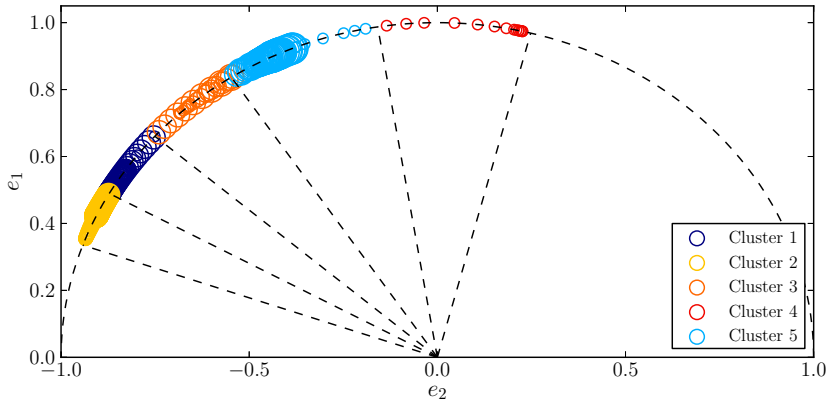

Figure 2.4: Scatter plot of the SGM first eigenvector for each DOF $\mathbf{x}_j$. $N_k = 5$.

Influence of N_k Here we investigate the effect of N_k. The other hyper-parameters are fixed: $N_m = 3$ and $N_c = 512$. The CS procedure is applied for N_k varying from 2 (n_p) to 334 ($N_\mathbf{x}$). Figure 2.5 shows the evolution of the KL divergence $KL(\rho|\rho^*)$ and the residual norm $\|\mathbf{R}\|_2$ with respect to the number of selected DOFs N_k. The KL divergence and the global residual norm $\|\mathbf{R}\|_2$ are not monotonic with respect to N_k but they both follow the same decreasing trend. From $N_k = 50$, there is no significant change in the KL divergence. Both observations confirm the relevance of the CS procedure and of the *a priori* error analysis. Table 2.2 summarizes the parameters estimated statistics (mean and standard deviation) with respect to N_k. It is clear that a certain convergence is reached as N_k increases, both in the KL divergence and in the parameters statistics themselves.

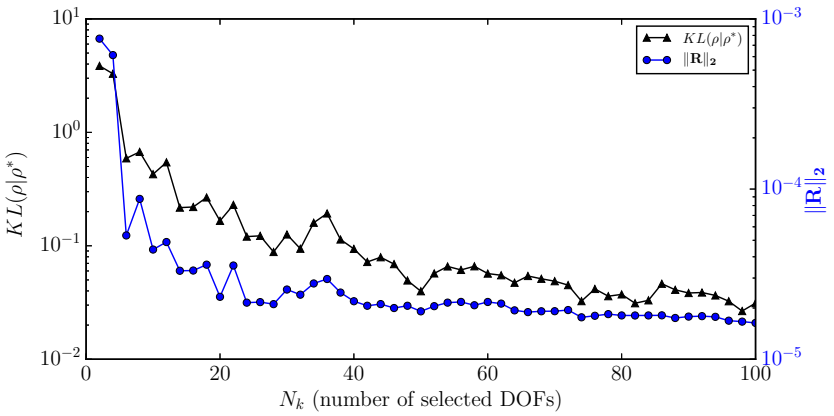

Figure 2.5: Convergence of the KL error and residual norm as the number of selected DOFs N_k increases.

Influence of N_c The effect of the number of stochastic collocation points N_c is investigated with $N_m = 3$ and $N_k = 50$. N_c varies from 2 to 2^{10} and $N_m = 3$ and

Table 2.2: Observable Moment Matching results for different values of N_k ($N_c = 512$ and $N_m = 3$).

Statistics	$KL(\rho\|\rho*)$	mean		std	
Number of DOFs		θ_1	θ_2	θ_1	θ_2
$N_k = 2$	3.84	1.2124	1.1458	0.343	0.231
$N_k = 5$	6.45×10^{-1}	1.1080	1.1071	0.150	0.127
$N_k = 10$	4.18×10^{-1}	1.1078	1.1118	0.140	0.135
$N_k = 20$	1.65×10^{-1}	1.1006	1.1068	0.119	0.121
$N_k = 50$	4.10×10^{-2}	1.0978	1.1037	0.108	0.103
$N_k = 100$	2.49×10^{-2}	1.0974	1.1037	0.106	0.103
$N_k = 200$	2.94×10^{-2}	1.0971	1.0383	0.105	0.103
$N_k = 334$	3.01×10^{-2}	1.0970	1.1039	0.105	0.103
Empirical	**0**	**1.0972**	**1.1042**	**0.104**	**0.102**

$N_k = 50$ are fixed. Table 2.2 shows the means and standard deviations of θ_1 and θ_2 estimated by the Observable Moment Matching algorithm as well as their empirical values. The empirical moments correspond to the moments computed directly from the synthetic parameter samples using the following formula:

$$\mu_{m,k} = \frac{1}{N} \sum_{i=1}^{N} \theta_{i,k}^{m}, \qquad m = 1, \dots, N_m, \ k = 1, \dots, n_p. \tag{2.42}$$

As expected, the estimation is more accurate when N_c increases. Note that the computational cost of increasing N_c is limited owing to the deterministic and nested nature of the Sobol sequence. If one already has evaluated the model for N_{c1} sample points and wants N_{c2} model evaluations, one only has to perform $N_{c2} - N_{c1}$ forward runs to complete the simulation set.

Influence of the noise level The synthetic measurements are corrupted by adding some noise to the numerical results. Table 2.4 shows the estimated means and standard deviations of θ_1 and θ_2 for different noise levels. As expected, the accuracy of the method decreases as the noise increases.

Non-normal distributions In order to assess the robustness of the method, a similar but more complex heart cell model [DMH+11] is used. It consists of a set of 29 nonlinear coupled ODEs and we aim at estimating the PDF of two parameters of this model. The synthetic dataset is generated by sampling the parameters of interest from two known distributions: a bivariate log-normal distribution $\text{Log}-\mathcal{N}(0, \sigma_1^2)$ and a bivariate Gaussian mixture $\mathcal{N}(1, \sigma_2^2) + \mathcal{N}(2, \sigma_2^2)$ with $\sigma_1 = 0.7$ and $\sigma_2 = 0.2$. In both cases, the synthetic dataset is corrupted by a zero-mean Gaussian noise of amplitude 5%.

Table 2.3: Observable Moment Matching results for different values of N_c ($N_k = 50$ and $N_m = 3$).

Statistics	$KL(\rho\|\rho*)$	mean		std	
Number of stochastic points		θ_1	θ_2	θ_1	θ_2
$N_c = 4$	1.62	1.1328	1.1378	0.187	0.189
$N_c = 8$	1.89	1.1000	1.1241	0.116	0.151
$N_c = 16$	8.48×10^{-1}	1.1006	1.1002	0.123	0.105
$N_c = 32$	2.69×10^{-1}	1.0995	1.1109	0.119	0.134
$N_c = 64$	1.02×10^{-1}	1.0968	1.1049	0.107	0.110
$N_c = 128$	5.04×10^{-2}	1.0965	1.1038	0.106	0.104
$N_c = 256$	4.99×10^{-2}	1.0979	1.1039	0.109	0.105
$N_c = 512$	4.10×10^{-2}	1.0978	1.1037	0.108	0.103
$N_c = 1024$	4.20×10^{-2}	1.0978	1.1037	0.108	0.104
Empirical	**0**	**1.0972**	**1.1042**	**0.104**	**0.102**

Table 2.4: Observable Moment Matching results for different noise levels ($N_c = 512$, $N_k = 50$ and $N_m = 3$).

Statistics	$KL(\rho\|\rho*)$	mean		std	
Noise level		θ_1	θ_2	θ_1	θ_2
80%	1.55	1.1027	1.1543	0.120	0.251
20%	1.23×10^{-1}	1.0967	1.1019	0.105	0.094
10%	6.97×10^{-1}	1.0994	1.1161	0.117	0.162
5%	4.10×10^{-2}	1.0978	1.1037	0.108	0.103
2%	3.92×10^{-2}	1.0978	1.1051	0.107	0.108
1%	3.79×10^{-2}	1.0977	1.1050	0.107	0.108
0%	3.70×10^{-2}	1.0977	1.1048	0.107	0.107
Empirical	**0**	**1.0972**	**1.1042**	**0.104**	**0.102**

The inverse procedure is applied to the log-normal case with the following numerical settings: $N_c = 2048$, $N_m = 3$ and convergence is reached at $n_{iter} = 1$ and $N_k = 21$. The PDF values are shown in Figure 2.6 and the marginal densities in Figure 2.7. Note that the strong skewness of the true distribution is well captured by the proposed inverse procedure.

The inverse procedure is then applied to the Gaussian mixture case with the following numerical settings: $N_c = 2048$, $N_m = 3$ and convergence is reached at $n_{iter} = 1$ and $N_k = 31$. The PDF values are shown in Figure 2.8 and the marginal densities in Figure 2.9. Note that strong correlation between θ_1 and θ_2 is fully captured.

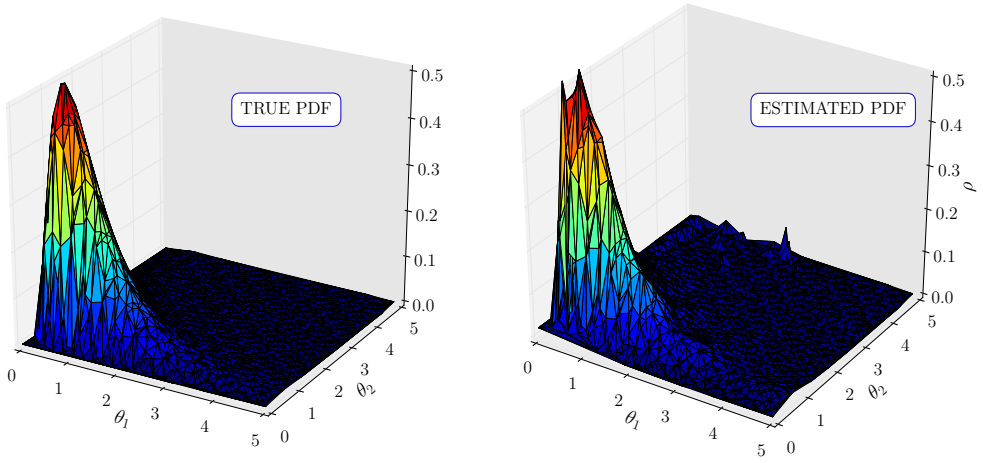

Figure 2.6: PDF estimation of a bivariate log-normal distribution: direct visualization.

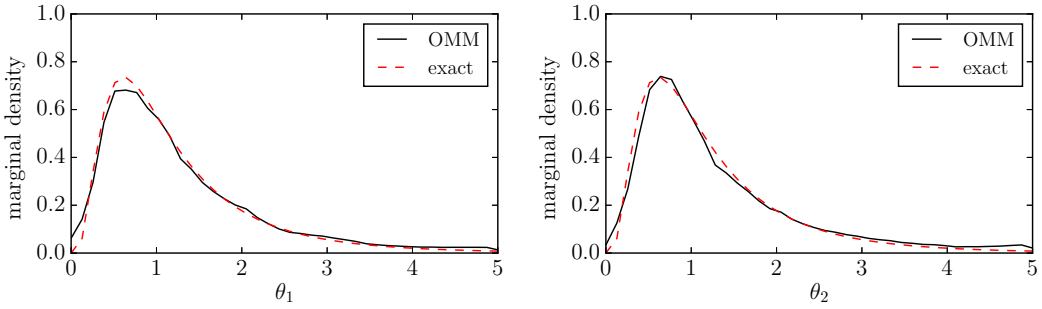

Figure 2.7: PDF estimation of a bivariate log-normal distribution: marginal densities.

2.3.3 Comparison with existing techniques

In this section, the proposed approach is compared to existing techniques on the reference test case described in 2.3.2. We show that all three approaches achieve

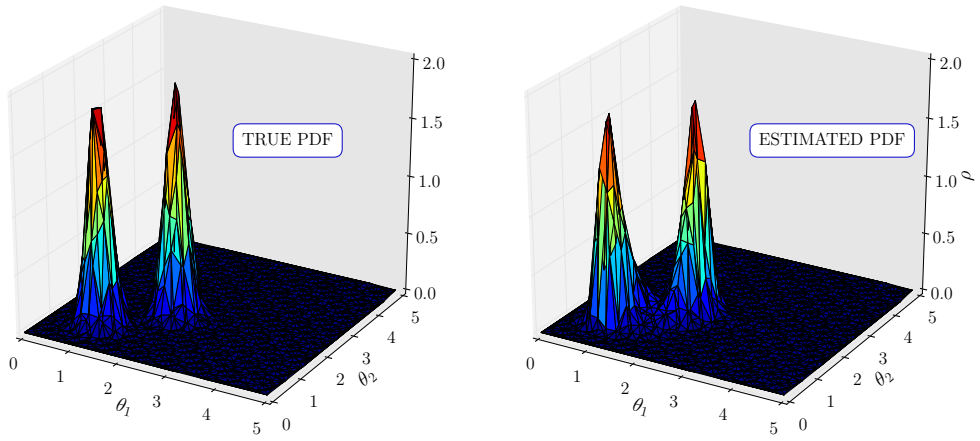

Figure 2.8: PDF estimation of a bivariate Gaussian mixture: direct visualization.

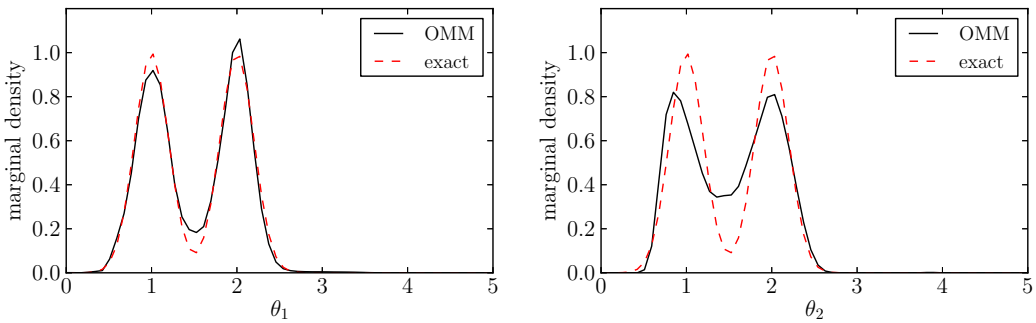

Figure 2.9: PDF estimation of a bivariate Gaussian mixture: marginal densities.

the same precision on the parameters estimations but with a different number of function evaluations.

Least-squares moment-matching An alternative to the present approach is to directly minimize the moment difference using a least-squares method. In [ZG08], the quantity of interest is represented as a finite polynomial expansion of d uncorrelated random variables $\xi = \{\xi^1, \ldots, \xi^d\}$. The methodology was applied to inverse heat conduction problems and to microstructure reconstruction. This approach was applied to our test case. Here, the quantities of interest are the two parameters θ_1 and θ_2 and the observable is the variable u. Using the methodology presented in [ZG08], the parameter θ_j is expanded on a sparse grid as follows:

$$\theta_j(\xi) = \sum_{k=1}^{n_k} \theta_j(\xi_k) L_k(\xi) = \sum_{k=1}^{n_k} q_{j,k} L_k(\xi),$$

where $q_{j,k} = \theta_j(\xi_k)$, the ξ_k are the sparse grid collocation points and L_k the members of the polynomial basis. Then, one can approximate the moments of the observable using the sparse grid quadrature rule:

$$\mu_m^*(\mathbf{x}_j) = \sum_{k=1}^{n_k} w_k g(\mathbf{x}_j, \xi_k)^m,$$

where the w_k are the sparse grid weights. The cost function J is defined as the squared difference between the approximated and experimental moments:

$$J = \frac{1}{2} \sum_{m=1}^{N_m} \sum_{j=1}^{N_{\mathbf{x}}} \alpha_m \left(\mu_m^*(\mathbf{x}_j) - \mu_m(\mathbf{x}_j)\right)^2,$$

where the α_m are user-defined weights. The problem now consists in minimizing J with respect to the coefficients $q_{j,k}$. In [ZG08], this is done by a gradient descent method which involves solving the sensitivity equations associated with the model. For the sake of simplicity, to avoid the tedious derivation of the sensitivity equations of the MV model, we used the Covariance Matrix Adaptation Evolution Strategy (CMA-ES) evolutionary algorithm [Han06] to minimize J. Since the minimization strategy differs from that of [ZG08], the number of model evaluations needed to reach convergence may differ. This is to be taken into account when comparing the three methods in Table 2.5.

Population approach (SAEM) Here we tackle the inverse problem from a radically different perspective, belonging to the so-called population approaches. It consists in seeking a Maximum Likelihood (ML) estimate of the unknown parameters. The MV test case can be seen as a mixed effects model where the observed data are the $y_{i,j}$, $i = 1, \ldots, N$, $j = 1, \ldots, N_{\mathbf{x}}$ and the parameters θ_1, θ_2 are the non-observed data. We assume that the observed data are outputs of the MV model

with an additive noise $\varepsilon_{i,j}$ assumed to be normally distributed: $\varepsilon \sim \mathcal{N}\left(0, \tau^2\right)$.

$$y_{i,j} = g(\boldsymbol{\theta}_i, \mathbf{x_j}) + \varepsilon_{i,j}.$$

Assuming each θ_j is normally distributed, $\theta_j \sim \mathcal{N}\left(\mu_j, \sigma_j^2\right)$, the likelihood L reads:

$$L(y, \theta; \tau, \mu_k, \sigma_k) = \left(2\pi\sigma_1^2\sigma_2^2\right)^{-N/2} \left(2\pi\tau^2\right)^{-NN_{\mathbf{x}}/2} \exp\left[-\frac{1}{2\tau^2}\sum_{i,j}\left(y_{i,j} - g(\boldsymbol{\theta}_i, \mathbf{x_j})\right)^2 - \frac{1}{2\sigma_1^2}\sum_i\left(\theta_{1,i} - \mu_1\right)^2 - \frac{1}{2\sigma_2^2}\sum_i\left(\theta_{2,i} - \mu_2\right)^2\right].$$

Note that this approach differs from the other two on two major aspects. First, it is a *parametric* approach, meaning we are not seeking a pointwise estimate of the PDF but a parameterization of it (here a Gaussian parameterization). Second, the method provides, by construction, an estimation of the noise level of the measurements. In the other two approaches, the noise structure and amplitude is assumed to be known. The parameters τ, μ_k, σ_k are found by maximizing the log-likelihood $\log(L)$, which is challenging due to the nonlinear relationship between g and θ_1, θ_2. This is called the Maximum Likelihood Estimation (MLE) method. In the case of linear models, the maximum likelihood is usually found using the Expectation Maximization (EM) algorithm [DLR77]. The paper by E. Kuhn and M. Lavielle [KL05] introduces a modified version of the EM algorithm to tackle cases where the models are nonlinear. The authors developed a Stochastic Approximation of the Expectation Maximization algorithm (SAEM) to solve the MLE problem. For the comparison study, we used Monolix® [Lix14], the Matlab® implementation of the SAEM algorithm. This software was initially designed to perform the parameter estimation of pharmacokinetics-pharmacodynamics (PK-PD) models. Compared to PDEs, those models are usually computationally cheap so that the software does not look for a solution with minimum model evaluations. However, one may reduce the computational cost by constructing a pre-computed grid of solutions and then interpolate in that grid instead of evaluating the full model. The Monolix software was successfully used in [GLV14] to estimate the parameters of a 1–D PDE model. Such a strategy was not adopted in this paper and the software was used as is.

Comparison We applied the Clustered Sensitivities / Observable Moment Matching algorithms and both the previously described methods to the reference test case described in 2.3.2. The numerical settings for our method are: $N_c = 512$, $N_m = 3$ and $N_k = 50$. For the least-squares method, we used a two-dimensional sparse grid using the Smolyak rule [HW08] to discretize the parameter space with $N_c = 9$ and the first $N_m = 3$ moments were matched. As explained before, the SAEM algorithm was applied using the Monolix software with default settings.
Table 2.5 shows the estimations of the parameters moments and the number of model evaluations needed for the three methods. For all three approaches, the

errors on the means are less than 1% and the errors on the standard deviations are less than 10%. Even though the SAEM appears to be more precise than the other two, the main difference lies in the number of model evaluations needed. Our approach requires much less model evaluations and those evaluations are made offline, once and for all. Again, our implementation of the least squares method presented in [ZG08] may require more model evaluations due to the minimization strategy adopted.

Table 2.5: Comparison with existing techniques

	Exact		SAEM		least-squares		OMM	
moment order	θ_1	θ_2	θ_1	θ_2	θ_1	θ_2	θ_1	θ_2
1	**1.0972**	**1.1042**	1.0975	1.1051	1.0972	1.1019	1.0963	1.1015
2	**1.2147**	**1.2297**	-	-	1.2133	1.2215	1.2125	1.2224
3	**1.3566**	**1.3810**	-	-	1.3522	1.3616	1.3520	1.3663
std	**0.104**	**0.102**	0.104	0.102	0.098	0.086	0.103	0.095
model evaluations	-		2.98×10^6		1.67×10^5		512	

2.4 Numerical illustrations

We now apply our strategy to the PDF estimation of parameters for two PDEs.

2.4.1 Application to an elliptic PDE: the Darcy equations

In this section, we focus on the following two-dimensional PDE posed in the bounded domain $\mathcal{D} = [0,1] \times [0,1]$:

$$\begin{aligned} -\nabla \cdot (K \boldsymbol{\nabla} p) &= 0, & \mathbf{x} &\in \mathcal{D}, \\ p &= f, & \mathbf{x} &\in \Gamma_D, \\ K \boldsymbol{\nabla} p \cdot \mathbf{n} &= 0, & \mathbf{x} &\in \Gamma_N, \end{aligned}$$

where p is the fluid pressure, f a deterministic function defined on the boundary Γ_D and $\{\Gamma_D, \Gamma_N\}$ is a partition of $\partial\mathcal{D}$. In what follows, f will be set to 1 at the inlet and to 0 at the outlet (see Fig. 2.10). The Darcy model states that the fluid velocity is linked to the pressure as follows by $\mathbf{u} = -K\boldsymbol{\nabla} p$. We assume that the source of variability comes from the heterogeneous permeability field $K(\mathbf{x})$. Using a similar example found in [ZG08], we assume that the spatial variation in the permeability field follows an exponential correlation: $c(\mathbf{x}_i, \mathbf{x}_j) = \exp\left(-\frac{|\mathbf{x}_i - \mathbf{x}_j|}{b}\right)$, where b is the correlation length, set to $b = 0.2$ in our case. From a physical viewpoint, this means

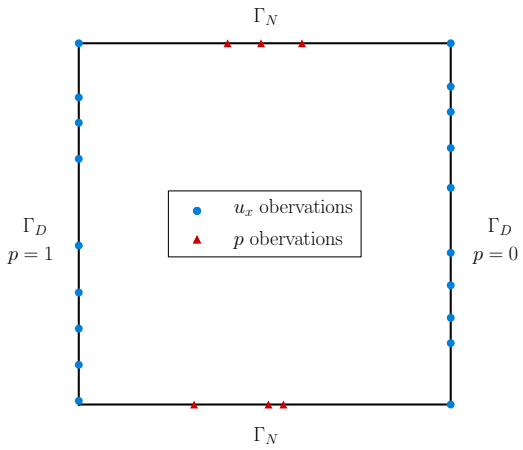

Figure 2.10: Schematic of the problem geometry and location of 25 sensors automatically selected by the CS procedure (out of 400 available sensors).

that the porous medium is relatively smooth. Then, we choose to represent the random field K as a linear combination of the first 5 eigenmodes $\hat{K}_k$ of the correlation kernel $K(\mathbf{x}) = 1 + \sum_{k=1}^{5} \theta_k \hat{K}_k(\mathbf{x})$, where the θ_k are the random parameters. Figure 2.11 shows the eigenmodes of the correlation kernel and Figure 2.12 shows one realization of the random permeability field, along with the outputs of the model, namely the pressure field p and the horizontal velocity u_x.
The objective is to apply the proposed approach to recover the PDF of the permeability field expansion coefficients θ_k from observations of u_x and p on the boundaries. Retrieving the permeability in the domain by exploiting only boundary measurements is a particular case of the Calderón problem, which is a difficult and generally ill-posed inverse problem.

Numerical settings The observable is defined as follows: 200 sensors for u_x (resp. p) are uniformly distributed over the boundary Γ_D (resp. Γ_N) so that $N_{\mathbf{x}} = 400$. The synthetic data set is generated by evaluating the model for $N = 10^4$ samples of $\boldsymbol{\theta} = (\theta_1, \dots, \theta_5)$. The samples are drawn from an uncorrelated multivariate normal distribution of mean $\boldsymbol{\mu} = 2.5 \times 10^{-2} \times [1, 1, 1, 1, 1]$ and covariance matrix $\boldsymbol{\Sigma} = 3.3 \times 10^{-2} \times \mathbf{I}_5$. $N_c = 2^{14}$ collocation points are generated using the Sobol sequence over the domain $\Theta = [-0.2, 0.2]^5$, the number of moments to be matched is set to $N_m = 3$ and the tolerance parameter is set to $\alpha = 1 \times 10^{-3}$. The PDE model is solved using the `FreeFem++` [Hec12] finite element software. A different discretization is used for both sets. For the synthetic dataset, the model is solved on a fine grid of 23550 triangles. For the simulation set, the model is solved on a coarse mesh of 944 triangles. In addition, a Gaussian zero-mean noise of amplitude 5% is added to the sensors measurements.

Results The proposed inverse procedure is applied and convergence is reached at $n_{\text{iter}} = 2$ and $N_k = 25$. Figure 2.10 shows the position of final selected DOFs. Note that points were automatically selected on each boundary even though this was not imposed in the CS procedure. Figure 2.13 shows the estimated marginals of the five parameters along with their exact distributions. Table 2.6 summarizes the estimated parameters statistics to be compared to their exact values. The means are in good agreement, with an error of the order of 1%. The standard deviations feature a higher error, especially for the fifth mode parameter. The sources of error are diverse. The mesh used to generate the simulation dataset is coarser than the one used for the synthetic dataset. This induces a higher numerical diffusion. Moreover, the added noise may also contribute to the error, especially for the higher order modes coefficients.

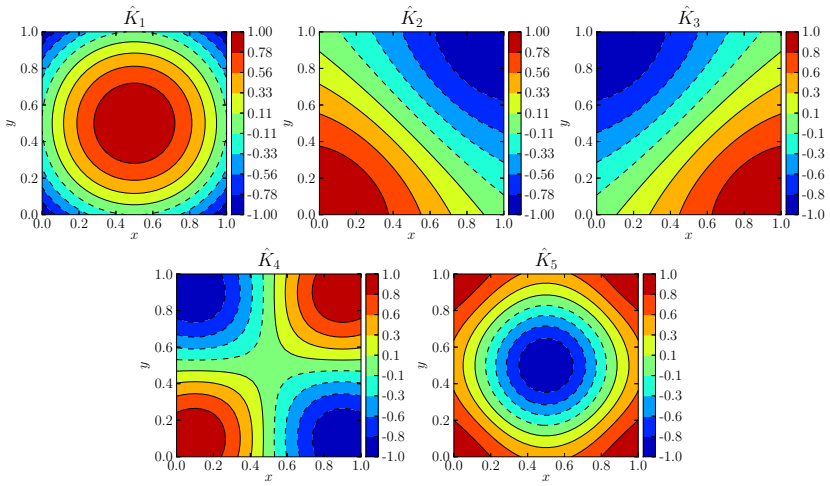

Figure 2.11: Contours of the first 5 eigenmodes of the correlation kernel.

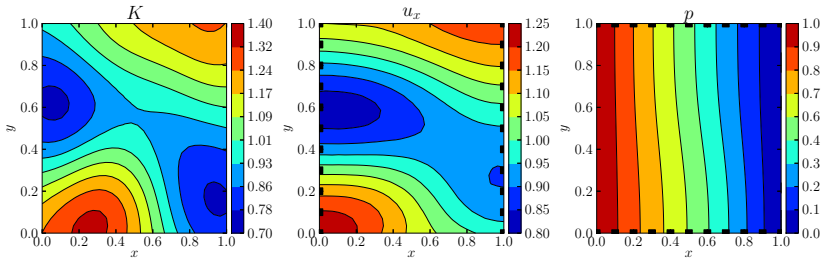

Figure 2.12: Contours of one realization of the Darcy model. Left: permeability, center:horizontal velocity, right: pressure. Black squares indicate where the velocity and pressure fields are observed.

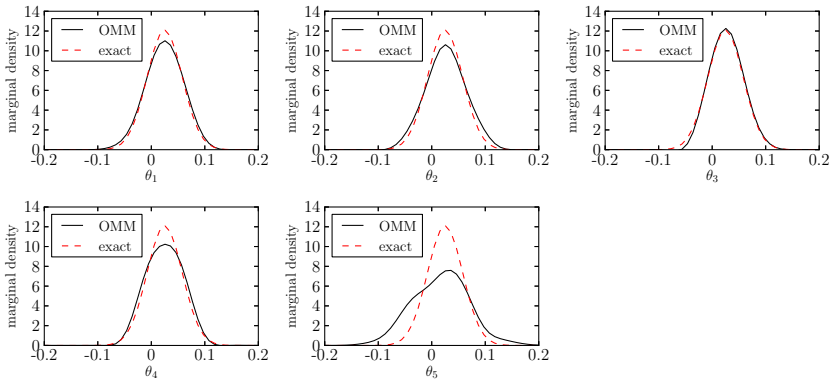

Figure 2.13: Marginal densities of five parameters estimated using the OMM method.

Table 2.6: Darcy model

Statistics	mean			std.		
Parameter	exact	OMM	rel. err.(%)	exact	OMM	rel. err.(%)
θ_1	**2.48e-02**	2.49e-02	0.5	**3.33e-02**	3.08e-02	7.4
θ_2	**2.46e-02**	2.49e-02	1.2	**3.35e-02**	3.39e-02	1.3
θ_3	**2.56e-02**	2.53e-02	0.9	**3.36e-02**	2.82e-02	16
θ_4	**2.55e-02**	2.58e-02	1.1	**3.33e-02**	2.90e-02	13
θ_5	**2.49e-02**	2.52e-02	1.4	**3.31e-02**	5.00e-02	51

2.4.2 Application to a parabolic PDE: the FKPP equation

In this section, we illustrate our strategy with the FKPP equation, originally introduced by Fisher [Fis30], later revisited by Kolmogorov, Petrovskii and Piskunov. It is a nonlinear reaction-diffusion equation defined by:

$$\begin{aligned}
\frac{\partial u}{\partial t} - \nu \Delta u &= Ru(1-u) + f(\mathbf{x},t), \qquad \mathbf{x} \in [0,1]^2, t \in [0,T], \\
\boldsymbol{\nabla} u \cdot \mathbf{n} &= 0, \qquad \mathbf{x} \in \partial[0,1]^2, t \in [0,T], \\
u(\mathbf{x}, t=0) &= 0, \qquad \mathbf{x} \in [0,1]^2,
\end{aligned}$$

where u is a time and space dependent variable, R is the reaction parameter and ν the diffusion field, here considered uniform and constant equal to 10^{-3}. Provided that $R/\nu \gg 1$ and given an *ad hoc* source term f, the FKPP equation admits travelling waves solutions. In practice, u exhibits a propagation front across which u switches from 0 to 1. It is often considered as the simplest PDE model presenting this feature. This has motivated the use of FKPP for a large variety of applications (examples include population dynamics, tumor growth and fire propagation). Here f, later referred to as the stimulation, was designed so that such a propagation would be observable: if $(x-x_0)^2 + (y-x_0)^2 \leq r_0^2, \quad t \in [t_0, t_0+\delta_0]$ then $f(\mathbf{x},t) = I_0$, otherwise $f(\mathbf{x},t) = 0$, where (x_0, y_0) are the coordinates of the stimulation, $I_0 = 1.0$ its amplitude, $r_0 = 3 \times 10^{-2}$ its radius and $\delta_0 = 5$ its duration. The total duration of the simulation is set to $T = 20$. Figure 2.14 shows an instance of the FKPP model output. The contour plots of u exhibit the propagating front (left and right) while the time dependence of u at a given location exhibits a logistic shape. The

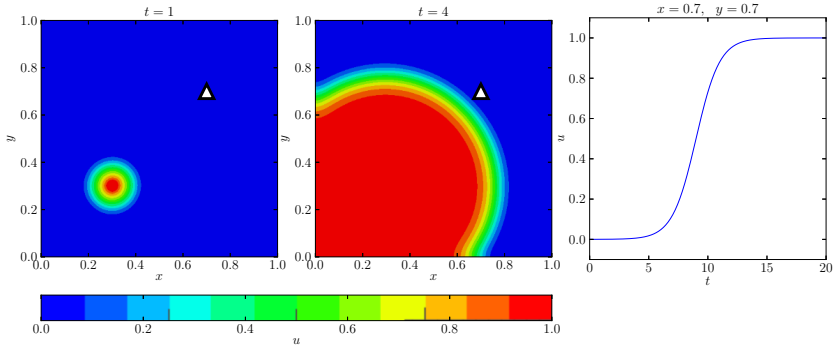

Figure 2.14: Solution of the FKPP model at different times (left, center) and time-dependent solution at a given point (right).

source of variability is assumed to come from the reaction parameter R and from the stimulation coordinates x_0 and y_0: $R = \bar{R}\theta_1$, $x_0 = \theta_2$, $y_0 = \theta_3$, where $\bar{R} = 10$.

Numerical settings The observations are the values of u at $N_t = 200$ time steps times $N_h = 81$ sensors locations, uniformly distributed over $[0,T] \times [0,1]^2$ so that $N_{\mathbf{x}} = 16200$. The synthetic dataset is generated by evaluating the model for

$N = 10^3$ samples of $\boldsymbol{\theta} = (\theta_1, \theta_2, \theta_3)$. The samples are drawn from a multivariate normal distribution of mean $\boldsymbol{\mu} = [0.55, 0.55, 0.50]$ and covariance matrix $\boldsymbol{\Sigma} = \sigma^2 \times \mathbf{I}_3$, where $\sigma = 0.1$. $N_c = 2048$ collocation points are generated using the Sobol sequence over the domain $\Theta = [0.1, 1.0]^3$, the number of moments to be matched is set to $N_m = 3$ and the tolerance parameter is set to $\alpha = 5 \times 10^{-3}$. The PDE model is solved using an in-house software implementing the finite element method. Time integration is performed using the Strang [Str68] splitting scheme with fixed time step. Its application to a similar reaction diffusion model is detailed in [SLT05]. Again, a different discretization is used for both simulation sets. The simulations used to generate the synthetic data are run on a mesh counting 40328 elements whereas the simulations used to solve the inverse problem are run on a coarse mesh counting 11478 elements. In addition, a Gaussian zero-mean noise of amplitude 5% is added to the sensors measurements.

Physical domain reduction This test case where the observable depends on time and space is a good illustration of the crucial need for a DOF selection procedure. Indeed, in this setting, $N_{\mathbf{x}} \simeq 10^4$ which makes the inverse problem both ill-conditioned and computationally intensive. In this example, it is particularly interesting to interpret the results of the CS procedure. Figure 2.15 shows the contours of the components of the SGM first eigenvector $\mathbf{e}_1^j$ (dominant direction) multiplied by its associated eigenvalue η_1^j over the physical domain $\mathcal{D}$. Each column corresponds to one component of $\mathbf{e}_j$, *i.e.* to one parameter, and each row to a different time. The space-time areas of interest now appear clearly. For small times, the parameters are the most identifiable in the vicinity of the domain center. As the front propagates outwards, the important areas are located near the domain boundaries.

Results The proposed inverse procedure is applied and convergence is reached at $n_{\text{iter}} = 3$ and $N_k = 48$ DOFs are selected. Figure 2.16 shows the location and time of the selected sensors. Again, note that they are concentrated around the center of the domain for small times (the stimulation occurs, in average, near the center of the domain) and that they gradually spread outwards as time increases. Figure 2.17 shows the estimated marginals of the three parameters of interest and Table 2.7 summarizes the parameters estimated statistics. Again, the method yields reasonably accurate results considering the low number of model evaluations and the difficulty of the inverse problem. As explained in the previous test case, the errors in the standard deviations estimates stem from the noise and the mesh differences. Note however that there is also a positive bias in the estimation of the reaction parameter R. This is due to the fact that the Sobol simulations mesh is coarser than the synthetic simulations one, inducing a higher numerical diffusion. The higher value obtained for R is therefore the result of a compensation. This explanation was confirmed by using identical meshes for both Sobol and synthetic simulations.

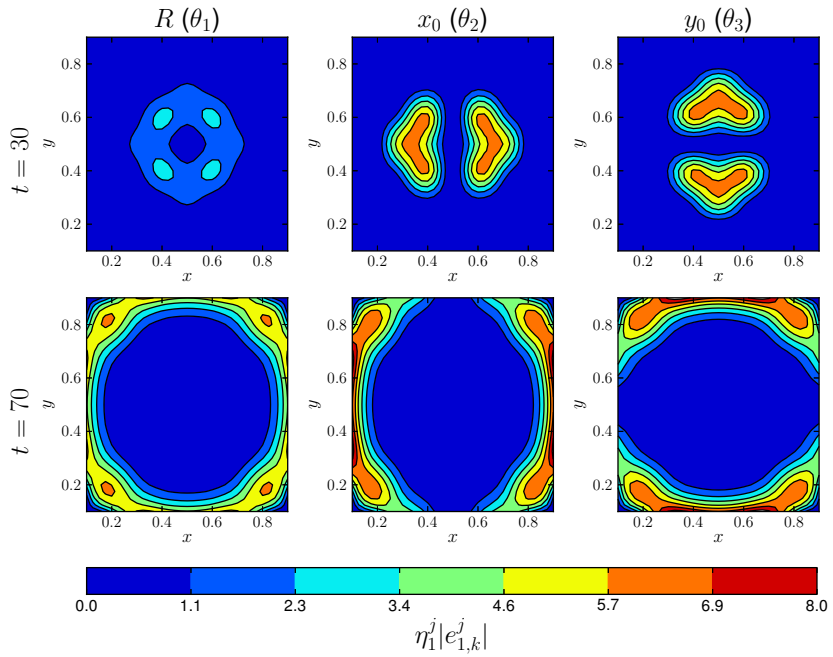

Figure 2.15: Measure of the sensitivity ($\eta_j|e_{j,k}|$) over the spatial domain at different times and for each parameter θ_k.

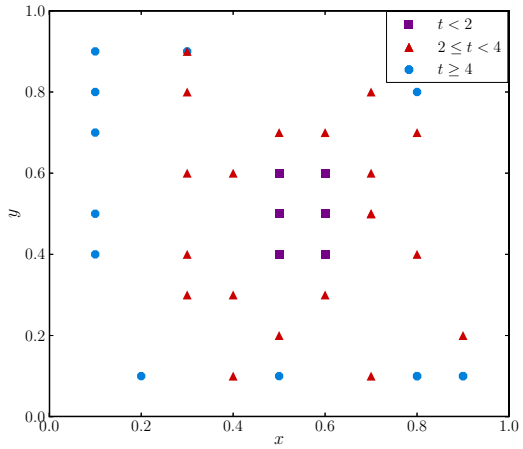

Figure 2.16: Representation of the 48 selected sensors locations and times.

Table 2.7: Results for the FKPP equation.

Statistics	mean			std.		
Parameter	exact	OMM	rel. err.(%)	exact	OMM	rel. err.(%)
θ_1	**0.55**	0.59	5.8	**0.098**	0.16	66
θ_2	**0.55**	0.55	0.4	**0.105**	0.12	9.3
θ_3	**0.50**	0.50	0.5	**0.103**	0.11	8.0

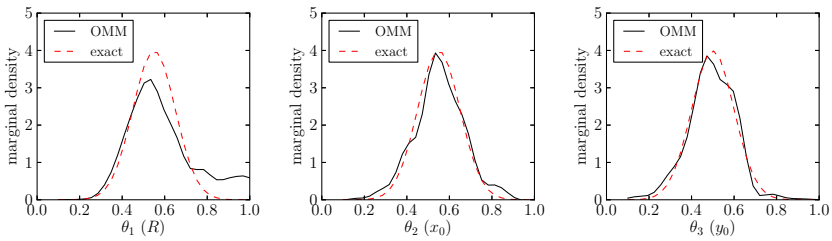

Figure 2.17: Marginal densities of three parameters of the FKPP model estimated using our strategy.

2.5 Limitations and Discussion

The authors would like to insist on the fact that the proposed method provides an estimation that is an approximation of the real underlying PDF of the parameters on the basis of the partial information we have. One of the main interests of our approach is to offer a relatively inexpensive way to estimate parameter variability. We chose to illustrate it with PDEs (including a nonlinear time-dependent diffusion reaction equation) to emphasize this aspect. For problems whose forward solution is less expensive, alternative methods, like Bayesian inference, should probably be preferred.

The proposed approach aims at providing a *point-wise* approximation of the PDF with no assumption of independence between the parameters. It is in fact possible to recover PDFs that exhibit a correlation between parameters as shown in Sections 2 and 3 of the Supplementary Material. This supposes however that such a dependence is observable, meaning it is present in the observable quantities. For example, if the model is the identity (*i.e.* one observes directly the parameters), then a possible correlation between the parameters cannot be directly recovered. In that case however, one can add to the observations the pairwise products of the parameters for instance. For any given model, it is possible to detect which DOFs are well suited for the observation of such correlations using the SGM matrix. Indeed, dominant directions in the parameter space that are not aligned with the axes reveal correlations between the parameters. Automatically selecting DOFs targetted to reveal correlations is not discussed here but will be the subject of future work.

The authors would also like to point out that the present approach has been applied in an electrophysiology context in [TLRG17] with both synthetic and experimental data. The data and codes related to that study are available on an online GitHub repository [1]. Another important point to be discussed is the case where some parameters of the model are unidentifiable. There exist many methods to assess the identifiability of parameters (such as in [PL15]) which are not the point of the present work and which are therefore not discussed here. Nevertheless, it is interesting to study how the proposed method behaves when confronted to unidentifiable parameters. In practice, an unidentifiable parameter is often characterized by a flat

[1] https://github.com/eltix/omm_jrsi

estimated PDF. To assess whether this means that the underlying parameter actually has a uniform PDF or if this means it is unidentifiable, we suggest the following numerical procedure. First, note that the estimated PDF satisfies, by construction, the constraints. We propose to add a small perturbation term to the PDF in the direction of the presumably unidentifiable parameter (so that the perturbed function is a PDF). If the constraints are still verified, this usually means the parameter in question is unidentifiable. If they are not, its distribution is probably uniform.
In the present work, the PDF is discretized using a quasi-random Sobol sequence. This choice was motivated in part by practical reasons as it is non intrusive and features a simple quadrature rule. Other discretizations could be investigated such as stochastic Galerkin-type discretization [BNT07] of the model or a polynomial expansion of the PDF [HLM14].

2.6 Concluding remarks

We have developed a procedure to estimate the PDF of uncertain parameters from the knowledge of experimental moments of an observable. This iterative procedure is based on two combined algorithms. The first one, the Observable Moment Matching (OMM) algorithm, computes an estimate of the parameters PDF using a given subset of the available model DOFs. It maximizes the PDF entropy under the constraints of matching the moments of the observable in the subset DOFs. The second one, the Clustered Sensitivities (CS) algorithm, selects a subset of the available model DOFs. The DOFs are clustered using a similarity measure and a representative for each cluster is chosen to maximize the sensitivity with respect to the parameters. Selecting a subset of N_k DOFs among the $N_{\mathbf{x}}$ available ones ensures a better-conditioned and less computationally expensive inverse problem solved in the OMM algorithm.
This approach has been compared to existing techniques on an ODE test case. While requiring much less model evaluations, our method has a similar accuracy. Then, it has been tested on more sophisticated cases involving an elliptic (resp. parabolic) PDE model with 5 (resp. 3) uncertain parameters. To conclude, we comment on details that have not been thoroughly investigated in this paper but still are worth mentioning. First, the choice of parameter box (or stochastic domain) is very important and conditions the overall success of the procedure. In our tests, we used a large box with respect to the exact PDF support and not centered on the exact mean to avoid any favorable bias. In the case of real experimental data, a reasonable strategy would be to first try a very large box and use the PDF estimate to recenter and rescale the box for a second run. Another strategy would be to locally refine the stochastic grid to capture the regions of interest. Applying different weights in the moment-matching constraints depending on the moment order has also not been investigated but could impact the precision of the method. One could use higher weights for the higher moment components or for certain DOFs. Finally, one possible use of the proposed approach could be to produce a cheap PDF estimation

used as a prior for more expensive methods such as Bayesian inference.

2.7 Appendix

2.7.1 Calculus of variations

Let us derive the Gâteaux derivative of $\mathcal{L}$ with respect to ρ. Let $v \in L_1(\Theta)$ and $\varepsilon > 0$, one reads:

$$\mathcal{L}(\rho + \varepsilon v, \lambda, \nu) = \int_\Theta (\rho + \varepsilon v)\log(\rho + \varepsilon v) \tag{2.43}$$

$$- \sum_{m=1}^{N_m} \int_\mathcal{D} \lambda_m(\mathbf{x}) \left(\int_\Theta g^m(\mathbf{x}, \boldsymbol{\theta})(\rho + \varepsilon v) - \tilde{\mu}_m(\mathbf{x}) \right) \mathrm{d}\mathbf{x} - \lambda_0 \left(\int_\Theta (\rho + \varepsilon v) - 1 \right) \tag{2.44}$$

$$- \int_\Theta (\rho + \varepsilon v)\nu, \tag{2.45}$$

$$\tag{2.46}$$

Let $-S(\rho + \varepsilon v) = \int_\Theta (\rho + \varepsilon v)\log(\rho + \varepsilon v)$, then:

$$-S(\rho + \varepsilon v) = \int_\Theta (\rho + \varepsilon v)(\log(\rho) + \varepsilon v \frac{1}{\rho} + \mathcal{O}(\varepsilon^2)), \tag{2.47}$$

$$= \int_\Theta \rho\log(\rho) + \varepsilon v(1 + \log\rho) + \mathcal{O}(\varepsilon^2). \tag{2.48}$$

Therefore, one has:

$$\mathcal{L}(\rho + \varepsilon v, \lambda, \nu) - \mathcal{L}(\rho, \lambda, \nu) = \varepsilon \int_\Theta \left[1 + \log(\rho) - \sum_{m=1}^{N_m} \int_\mathcal{D} \lambda_m(\mathbf{x}) g^m(\mathbf{x}, \boldsymbol{\theta}) \mathrm{d}\mathbf{x} - \lambda_0 - \nu \right] v + \mathcal{O}(\varepsilon^2) \tag{2.49}$$

and finally the derivative in the direction of v reads:

$$\left\langle \frac{\partial \mathcal{L}}{\partial \rho}, v \right\rangle_\Theta := \lim_{\varepsilon \to 0} \frac{\mathcal{L}(\rho + \varepsilon v, \lambda, \nu) - \mathcal{L}(\rho, \lambda, \nu)}{\varepsilon}, \tag{2.50}$$

$$= \int_\Theta \left[1 + \log(\rho) - \sum_{m=1}^{N_m} \int_\mathcal{D} \lambda_m(\mathbf{x}) g^m(\mathbf{x}, \boldsymbol{\theta}) \mathrm{d}\mathbf{x} - \lambda_0 - \nu, \right] v \tag{2.51}$$

so that

$$\frac{\partial}{\partial \rho}\mathcal{L}(\rho, \lambda, \nu) = 1 + \log(\rho) - \sum_{m=1}^{N_m} \int_\mathcal{D} \lambda_m(\mathbf{x}) g^m(\mathbf{x}, \boldsymbol{\theta}) \mathrm{d}\mathbf{x} - \lambda_0 - \nu. \tag{2.52}$$

The first variations of $\mathcal{L}$ with respect to λ_0 and λ are, by construction of the Lagrangian, the constraints:

$$\frac{\partial}{\partial \lambda_0}\mathcal{L}(\rho,\lambda,\nu) = \int_\Theta \rho(\boldsymbol{\theta})\,\mathrm{d}\boldsymbol{\theta} - 1, \tag{2.53}$$

$$\frac{\partial}{\partial \lambda_m}\mathcal{L}(\rho,\lambda,\nu) = \int_\Theta g^m(\mathbf{x},\boldsymbol{\theta})\rho(\boldsymbol{\theta})\,\mathrm{d}\boldsymbol{\theta} - \tilde{\mu}_m(\mathbf{x}), \quad m = 1,\dots,N_m \tag{2.54}$$

2.7.2 Illustration of the analysis hypotheses

In this section, we provide examples of models and PDFs which satisfy the hypotheses of Lemma 2.2 of the main document: there exist $C, \delta > 0$ such that, for all $p \in \mathbb{N}^*$,

$$\|g\|_{L^p(\mathcal{D}\times\Theta),\rho_e} := \left(\int_{\mathcal{D}}\int_\Theta g(\mathbf{x},\boldsymbol{\theta})^p \mathrm{d}\mathbf{x}\rho_e \mathrm{d}\boldsymbol{\theta}\right)^{1/p} \leq \left(\frac{C}{p^{1+\delta}}\right)^{1/p}. \tag{2.55}$$

Example 1 Let us consider the following ODE model:

$$\begin{cases} \dot{u}(t) &= -u(t), \quad t \in [0,T]. \\ u(0) &= \theta. \end{cases} \tag{2.56}$$

The solution simply is $u(t,\theta) = \theta e^{-t}$. The observable g is defined as $g := u$. The parameter space is $\Theta = [0,1]$ and the physical space $\mathcal{D} = [0,T]$. Let us now evaluate the quantities in Equation 2.55:

$$\begin{aligned}
\int_{\mathcal{D}}\int_\Theta g(\mathbf{x},\boldsymbol{\theta})^p \mathrm{d}\mathbf{x}\rho_e \mathrm{d}\boldsymbol{\theta} &= \int_0^T \int_0^1 g(t,\theta)^p \rho_e(\theta)\mathrm{d}t\mathrm{d}\theta, \\
&= \left(\int_0^T e^{-pt}\mathrm{d}t\right)\left(\int_0^1 \theta^p \rho_e(\theta)\mathrm{d}\theta\right), \\
&= \frac{1}{p}\left(1-e^{-pT}\right)\left(\int_0^1 \theta^p \rho_e(\theta)\mathrm{d}\theta\right), \\
&\leq \frac{1}{p}\left(\int_0^1 \theta^p \rho_e(\theta)\mathrm{d}\theta\right).
\end{aligned}$$

Therefore, a sufficient condition to satisfy the hypothesis in (2.55) with $C = 1$ and $\delta = 1/2$ is that, for all $p \in \mathbb{N}^*$,

$$\int_0^1 \theta^p \rho_e(\theta)\mathrm{d}\theta \leq \frac{1}{\sqrt{p}}. \tag{2.57}$$

Examples of densities ρ_e that verify (2.57) are for instance $\mathcal{U}([0,1])$, $\mathcal{N}(1/2,\tau)$ for any $\tau > 0$.

Example 2 Let us consider the following ODE model:

$$\begin{cases} \dot{u}(t) &= -\theta u(t), \quad t \in [0, +\infty[. \\ u(0) &= 1. \end{cases} \tag{2.58}$$

The solution reads $u(t, \theta) = e^{-\theta t}$. The observable g is defined as $g := u|_{t \geq t_0}$, with $t_0 > 0$. The parameter space is $\Theta = [0, 1]$ and the physical space $\mathcal{D} = [t_0, +\infty[$. Let us now evaluate the quantities in Equation 2.55:

$$\begin{aligned} \int_{\mathcal{D}} \int_{\Theta} g(\mathbf{x}, \boldsymbol{\theta})^p \mathrm{d}\mathbf{x} \rho_e \mathrm{d}\boldsymbol{\theta} &= \int_{t_0}^{\infty} \int_0^1 g(t, \theta)^p \rho_e(\theta) \mathrm{d}t \mathrm{d}\theta, \\ &= \int_0^1 \frac{1}{\theta p} e^{-\theta p t_0} \rho_e(\theta) \mathrm{d}\theta, \\ &= \frac{1}{p} \left(\int_0^1 \frac{1}{\theta} e^{-\theta p t_0} \rho_e(\theta) \mathrm{d}\theta \right). \end{aligned}$$

For example, we consider the probability distribution $\rho_e(\theta) = 2\theta$:

$$\begin{aligned} \int_{\mathcal{D}} \int_{\Theta} g(\mathbf{x}, \boldsymbol{\theta})^p \mathrm{d}\mathbf{x} \rho_e \mathrm{d}\boldsymbol{\theta} &= \frac{1}{p^2} \frac{1 - e^{-p t_0}}{t_0}, \\ &\leq \frac{1/t_0}{p^2}. \end{aligned}$$

Therefore (2.57) is verified by choosing $\delta = 1$ and $C = 1/t_0$.

2.7.3 Illustration with an unidentifiable model

Consider the following simple model:

$$\begin{cases} u(\theta_1, \theta_2) &= \theta_1 - \theta_2, \quad (\theta_1, \theta_2) \in \boldsymbol{\Theta} \\ g := u \end{cases} \tag{2.59}$$

Let us now assume that the observations are generated by sampling (θ_1, θ_2) from an unknown distribution such that θ_1 and θ_2 are perfectly correlated. This means that, for each sample, $\theta_1 = \theta_2$. Then, the model output and therefore all its moments are identically 0. It is interesting to study how the OMM algorithm behaves in such a degenerated case and if it is able to capture the dependence between the parameters. The analytical solution to the observable moment matching problem is as follows:

$$\rho(\theta_1, \theta_2) = \exp(\lambda_0 - 1) \exp(\sum_{k=1}^{m} \lambda_k (\theta_1 - \theta_2)^k), \tag{2.60}$$

$$\iint_{(\theta_1, \theta_2) \in \Theta} (\theta_1 - \theta_2)^p \exp\left(\sum_{k=1}^{m} \lambda_k (\theta_1 - \theta_2)^k \right) \mathrm{d}\theta_1 \mathrm{d}\theta_2 = 0, \quad 1 \leq p \leq m \tag{2.61}$$

where m is the number of observed moments. In what follows, we choose $\boldsymbol{\Theta} = [-1, 1]^2$.

$\underline{m = 1}$ In that case, the Lagrange multiplier λ_1 is the root of:

$$\frac{8 \sinh(\lambda_1)}{\lambda_1^3} \left[\lambda_1 \cosh(\lambda_1) - \sinh(\lambda_1)\right], \tag{2.62}$$

whose only root is $\lambda_1 = 0$ (the previous expression is undefined for $\lambda_1 = 0$ but a Taylor expansion shows that its limit is 0 when $\lambda_1 \to 0$). The resulting PDF is therefore a uniform distribution over $[-1, 1]^2$. The numerical experiments confirm this analytical result.

$\underline{m = 2}$ If $m = 2$, $\lambda_2 \to -\infty$ analytically. We can however study the case where the second order moment is not 0 but $\varepsilon > 0$ and then make ε tend to 0. This would correspond to the case where there is a Gaussian noise added to the measurements and whose amplitude would tend to 0. The resulting PDFs are shown in Figure 2.18 with different values of ε. For a given value of $\varepsilon > 0$, the PDF is a univariate normal distribution of standard deviation $(-2\lambda_2)^{-1/2}$ in the direction $\theta_1 = \theta_2$. This is equivalent to a bivariate normal distribution in the degenerate case where θ_1 and θ_2 are perfectly correlated (and therefore the covariance matrix is not invertible).

Analytically, when $\varepsilon \to 0^+$, $\lambda_2 \to -\infty$ and the PDF tends to a Dirac distribution in the direction $\theta_1 = \theta_2$. Numerically, λ_2 takes finite values when $\varepsilon = 0$. However, we observe in Figure 2.19 that $\lambda_2 \to -\infty$ when the number of quadrature points $N_c \to +\infty$. The estimated PDF (lower right corner of Figure 2.18) corresponds to a discretized approximation of the Dirac distribution.

As a conclusion, the dependence between the two parameters, and in particular their perfect correlation, is captured by the OMM method as soon as two or more moments are observed. However, the true distribution cannot be recovered due to the non-identifiability of the model.

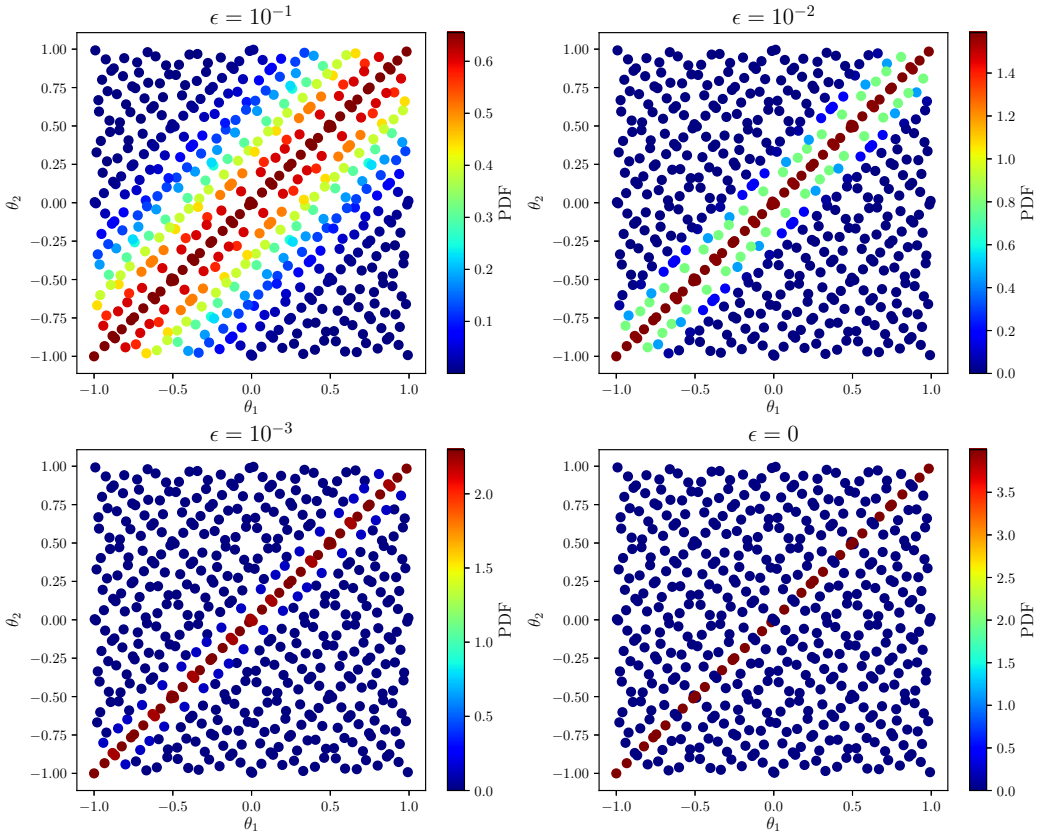

Figure 2.18: Model (2.59). Point-wise visualization of the estimated PDF for different values of ε.

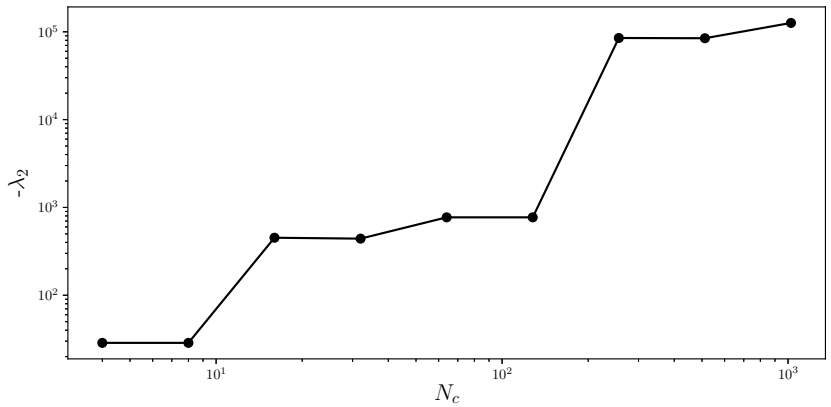

Figure 2.19: Numerical experience: λ_2 as the number of quadrature points N_c increases.

Chapter 3

Modeling Variability in Cardiac Electrophysiology: A Moment Matching Approach

---

This chapter is based on [TLRG17]

The variability observed in action potential (AP) cardiomyocyte measurements is the consequence of many different sources of randomness. Often ignored, this variability may be studied to gain insight into the cell ionic properties. In this chapter, we focus on the study of ionic channel conductances and we describe a methodology to estimate their probability density function (PDF) from action potential recordings. The method relies on the matching of observable statistical moments and on the maximum entropy principle. We present four case studies using synthetic and experimental AP measurements sets from human and canine cardiomyocytes. In each case, the proposed methodology is applied to infer the PDF of key conductances from the exhibited variability. The estimated PDFs are discussed and, when possible, compared to the true distributions. We conclude that it is possible to extract relevant information from the variability in AP measurements and discuss the limitations and possible implications of the proposed approach.

Contents

3.1 Introduction 57
3.2 Methods 58
3.2.1 Electrophysiology Measurements 58
3.2.2 Electrophysiology Cell Models 59
3.2.3 Observable Moment Matching Method 63
3.3 Results 66
3.3.1 Test Case 1: Decker Model with Synthetic Data 66
3.3.2 Test Case 2: Synthetic Data at Different Pacing Frequencies . 70
3.3.3 Test Case 3: Experimental Data from Canine Ventricular Cells 71
3.3.4 Test Case 4: Experimental Data from Human Atrial Cells . . 73
3.4 Discussion 76
3.5 Supplementary Material 83

3.1 Introduction

The variability observed in action potential (AP) measurements is, like in most biological systems, the consequence of many different sources of randomness. In this paper we focus on parameter randomness which, in the context of AP modeling, corresponds to the natural variability of the cardiomyocyte electrical properties such as its capacitance, ionic channel conductances and gate time constants. Due to the large number of free parameters in AP models, these parameters are in practice unidentifiable [SS10, DL04]. In fact, different combinations of these parameters can lead to the same AP. Therefore, we choose to restrict our analysis to ionic channel maximal current densities which for convenience are referred to as conductances in the following. Among these conductances, a subset is selected to account for the observed variability depending on the available data set. AP measurements may result from heterogeneity within a population of cells (inter-subject variability) [SBOW+14] or from dynamic variations within a single cell (intra-subject variability) [JCB+15, PDB+16]. In this paper, we propose a novel way to study the variability of AP models parameters in both contexts. From a modeling point of view, it is convenient to ignore the variability of electrophysiology measurements (and therefore of the underlying parameters) since a set of fixed parameters is sought. However, investigating the variability of AP models parameters has several motivations. It can be used to predict the response of cardiomyocytes to certain drugs [BBOVA+13]. It can also provide insight into cell modifications at the origin of common heart diseases such as atrial fibrillation [WHC+04, SBOW+14] or ventricular arrythmia [GBRQ14].

There are two main strategies to estimate the parameters variability given a set of AP measurements. First, one could fit the AP model to each measurement individually and therefore obtain a set of parameters from which useful statistics may be computed. The problem of fitting an individual AP has been addressed many times and using a large variety of methods [HDL07, DL04, SVNL05, CCY+12, KNV14, LFNR16]. However, the computational cost of such a strategy scales with the number of available experimental samples and may therefore be prohibitive. As a consequence, only a low number of cells can be analyzed this way. The second strategy belongs to the so-called population of models approach. The experimental set is considered as a whole and the parameters statistics are estimated by solving a statistical inverse problem. Several techniques were developed to solve such problems [Kou09, GLV14] and their application to electrophysiology has recently generated much interest [RPFR09, MT11, BBOVA+13, SBOW+14, DCP+16]. The present approach belongs to the second strategy. The AP model parameters are described as random variables associated with an unknown probability density function (PDF). The proposed method aims at estimating the parameters PDF, thus generalizing the commonly used mean $\pm$ standard deviation intervals. The PDF is sought so that it "explains" the observed variability featured by a given set of AP measurements. More precisely, the estimated PDF is the solution of a constrained optimization problem which is an adaptation of the maximum entropy principle [Jay57].

The method, later referred to as Observable Moment Matching (OMM), is detailed in [GLT16]. Contrary to other approaches such as Monte-Carlo Markov Chains (MCMC) [Ros95] or Approximate Bayesian Computation [BVW+15], the present method does not guarantee to converge to the true parameters distribution. Instead, it proposes a way to obtain an approximation of the underlying PDF at the fraction of the cost of other finer methods. In this paper, the OMM method is applied to the estimation of the PDF of key conductances from AP measurements. These measurements may be the AP time series (sometimes referred to as waveforms or traces) or be in the form of biomarkers, i.e. features extracted from the time series. Four different case studies are presented to illustrate the use of the OMM method in different scenarios. Test cases 1 and 2 feature synthetic data sets with AP biomarkers and time series. Test case 3 features an experimental data set with intra-subject variability and Test case 4 features an experimental data set with inter-subject variability.

3.2 Methods

3.2.1 Electrophysiology Measurements

3.2.1.1 Synthetic datasets

For validation purposes, the proposed method to solve our statistical inverse problem is first applied to synthetic measurements, i.e. APs generated by a computational model and corrupted by some noise. An example of such synthetic measurements is shown in Figure 3.2. Here, the noise is an independent zero-mean normally distributed random variable. The signal-to-noise ratio (SNR) is written in dB and defined as:

$$\mathrm{SNR} = 10 \log_{10} \left(\frac{A^2}{2\tau^2} \right), \tag{3.1}$$

where τ is the noise standard deviation and A the AP amplitude.
In Test Cases 1 and 2, the synthetic data sets are generated by evaluating the AP computational model for different values of the parameters, i.e. conductances, of interest. The parameters are sampled from a known distribution so that the estimated PDF may be compared to the true one.

3.2.1.2 Experimental datasets

In what follows, we are using published AP recordings that are readily available online. In Test Case 3, the experimental data set consists of several APs recorded on a single canine ventricular cell [JCB+15] [1]. This allows us to investigate beat-to-beat variability which is a type of intra-subject variability. About 570 cycles are available, 200 in control conditions and the remaining after the addition of a drug and the modification of the bath ionic centrations. In Test Case 4, the experimental data

[1] Data are available here http://www.cs.ox.ac.uk/chaste/download.html

set consists of human atrial cardiomyocytes measurements coming from different subjects [SBOW+14] [2]. Interestingly, the data set is divided into two groups: one counting 254 Sinus Rythm (SR) patients and another one counting 215 chronic Atrial Fibrillation (AF) patients.

3.2.2 Electrophysiology Cell Models

3.2.2.1 Cell models

Throughout the four test cases presented in this paper, three different AP computational models are used. Using different models serves two purposes. First, it illustrates the fact that the OMM method can successfully be applied to different scenarios. Different cardiac cellular models were used to illustrate that our methods are not model specific. Second, it is more natural to use models that were designed from experimental setups that are close to those of the available data sets. In Test Cases 2 and 4, the human atrial model by Courtemanche *et al.* [CRN98] was used. It is one of the first human heart cell models. Mostly based on the Luo and Rudy [LR94] membrane currents formulations, it was developed using experimental recordings from human atrial cells. In Test Case 1 (resp. 3), the canine ventricular model by Decker *et al.* [DHS+09] (resp. Davies *et al.* [DMH+11]) was used. Both models are improvements of the Hund and Rudy model [HR04] with updated current formulations to fit canine epicardium (for the Decker model) and mid-myocardial (for the Davies model) cells. All three models belong to the so-called second generation [Kog09] for they provide detailed descriptions of the main ionic channels, pumps and exchangers as well as the internal calcium dynamics. For the sake of convenience, these models will be referred to by their first author's name. We will focus on the PDF estimation of six key conductances corresponding to the following currents: the fast sodium current I_{Na}, the inward rectifier potassium current I_{K1}, the transient outward potassium current I_{to} (I_{to1} in the canine models), the rapid (resp. slow) delayed rectifier potassium current I_{Kr} (resp. I_{Ks}) and the L-type calcium current I_{CaL}. For the sake of clarity, g_{Na}, g_{K1}, g_{to}, g_{Kr}, g_{Ks}, g_{CaL} will refer to a multiplicative coefficient for the corresponding values found in the literature. For instance, $g_{Na} = 1$ means that g_{Na} is set to the same value as that of the original paper. When necessary, a table will summarize the conductances that have been modified from their reference values.

3.2.2.2 Numerical Methods

The previously mentioned models consist of a set of coupled ordinary differential equations (ODEs) whose formulae are detailed e.g. on the CellML project website [CLN+03]. The Courtemanche and Davies models were implemented in an in-house C++ code and the simulation outputs were compared with those of the Matlab implementations found on the CellML website. The time integration

[2] Data are available here http://journals.plos.org/plosone/article?id=10.1371/journal.pone.0105897

of the ODEs is carried out using the CVODE library [CH96] which implements the Backward Differentiation Formulae. This state-of-the-art time integrator is well suited to stiff problems as those encountered in electrophysiology. It is adaptive, in time step and order, which can significantly save computational time. For all the test cases, the absolute and relative tolerances of the CVODE solver were set to 10^{-6}. For the Decker model, the time integration was carried out using variable but non-adaptive time steps. The stimulation protocol consists in stimulating at a frequency of 1 Hz (or 2 Hz for Test Case 2) over a few cycles so that the recorded AP lies in a permanent regime. In practice, the number of these transition cycles was set to 5 (10 for APs stimulated at 2Hz) and the relative difference norm between two consecutives APs is less than 0.1%. Unless stated otherwise, the stimulation duration is set to 2 ms and its amplitude to 20 μA.

3.2.2.3 AP time series

In Test Case 1, the AP time series are used as the observable. This means that the inverse procedure possibly uses the AP value at every available time step. This has the advantage of capturing all of the available information but also the disadvantage of increasing the computational cost of the inverse procedure since the number of time steps may be large. To tackle this issue, a time step selection algorithm was developed and is described in [GLT16]. It uses the pre-computed simulation database to approximate the sensitivities with respect to each parameter and for each time step. Using these sensitivities, the time steps are clustered using an agglomerative clustering algorithm and a representative is chosen for each cluster. Only the representatives are retained for the inverse procedure. In practice their number is much lower than the total number of time steps, thus alleviating the computational cost of the inverse procedure. Indeed, as described in [GLT16], the OMM procedure cost is dominated by the inversion of a dense matrix of size $(N_m \times N_t)^2$. Furthermore, reducing the number of time steps is motivated by numerical considerations since the conditionning of this matrix deteriorates as the number of time steps increases. This time step selection comes at no cost since it uses the already computed simulation database.

Since the ODEs are solved using an adaptive time-stepping, each AP simulation is discretized on a different time grid and later interpolated on a common grid. This interpolation procedure introduces a numerical error which may be considered as a numerical noise, alongside the noise in the measurements (whether synthetic or experimental).

3.2.2.4 AP biomarkers

In Test Cases 2, 3 and 4, the inverse procedure is applied to so-called biomarkers, which are quantities computed from the AP time series. They describe the main features of the AP such as its shape or its duration. We will focus on the following

biomarkers (see Figure 3.1): the AP duration APD90 (resp. APD50, APD30, etc.) at 90% repolarization (resp. 50%, 30%, etc.), the resting membrane potential RMP, the maximum upstroke velocity dV/dt_{max}, the AP value at 20% repolarization V20 (which roughly corresponds to the AP plateau value), the AP value 30 ms after depolarization V_{notch} and the Area Under the Curve (AUC), i.e. the AP time integral over one cycle.

Even though these quantities seem to well capture the main features of a given AP, they generally don't convey enough information about the underlying parameters for the inverse procedure. Therefore, the pairwise products (APD90×APD50, APD90×APD20 and so on) of the above biomarkers are added to the moments constraints. Note that the AP triangulation is a commonly used biomarker and may be interpreted as the pairwise product between APD90 and 1/APD30. For the synthetic measurements, the noise is added to the AP time series before computing the biomarkers.

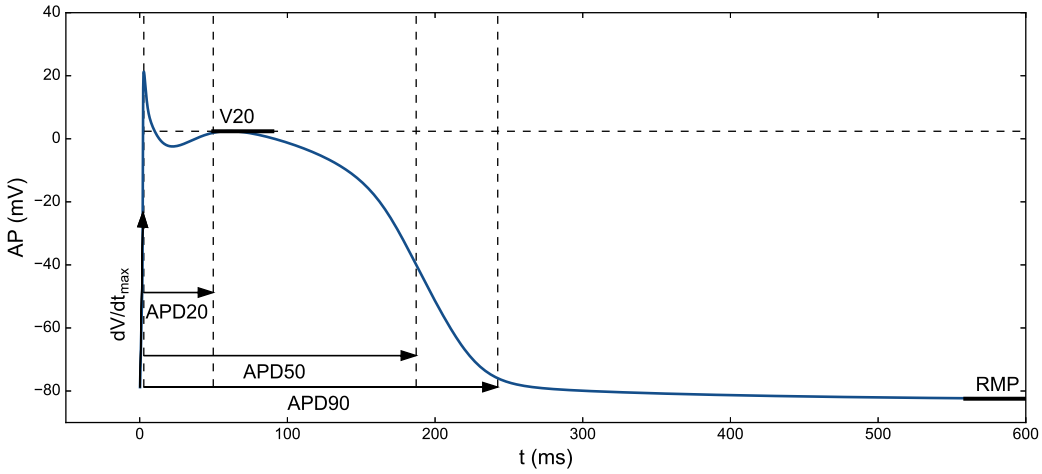

Figure 3.1: Biomarkers computed from an AP.

3.2.2.5 Parameter calibration

We restrain our parameter estimation study to three to six conductances. This assumption is critical and is discussed in the Discussion section. This means that the parameters of interest are allowed to vary while all the other parameters of the model remain fixed. While it seems reasonable to choose the values found in the literature for these parameters, it often proves to be a bad choice when dealing with real data. Therefore, one needs to calibrate these parameters before performing the inverse procedure using the most representative experimental sample of the available sata set. In Test Case 3, the most representative sample is the one whose biomarkers are the closest to the median values (there is one representative for each group). In Test Case 4, the most representative sample is the AP whose APD90 is the closest to the median value. Once these representative samples are identified, a parameter

calibration procedure is performed for all ionic conductances. Courtemanche model: experimental parameter calibration. shows the values obtained from the literature for these parameters as well as their estimated counterparts for both Courtemanche and Davies models. The Table also shows some external ions concentrations. These were directly set using the bath descriptions available in the publications associated with the experimental data sets. The parameter calibration is actually a constrained minimization problem where the cost function J to be minimized reads:

$$J(\mathbf{g}) = \sum_{i=1}^{N_t} \left((u(t_i, \mathbf{g}) - y(t_i))^2 + K \sum_{j=1}^{n_p} (g_j - \hat{g}_j)^2 \right), \tag{3.2}$$

where y is the experimental quantity of interest, u the corresponding simulation output and N_t the number of values to be fitted (number of biomarkers or number of time steps depending on the test case). The second part of the cost function is a regularization term where n_p is the number of conductances to fit, g_j the estimated value of the j^{th} conductance, $\hat{g}_j$ its nominal value and K is a user-defined regularization parameter. This term ensures that the conductances remain within a reasonable range around the nominal values. In practice, this parameter is chosen to be small compared to the first term in (3.2) so that the conductances are weakly constrained around relevant values without too much impact on the fitting quality. When possible, this parameter K may even be set to zero. In The "L-curve" is obtained for the first two parameters of the test case presented in Section 4.4.1. The ℓ^1-norm of $\boldsymbol{\beta}^{(h)}$ is plotted against the training error for different values of λ_h. Here, λ_h varies between 10^{-6} and 2×10^1., a brief study of the effect of K is performed. The models considered in this work are not well suited to classical gradient optimization techniques as they consist of many and strongly nonlinear ODEs, making the gradient computations challenging and the cost function highly irregular. For the sake of simplicity, we therefore used gradient-free optimization techniques such as genetic algorithms [SVNL05]. We chose the Covariance Matrix Adaptation Evolution Strategy (CMA-ES) evolutionary algorithm [Han06] for it is currently one of the most performant genetic algorithm and was used successfully in a variety of applications. Furthermore, a Python (as well as other languages) implementation of the CMA-ES algorithm is available online [3] and behaves like a black-box optimization tool. The CMA-ES algorithm was recently used in a similar context in [JCB+15], where conductances of several models (including the Davies model) were estimated from both synthetic and experimental measurements. Note that all parameters values are not allowed to take negative values but they are not limited by any upper bound. An exception is made for the fast sodium conductance g_{Na} (which is limited to five times its nominal value) for numerical reasons. Indeed, a high value of g_{Na} may lead to a failure of the time integration around the upstroke.

[3] https://www.lri.fr/~hansen/cmaes_inmatlab.html#python

3.2.3 Observable Moment Matching Method

We now give an overview of the OMM method. This method aims at obtaining an approximation of the parameters PDF at a low computational cost. This approximation is however not meant to reach the precision of finer methods such as MCMC. The interested reader is referred to [GLT16] where more details are provided.

3.2.3.1 Construction of the simulation database

The OMM method relies on the pre-computation of a simulation database of many APs (or AP biomarkers) by varying the parameters of interest. We introduce the parameter space Θ, which is a subset of $\mathbb{R}^{n_p}$ where n_p is the number of parameters (the conductances in our case). A point in Θ, or parameters sample, is denoted by $\boldsymbol{\theta} = (\theta_1, \ldots, \theta_{n_p})$. The parameter space is discretized using the Sobol sequence [Sob76]. This sampling method is well-suited to the present framework: it uniformly spans the parameter space in a low-discrepancy manner while featuring a simple Monte-Carlo quadrature rule; it requires little knowledge of the true parameters distribution; furthermore, as the latin hypercube method used in [BBOVA+13], it only requires a lower and upper bound for each parameter and the total number of samples. Points in the discretized space will be called collocation points and the total number of these points will be denoted by N_c. The discretization of the parameter space is therefore given by the set $\{\boldsymbol{\theta}_1, \ldots, \boldsymbol{\theta}_{N_c}\}$. For each collocation point, one AP is simulated using the numerical protocol described above and stored. Note that once this simulation database is built, no additional AP simulation is required during the inverse procedure.

3.2.3.2 Optimization problem

Given a PDF ρ, the moment of order m of the simulations at a given point t (time step or biomarker index) is defined by:

$$\mu_m^\rho(t) = \int_{\boldsymbol{\theta}\in\Theta} u(\boldsymbol{\theta}, t)^m \rho(\boldsymbol{\theta}) \mathrm{d}\boldsymbol{\theta},$$

where $u(\boldsymbol{\theta}, t)$ is the simulation output, already computed and stored in the database. The empirical moments of order m of the measurements at a given point t is defined by:

$$\hat{\mu}_m(t) = \frac{1}{N} \sum_{i=1}^{N} y_i(t)^m,$$

where $y_i(t)$ is the observable value at point t of the i^{th} experimental sample and N is the total number of experimental samples. The goal of the OMM method is to find the PDF ρ such that the moments, up to a certain order N_m, of the simulations and of the experiments match at every point t. This moment matching condition will later be referred to as the moment matching constraints. As explained above, in the case where many observable quantities are available, a procedure has been set

up to select a subset for which the moment matching constraints hold. In general however, the stated moment problem is under-determined, meaning there exists an infinity of different ρ that satisfy the moment constraints. We propose to regularize the problem using the maximum entropy principle where the entropy of a given PDF ρ is given by:

$$S(\rho) = -\int_{\boldsymbol{\theta}\in\Theta} \rho(\boldsymbol{\theta}) \log\left[\rho(\boldsymbol{\theta})\right] \mathrm{d}\boldsymbol{\theta}$$

This type of regularization roots in information theory [Jay57], it is considered the most natural choice when limited information about a PDF is available. It is also well-suited to our optimization problem for practical mathematical reasons. In Section 2.4.2. of [GLT16], we propose an analysis of the error on the PDF estimation made by adopting the maximum entropy regularization. In Prop. 1. of the same paper, it is shown that under certain conditions on the regularity of the observable and identifiability of the parameters, the error on the PDF is bounded. The conditions on the regularity of the observable may not be easy to check formally because of the nonlinearities of the state equations. Nevertheless, for the practical problems considered in this work, they do not seem critical. The condition on the identifiability may also be difficult to assess in general. In our algorithm, the identifiability issues are circumvented by regularizing the Hessian in the optimization problem and by selecting the points where the moments are matched (see Discussion section).Finally, the estimated PDF is the solution of the following constrained optimization problem:

$$\begin{cases} \max\limits_{\rho} & S(\rho) \\ \text{s.t.} & \begin{cases} \mu_m^{\rho}(t) & = & \hat{\mu}(t) & \text{(moment constraints)} \\ \int_{\boldsymbol{\theta}} \rho(\boldsymbol{\theta})\mathrm{d}\boldsymbol{\theta} & = & 1 & \text{(normalization)} \end{cases} \end{cases} . \tag{3.3}$$

The optimization problem is recast using Lagrange multipliers for the constraints and the corresponding Euler-Lagrange multipliers are solved using a quasi-Newton method. Denoting by $|\Theta|$ the volume of Θ, the integrals over the parameter space of a given quantity f are approximated using the Monte-Carlo quadrature rule:

$$\int_{\boldsymbol{\theta}\in\Theta} f(\boldsymbol{\theta})\mathrm{d}\boldsymbol{\theta} \simeq \frac{|\Theta|}{N_c} \sum_{1}^{N_c} f(\boldsymbol{\theta}_i). \tag{3.4}$$

In Appendix A of the Supplementary Material, an illustration of the OMM method on a simple test case using the Davies model is provided.

3.2.3.3 Post-processing

The PDF is a real-valued multivariate function of n_p variables. The output of the OMM method is the estimated PDF values at each collocation point in the parameter space. We insist on the fact that the estimated PDF does not take any parametric form (such as a multivariate Gaussian for instance) but is defined point-

wise. However, beyond two dimensions, its visualization becomes complex and may not provide much information. Therefore, as it is the case in the remainder of the article, the PDF is post-processed so that the marginal densities of the parameters may be visualized. The marginal density $z_p(x)$ of parameter p at point x reads:

$$z_p(x) = \int_{(\theta_1,\ldots,\theta_{p-1},x,\theta_{p+1},\ldots,\theta_{n_p})\in\Theta} \rho(\boldsymbol{\theta})\mathrm{d}\theta_1 \ldots \mathrm{d}\theta_{p-1}\mathrm{d}\theta_{p+1} \ldots \mathrm{d}\theta_{n_p}.$$

This step actually needs a finer grid in the parameter space than that provided by the Sobol sequence. The estimated PDF is interpolated on the finer grid using kernel smoothing. This step is discussed in detail in [GLT16]. In addition to the marginal densities, the estimated parameter moments $\mu_m(\theta_p)$ may also be computed directly from the PDF:

$$\mu_m(\theta_p) = \int_{\boldsymbol{\theta}\in\Theta} \rho(\boldsymbol{\theta})\theta_p^m \mathrm{d}\boldsymbol{\theta}.$$

Then, one can compare $\mu_1(\theta_p)$, the mean of parameter p and its standard deviation $\sqrt{\mu_2(\theta_p) - \mu_1(\theta_p)^2}$ to their true values when known. In practice, the integral quantities are all approximated using (3.4).

3.2.3.4 Implementation details

An online repository in open access [4] has been created to make available data and codes used in this paper.
In each test case, the computational time of the inverse procedure is strongly dominated by the simulation database construction. All other steps of the method, including the OMM method itself have a negligible computational time. The approximative CPU times given for each test case are meant for one processor. This means the real time may be reduced by simulating the APs in parallel, which is done in practice. Simulations were performed on a Linux machine counting 12 Intel(R) Xeon(R) CPU E5-2640 @ 2.50GHz processors.
External libraries are used in our code: Eigen 3 and GSL-BLAS for the matrix/vector manipulations and algebra and the Python library Scikit-learn [PVG+11] for the time-step selection algorithm.

3.2.3.5 Comparison with existing methods

As discussed earlier, it is possible to infer the PDF of conductances of interest by performing an individual inverse problem (or fitting) for each sample of the experimental measurements. However, if there are N experimental samples, the cost of such an approach would be N times the cost of a single fitting. On the contrary, the proposed approach performs the PDF estimation by taking into account only the statistical moments of the measurements set. Its main advantage is that it does not scale with the number of measurements samples. In that regard it is, in most scenarios, computationally cheaper than individually estimating the parameters from

[4] https://github.com/eltix/omm_jrsi

each sample. Furthermore, all model evaluations are performed offline and once and for all so that the main cost of the inverse procedure can be decided in advance.
Another popular method performing estimations of PDFs is the Bayesian inference. It guarantees to converge to the true PDF, which the present approach does not claim to do, at the expense of many forward model evaluations. The present approach may therefore be seen as a less precise but computationally cheaper alternative to Bayesian inference.

In [GLT16], we provide a comparison of our method to two other approaches.

3.3 Results

The observable moment matching method is now applied to four test cases, using both experimental and synthetic AP measurements.

3.3.1 Test Case 1: Decker Model with Synthetic Data

In this test case, the OMM method is applied to a synthetic data set using the Decker model with different scenarios: one in control conditions and one with a blocked channel (which models for example the effect of a drug). We show that combining data from both scenarios increases the precision of the PDF estimation of the conductances of interest.

3.3.1.1 Control Conditions

For the synthetic data set, $N = 10^4$ APs were generated using the Decker model with six uncertain parameters: g_{Na}, g_{K1}, g_{to}, g_{Kr}, g_{Ks}, g_{CaL}. The N samples were drawn from an uncorrelated multivariate normal distribution of mean 1.1 and standard deviation 0.15. The SNR is equal to 41 dB. The simulation database was built by sampling the same six parameters over the domain $\mathbf{\Theta} = [0.5, 2.0]^6$. $N_c = 2^{15}$ samples were drawn and the corresponding APs are shown in Figure 3.2. The construction of the simulation database required a CPU time of approximately 1000 minutes for one processor. For both the synthetic data set and simulation database, all remaining parameters are fixed and set to their reference values. In this test case, the observable quantities used in the OMM method are the whole AP time series. The observable quantities are therefore the AP values at each of the 449 time steps sampled from the time integration grid. The number of moments to be matched is set to $N_m = 3$. As mentioned earlier, a procedure has been set up to select only a subset of the available time steps to perform the inverse problem.
The OMM method is applied and the resulting estimated marginal densities are shown in Figure 3.3. This allows us to make a clear comparison between the parameters true densities and their estimated ones. Statistics summary of the estimated parameters from the Decker model in control conditions (no drug block). shows a more thorough comparison between the estimated parameters statistics and their true ones. Except for g_{Ks}, their mean values are accurately estimated (the error is

always below 1%) and the errors on the standard deviations range from 3 to 21%. Five out of six conductances are correctly estimated while the estimation of g_{Ks} is poor. This is actually a conductance which is known to be difficult to estimate when others vary, mainly due to the fact that its effect is hidden by other conductances (mainly g_{Kr}). Therefore, a strategy was devised to reduce the uncertainty on the parameter g_{Ks}.

3.3.1.2 Block Conditions

To unveil the effects of g_{Ks} onto the AP waveform, a drug block scenario is devised to "mask" the effects of the other conductances that compete with g_{Ks}. Here, we simulate the effect of a hypothetical drug by blocking 90% of the I_{to}, I_{Kr}, I_{CaL} channels, i.e. by setting the corresponding conductances to 10% of their reference values. The same protocol as in the control conditions is followed to generate the synthetic data set and the simulation database, this time varying only the three remaining conductances (g_{Na}, g_{K1} and g_{Ks}) with $N = 10^4$ samples for the synthetic data set and $N_c = 2^{12}$ collocation points for the simulation database. The construction of the simulation database required a CPU time of approximately 125 minutes for one processor.
The OMM method is applied and the results are shown in Statistics summary of the estimated parameters from the Decker model in drug block conditions (90% block for I_{to},I_{Kr} and I_{CaL}). and Figure 3.3. The density of g_{Ks} is now recovered with a good precision as the conductances previously responsible for its non-identifiability remain fixed.

3.3.1.3 Combining Control and Drug Block Conditions

The drug block and control conditions are now combined to simultaneously estimate the PDF of the six conductances of interest. This is done by slightly modifying the inverse procedure. In addition to enforcing the moment constraints of the AP values in the control conditions, the moments of the parameters themselves (g_{Na}, g_{K1} and g_{Ks}) are also constrained to match those estimated in the drug block conditions. In practice, this is easily done by adding these new constraints to the initial set of constraints (see Eq. (3.3)). This is therefore analogous to solving the inverse problem in the control conditions with the additional knowledge of the parameters statistics obtained in the drug block conditions.
The final results are shown in Statistics summary of the estimated parameters from the Decker model in control conditions with moments constraints from drug block estimation. and in Figure 3.3. This procedure achieves a much better estimation of the density of g_{Ks}. The errors on the mean and standard deviation of g_{Ks} are significantly reduced while the accuracy of the estimation of the other conductances is similar to that of the control conditions.

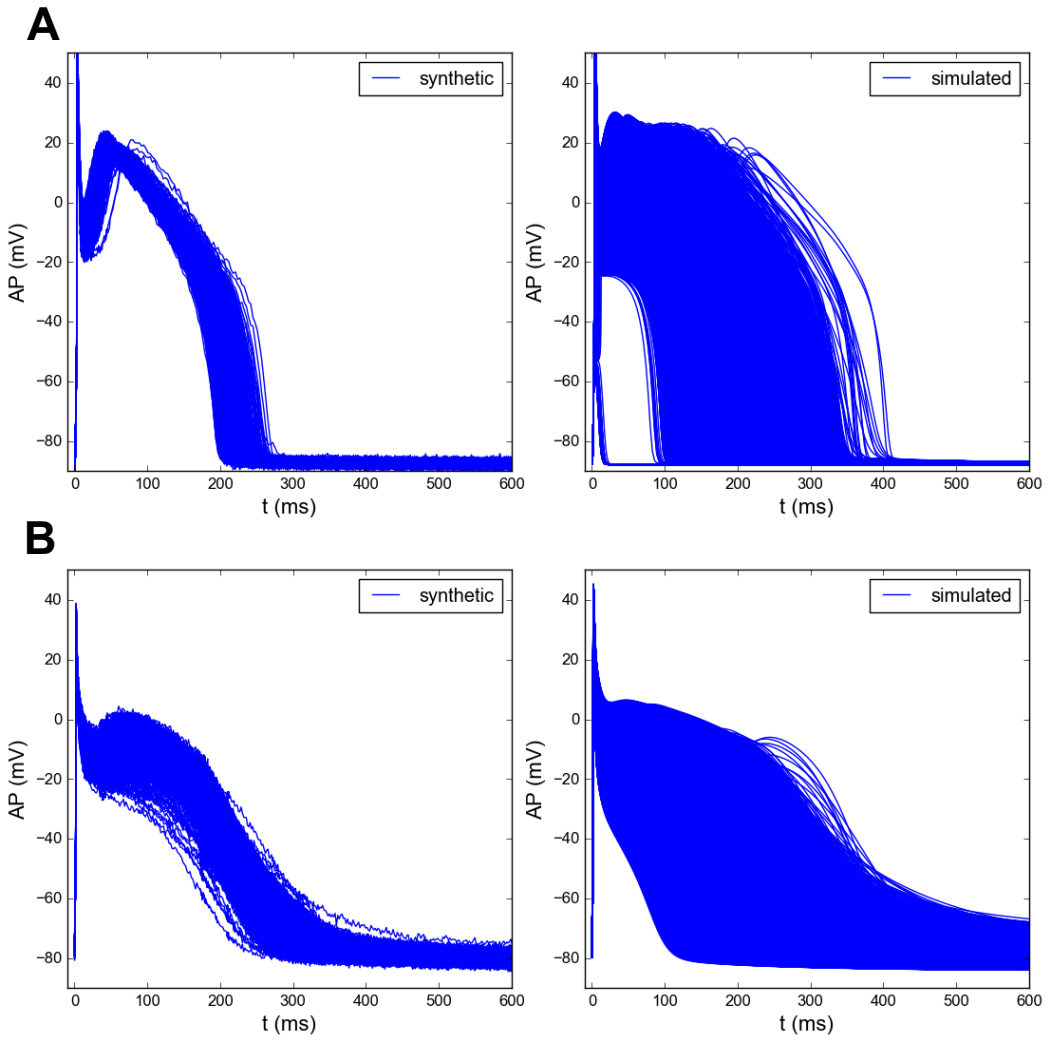

Figure 3.2: (A) AP data sets generated using the Decker model: synthetic data used for the observations (left) and simulation database (right). (B) AP data sets generated using the Courtemanche model: synthetic data used for the observations (left) and simulation database (right).

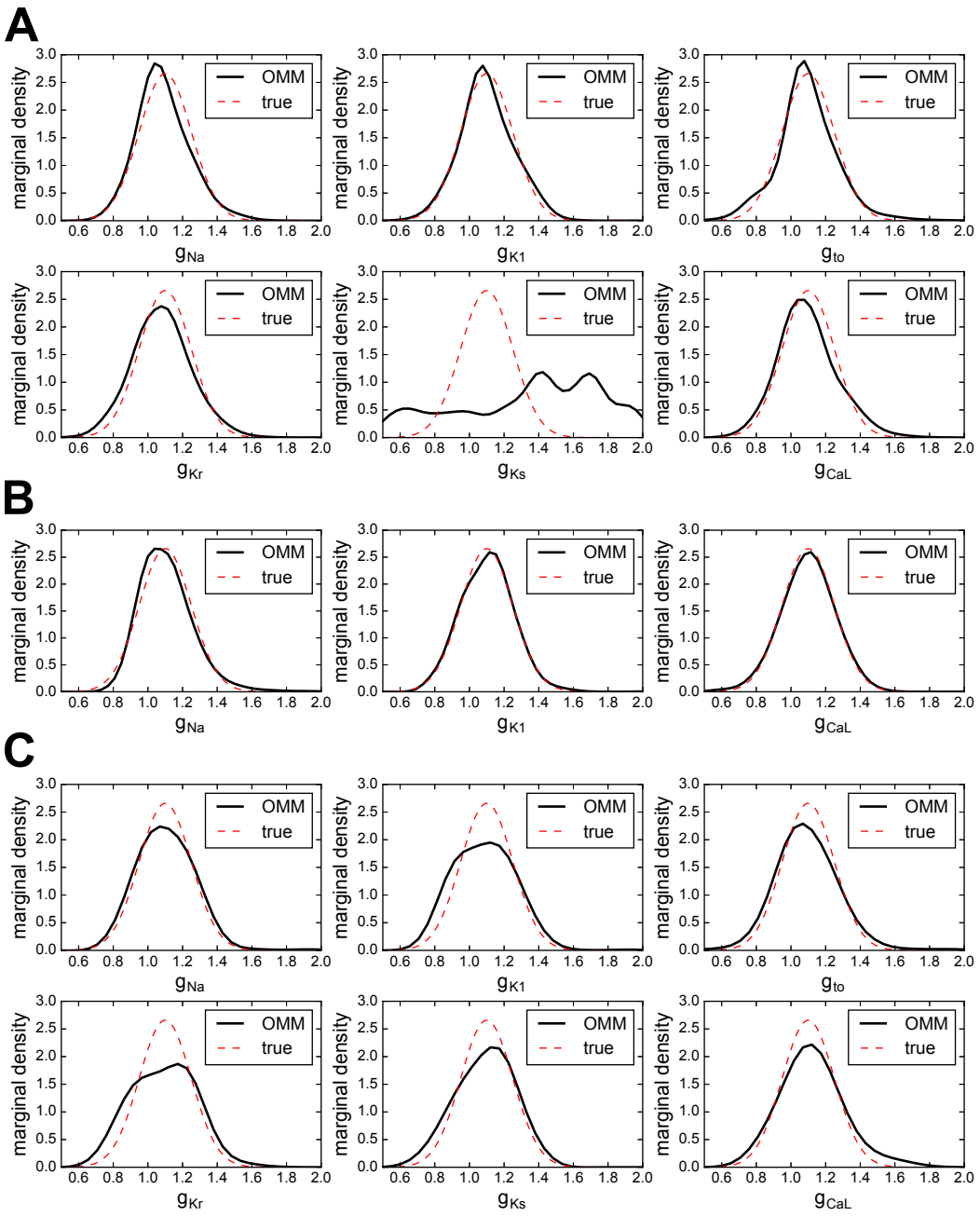

Figure 3.3: Test Case 1 using the Decker model and synthetic data. Conductances estimated marginal densities (A) in control conditions (no drug block), (B) in drug block conditions (90% block of I_{to}, I_{Kr} and I_{CaL}) and (C) using combined data from control and drug block conditions.

3.3.2 Test Case 2: Synthetic Data at Different Pacing Frequencies

In this test case, the OMM method is applied to a synthetic data set using the Courtemanche model. Different scenarios are investigated by varying the frequency of the stimulations that trigger the APs.

3.3.2.1 Control Conditions with 1Hz Pacing

For the synthetic data set, $N = 10^4$ APs were generated using the Decker model with six uncertain parameters: g_{Na}, g_{K1}, g_{to}, g_{Kr}, g_{Ks}, g_{CaL}. The N samples were drawn from an uncorrelated multivariate normal distribution of mean 1.1 and standard deviation 0.15. The SNR is equal to 43 dB. The simulation database was built by sampling the same six parameters over the domain $\mathbf{\Theta} = [0.5, 2.0]^6$. $N_c = 2^{15}$ samples were drawn and the corresponding APs are shown in Figure 3.2. The construction of the simulation database required a CPU time of approximately 1100 minutes for one processor. In this test case, the observable quantities are the following 9 AP biomarkers: APD90, APD50, APD30, APA, RMP, V20, $\mathrm{dVdt}_{\mathrm{max}}$, $\mathrm{V}_{\mathrm{notch}}$ and AUC and the maximum moment order is set to $N_m = 2$. Adding the biomarkers pairwise products, the number of moments constraints add up to 54. The OMM method was applied to this test case and the estimated parameters statistics are presented in Statistics summary of the estimated parameters from the Courtemanche model in control conditions.. The estimated marginal densities for each of the six parameters are shown in Figure 3.4. While four out of six conductances are estimated with a reasonable precision, g_{Kr}, and to bigger extent g_{Ks}, are not well estimated.

3.3.2.2 2Hz Pacing

The same simulation protocol is followed, this time by stimulating the APs at a 2Hz frequency. The accelerated simulation pace induces modifications to the AP morphology (such as a reduced APD) which should reveal new information about the parameters compared to a 1Hz stimulation. The OMM method was applied to this modified test case. While the exhibited variability differs from the 1Hz case, no significant improvement over the parameters estimation may be noticed. Results are shown in Figure 3.4 and Statistics summary of the estimated parameters from the Courtemanche model at 2Hz pacing frequency..

3.3.2.3 Combining 1Hz and 2Hz data

A way to take advantage of the information available in the previous two scenarios consists in combining data obtained at 1Hz and 2Hz pacing frequency both for the synthetic data set and the simulation set. The same inverse procedure as before is applied with the following extended set of biomarkers:
$\{\mathrm{APD90}_{\mathrm{1Hz}}, \mathrm{APD50}_{\mathrm{1Hz}}, \mathrm{APD30}_{\mathrm{1Hz}}, \mathrm{RMP}_{\mathrm{1Hz}}, \mathrm{dV/dt}_{\mathrm{max,1Hz}}, \mathrm{V20}_{\mathrm{1Hz}}, \mathrm{V}_{\mathrm{notch,1Hz}}, \mathrm{AUC}_{\mathrm{1Hz}}, \mathrm{APD90}_{\mathrm{2Hz}}, \mathrm{APD50}_{\mathrm{2Hz}}, \mathrm{V20}_{\mathrm{2Hz}}, \mathrm{V}_{\mathrm{notch,2Hz}}, \mathrm{AUC}_{\mathrm{2Hz}}\}$.

These biomarkers are enriched by their pairwise products which amounts to a total of 119 quantities to be matched. Results are shown in Figure 3.4 and Statistics summary of the estimated parameters from the Courtemanche model (combined 1Hz+2Hz data).. While g_{Ks} is still not correctly estimated, this strategy succeeds in reducing the uncertainty for parameters g_{Kr} and g_{CaL}.

3.3.3 Test Case 3: Experimental Data from Canine Ventricular Cells

This experimental data set (used in [JCB+15] and available online [5]) features beat-to-beat variability of APs recorded from a single canine ventricular cardiomyocyte. Here, only a subset (traces #100 to #199) of the available data set is used.

3.3.3.1 Calibration of the Davies model

The Davies model was chosen to study this data set since it is one of the most recent canine ventricular cell models. In addition, this model was also used in [JCB+15] to study the same data set. The parameter calibration procedure was carried out using the most representative AP of the experimental set and a regularization parameter $K = 0$ (*i.e.* no regularization). Figure 3.5 shows the representative AP as well as its fitted counterpart using the Davies model. In Figure 3.5 is plotted the history of six conductances values for each iteration of the CMA-ES algorithm. The conductances are normalized with respect to the values found in the reference paper. Note that the values obtained after the calibration are far from the reference values (equal to one by definition), confirming the necessity of such a procedure. This is also true for the other fitted parameters which are not shown in the figure for the sake of clarity but whose values are given in Davies model: experimental parameter calibration and observable moment matching results.. Note that g_{Ks} seems to reach an extremely high value. It is however consistent with the values found in [JCB+15] and may be explained by a difference in the experimental settings.

3.3.3.2 Inverse procedure

The OMM procedure is applied with the following biomarkers as observable quantities: APD90, APD50 and V_{notch}. Here, V_{notch} is the notch potential corresponding to the AP value 8 ms after the depolarization peak. The reason V_{notch} was preferred over previously introduced V20 is that the latter was not suited to the AP shape and its value was almost constant over the experimental set. We made the assumption that the observed variability was due to variations of g_{Kr}, g_{Ks} (commonly associated with APD variations) and g_{to1} (commonly associated with variations of V_{notch}). These conductances are among the most responsible for beat-to-beat variability [PDB+16]. The simulation database was built by sampling

[5] http://www.cs.ox.ac.uk/chaste/download.html

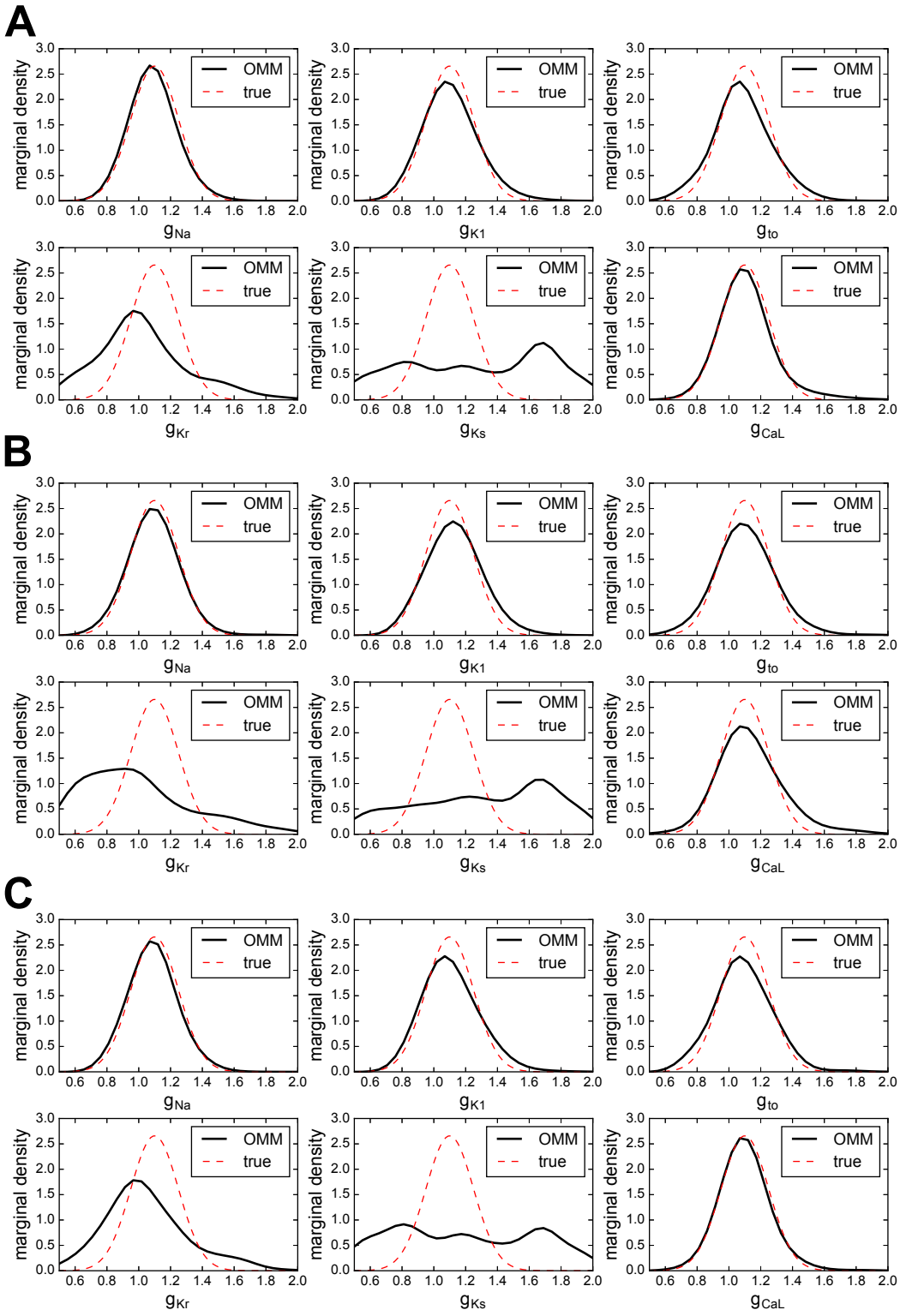

Figure 3.4: Test Case 2 using the Courtemanche model and synthetic data. Conductances estimated marginal densities in (A) control conditions (1Hz stimulation frequency), (B) fast pacing conditions (2Hz stimulation frequency) and (C) with combined data from 1Hz and 2Hz pacing.

these three conductances over the domain $\boldsymbol{\Theta} = [0.4, 1.8]^3$ and $N_c = 2^{13}$ samples were drawn. The construction of the simulation database required a CPU time of approximately 175 minutes for one processor. The marginal distributions of the three parameters of interest are shown in Figure 3.6 and the estimated statistics are summarized in Davies model: experimental parameter calibration and observable moment matching results..

3.3.3.3 Comparison with individually fitted APs

Since the exact distributions of the parameters of interest are unknown, a comparison study is carried out using two other PDF estimation techniques. The experimental APs are individually fitted to the Davies model using the CMA-ES algorithm. The same fitting procedure is used as in the calibration step using the AP values at different times (see Figure 3.5). In the first case, only the three conductances of interest are allowed to vary while the others remain fixed. In the second case, all conductances (those concerned by the calibration step) are allowed to vary. In both cases, the fitting procedure yields a collection of $N = 100$ values for the three conductances of interest. The distributions are then approximated using histograms, shown in Figure 3.6. Even though biomarkers were used for the OMM procedure and time series were used for both individual fitting procedures, the parameters distributions show a striking similarity, especially for the case where only the three conductances of interest are allowed to vary. This suggests that the set of biomarkers retained is enough to account for the observed variability. This also shows the overall satisfactory performances of the observable moment matching method which achieves comparable results to individual CMA-ES fits at a fraction of the computational cost. Indeed, the 100 individual CMA-ES fits required around 10^5 model evalutions while the OMM method only required 8192.

3.3.4 Test Case 4: Experimental Data from Human Atrial Cells

This experimental dataset (used in [RKÖW+15, SBOW+14] and available online [6]) features AP biomarkers recorded from two populations of human atrial cells. The OMM procedure is independently applied to both groups and the distributions of the conductances of interest between the two groups are compared.

3.3.4.1 Human biomarkers dataset

The data set consists of 469 experimentally recorded sets of 7 human AP biomarkers divided in two groups: sinus rythm (SR) with 254 samples and chronic atrial fibrillation (AF) with 215 samples. Both groups exhibit a strong inter-subject variability in addition to the inter-group variability. The available biomarkers are: APD90, APD50, APD20, APA, RMP, $\mathrm{dV/dt_{max}}$, V20.

[6] http://journals.plos.org/plosone/article?id=10.1371/journal.pone.0105897

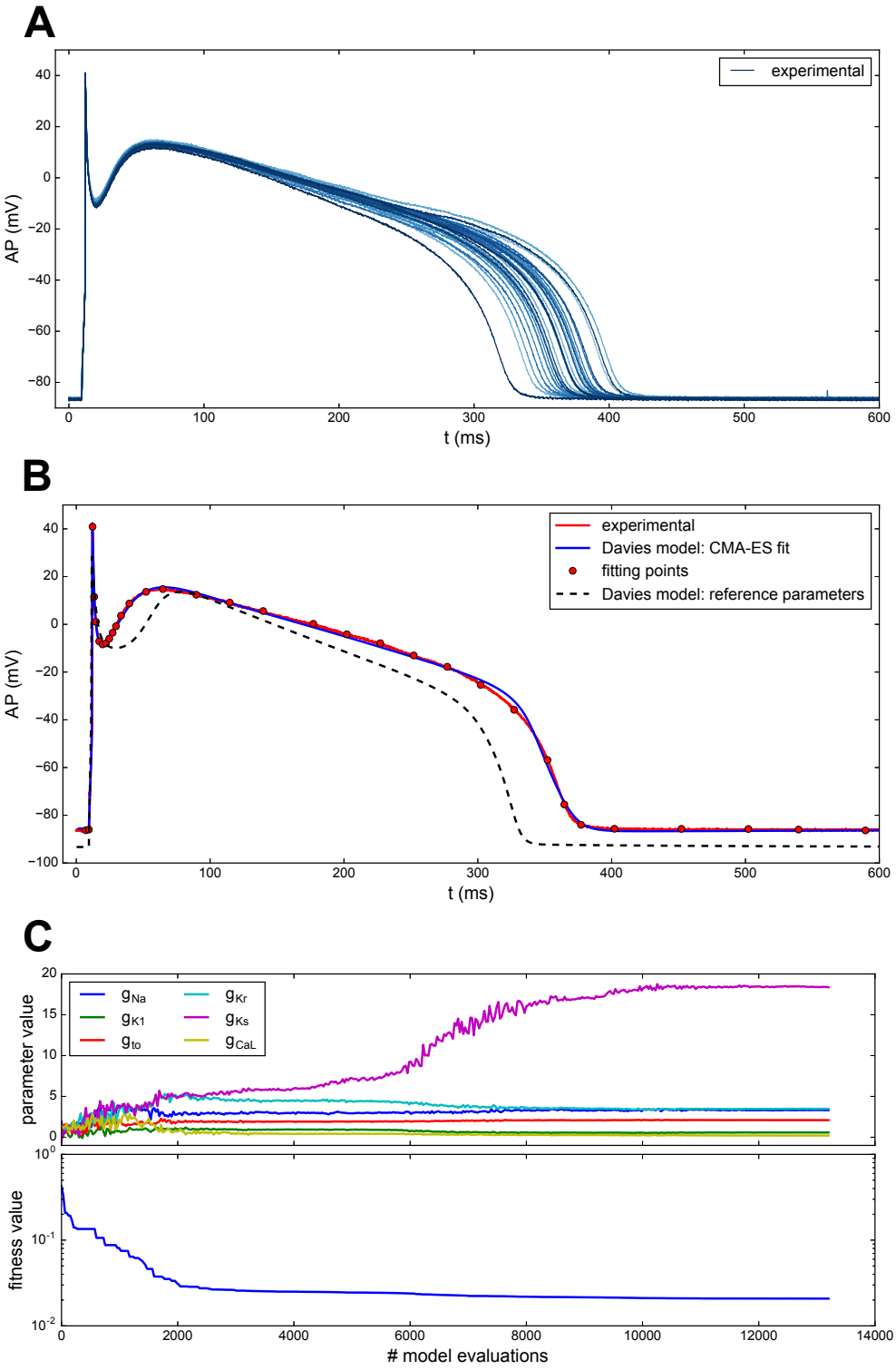

Figure 3.5: (A) Canine ventricular AP experimental set [JCB+15]. (B) Davies model calibration step: experimental representative AP (solid red), corresponding CMA-ES fit (solid blue) and reference parameters (dashed). (C) CMA-ES iterations: (top) main conductances values are plotted against the number of model evaluations carried out by the CMA-ES algorithm, (bottom) corresponding fitness function values.

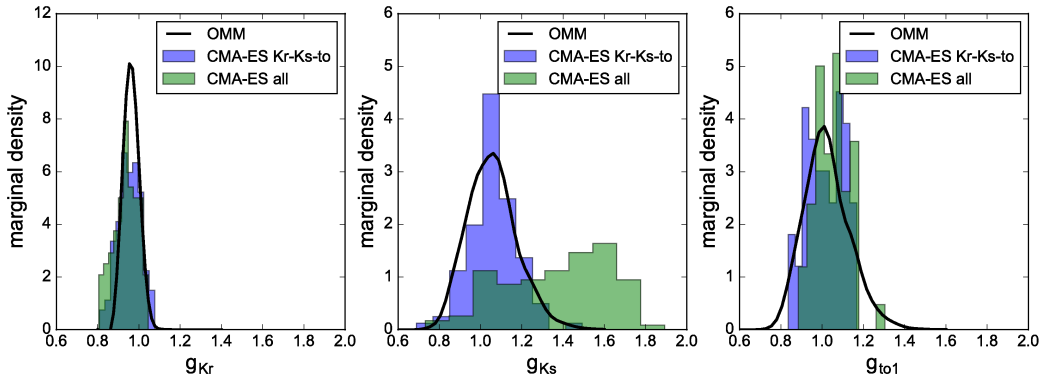

Figure 3.6: Test Case 3 using the Davies model and 100 AP recordings from a canine ventricular cardiomyocyte. Conductances marginal densities estimated using the OMM method (solid lines) and individual CMA-ES fits (blue and green bins). Conductances are normalized by the calibrated values.

3.3.4.2 Courtemanche model calibration

The Courtemanche model was chosen to study this data set. Prior to the inverse procedure, a model calibration step is independently carried out for both groups. The regularization parameter is set to $K = 5 \times 10^{-3}$. The CMA-ES algorithm is applied to fit the Courtemanche model parameters to the most representative sample within each group. The representative sample is the one which minimizes its euclidean distance to the median biomarkers values of its group. Human biomarkers dataset statistics. shows the most representative samples from each group as well as some global statistics of the biomarkers set. In Courtemanche model: experimental parameter calibration. are displayed 11 conductances of the Courtemanche model that were estimated during the calibration step. First, for both groups, the estimated parameters values differ from those found in the literature. Second, there is a significant increase in g_{K1} and a significant decrease in g_{to}, g_{CaL} and g_{Kur} from the SR to the AF group. These modifications are commonly considered as a good AF remodeling strategy [DR03, CWV+08, WHM+13]. For each set of estimated conductances, an AP is simulated using the Courtemanche model. One obtains a typical or most representative AP for each group. Figure 3.7 shows such APs along with the AP obtained with the reference parameters found in the literature. The AF AP features a shorter APD and a more triangular shape than the SR one, which is typical of atrial fibrillation [VWPL+99, LHS+16]. This figure also highlights the fact that choosing the literature values as baseline may not be a good choice for the SR group, and to a greater extent for the AF group. In the same figure is added an AP that was obtained by applying the suggested AF remodeling found in [WHM+13] to the SR model (65% decrease of g_{CaL} and g_{to}, 49% decrease of g_{Kur} and 110% increase of g_{K1}). Both AF APs are very different and this suggests that AF remodeling should be designed specifically for a given experimental set.

3.3.4.3 Inverse procedure

The OMM method is applied with four biomarkers of interest as observable quantities: APD90, RMP, dV/dt_{max} and $V20$. For each group, a simulation database is built by sampling the following four conductances: g_{Na}, g_{K1} and g_{to} and g_{Kr}. $N_c = 2^{14}$ samples are drawn using the Sobol sequence and the number of moments to be matched is set to $N_m = 2$. The construction of the simulation database required, for each group, a CPU time of approximately 550 minutes for one processor. The results of the inverse procedure are presented in Statistics summary of the estimated parameters from the Courtemanche model with experimental data (SR and AF group), normalized by the reference values. and Figure 3.7. Since no exact solution is known, one may only qualitatively interpret the result. While g_{Na} follows a common distribution in both groups, the other three conductances show striking differences. One way to validate the results is to compare the estimated PDF of the obervable quantities (the four biomarkers of interest) with the experimental one. By construction, they must have the same mean and standard deviation since 2 moments are matched for each biomarkers. However, this does not guarantee that the distributions are identical since an infinite number of distributions satisfy the moment constraints. In Figure 3.7 are plotted the histograms of the experimental biomarkers along with the estimated biomarkers PDF obtained with the OMM method. In Normalized histograms of the experimental biomarkers pairwise products for both SR (blue) and AF (red) groups. The black solid lines correspond to the PDF of each pairwise product estimated by the observable moment matching method. Biomarkers computed from an AP. This figure is an extension of Fig.7(C) in the main article., we replicated the same plot for the pairwise products of the biomarkers. The distributions are very similar for each biomarkers which suggests that chossing $N_m = 2$ is sufficient in this particular case. Note also that, even though the biomarkers distributions are close to Gaussian ones, this is definitely not true for the conductances distributions.

3.4 Discussion

In this study, we have presented the OMM method which serves the general purpose of estimating the PDF of uncertain model parameters from a set of measurements. It has been applied to electrophysiology measurements and illustrated with four different test cases.

Test Cases 1 and 2 illustrate the proposed method with synthetic data sets, which has two advantages. First, one may try a large variety of parameters configurations which may be difficult or impossible to obtain in experimental conditions. Second, knowing the true distributions of the parameters allows for a thorough evaluation of the estimated parameters PDF. In Test Case 1, the proposed method is applied to synthetic measurements generated from the Decker canine model. The OMM method was applied to estimate the PDF of six uncertain conductances. It showed that the OMM method is able to simultaneously estimate the PDF of several

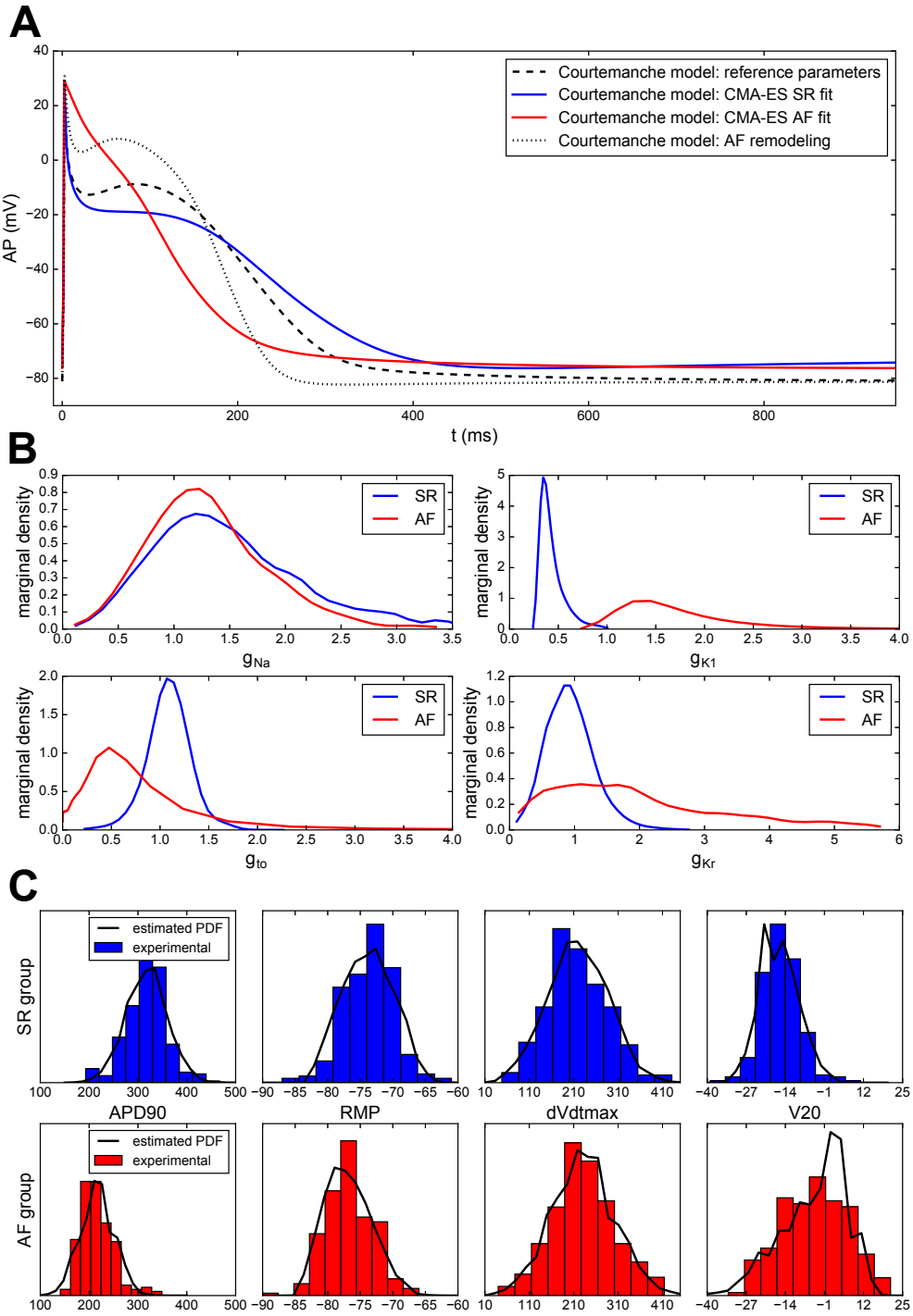

Figure 3.7: (A) CMA-ES parameter calibration of the Courtemanche model prior to the inverse procedure. APs obtained for the most representative samples of the SR (blue) and AF (red) groups, with the reference parameters (dashed) and after AF remodeling (dotted). (B) Courtemanche conductances estimated marginal densities for the SR group (blue) and AF group (red). Conductances are normalized by the literature values. (C) Normalized histograms of the four experimental biomarkers of interest for both SR (blue) and AF (red) groups. The black solid lines correspond to the PDF of each biomarker estimated by the observable moment matching method.

conductances.
The authors would like to stress out that the proposed method provides an estimation that is an approximation of the real underlying PDF of the parameters. This approximation is less precise than what would be achievable with finer methods such as Bayesian inference but has the advantage of being computationally less demanding in general. In [GLT16], the authors suggest that the present approach could serve as a prior generator for Bayesian inference.
The quality of the estimation obtained depends on the identifiability of the parameters given the available data. However, if a parameter is poorly identifiable (which is the case of g_{Ks} in this particular scenario) or even unidentifiable, the method does not fail owing to the approximation of the Hessian associated with the problem in (3.3) and the regularization induced by the choice of a subset of time steps where the moments are matched. In that case, such a parameter is characterized by a flat estimated distribution. In the context of experimental data, a strategy may be set up to assess which parameters of the model are actually identifiable, prior to applying the inverse procedure. Such strategies exist (see e.g. [PL15]) but were not investigated in the present work. Nevertheless, when faced with an estimated flat distribution for one parameter, it is possible to perform the following numerical experiment to assess whether this parameter is unidentifiable or its PDF is in fact uniform. Small perturbations (that conserve the norm and positivity of the PDF) may be added to the estimated PDF along the direction of the seemingly unidentifiable parameter. If the moment constraints are still verified, then it probably means that the parameter is in fact unidentifiable. To improve the estimation of the hidden g_{Ks} parameter, an artifical drug block remodeling was applied to the Decker model. This drug was designed to block the currents that were responsible for the unidentifiability of g_{Ks}. This remodeling consisted in practice in reducing the corresponding parameters values to 10% of their nominal values. This strategy proved to significantly improve the estimation of g_{Ks} and showed that the OMM has potential applications in two contexts. First, it may be used to infer the effect (or toxicity) of a drug using actual experimental data. Second, it may help gain insight into experimental protocols that can be set up to estimate quantities that are otherwise hidden. These findings must however be mitigated by the fact that, in real cells, it is improbable that a given drug only affects a set of targeted ionic currents. It most probably affects the whole cell kinetics and dynamics, including quantities that were supposed to remain unchanged in our artificial scenario. It is also important to note that some stimulation protocols or drug block experiments are not easily achievable in real experiments. In most cases, especially when using human tissue, it is simply not possible to conduct additional experiments because the tissue is critical to answer more novel research questions. It is an important practicality that makes recordings using animals different to those possible using human tissue. Nevertheless, it may prove useful to inform novel experiments that can be conducted to reduce the uncertainty in the estimation of conductances profiles based on successful numerical scenarios.
The OMM method is related to the populations of models (POM) approach but dif-

fers from it on certain aspects. Whereas the focus of our method is to approximate parameters distributions, POM studies intend to investigate the implications of potential parameters ranges. It would indeed not be possible to confidently estimate conductances from ranges of action potential biomarkers and additional constrains would be required, as shown in our study. Other studies such as [BBOVA+13], and those reviewed by Muszkiewicz *et al.* [MBG+16] have triggered important discussions and increased interest in an important area of research that requires diversity of techniques and approaches, as shown here. In this context, our study suggests a new method for PDF estimation that may indeed be very useful for new applications.

In Test Case 2, the OMM method is applied to synthetic measurements generated from the Courtemanche human atrial model. The distribution of six conductances were estimated from AP biomarkers obtained in control conditions. Interestingly, the variability observed in the biomarkers set is less informative than that of the AP traces themselves. This is highlighted by the fact that two conductances distributions are poorly estimated compared to the first test case. Indeed, the biomarkers are features computed from the AP traces themselves and are therefore doomed to carry as much or less information about the underlying parameters. However, studying biomarkers instead of AP traces is justified by the fact that, in practice, certain experimental sets only contain biomarkers values. To tackle this, a strategy was set up to extract more information from the AP biomarkers. This was done by changing the stimulation frequency which unveiled new dynamics and therefore new information about the parameters. Interestingly, such a strategy may easily be transposed to an actual experimental protocol. It is in fact commonly practiced in cardiomyocyte experimental studies [ZBOO+16]. Combining the data obtained using two different frequencies improved the estimation of g_{Kr} and g_{CaL}. g_{Ks} was however still poorly estimated, mainly due to the fact that its effect is very similar to that of g_{Kr}, with a lower amplitude. The investigation of richer stimulation protocols, such as in [DL04], in order to improve the estimation of poorly identifiable parameters could be the focus of future investigations. It is, in certain cases, possible to successfully estimate g_{Ks} by conducting an adequate numerical experiment. In [JCB+15] for instance, the authors use the combined recordings of an AP in normal conditions and with g_{Ks} set to zero.
In Test Case 3, the OMM method is applied to a set of experimental canine APs recorded from a single canine ventricular cardiomyocyte. This experimental set is an illustration of beat-to-beat variability which is mostly characterized by variations of the APD. It is therefore natural to make the hypothesis that these variations are in fact due to fluctuations of the delayed-rectifier potassium currents magnitudes (g_{Kr} and g_{Ks}) which are the most responsible for APD variations. The APs also exhibit variations around the notch region which motivated the addition of g_{to} as the third uncertain parameter. These conductances are known to be the most contributing to beat-to-beat variability [PDB+16]. All the other parameters were set to a fixed value using a calibration procedure. Many conductances values deviate a lot from their reference values which suggests that this step is necessary prior to any

variability study. The estimated PDF shows that the large variability observed in the APD is in fact caused by small variations of the underlying parameters. These findings were confirmed by carrying out two other independent parameter estimations which yielded similar distributions for the conductances of interest. For g_{Ks}, the distribution differs when all the conductances are allowed to vary. This may be explained by the fact that this parameter is less identifiable compared to g_{Kr}, so that its effect may be compensated or may interfere with other conductances. Some limitations pertaining to the experimental set must be considered. Indeed, the isolation of cardiomyocytes is known to affect the membrane ionic channels [YFLN96] and therefore the distributions obtained for the conductances of interest may not reflect the *in vivo* ones. Furthermore, the experimental traces considered are just a snapshot of the cell at a certain state. Therefore, extrinsic factors operating at a long time scale and contributing to variations of the AP features are neglected. For instance, monitoring the APD over the full experimental set reveals that there are long time scale increasing and decreasing trends in the APD (see the Supplementary Materials in [JCB+15]).

In Test Case 4, the OMM method is applied to an experimental set containg AP biomarkers obtained from two different populations: sinus rythm (SR) and atrial fibrillation (AF). To each group is associated a most representative individual whose biomarkers values are the closest to the median ones of its group. The calibration step is very informative as it allows for a first comparison between the two groups, or more precisely between the two representatives of each group. The calibration leads to high differences for g_{K1} (+220%), g_{to} (-100%), g_{CaL} (-63%) and g_{Kur} (-60%) which are qualitatively similar to those reported in [SBOW+14]. These differences between the two groups are also in agreement with the AF remodeling mechanisms documented in [DR03, CWV+08, WHM+13, KSMT14]. The role of I_{Kur} seems to be prominent in the onset of AF [WHC+04] along with perturbations of the intracellular Ca^{2+} dynamics [VWPL+99] which is coupled to the L-type calcium current I_{CaL}. Beyond these inter-group variations captured in the calibration step, the inter-group variability is revealed by the study of the estimated PDFs. The results highlight the distribution differences of g_{to} and g_{Kr} between the two groups. In the SR group, these two conductances feature a normal-like distribution that does not deviate much from the mean value whereas in the AF group those distributions are skewed and much more spread. The distribution of g_{Na} are similar between the two groups which suggests that it does not play an important role in the AF mechanisms. g_{K1} also features a much higher mean value and higher variance in the AF group. A posteriori distributions of the biomarkers of interest may be computed from the estimated PDF. When compared to the actual distributions (approximated by histograms of the experimental biomarkers), it shows that the OMM method succeeded in matching the variability in the measurements. In the future, studying other biomarkers or other types of measurements may lead to a better understanding of the AF mechanisms and of the sources of variability within each group.

We now discuss limitations concerning inverse problems in electrophysiology in gen-

eral and the OMM method in particular. Akin to many inverse problem studies in electrophysiology, we make the assumption that all variability observed in the experimental data set can be explained by the variation of only a few conductances. Not only are there a large number of different conductances but there are also other parameters such as the parameters governing the dynamics of the channel gates. However, such a simplification is supported by two main considerations. First, the proposed approach is limited by its computational cost. Considering a large number of free parameters means that more samples are required to span the high-dimensional parameter space, which may be intractable in practice. Second, the information available in the AP traces is not enough to constrain all the model parameters. Adding other sources of information such as intracellular calcium concentrations revealed by fluorescence [SHM+15] or cell impedence [AXL+12] may allow the estimation of more than 6 parameters. Considering that, choosing the right set of varying conductances is still paramount.

The rationale for choosing the six conductances investigated in this work was based on their known importance in determining the cardiac action potential, and key properties including upstroke velocity, plateau duration, resting potential, and action potential duration. Amongst them, we included gKs knowing that due to the redundancy of currents during repolarization it would be expected to be poorly identifiable. Our method can however be extended to include variability in additional parameters if needed.

Another limitation comes from the experimental sets themselves. Cells coming from different regions of the heart exhibit different variability patterns in their APs. In the context of assessing the effect of a drug or investigating the causes of a heart disease, this approach should be repeated with a wider variety of cell locations. Furthermore, the electrical behavior of an isolated cell differs from one that is embedded in a tissue. Therefore, using measurements at the tissue scale [CBC+11] (for example using MEA measurements [CT14]) may yield results that are closer to the *in vivo* conditions.

Another point to be discussed is the use of biomarkers versus time traces. This is often imposed by the type of experimental data available. Ranges of biomarkers using standard protocols are easily accessed by experimentalists, and raw action potential data are not always available. It is therefore important to evaluate the use of both biomarker ranges and action potential traces. The set of available biomarkers is often dictated by experimental constraints. It is however possible, when there are many available biomarkers, to conduct a preliminary study to determine which biomarkers should be taken into account in order to recover certain parameters of interest. Such a study would consist in applying the proposed method several times with different underlying parameters variations. Then, for a given set of experimental constraints, it would be possible to assess whether the proposed method would be able to recover the underlying parameters distributions. Finally, the choice of numerical settings pertaining to the OMM method is discussed. The OMM method relies on the matching of the statistical moments of some observable quantities. The number of moments N_m to be matched is therefore important. In most applications,

choosing $N_m = 2$ or 3 is sufficient to capture the parameters distribution. A common heuristics is to increase N_m until no siginificant change in the estimated PDF is observed. Note that using high N_m often leads to numerical instability, all the more so if the noise level in the measurements is high.
In summary, we have presented a new method for estimating the PDF of action potential models parameters from various sets of AP measurements. The AP measurements may come in the form of waveforms (time series) or biomarkers. The method has been illustrated with both synthetic and experimental sets which exhibit both inter-subject and intra-subject variability. The approach we describe has potentially important implications in drug safety pharmacology and more generally in the understanding of variability in cardiomyocytes ionic properties. It intends to be in line with recent works suggesting that computational models are a powerful tool to evaluate drug toxicity [DWM+16]. More generally, the proposed approach may be a new way to investigate the sources of variability observed in electrophysiology that are experimentally difficult to assess.

3.5 Supplementary Material

Table 3.1: Statistics summary of the estimated parameters from the Decker model in control conditions (no drug block).

Parameter	μ	μ_{ex}	rel. err.	σ	σ_{ex}	rel. err.
g_{Na}	1.104	1.100	**0.4%**	0.155	0.150	**3.1%**
g_{K1}	1.099	1.100	**0.1%**	0.164	0.150	**9.2%**
g_{to}	1.103	1.100	**0.3%**	0.182	0.150	**21.2%**
g_{Kr}	1.091	1.100	**0.9%**	0.172	0.150	**14.4%**
g_{Ks}	1.264	1.100	**14.9%**	0.426	0.150	**184.0%**
g_{CaL}	1.102	1.100	**0.2%**	0.177	0.150	**17.8%**

Table 3.2: Statistics summary of the estimated parameters from the Decker model in drug block conditions (90% block for I_{to},I_{Kr} and I_{CaL}).

Parameter	μ	μ_{ex}	rel. err.	σ	σ_{ex}	rel. err.
g_{Na}	1.104	1.100	**0.4%**	0.158	0.150	**5.5%**
g_{K1}	1.102	1.100	**0.1%**	0.154	0.150	**2.6%**
g_{Ks}	1.100	1.100	**0.0%**	0.158	0.150	**5.1%**

Table 3.3: Statistics summary of the estimated parameters from the Decker model in control conditions with moments constraints from drug block estimation.

Parameter	μ	μ_{ex}	rel. err.	σ	σ_{ex}	rel. err.
g_{Na}	1.104	1.100	**0.4%**	0.158	0.150	**5.5%**
g_{K1}	1.102	1.100	**0.1%**	0.154	0.150	**2.6%**
g_{to}	1.104	1.100	**0.4%**	0.182	0.150	**21.3%**
g_{Kr}	1.101	1.100	**0.1%**	0.173	0.150	**15.6%**
g_{Ks}	1.100	1.100	**0.0%**	0.158	0.150	**5.1%**
g_{CaL}	1.102	1.100	**0.2%**	0.176	0.150	**17.1%**

Table 3.4: Statistics summary of the estimated parameters from the Courtemanche model in control conditions.

Parameter	μ	μ_{ex}	rel. err.	σ	σ_{ex}	rel. err.
g_{Na}	1.098	1.100	**0.2%**	0.149	0.150	**0.7%**
g_{K1}	1.102	1.100	**0.2%**	0.163	0.150	**9.1%**
g_{to}	1.109	1.100	**0.8%**	0.180	0.150	**20.1%**
g_{Kr}	1.087	1.100	**1.0%**	0.302	0.150	**102%**
g_{Ks}	1.201	1.100	**9.2%**	0.426	0.150	**184%**
g_{CaL}	1.104	1.100	**0.4%**	0.178	0.150	**18.3%**

Table 3.5: Statistics summary of the estimated parameters from the Courtemanche model at 2Hz pacing frequency.

Parameter	μ	μ_{ex}	rel. err.	σ	σ_{ex}	rel. err.
g_{Na}	1.099	1.100	**0.1%**	0.151	0.150	**1.0%**
g_{K1}	1.110	1.100	**0.9%**	0.167	0.150	**11.6%**
g_{to}	1.109	1.100	**0.8%**	0.185	0.150	**23.3%**
g_{Kr}	1.064	1.100	**3.2%**	0.366	0.150	**144%**
g_{Ks}	1.263	1.100	**14.9%**	0.424	0.150	**183%**
g_{CaL}	1.132	1.100	**2.9%**	0.208	0.150	**38.4%**

Table 3.6: Statistics summary of the estimated parameters from the Courtemanche model (combined 1Hz+2Hz data).

Parameter	μ	μ_{ex}	rel. err.	σ	σ_{ex}	rel. err.
g_{Na}	1.098	1.100	**0.2%**	0.149	0.150	**0.4%**
g_{K1}	1.103	1.100	**0.2%**	0.166	0.150	**11.0%**
g_{to}	1.106	1.100	**0.6%**	0.165	0.150	**9.7%**
g_{Kr}	1.096	1.100	**0.4%**	0.266	0.150	**77.2%**
g_{Ks}	1.150	1.100	**4.6%**	0.424	0.150	**183%**
g_{CaL}	1.102	1.100	**0.2%**	0.161	0.150	**7.4%**

Table 3.7: Davies model: experimental parameter calibration and observable moment matching results.

Conductance	OMM results		Reference values		
	μ	σ	exp. calibration	literature	unit
g_{Na}	-	-	27.4	8.25	nS/pF
g_{NaL}	-	-	7.26×10^{-2}	1.1×10^{-2}	nS/pF
g_{Kr}	**0.96**	**0.03**	4.82×10^{-2}	1.39×10^{-2}	nS/pF
g_{Ks}	**1.06**	**0.12**	1.38×10^{-1}	7.47×10^{-3}	nS/pF
g_{K1}	-	-	2.91×10^{-1}	5.0×10^{-1}	nS/pF
g_{Kp}	-	-	7.93×10^{-3}	2.76×10^{-3}	nS/pF
g_{to1}	**1.03**	**0.11**	0.38	0.18	nS/pF
g_{CaL}	-	-	2.0×10^{-4}	9.7×10^{-4}	nS/pF
g_{bCa}	-	-	5.88×10^{-6}	7.98×10^{-7}	nS/pF
g_{pCa}	-	-	9.84×10^{-4}	5.75×10^{-2}	pA/pF
g_{Clb}	-	-	9.45×10^{-6}	2.25×10^{-4}	nS/pF
g_{to2}	-	-	4.54×10^{-9}	4×10^{-7}	L/F.ms
g_{NaCa}	-	-	6.95×10^{-2}	5.85	pA/pF
g_{NaK}	-	-	6.6×10^{-3}	6.19×10^{-1}	pA/pF

Table 3.8: Human biomarkers dataset statistics.

group		APD90	APD50	APD20	APA	RMP	dV/dt_{max}	V20
SR	representative (#163)	**324**	**142**	**5**	**93**	**-74**	**214**	**-19**
	median	319	151	5	95	-74	213	-16
	mean	317.7	138.7	7.1	94.8	-73.8	219.7	-16.1
	std	42.7	44.1	8.2	7.1	3.9	67.9	6.4
AF	representative (#131)	**213**	**105**	**38**	**98**	**-76**	**237**	**0**
	median	213	101	27	102	-77	229	-4
	mean	216.4	101.5	30.2	101.6	-76.8	232.0	-4.4
	std	34.4	27.7	17.9	7.6	3.6	70.3	10.9

Table 3.9: Courtemanche model: experimental parameter calibration.

Conductance	Experimentally calibrated (normalized)			reference value	unit
	SR group	AF group	AF/SR rel. change		
g_{Na}	1.17	1.11	-5%	7.8	nS/pF
g_{K1}	0.45	1.45	**+220%**	9.0×10^{-2}	nS/pF
g_{to}	1.12	2.83×10^{-3}	**-100%**	1.65×10^{-1}	nS/pF
g_{Kr}	1.15	1.41	+23%	2.94×10^{-2}	nS/pF
g_{Ks}	1.10	1.21	+10%	1.29×10^{-1}	nS/pF
g_{CaL}	0.87	0.32	**-63%**	1.24×10^{-1}	nS/pF
g_{bNa}	1.26	1.31	+4%	6.74×10^{-4}	nS/pF
g_{bCa}	1.14	1.85	+63%	1.13×10^{-3}	nS/pF
g_{NaK}	0.78	0.80	+3%	0.6	pA/pF
g_{NaCa}	4.65×10^{-2}	2.01	×43	1.6×10^{3}	pA/pF
g_{Kur}	0.54	0.21	**-60%**	1.0	dimensionless

Table 3.10: Statistics summary of the estimated parameters from the Courtemanche model with experimental data (SR and AF group), normalized by the reference values.

Group	SR		AF	
Parameter	μ	σ	μ	σ
g_{Na}	1.464	0.652	1.310	0.533
g_{K1}	0.431	0.125	1.744	0.656
g_{to}	1.090	0.219	0.310	0.392
g_{Kr}	0.934	0.375	1.997	1.314

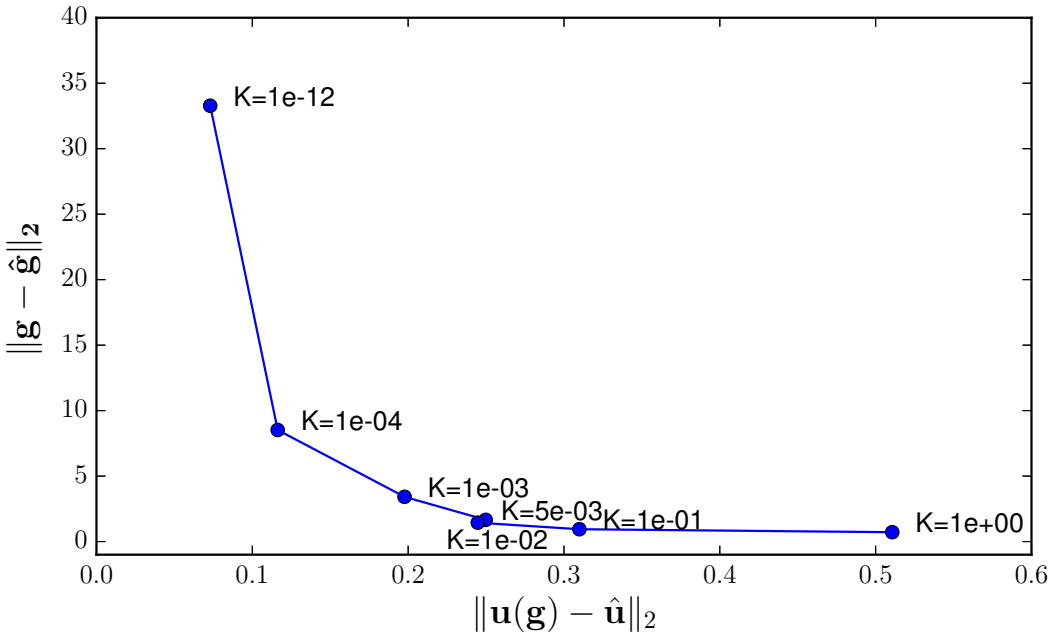

Figure 3.8: L-curve: calibration fitness plotted against the distance to reference conductances.

Influence of K in the calibration step We replicated the calibration procedure in Test Case 4 with the SR group representative several times by varying the regularization parameter K. In Figure 3.8, the fitness is plotted against the distance to the reference conductances values for different values of K. $\mathbf{g}$ denotes the conductance values estimated by the CMA-ES algorithm, $\hat{\mathbf{g}}$ are the reference values for these conductances, $\mathbf{u}(\mathbf{g})$ are the simulated biomarkers and $\hat{\mathbf{u}}$ are the experimental biomarkers to be fitted. We obtain a so-called "L-curve" which is typical of such hyper-parameter studies. We see that K=5e-3 is a reasonable choice as it is close the curve's elbow and therefore a good trade-off between goodness of fit and distance to the reference values.

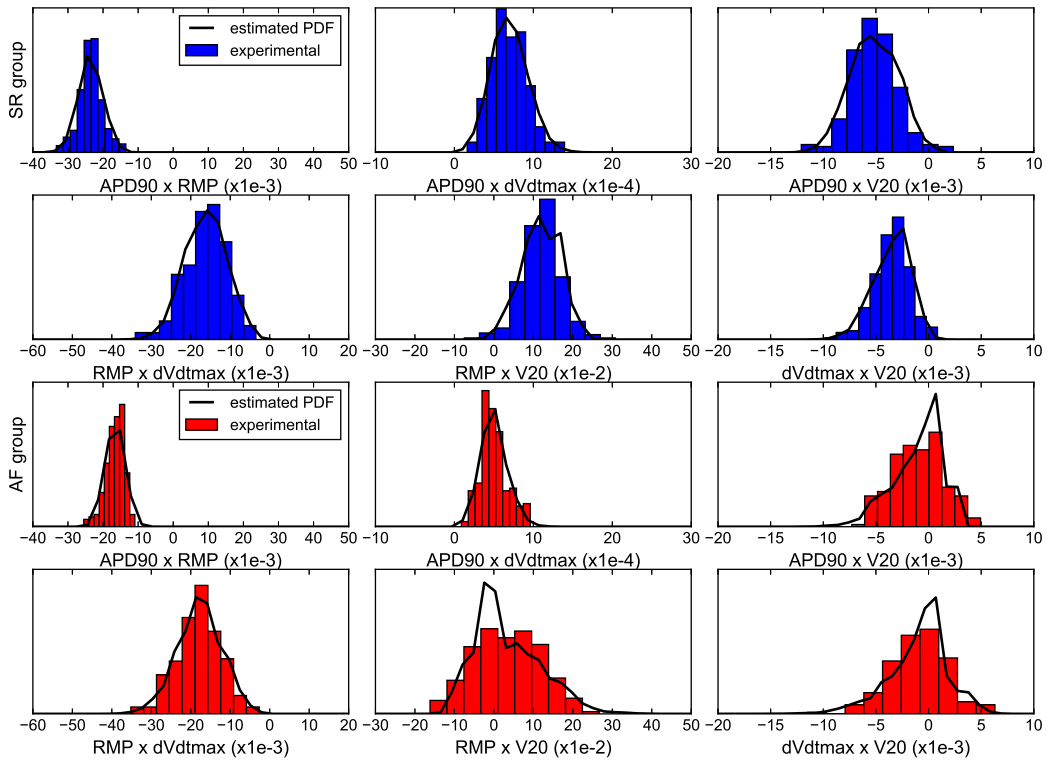

Figure 3.9: Normalized histograms of the experimental biomarkers pairwise products for both SR (blue) and AF (red) groups. The black solid lines correspond to the PDF of each pairwise product estimated by the observable moment matching method. Biomarkers computed from an AP. This figure is an extension of Fig.7(C) in the main article.

Appendix A: Illustration of the OMM method using the Davies model

We propose to illustrate the OMM approach using a simple test case that highlights its non-parametric nature. Indeed, the PDF is estimated point-wise in the parameter space and therefore potentially any distribution may be recovered. We propose to study a test case where one of the parameters has a uniform distribution and two of them are correlated.

For the synthetic data set, $N = 10^4$ APs were generated using the Davies model with three uncertainparameters: g_{Na}, g_{Kr}, g_{CaL}. g_{Kr} and g_{CaL} were drawn from a bivariate normal distribution of mean vector $\boldsymbol{\mu} = (1, 1)$ and of covariance matrix:

$$A = 10^{-2} \times \begin{pmatrix} 2.25 & 2.03 \\ 2.03 & 2.25 \end{pmatrix}$$

which means g_{Kr} and g_{CaL} have a standard deviation of 0.15 and a Pearson correlation coefficient of 90%. g_{Na} is sampled from an uncorrelated uniform distribution over $[0.5, 2.]$. The simulation database was built by sampling the same three parameters over the domain $\boldsymbol{\Theta} = [0.3, 2.0]^3$. $Nc = 2^{12}$ samples were drawn and the number of moments to be matched was set to $N_m = 3$. The estimated marginals are shown in Fig. 3.10. We also plotted the estimated correlation matrix of the three conductances in Fig. 3.11. The correlation between g_{Kr} and g_{CaL} is captured by the method even though it is under-estimated at 60% instead of the 90% of the true distribution.

The discrepancy observed between the true and estimated correlation would be not be observed when using Bayesian inference techniques. This is a limitation of the proposed method. In this particular case, the observable quantities could be enriched with auto-correlation quantities to be able to correctly estimate the parameters correlation.

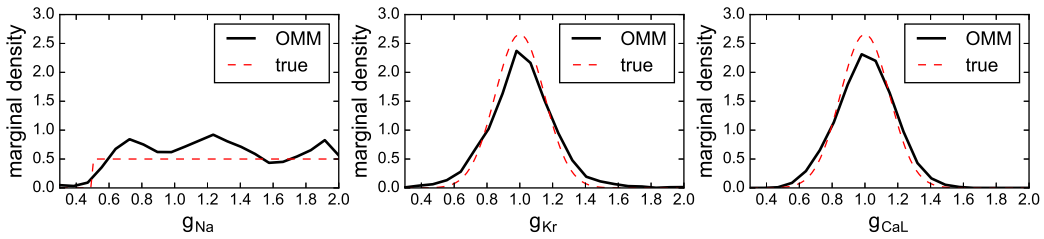

Figure 3.10: Conductances estimated marginal densities.

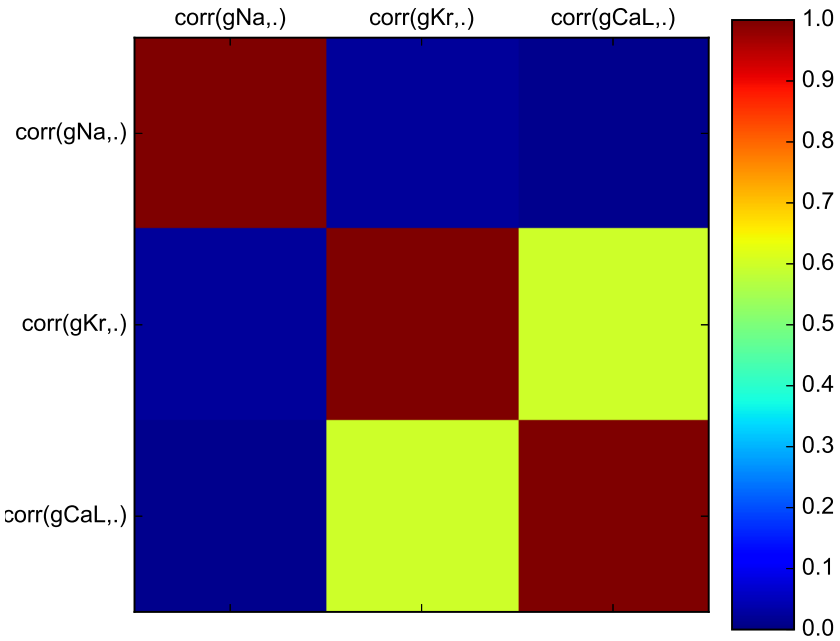

Figure 3.11: Estimated correlation matrix.

Chapter 4

How to Choose Biomarkers in View of Parameter Estimation

This chapter is based on [GLT17]

In numerous applications in biophysics, physiology and medicine, the system of interest is studied by monitoring quantities, called biomarkers, extracted from measurements. These biomarkers convey some information about relevant hidden quantities, which can be seen as parameters of an underlying model. In this chapter we propose a strategy to automatically design biomarkers to estimate a given parameter. Such biomarkers are chosen as the solution of a sparse optimization problem. The method is in particular illustrated with three realistic applications, two in electrophysiology and one in hemodynamics. In both cases, our algorithm provides numerical biomarkers which improve the parameter estimation problem.

Contents

4.1 Introduction 93
4.2 Numerical Method 95
4.2.1 ℓ^1 regularization 96
4.2.2 Problem discretization 97
4.2.3 Regularization parameters setting 97
4.2.4 Numerical Analysis 98
4.2.5 Application to inverse problems 100
4.3 Numerical Experiments 101
4.3.1 A synthetic model 101
4.3.2 A reaction diffusion model 104
4.4 Application to electrophysiology and hemodynamics 106
4.4.1 A model in electrophysiology 106
4.4.2 A model of systemic blood flow circulation 112
4.4.3 Application to synthetic MEA measurements 115
4.5 Conclusions and Perspectives 116

4.1 Introduction

In numerous applications in biophysics, physiology and medicine, the system of interest is studied by monitoring a number of quantities, called biomarkers. For example in electrophysiology, an action potential can be viewed through simple quantities like the action potential duration, the amplitude, the rate of depolarization, *etc.* In hemodynamics, the systolic and diastolic pressures, or the pulse wave velocity, are typical biomarkers extracted from pressure measurements.

The biomarkers are obtained by applying a nonlinear map to the signal measured during experiments or clinical observations. They convey some information on hidden quantities, that are not directly measured. For example in hemodynamics, the pulse wave velocity can be linked to the arterial stiffness. When performing parameter estimation for a biophysical model, it is often much more convenient to work with biomarkers than with the whole signals. A natural question is therefore: which biomarker should be chosen to estimate a given parameter?

Biomarkers are usually proposed by the community, based on physical intuition and experimental observations. They are often relevant in qualitatively describing the hidden quantities. However, in most practical applications, although the biomarkers exhibit a good correlation with respect to the hidden quantity they are designed to monitor, they have a non-negligible correlation with respect to others, making them less robust or of difficult interpretation.

In the present work, we propose a strategy to automatically design biomarkers. The basic ideas of our approach are: (1) to design numerical biomarkers that are maximally correlated with the hidden quantities they have to reveal, and minimally correlated with respect to all the others; (2) to provide a set of quantities making the parameter estimation better conditioned.

The biomarker design problem may be interpreted as a feature selection problem. Most of the literature considers the problem of selecting features in the input space in order to predict a given output (that may be the output of a computational model). Even though the aim of this work is reverse we will momentarily consider, for the sake of comparison, the biomarkers to be inputs and the parameters of interests to be the outputs. A common strategy to select a subset of the available features is by ranking or eliminating them according to a given criterion or score. This score may be based on a sensitivity analysis (e.g. first-order sensitivity indices [GB15]), based on information theory (e.g. Fisher information matrix [CABCL09] or mutual information [KFWV06]) or on the input covariance matrix [OMO14]. For other feature selection techniques and an overview of the field, the interested reader is referred to [GE03]. Other methods consist in selecting directions in the parameter space. In other words, instead of selecting a subset of features, linear combinations of the features are sought. In Principle Component Analysis directions of maximum variance in the parameter space are sought [AM87]. The same principle holds for functional-PCA [GLMG06], its counterpart applied to the case where the input space is a function space. Neither of these approaches take into account the relationship between inputs and outputs. In Active Subspaces [Con15], directions in the input

space are sought so that the gradient of the output with respect to these directions is maximum. In Partial Least Squares [WRWD84], directions are sought in the parameter space so that their covariance with the output is maximum. In this regard, this approach bears some similarities with the present work. Indeed, we look for biomarkers that are maximally correlated with their respective parameters. The main difference is that we also add the constraint that they are minimally correlated with all remaining parameters. Another way to reduce the input space is to perform a sparse linear regression using the Lasso algorithm [YGPD13]. The use of the ℓ^1 norm penalization makes this approach similar to the present work even though the cost function to be minimized is different.

Another aspect which makes the present approach different from previous works is that the feature, or biomarker, selection is performed in order to simplify future inverse problems. This issue has been addressed in [DDM17] but is rarely the focus of feature selection studies. For a comprehensive review of inverse problem techniques, the reader is referred to [KS06].

Our method is based on a semi-empirical approach. A mathematical model of the system of interest is considered and a database of simulations is built, by taking meaningful scenarios into account. Then, a dictionary of linear and nonlinear forms of the observable is considered. The numerical biomarker is defined as a linear combination of the elements of the dictionary. The linear combination is sought such that the resulting biomarker is maximally correlated to the hidden quantity it refers to, and minimally correlated with respect to all the others.

From a practical point of view, at the expense of one single *offline* database computation (done once for all), the expansion coefficients of the biomarkers on a dictionary of observable forms are computed, for a given experimental setup or physical system. Then this result can be exploited for an unlimited number of experiments. As a by-product, when doing inverse problems, the 2-distance in the space of the biomarkers defines a metric which is, up to a controlled perturbation, the 2-distance in the space of the hidden quantities. This makes the inverse problem less ill-conditioned and, in general, easier to solve.

The structure of the work is as follows. In section 4.2 the numerical method is described and its matrix formulation detailed. Then, a numerical analysis is presented. In section 4.3, two numerical experiments are shown. In the first one, a synthetic case is considered to illustrate the approach and highlight its features and performances. In the second one, we illustrate the approach further with a non-linear PDE model. In Section 4.4, three realistic synthetic examples are considered, one with a 0-D electrophysiology model, one with a realistic PDE model of a human body hemodynamics and the last one with synthetic MEA measurements. In all three cases, our algorithm provides numerical biomarkers which lead to more efficient inverse problems.

4.2 Numerical Method

Let a generic model be written as $\mathcal{F}(u;\boldsymbol{\theta}) = 0$, where $\mathcal{F}$ denotes a generic possibly nonlinear algebraic or differential operator, u is the unknown describing the state of the system, $\boldsymbol{\theta} \in \mathbb{R}^p$ a vector of p parameters and let $(\Theta, \mathcal{A}, \mathcal{P})$ be a complete probability space, Θ being the set of outcomes, $\mathcal{A}$ a σ–algebra and $\mathcal{P}$ a probability measure. Let $\mathbf{v}$ be the observable, *i.e.* the measurable model outputs. Let v be a vector function of the solution, $v : \mathcal{U} \to \mathcal{V}$, where $\mathcal{U}, \mathcal{V}$ are suitable functional spaces. The observable is assumed to be given by $v(u)$ perturbed by an additive noise:

$$\mathbf{v} = v(u) + \eta.$$

Let $\mathcal{Y}$ denote a set of functions from the space of the observables $\mathcal{V}$ to $\mathbb{R}$. A numerical biomarker associated with the parameter θ_h is an element of $\mathcal{Y}$ denoted by y_h. The numerical biomarker design problem can be stated as follows:

$$\forall h \in \{1, \dots, p\}, \quad \begin{cases} \max\limits_{y_h \in \mathcal{Y}} & \operatorname{cov}\left(y_h(\mathbf{v}), \theta_h\right) & \text{(4.1a)} \\ \min\limits_{y_h \in \mathcal{Y}} & \left|\operatorname{cov}\left(y_h(\mathbf{v}), \theta_k\right)\right|, \forall k \neq h & \text{(4.1b)} \\ \text{s.t.} & \operatorname{var}\left(y_h(\mathbf{v})\right) = 1 & \text{(4.1c)} \end{cases}$$

where $\operatorname{var}(\cdot)$ and $\operatorname{cov}(\cdot,\cdot)$ are respectively the variance and covariance operators. The parameters $\theta_1, \dots, \theta_p$ are supposed to be zero-mean unit-variance random variables. Under the condition that $\operatorname{var}\left(y_h(\mathbf{v})\right) = 1$, the Pearson correlation coefficient between $y_h(\mathbf{v})$ and θ_h and their covariance coincide and they range, in absolute value, from 0 to 1. For the sake of simplicity and efficiency, we propose to relax the multi-objective constrained optimization problem (4.1) as follows. We solve:

$$\begin{aligned} y_h^* &= \arg\min_{y_h \in \mathcal{Y}} \mathcal{L}_h(\mathbf{y}_h), \\ \mathcal{L}_h(\mathbf{y}_h) &= \frac{1}{2}\left[\sum_{k=1}^{p} \left[\mathbb{E}\left[(\mathbf{y}_h - \mathbb{E}(\mathbf{y}_h))\theta_k\right] - \delta_{kh}\right]^2 + \xi\left[\mathbb{E}\left[(\mathbf{y}_h - \mathbb{E}(\mathbf{y}_h))^2\right] - 1\right]^2\right], \end{aligned} \tag{4.2}$$

where $\mathbf{y}_h = y_h(\mathbf{v})$, $\mathbb{E}[\cdot]$ is the expectation operator, δ_{kh} is the Kronecker delta and ξ a penalization parameter which results from the relaxation of the constraint (4.1c). The necessary conditions for the optimality read:

$$\sum_{k=1}^{p} \left(\mathbb{E}\left[(\mathbf{y}_h - \mathbb{E}(\mathbf{y}_h))\theta_k\right] - \delta_{kh}\right)\theta_k + 2\xi\left(\mathbb{E}\left[(\mathbf{y}_h - \mathbb{E}(\mathbf{y}_h))^2\right] - 1\right)(\mathbf{y}_h - \mathbb{E}(\mathbf{y}_h)) = 0. \tag{4.3}$$

In order to discretize Eq.(4.3), a set of linear and nonlinear forms on $\mathcal{V}$ is introduced: $\mathcal{G} = \{g_1, \dots, g_{N_g}\}$ where $g_j \in \mathcal{Y}$ for $j = 1, \dots, N_g$. This set will later be referred to as the biomarkers dictionary. The biomarker y_h is represented as a linear combination

of the dictionary elements:

$$y_h = \sum_{j=1}^{N_g} \beta_j^{(h)} g_j, \tag{4.4}$$

The equations for $\beta_j^{(h)}$ are obtained by a Galerkin projection of (4.3) on g_l:

$$\begin{aligned} &\sum_{k=1}^{p} \left(\sum_{j=1}^{N_g} C_{kj}\beta_j^{(h)} - \delta_{kh} \right) C_{kl} + 2\xi\,(\nu_h - 1) \sum_{j=1}^{N_g} G_{jl}\beta_j^{(h)} = 0, \\ &\text{with} \quad \nu_h := \sum_{i,j=1}^{N_g} G_{ij}\beta_i^{(h)}\beta_j^{(h)}, \quad G_{ij} := \mathbb{E}(\tilde{\mathbf{g}}_i\tilde{\mathbf{g}}_j), \quad C_{kj} := \mathbb{E}(\theta_k\tilde{\mathbf{g}}_j) \\ &\text{and} \quad \tilde{\mathbf{g}}_j := g_j(\mathbf{v}) - \mathbb{E}(g_j(\mathbf{v})), \end{aligned} \tag{4.5}$$

which is a nonlinear system of equations to be solved for $\boldsymbol{\beta}^{(h)} \in \mathbb{R}^{N_g}$. This equation can also be obtained as the solution of the following minimization problem:

$$\begin{aligned} \boldsymbol{\beta}_*^{(h)} &= \arg \min_{\boldsymbol{\beta}^{(h)} \in \mathbb{R}^{N_g}} \mathcal{J}(\boldsymbol{\beta}^{(h)}), \\ \mathcal{J}(\boldsymbol{\beta}^{(h)}) &= \frac{1}{2}\|\mathbf{C}\boldsymbol{\beta}^{(h)} - \boldsymbol{e}^{(h)}\|^2 + \frac{\xi}{2}\left(\nu_h(\boldsymbol{\beta}^{(h)}) - 1\right)^2, \end{aligned} \tag{4.6}$$

where $\boldsymbol{e}_i^{(h)} = \delta_{hi}$.

4.2.1 ℓ^1 regularization

To regularize the problem, an ℓ^1 penalty term is added which tends to promote sparsity since it is an approximation of an ℓ^0 penalty [Tib96]. The motivation behind the sparsity promotion is twofold. First, the obtained biomarkers, if most values of $\beta_j^{(h)}$ are zero, can be easily interpreted as a correction of possibly existing biomarkers for a given parameter. Second, ℓ^1–penalyzed models tend to be more predictive and less prone to overfitting than ℓ^2–penalyzed ones.
The equation for the coefficients $\boldsymbol{\beta}^{(h)}$ is recast by adding to the functional $\mathcal{J}$ in Eq.(4.6) an ℓ^1 penalization:

$$\boldsymbol{\beta}_*^{(h)} = \arg \min_{\boldsymbol{\beta}^{(h)} \in \mathbb{R}^{N_g}} \mathcal{J} + \frac{\lambda_h}{N_g}\|\boldsymbol{\beta}^{(h)}\|_1, \tag{4.7}$$

where λ_h is a penalization parameter. In what follows, $\mathcal{J}_\lambda$ denotes the penalized functional.

A drawback of the modified functional is that the new term is not differentiable. A standard way to deal with this difficulty is to introduce the change of variables $\boldsymbol{\beta}^{(h)} = \boldsymbol{\beta}^+ - \boldsymbol{\beta}^-$, where $\boldsymbol{\beta}^+$ (resp. $\boldsymbol{\beta}^-$) is the positive (resp. negative) part of

$\boldsymbol{\beta}^{(h)}$ [BJM+11]. The minimization problem can then be recast as follows:

$$\begin{cases} \min\limits_{\boldsymbol{\beta}^+,\boldsymbol{\beta}^-} & \mathcal{J}(\boldsymbol{\beta}^+ - \boldsymbol{\beta}^-) + \frac{\lambda_h}{N_g}\left(\mathbf{1}\cdot\boldsymbol{\beta}^+ + \mathbf{1}\cdot\boldsymbol{\beta}^-\right) \\ \text{s.t.} & \boldsymbol{\beta}^+ \geq 0 \\ & \boldsymbol{\beta}^- \geq 0 \end{cases} . \tag{4.8}$$

Note that while the non-differentiability issue of the ℓ^1–norm is avoided, the number of unknowns is doubled and $2N_g$ (easy) inequality constraints are added.

4.2.2 Problem discretization

We choose to approximate the expectation operator by a Monte-Carlo method. In the *offline phase*, N samples $\boldsymbol{\theta}^{(i)} \in \mathbb{R}^p$, $i = 1 \dots N$, are drawn and stored in the matrix $\boldsymbol{\Theta} \in \mathbb{R}^{N\times p}$. For each sample the model $\mathcal{F}(u^{(i)};\boldsymbol{\theta}^{(i)}) = 0$ is evaluated and a noise η is added to the model output $v(u^{(i)})$. We define $\mathbf{v}(\boldsymbol{\theta}^{(i)}) = v(u^{(i)}) + \eta$. The intensity of the noise is chosen such that it is representative of a realistic scenario under investigation. This contributes to the robustness of the biomarkers.

In what follows, $\mathbf{y}^{(h)} \in \mathbb{R}^N$ denotes the vector of components $y_h(\mathbf{v}(\boldsymbol{\theta}^{(i)}))$, $i = 1,\dots,N$. The biomarkers dictionary entries are computed from the noisy model outputs and stored in the matrix $\mathbf{G} = [g_j(\mathbf{v}(\boldsymbol{\theta}^{(i)})) - \mathbb{E}(g_j(\mathbf{v}))] \in \mathbb{R}^{N\times N_g}$. The set $\{\boldsymbol{\Theta}, \mathbf{G}\}$ will later be referred to as the training set.

Many algorithms can be used to solve the constrained optimization problem in (4.8). In the present work, we choose the Nesterov accelerated gradient descent method [Nes83, OC15] in which, at each step, the unknowns are projected onto the constraint set if they do not satisfy the inequality constraints. Given the type of constraints, this projection is straightforward. The gradient to be used in the Nesterov gradient descent iterations reads:

$$\begin{aligned} \boldsymbol{\partial}_{\boldsymbol{\beta}^+}\mathcal{J}_\lambda &= \frac{1}{N}\mathbf{G}^T\boldsymbol{\Theta}(\mathbf{C}\boldsymbol{\beta}^{(h)} - \boldsymbol{e}^{(h)}) + \frac{2\xi(\nu_h - 1)}{N}\mathbf{G}^T\mathbf{G}\boldsymbol{\beta}^{(h)} + \frac{\lambda_h}{N_g}\mathbf{1}, \\ \boldsymbol{\partial}_{\boldsymbol{\beta}^-}\mathcal{J}_\lambda &= -\frac{1}{N}\mathbf{G}^T\boldsymbol{\Theta}(\mathbf{C}\boldsymbol{\beta}^{(h)} - \boldsymbol{e}^{(h)}) - \frac{2\xi(\nu_h - 1)}{N}\mathbf{G}^T\mathbf{G}\boldsymbol{\beta}^{(h)} + \frac{\lambda_h}{N_g}\mathbf{1}, \end{aligned} \tag{4.9}$$

where the first two terms in the gradient correspond to the discretization of Eq.(4.5), and the last term accounts for the ℓ^1 penalization.

4.2.3 Regularization parameters setting

Two methods are proposed to set the regularization parameters $\lambda_1,\dots,\lambda_p$. In this section, the penalization parameter ξ is set to 1.

"L-curve" criterion A common way to set the regularization parameters involves computing the so-called "L-curve" which represents the balance between the sparsity of the solution and the corresponding training error. Here, the sparsity of the solution is measured by $\|\boldsymbol{\beta}_h\|_1$. The training error corresponding to the biomarker

y_h is defined as $\|\frac{1}{N}\mathbf{\Theta}^T\mathbf{y}^{(h)} - \mathbf{e}^{(h)}\|_2$ and quantifies how well the discrete biomarker $\mathbf{y}^{(h)}$ fulfills the objectives for a given training set $\{\mathbf{\Theta}, \mathbf{G}\}$. The problem in (4.8) is solved for different values of λ_h and therefore one L-curve is obtained for each biomarker y_h (i.e. for each parameter θ_h) for $h = 1, \ldots, p$. In Figure 4.1 an example of L-curves is provided, when considering the first two parameters of the model presented in Section 4.4.1. A natural way to determine λ_h from the L-curve is to

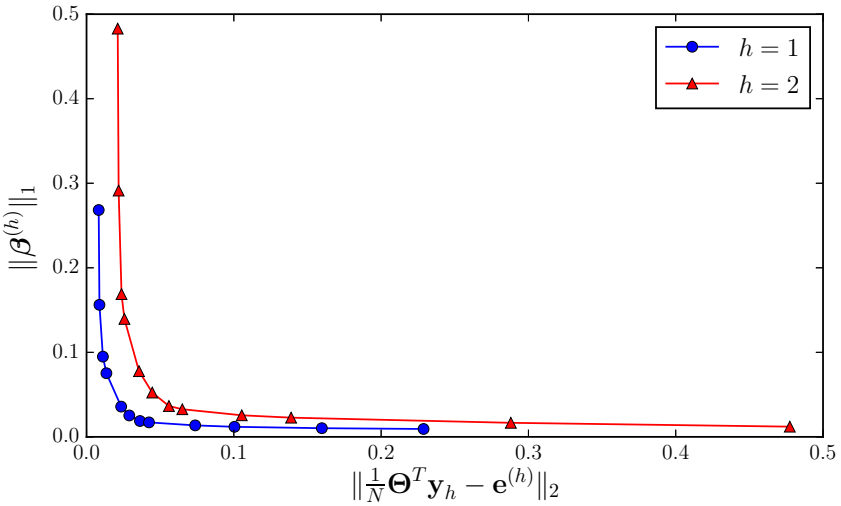

Figure 4.1: The "L-curve" is obtained for the first two parameters of the test case presented in Section 4.4.1. The ℓ^1-norm of $\boldsymbol{\beta}^{(h)}$ is plotted against the training error for different values of λ_h. Here, λ_h varies between 10^{-6} and 2×10^1.

choose the λ_h that maximizes its curvature. It is, in practice, a good compromise between an over-fitted (λ_h is too small) and an over-regularized (λ_h is too large) solution [JG00]. It also has the advantage of not requiring other hyperparameters.

Training error threshold Another way to set the regularization parameters is to choose the largest λ_h so that a user-defined training error is respected. While easy to implement, this requires an additional tuning parameter.

4.2.4 Numerical Analysis

The analysis proposed hereafter is carried out in the non-regularized case, *i.e.* when $\lambda_h = 0$. To assess the relevance of the biomarkers dictionary $\mathcal{G}$ in defining the biomarker, it is interesting to study the map $\mathbf{y}_h$ as a function of the parameters, rather than of the observables. From a parameter identification perspective, an ideal configuration would be to have $\mathbf{y}_h$ proportional to θ_h. So we propose here to assess how far we are from this configuration.

The numerical biomarker, after the coefficients $\boldsymbol{\beta}^{(h)}$ have been found, can be seen as a map from the space of the parameters into real numbers $\mathbf{y}_h : \Theta \to \mathbb{R}$. We assume that the θ_h are zero-mean unit-variance and mutually uncorrelated random

variables, *i.e* $\mathbb{E}(\theta_h) = 0$, $\mathbb{E}(\theta_h\theta_k) = \delta_{hk},\ \forall h, k$. The expression of the biomarker $\mathbf{y}_h$ can be decomposed as follows:

$$\mathbf{y}_h = (\boldsymbol{\alpha}^{(h)})^T\boldsymbol{\theta} + q^{(h)}(\boldsymbol{\theta}), \tag{4.10}$$

where $q^{(h)}$ is a function such that $\mathbb{E}(q^{(h)}\theta_k) = 0,\ \forall\theta_k$.

PROPOSITION 1
Decomposing the biomarker $\mathbf{y}_h$ *as in* (4.10)*, we have:*

$$\|q^{(h)}\|_2 \leq C\mathcal{L}_h^{1/4},$$

where C *is a constant,* $\mathcal{L}_h = \mathcal{L}_h(\mathbf{y}_h)$ *is defined in* (4.2)*, and* $\|v\|_2^2 = \mathbb{E}(v^2)$.

Proof For convenience, the vector $\boldsymbol{\alpha}^{(h)}$ is decomposed in $\mathbf{e}^{(h)} + \boldsymbol{\gamma}^{(h)}$, where $\boldsymbol{e}_i^{(h)} = \delta_{hi}$. Let $\boldsymbol{\Delta}_h = (\boldsymbol{\gamma}^{(h)})^T\boldsymbol{\theta}$. The expression of $\mathbf{y}_h$ is injected into Eq.(4.2) leading to:

$$\mathcal{L}_h = \frac{1}{2}\|\boldsymbol{\Delta}_h\|_2^2 + \frac{\xi}{2}\left[\|q^{(h)}\|_2^2 + \|\boldsymbol{\Delta}_h\|_2^2 + 2\mathbb{E}(\boldsymbol{\Delta}_h, \theta_h)\right]^2, \tag{4.11}$$

First, we notice that $\|\boldsymbol{\Delta}_h\|_2 \leq \sqrt{2}\mathcal{L}_h^{1/2}$. Then, applying the Cauchy-Schwarz inequality and observing that $\|\theta_h\|_2 = 1,\ \forall h$, we have:

$$\begin{aligned}\|q^{(h)}\|_2^2 &\leq \frac{1}{\sqrt{\xi}}\left(2\mathcal{L}_h - \|\boldsymbol{\Delta}_h\|_2^2\right)^{1/2} - \|\boldsymbol{\Delta}_h\|_2^2 - 2\mathbb{E}(\boldsymbol{\Delta}_h, \theta_h)\\ &\leq \sqrt{\frac{2}{\xi}}\mathcal{L}_h^{1/2} - \|\boldsymbol{\Delta}_h\|_2^2 + 2\|\boldsymbol{\Delta}_h\|_2 \leq \sqrt{\frac{2}{\xi}}\mathcal{L}_h^{1/2} + 2\|\boldsymbol{\Delta}_h\|_2 \leq C^2\mathcal{L}_h^{1/2}\end{aligned}$$

with $C^2 = \sqrt{2/\xi} + 2\sqrt{2}$. ♢

The result of the proposition shows that the 2-norm of $q^{(h)}$, which is the nonlinear term of the biomarker map $\mathbf{y}_h$ is controlled by the value of the functional $\mathcal{L}_h$, which is minimized. If the value of the functional is close to zero, then, the norm of q is close to zero. Thus, the biomarker, which is a nonlinear map of the observable, is close to a linear map of the parameters.

In addition, this linear map is a perturbation of the identity. The amplitude of this perturbation is measured by the quantity $\|\boldsymbol{\Delta}_h\|_2$ introduced in the proof of Proposition 1, and it was noticed that $\|\boldsymbol{\Delta}_h\|_2 \leq \sqrt{2}\mathcal{L}_h^{1/2}$. This shows that if the value of $\mathcal{L}_h$ is small, then the 2-distance of the biomarkers is close to the 2-distance of the parameters. This property is particularly appealing when considering parameter identification problems, as will be shown below.

In conclusion, it is desirable that the value of $\mathcal{L}_h(\mathbf{y}_h)$ be as small as possible. Thus, the value reached by $\mathcal{L}_h(\mathbf{y}_h)$ once the minimization has been performed can be seen as an *a posteriori* indicator of the quality of the dictionary.

4.2.5 Application to inverse problems

One of the outcomes of the presented method is to make the parameter estimation easier. It is assumed here that the parameter estimation is formulated as an optimization problem, in which the 2–norm of the discrepancy between measurements and the simulated observables is minimized. The cost function has the following form:

$$J_1(\boldsymbol{\theta}) = \frac{1}{2} \left\| \mathbf{v}(\boldsymbol{\theta}) - \mathbf{v}^* \right\|_2^2 , \tag{4.12}$$

where $\mathbf{v}^*$ denotes the measured observable from which the parameters true value $\boldsymbol{\theta}^*$ are to be estimated. When considering the numerical biomarkers, the cost function reads:

$$J_2(\boldsymbol{\theta}) = \frac{1}{2} \sum_{h=1}^{2} \left[y_h(\mathbf{v}(\boldsymbol{\theta})) - y_h(\mathbf{v}^*) \right]^2 . \tag{4.13}$$

To minimize J_2 we propose to use a convenient algorithm which is a simplification of Powell's BOBYQA algorithm [Pow09] and relies on successive quadratic approximations of the cost function. Starting from an initial guess, the cost function is locally evaluated and approximated by a quadratic function from which the minimum is easily computed. This iterative process does not require any gradient evaluation and converges, in practice, faster than the classical gradient descent. The algorithm, later referred to as gradient-free minimization, is presented in Algorithm 4.

Algorithm 4: Cost function minimization using alternate directions descent quadratic approximations.

Input:

- Cost function: $J(\boldsymbol{\theta})$ (see Eqs. (4.12),(4.13))
- Initial guess: $\boldsymbol{\theta}^{(0)}$
- Bracket size: γ
- Stopping criterions: absTol and relTol

$i \leftarrow 0$;
$r^{(0)} := J(\boldsymbol{\theta}^{(0)})$;
while $r^{(i)} <$ absTol *or* $\left| r^{(i)} - r^{(i-1)} \right| <$ relTol $\times\, r^{(i)}$ **do**
  for $h = 1$ **to** p **do**
    Fit quadratic model $Q(\xi)$ to $f(\xi) = J(\ldots, \theta_{h-1}^{(i)}, \xi, \theta_{h+1}^{(i)}, \ldots)$ for $\xi \in I_h^{(i)} = [\theta_h^{(i)} - \gamma, \theta_h^{(i)} + \gamma]$;
    Update: $\theta_h^{(i+1)} := \underset{\xi \in I_h^{(i)}}{\arg\min}\, Q(\xi)$;
  end
  Update residual: $r^{(i+1)} := J(\boldsymbol{\theta}^{(i+1)})$;
  $i \leftarrow i + 1$;
end

4.3 Numerical Experiments

In the following examples, the penalization parameter ξ is set to 1. It is a reasonable compromise between efficiency and precision for all the test cases presented in this work. Indeed, with $\xi = 1$, the constraint in (4.1c) is satisfied with an error of at most 10^{-2} while the number of iterations needed in the accelerated gradient descent ($\sim 10^4$) is deemed low enough for practical use.

4.3.1 A synthetic model

To start with, we illustrate our algorithm with a simple algebraic model defined as follows:

$$\begin{aligned} u(\theta_1, \theta_2, x) = x^2 \exp\left(-\frac{(\theta_1^2 + \theta_2^2 - R^2)^2}{2\sigma_0^2}\right) + \theta_1 \exp\left(-\frac{(x - (x_1 + \alpha\theta_1))^2}{2\sigma_1^2}\right) \\ + \theta_2 \exp\left(-\frac{(x - (x_2 + \alpha\theta_2))^2}{2\sigma_2^2}\right), \quad x \in [-1, 1] \end{aligned} \tag{4.14}$$

with the following fixed parameters: $R = 0.75$, $x_1 = -0.5$, $x_2 = 0.5$, $\alpha = 0.1$, $\sigma_0 = 0.2$ and $\sigma_1 = \sigma_2 = 0.1$. Here, x is the state variable and the uncertain parameters are θ_1 and θ_2. The segment $[-1, 1]$ is discretized into a uniform grid of $N_g = 201$ nodes. The observable is $\mathbf{v} = u + \eta$, where $\eta \sim \mathcal{N}(0, \tau^2)$ with $\tau = 2.10^{-2}$. This corresponds to a signal-to-noise ratio (SNR) of 31 dB. The biomarkers dictionary entries are the values of the model at each node of the discretized domain $u(x_1), \ldots, u(x_{N_g})$. The training set is generated with $N = 10^3$ samples of (θ_1, θ_2) drawn from the normal distribution $\mathcal{N}(\boldsymbol{\mu}, \boldsymbol{\Sigma})$, where $\boldsymbol{\mu} = (0, 0)$ and $\boldsymbol{\Sigma} = 2.5.10^{-1} \times \mathbf{I}_2$.

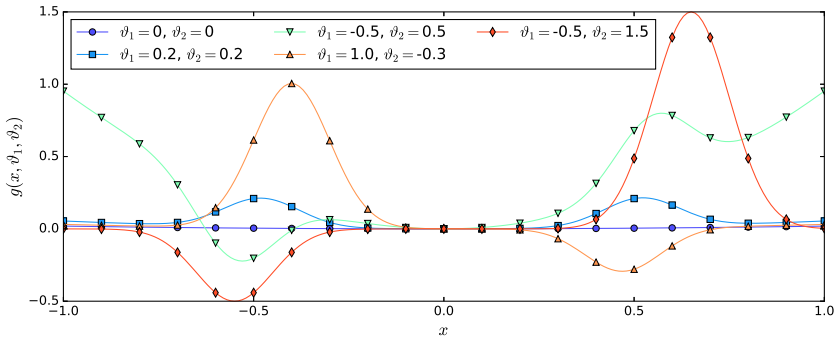

Figure 4.2: Model outputs for different values of θ_1, θ_2.

4.3.1.1 Biomarkers computation

The procedure described in Section 4.2 is applied to the present test case and the thresholding method is used to choose the regularization parameters λ_1 and λ_2. The threshold on the training error is set to 10^{-2} which yields $\lambda_1 = 0.11$ and $\lambda_2 = 0.09$. The obtained biomarkers weights $\boldsymbol{\beta}_1$ and $\boldsymbol{\beta}_2$ are represented in Fig. 4.3 as well as the

biomarkers themselves with respect to the parameters. Note that most coefficients are zero, as expected with the sparsity promoting ℓ^1 penalty.

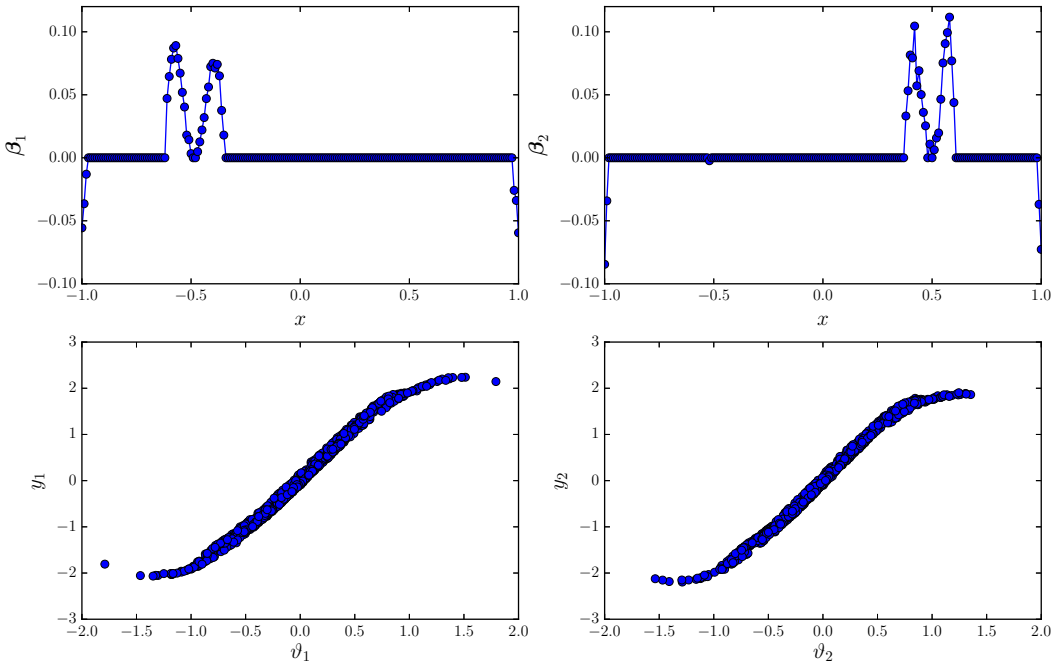

Figure 4.3: Analytical model: biomarkers weights (top) and corresponding biomarkers (bottom).

4.3.1.2 Parameter estimation

Here, we highlight how using the previously obtained biomarkers leads to easier inverse problems. In the context of a parameter estimation problem, one seeks the true values of the uncertain parameters $\boldsymbol{\theta}^*$ from a measurement $\mathbf{v}^*(x)$. We assume that such a measurement is a noisy output of the model in (4.14):

$$\mathbf{v}^*(x) = u(\boldsymbol{\theta}^*, x) + \eta \tag{4.15}$$

We propose to perform a parameter estimation with the true solution $\boldsymbol{\theta}^* = (0.3, 0.3)$ using J_1 and J_2 and with both minimization methods: gradient descent and gradient-free minimization. The cost functionals J_1 and J_2 as function of θ_1, θ_2 are plotted in Fig. 4.4. While J_1 features local minima and is non convex, the functional J_2 has only one global minimum, corresponding to the true solution. The results of the parameter estimations are summarized in Table 4.1. As expected, the parameter estimation fails when using J_1 in the sense that the distance to the true solution at the end of the minimization procedure is large. The minimization method falls, for J_1, into a local minimum as seen in Fig. 4.4. On the contrary, the minimization succeeds in finding the true solution when using J_2 (using the numerical biomarkers).

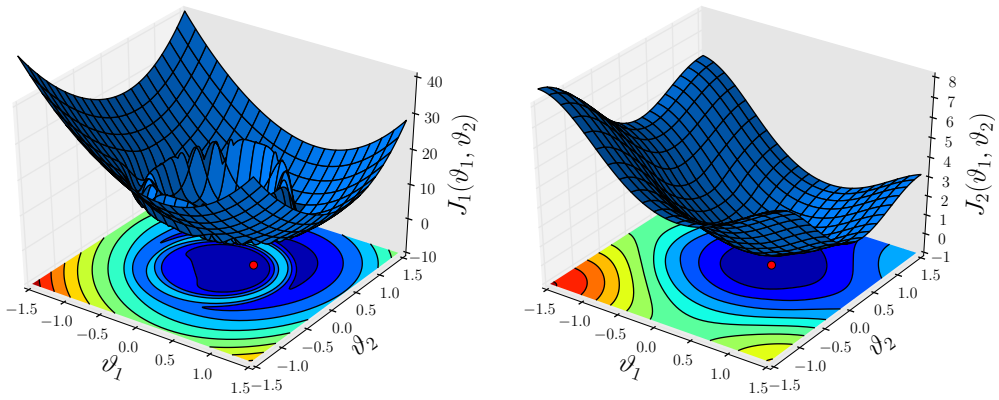

Figure 4.4: Contours of the inverse problem cost function with true solution $\boldsymbol{\theta}^* = (0.3, 0.3)$ represented by a red dot. J_1 using the raw model outputs (left) and J_2 using the numerical biomarkers (right).

	Powell's method	
	$\|\boldsymbol{\theta}^{(n_{\text{iter}})} - \boldsymbol{\theta}^*\|_2$	n_{iter}
J_1	6.3×10^{-1}	33
J_2	6.8×10^{-3}	13

Table 4.1: Parameter estimation.

4.3.1.3 Influence of hyperparameters

Using the analytical model, we now investigate the influence of the regularization parameters λ_1, λ_2 and the training set parameters samples $\boldsymbol{\Theta}$. For the sake of simplicity and because θ_1 and θ_2 have essentially symmetrical effects, we will restrict to the cases where $\lambda_1 = \lambda_2$. In Figure 4.5 is represented $J_2(\theta_1, \theta_2)$, the cost function associated to the inverse problem in (4.13) as the regularization parameters increase from 10^{-5} to 10^1. For high values of λ_h, the cost function loses its convexity since the penalty term in (4.7) becomes predominant.
In Figure 4.5 is represented $J_2(\theta_1, \theta_2)$ for different training set parameters samples $\boldsymbol{\Theta}$. Using the same number of samples ($N = 10^3$) and same standard deviation, the samples are drawn from a normal distribution with different means. The method is robust with respect to the choice of training set in the sense that the cost function remains convex even when the training set center is far from the true solution, except in the last case ($\boldsymbol{\mu} = (-2, -2)$).

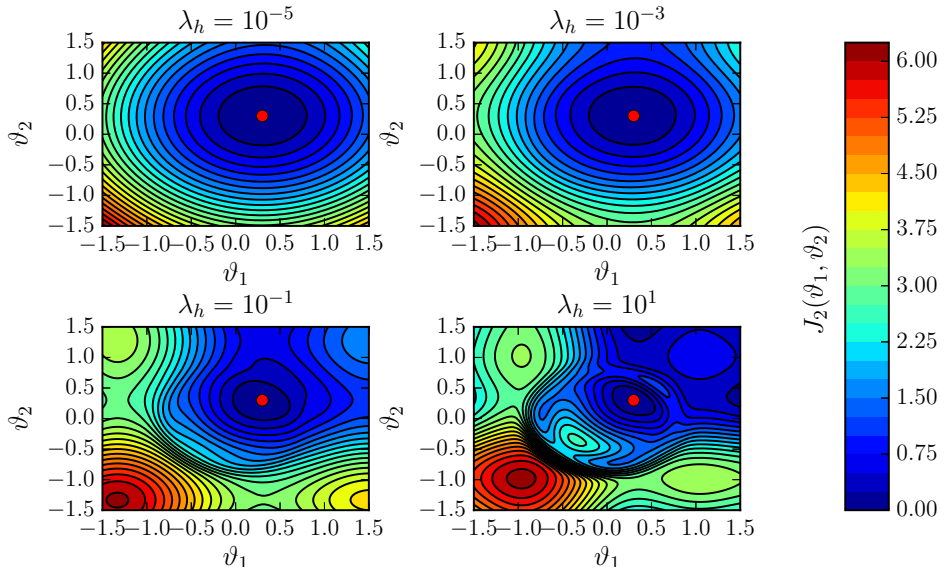

Figure 4.5: Cost function $J_2(\theta_1, \theta_2)$ with different regularization parameters $\lambda = \lambda_1 = \lambda_2$ and parameters samples centered on $\boldsymbol{\mu} = (0, 0)$. The red dot materializes the position of the true solution $\boldsymbol{\theta}^*$.

4.3.2 A reaction diffusion model

We now illustrate the numerical biomarkers method with a one dimensional PDE model, namely the Fisher, Kolmogorov, Petrovskii and Piskunov. It is a nonlinear reaction-diffusion equation which exhibits, under certain conditions, a propagation

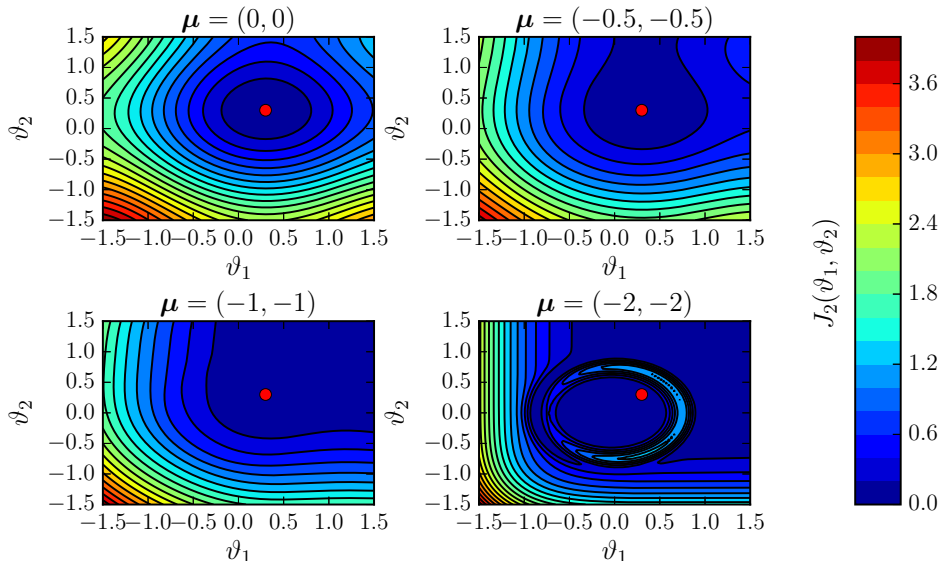

Figure 4.6: Cost function $J_2(\theta_1, \theta_2)$ with different training sets and $\lambda_1 = \lambda_2 = 10^{-3}$. The red dot materializes the position of the true solution $\boldsymbol{\theta}^*$.

front. The model reads:

$$\begin{aligned} \frac{\partial u}{\partial t} - \Delta u = \alpha u(1-u), \qquad & x \in [0,1], t \in [0,T], \\ \frac{\partial u}{\partial x} = 0, \qquad & x = 0, x = 1, t \in [0,T], \\ u(x, t=0) = \exp\left[-\frac{(x-x_0)^2}{2\sigma^2}\right], \qquad & x \in [0,1]. \end{aligned}$$

Note that it is a 1–D version of the model presented in Chapter 2 but this stime the "stimulation" comes from the initial solution and not an additional term in the right hand side. The initial condition considered here is a non-normalized Gaussian function of varying center and width (standard deviation). The parameters of interest are the reaction coefficient α and two parameters related to the initial condition: x_0 the center of the Gaussian and σ its standard deviation. The uncertain parameters are defined as follows:

$$\theta_1 := \alpha/\bar{\alpha}, \quad \theta_2 := x_0, \quad \theta_3 := \sigma/\bar{\sigma},$$

where $\bar{R} = 500$ and $\bar{\sigma} = 5.10^{-2}$.
The segment $[0, 1]$ is discretized using a uniform grid of $N_g = 101$ nodes and the time is discretized on the segment $[0, T]$ where $T = 4.10^{-2}$ with a time step of $\Delta t = 10^{-4}$. The observable is the state variable at each node in space and once every 10 time steps, which amounts to a total of 400 DOFs. In this example, the entries of the dictionary of features are the observable values at each of the 400 DOFs with the addition of a noise η, where $\eta \sim \mathcal{N}(0, \tau = 10^{-2})$. The training set

is generated with $N = 10^3$ samples of $(\theta_1, \theta_2, \theta_3)$ drawn from a uniform distribution over $[1, 2] \times [0.1, 0.9] \times [0.5, 2]$. A sample noisy solution of the model is shown in Figure 4.7 and in the top left corner of Figure 4.8.
The procedure described in Section 4.2 is applied. The obtained numerical biomarkers weights are represented in Figure 4.8 as functions of time and space. This representation allows for a qualitative discussion of the obtained non-zero weights. For the x_0 parameter (which indicates the center of the Gaussian), the numerical biomarker is asymmetrical and is "active" right after the initial condition. It multiplies the right part of the solution by +1 and the left part of the solution by -1. For the σ parameter, the numerical biomarker seems to compute the integral of the solution right after the initial condition. Since the initial condition is not normalized, the higher the σ the higher its integral in space is. Finally, it is not easy to interpret the numerical biomarker associated with the reaction parameter α. Note that it substracts the initial condition to the solution at the boundary of the domain later in time. This could be a way of measuring the front propagation velocity which we know is linked to the reaction coefficient (and to the diffusion coefficient which is identically 1 in our case).

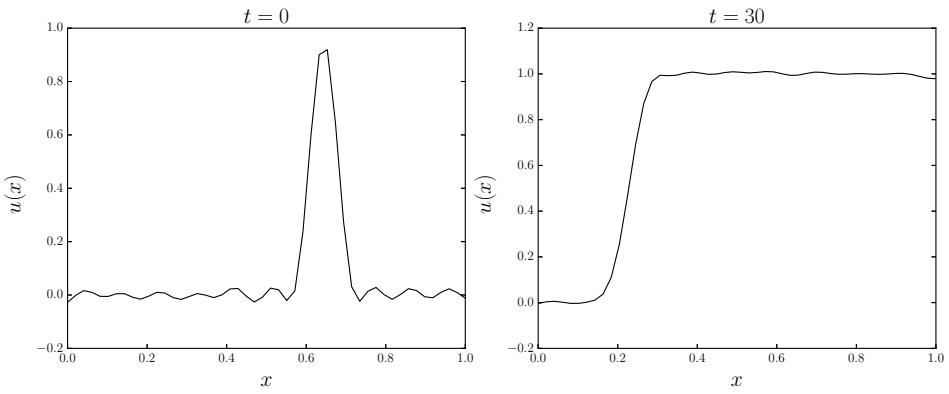

Figure 4.7: Sample solution of the 1–D FKPP model at two different times (here, time is multiplied by a factor 10^3).

4.4 Application to electrophysiology and hemodynamics

4.4.1 A model in electrophysiology

In this section, the proposed methodology is applied to a cardiomyocyte (heart muscle cell) electrophysiology model. Cardiomyocytes are contractible cells that react to an electrical activation. Detailed electrophysiology models have been developed to reproduce the cardiomyocytes complex electrical activity. Such models

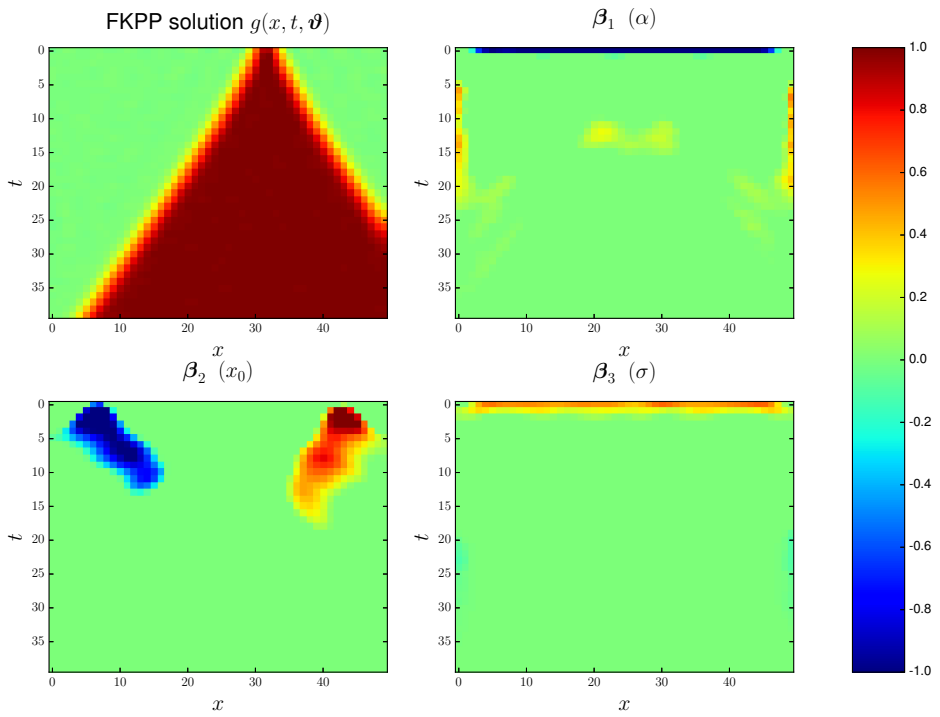

Figure 4.8: Numerical biomarkers weights for the FKPP model. y-axis is the time multiplied by 10^3.
top left: visualization of a sample solution in time and space, top right: weights of biomarker of θ_1 $(\alpha/\bar{\alpha})$, bottom left: weights of biomarker of θ_2 (x_0), bottom right: weights of biomarker of θ_3 $(\sigma/\bar{\sigma})$.

consist in general in a set of nonlinear coupled ODEs of the following form:

$$\begin{cases} \dfrac{\mathrm{d}V}{\mathrm{d}t} &= \displaystyle\sum_{i=1}^{m} J_i(V,t), \\ J_i(V,t) &= \kappa_i f_i(V,\mathbf{w}_i) \qquad \text{for } 1 \leq i \leq m, \\ \dfrac{\mathrm{d}\mathbf{w}_i}{\mathrm{d}t} &= \boldsymbol{\zeta}_i(V,\mathbf{w}_i) \qquad \text{for } 1 \leq i \leq m. \end{cases} \tag{4.16}$$

Despite a wide variety of models, most of them share this common structure. m corresponds to the number of different kinds of ionic currents and ranges from 1 to more than 30 depending on the model's precision level. In this paper, the model by Davies *et al.* [DMH+11] was chosen. It counts $m = 17$ ionic currents, 29 ODEs and is designed to model cardiomyocytes belonging to the ventricular region of the canine heart. The observable quantity is the action potential (AP), denoted by V in (4.16). It corresponds to the electrical potential difference between the inside and the outside of the cell. It drives the heart contraction and its alteration is at the origin of many cardiac diseases. In Figure 4.10 is plotted a typical AP along with some biomarkers that are commonly extracted from it. In our case, the parameters of interest are the conductances, κ_i in (4.16). They are the parameters commonly calibrated to fit different kind of cells or to model diseases and drug-induced AP alterations. We chose to retain 5 of these conductances as the parameters of interest, namely D_{Kr}, D_{K1}, C_{to1}, $D_{Ca,L}$ and D_{NaCa}. Each parameter θ_h is a multiplicative factor of the corresponding parameter reference value. Estimating this kind of parameters has many applications in electrophysiology, ranging from fitting models to experiments [SVNL05, SS10, KNV14] to obtaining insights into disease-induced cell modifications [SBOW+14]. Most often, this inverse problem is solved by using biomarkers.

Figure 4.11 shows how correlated these 5 parameters of interest are with their classically associated biomarkers. The latter are, respectively, APD_{90}, RMP, V_{notch}, $\mathrm{APD}_{50}/\mathrm{APD}_{90}$, APD_{50} (see Figure 4.10). This choice of biomarkers reflects the common associations made in the literature [DMH+11, CRN98, KSMT14]. Without surprise, this result shows that the classically adopted biomarkers are indeed correlated with the parameters of interest. Nevertheless, it also shows that each feature is not maximally correlated with its corresponding parameter and that it is also correlated with the other parameters. There is therefore room for improvement, and we propose to test if our strategy to define numerical biomarkers can lead to a better parameter estimation.

We apply our method to a dictionary of 104 quantities computed from $V(t) + \eta$, where $\eta \sim \mathcal{N}(0, \tau)$ with $\tau = 0.5$. This corresponds to a SNR of 43 dB. The dictionary entries are the AP values at different times, the products of AP values at different times, the time derivatives, the integral over time, the PCA coefficients and the "classical" biomarkers (see Figure 4.10). The training set is generated with $N = 5 \times 10^4$ samples drawn from a uniform distribution over the hypercube $[0.5, 3]^5$. This means the conductances κ_i are allowed to vary from half to three times their

reference values. The regularization parameters are set using the L-curve criterion.

As an example, Figure 4.9 shows the resulting biomarker for parameter θ_3. Interestingly, the algorithm finds that the numerical biomarker is a correction of $\mathrm{V}_{\mathrm{notch}}$, which is indeed the biomarkers classically associated with parameter θ_3.

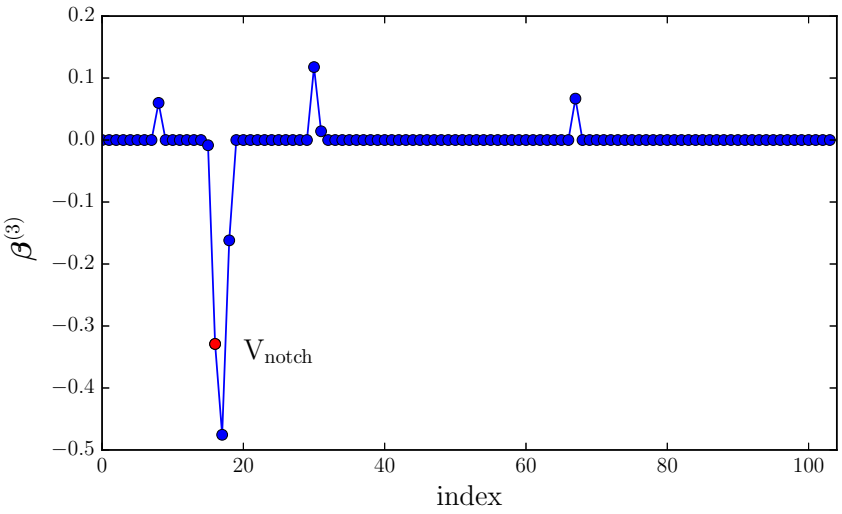

Figure 4.9: Biomarker weights $\boldsymbol{\beta}^{(3)}$ associated with θ_3. The numerical biomarker is actually a correction of the classically associated one $\mathrm{V}_{\mathrm{notch}}$.

The obtained numerical biomarkers are now used to solve parameter estimation problems. Figure 4.12 shows an example of such an inverse problem. Given a certain true value $\boldsymbol{\theta}^*$ and initial guess $\boldsymbol{\theta}^{(0)}$, both in $[0.5, 3]^5$, the parameter estimation is carried out by minimizing $J_1(\boldsymbol{\theta})$ and $J_2(\boldsymbol{\theta})$ with the gradient-free algorithm. In this specific example, minimizing J_1 fails to reach the true solution because it falls into a local minimum, whereas minimizing J_2 leads to the true solution.

We now propose to illustrate the advantage of using numerical biomarkers instead of the time series to identify parameters. Since the efficiency and the accuracy of the parameter estimation strongly depends on the initial guess and the sought values, we carry out a statistical survey: 25 samples are randomly drawn from $[0.5, 3]^5$ and an inverse problem is executed for each two-point combination. This amounts to 625 inverse problems. Each inverse problem is carried out twice by minimizing J_1 and J_2 and the estimation error is stored. Here, the estimation error is simply defined as the 2–norm between the true solution and the solution of the minimization problem. Figure 4.13 shows the histogram of estimation errors in both cases. When using the numerical biomarkers instead of the whole time series, the estimation error is in average smaller and is less spread (lower standard deviation). In the first case, the estimation error has mean 0.12 and standard deviation 0.16. In the second case, the estimation error has mean 0.44 and standard deviation 0.43.

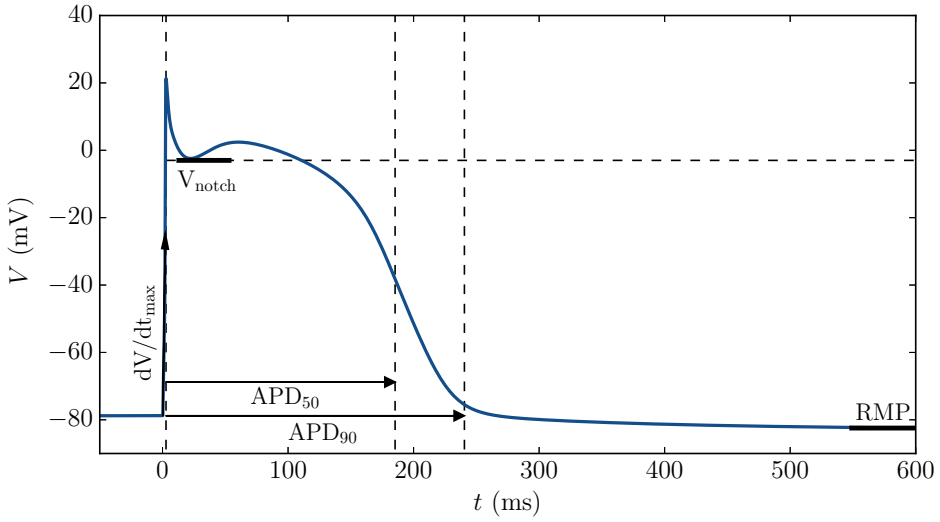

Figure 4.10: Action potential ($V(t)$) computed using the Courtemanche model. Common features associated to the parameters of interest used in the literature are also represented.

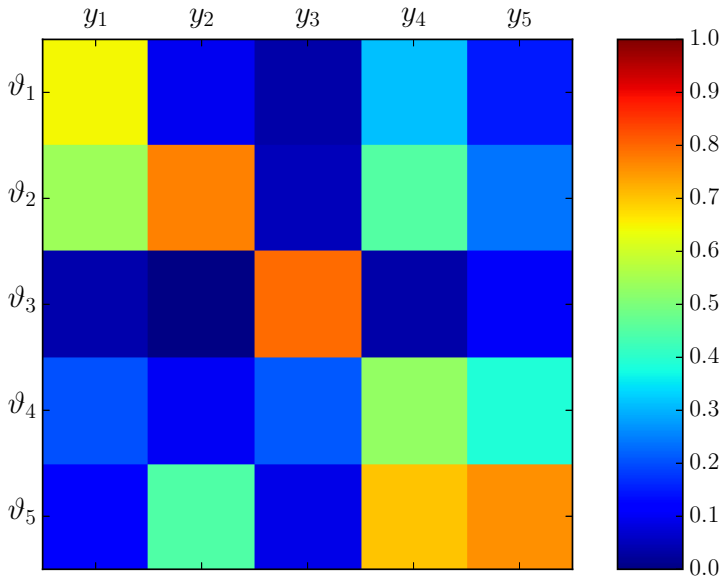

Figure 4.11: Covariance matrix between the four parameters of interest of the Davies model and their classically associated biomarkers.

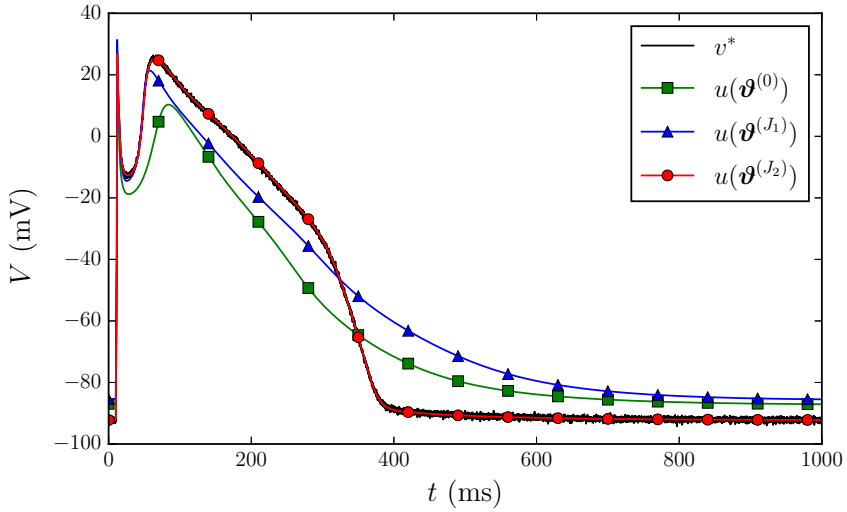

Figure 4.12: Example of a parameter estimation from a synthetic AP using the gradient-free minimization algorithm. v^* is the synthetic measurement, $\boldsymbol{\theta}^{(0)}$ the initial guess and $\boldsymbol{\theta}^{(J_1)}$ (resp. $\boldsymbol{\theta}^{(J_2)}$) the solution of the minimization of $J_1(\boldsymbol{\theta})$ (resp. $J_2(\boldsymbol{\theta})$).

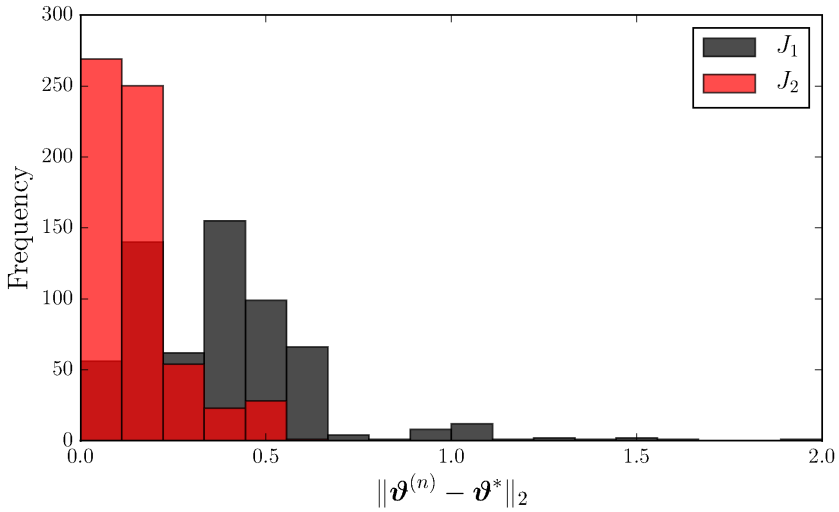

Figure 4.13: Histograms of the parameter estimation error for the 625 inverse problems carried out with both J_1 and J_2 as the inverse problem cost function.

4.4.2 A model of systemic blood flow circulation

We now present an application concerning the hemodynamics in a networks of arteries. The motivation is for example the monitoring of hypertensive patients, for which it is important to assess arteries stiffening from non-invasive measurements. The biomarker which is typically used in practice is the Pulse Wave Velocity (PWV), which is the average speed of the pressure waves travelling from carotid to femoral arteries. But arterial stiffness is not the only property affecting the PWV. Daily fluctuations of PWV can be explained as the interplay of different phenomena occurring in the cardiovascular system, such as the different metabolic need of the peripheral organs or the fluctuation in the heart rate due to physical activity. In what follows, the possibility of correcting PWV is studied, in order to have a biomarker which is more intrinsically related to arteries stiffness.

The main 55 arteries of the human body (see Figure 4.14) are considered, and the fluid-solid interaction occurring in blood vessels is described by means of a simplified 1-D model (see e.g. [FQV10, RMP+09, MAP+07]). The resulting system is a set of coupled hyperbolic partial differential equations in the unknowns (A_i, u_i), where $A_i(x,t)$ is the cross-sectional area of the i-th vessel and $u_i(x,t)$ is the sectional averaged blood velocity, $x \in [0, \ell_i]$ being the axial coordinate of the i-th vessel, $t \in \mathbb{R}^+$ being the time. The system takes the following form:

$$\partial_t A_i + \partial_x \left(A_i u_i\right) = 0, \tag{4.17}$$

$$\partial_t u_i + \partial_x \left(\frac{u_i^2}{2} + \frac{p_i}{\varrho}\right) = -\kappa \frac{u_i}{A_i}, \tag{4.18}$$

where ϱ is the blood density, κ a friction coefficient, $p_i(x,t)$ is the pressure in the vessels which is related to the cross-sectional area through the following algebraic relation: $p_i = p_0 + \beta\left(A_i^{1/2} - A_i^{(0)^{1/2}}\right)$, where β is the elastic coefficient [FQV10] and $A_i^{(0)}$ is the cross sectional area of the i-th vessel, at rest. The boundary conditions for the model are: imposed flow in the ascending aorta ($A_1(0,t)u_1(0,t) = q(t)$, that mimics the heart activity), standard three-element Windkessel models at the outlets (to account for organs and micro-circulation [MAP+07]), mass conservation and continuity of total pressure at the bifurcations. The model has been discretized and solved following [ABB+16]. The model having more than 100 free parameters, it suffers from a severe identifiability issue when using realistic data. Hence, the model has been reparametrised by introducing 8 hyper-parameters, accounting for the main source of variability in the observed data. In particular, the main goal is to be able to represent (in a simple way) the daily fluctuations of the blood flow in the network as well as the variability in the material properties of the arteries. The stiffness of the different segments has been parametrized as follows:

$$\beta_i = \theta_0 + \theta_1 \beta_i^{(ref)}, \tag{4.19}$$

where $\beta_i^{(ref)}$ is a reference elastic coefficient for the i-th vessel, available in the

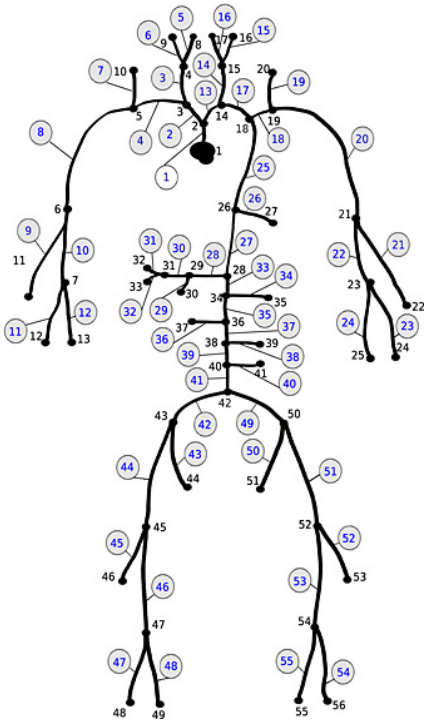

Figure 4.14: Human body hemdoynamics modeled as a network of 55 arteries.

literature [RMP+09]. The three-element Windkessel model parameters have been grouped into three sets: the first one gathers the terminal models of the upper part of the body, the second one gathers those of the central part and the last one the lumped models of the lower body. For each, the distal resistance is rescaled, and the capacitance is set in such a way that the characteristic time of the circuit remains unchanged:

$$R_{u,j} = \theta_2 R_{u,j}^{(ref)}, \quad C_{u,j} = \frac{C_{u,j}^{(ref)}}{\theta_2}, \tag{4.20}$$

$$R_{c,j} = \theta_3 R_{c,j}^{(ref)}, \quad C_{c,j} = \frac{C_{c,j}^{(ref)}}{\theta_3}, \tag{4.21}$$

$$R_{l,j} = \theta_4 R_{l,j}^{(ref)}, \quad C_{l,j} = \frac{C_{l,j}^{(ref)}}{\theta_4}. \tag{4.22}$$

Three additional parameters account for variations in the cardiac output and cardiac rhythm:

$$q(t) = \begin{cases} \theta_5 \sin\left(\frac{\pi}{\theta_6 T_s} t\right) & 0 \leq t \leq \theta_6 T_s \\ 0 & \theta_6 < t \leq \theta_7 T \end{cases}, \tag{4.23}$$

where $T_s = 0.25$s is the systolic period and $T = 0.8$s is a reference cardiac period.

The training set is generated by drawing $N = 1024$ samples of $\boldsymbol{\theta}$ from the normal

distribution $\mathcal{N}(\mu, \Sigma)$, where $\boldsymbol{\mu} = (0, 1, 1, 1, 1, 1, 1, 1)$ and $\boldsymbol{\Sigma} = 0.05^2 \times \mathbf{I}_8$. The flow and pressure signals are computed by integrating the model for these samples. With the variability considered, the fluctuations in terms of pressure and flow are about 20%, which is enough to cover meaningful scenarios of daily fluctuations.

The dictionary is built as follows. In three distinct locations – the carotid, the subclavian artery and the femoral artery – average in time, maximum and minimum value of pressure, flow, and mechanical power $w = pQ$ are taken. The last three elements of the dictionary are PWV taken from carotid to femoral, from carotid to subclavian and from subclavian to femoral. The dictionary is ordered as follows:

$$g = (Q_0, \ldots, Q_8, p_0, \ldots, p_8, w_0, \ldots, w_8, PWV_0, PWV_1, PWV_2).$$

The method is used with $\lambda_h = 10^{-3}$, $\forall h$.

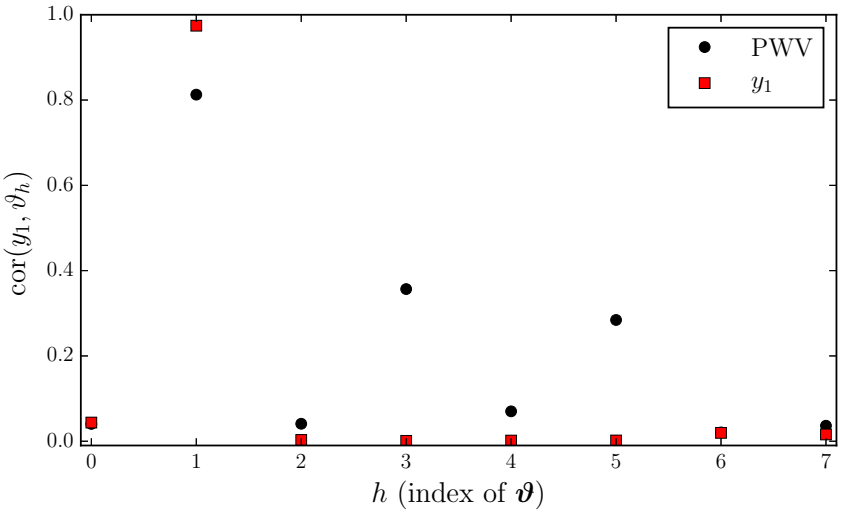

Figure 4.15: Correlation ($cor(y_1, \theta_i)$) of the biomarker related to θ_1 and all the parameters, when considering PWV, and the numerically corrected biomarker.

In Fig.4.15, the red squares (resp. the black dots) show the correlation coefficients between the biomarker y_1 provided by our algorithm (resp. the PWV) and each of the 9 parameters. The PWV is significantly correlated to θ_1, which is not a surprise since the arterial stiffness is known to be linked to the PWV. But the PWV also has a significant correlation (of about $0.3 - 0.4$) with the peripheral resistances of the central body and with the cardiac output. This provides a possible explanation for the observed daily fluctuations of the PWV. On the contrary, the biomarker y_1 provided by our method has a higher correlation with respect to θ_1 and a negligible correlation with respect to all the other parameters.

Interestingly, the decomposition of the biomarker onto the dictionary sheds some light onto the physical interpretation of the correction. In Fig.4.16 the expression of $\boldsymbol{\beta}^{(1)}$ is shown. We can observe that it is sparse. As expected, the PWV from carotid to subclavian is selected. Then, the correction is provided by a combination

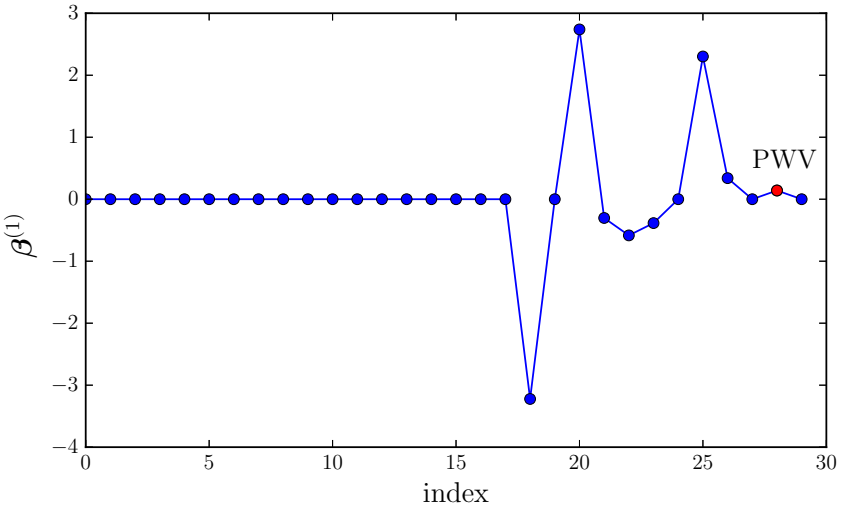

Figure 4.16: Biomarker expression on the dictionary, for y_1

of the mechanical power. It is remarkable that the relevant quantity proves to be the product of the flow and the pressure, but not the flow and the pressure separately.

In conclusion, if we are interested in estimating the arterial stiffness, the algorithm suggests that it could be more relevant to consider a combination of PWV and mechanical power rather than just the PWV. This result is preliminary and would require a deeper investigation. Nevertheless, it shows an example of possible applications of the proposed method to correct the expression of standard biomarkers used in hemodynamics.

4.4.3 Application to synthetic MEA measurements

Finally, we slightly anticipate the next chapter and present an application of the method to micro-electrode array (MEA) measurements. The objective of this test case is to show that using numerical biomarkers may improve the PDF estimation of some parameters of the MEA model when using the observable moment matching method (OMM, see Chapter 2). To simulate the MEA measurements, we use the same procedure as described in 5.2 and the uncertain parameters considered here are $(\theta_1, \theta_2, \theta_3) := (g_{fi}, g_{so}, g_{si})$.
The observable is defined as the field potential measured at the first electrode of the MEA at 1200 time steps ($N_{\mathbf{x}}$=1200). The synthetic data set is generated by evaluating the model for $N = 2048$ samples of $(\theta_1, \theta_2, \theta_3)$.
(θ_2, θ_3) are mutually dependent and drawn from the bivariate Gaussian mixture $\mathcal{N}(\boldsymbol{\mu}_1, \sigma^2\mathbf{I}_2) + \mathcal{N}(\boldsymbol{\mu}_2, \sigma^2\mathbf{I}_2)$, where

$$\boldsymbol{\mu}_1 = (1, 1), \quad \boldsymbol{\mu}_2 = (0.7, 1.2), \quad \sigma = 0.05.$$

θ_1 is indenpendent of θ_2 and θ_3 and is drawn from a normal distribution $\mathcal{N}(1, \sigma^2)$.
The simulation set is generated by evaluating the model for $N_c = 4096$ collocation

points using the Sobol sequence for the parameter domain $\Theta = [0.4, 1.2] \times [0.5, 1.5]^2$.

4.4.3.1 Observable moment matching with the whole signal

Following the same procedure as the one presented in Chapter 2, we try to estimate the PDF of $(\theta_1, \theta_2, \theta_3)$ given the set of synthetic measurements. The inverse procedure described in Chapter 2. The number of moments to be matched is set to $N_m = 4$ and the tolerance parameter to $\alpha = 10^{-3}$. Convergence is reached at $n_{\text{iter}} = 3$ and $N_k = 44$.

4.4.3.2 Observable moment matching with the numerical biomarkers

The numerical biomarker procedure is applied to our test case using the simulation set (of the OMM method) as the training set. Using $\lambda_1 = \lambda_2 = \lambda_3 = 0.1$ as the ℓ^1 penalization parameters, we obtain three numerical biomarkers which are used as the observable quantities in the OMM method. We denote by y_1 (resp. y_2, y_3) the numerical biomarker associated with θ_1 (resp. θ_2, θ_3). By construction, the numerical biomarkers are minimally correlated with all the parameters except for the one it is associated with. For instance, y_1 contains almost no information about θ_2. To capture the dependence structure between the parameters, we use pairwise products of the biomarkers in the same spirit as what is done in 3.2.2.4. More precisely, we use the following 15 quantities whose expectations are to be matched:

$$y_1,\ y_2,\ y_3,\ y_1^2,\ y_2^2,\ y_3^2,\ y_1y_2,\ y_1y_3,\ y_2y_3,\ y_2^3,\ y_3^3,\ y_2^2y_3,\ y_3^2y_2,\ y_2^4,\ y_3^4 \tag{4.24}$$

4.4.3.3 Results

We now compare the two strategies by analyzing the results. In Table 4.2 are shown the estimated moments of the parameters. In Figure 4.17, we show the estimated PDF in both cases, to be compared with the actual parameters samples used to generate the synthetic measurements. Because we are in dimension 3, it is not possible to directly visualize the PDF. Since the interesting point in this example is the dependence structure between θ_2 and θ_3, we choose to observe the PDF in a cuboid of the parameter space defined by $0.9 \leq \theta_1 \leq 1.1$. With the whole signal, the OMM method does capture the dependence but fails to approximate properly the PDF. This is also visible with the large errors made on the parameters moments approximations in Table 4.2. Using the numerical biomarkers however, the PDF is remarkably well approximated with the two modes of the Gaussian mixture clearly visible and properly located. This is consistent with the relatively low errors made on the parameters moments approximations in Table 4.2.

4.5 Conclusions and Perspectives

In this work a method is proposed to define numerical biomarkers. A semi-empirical approach is used, that consists in building a database of simulations and

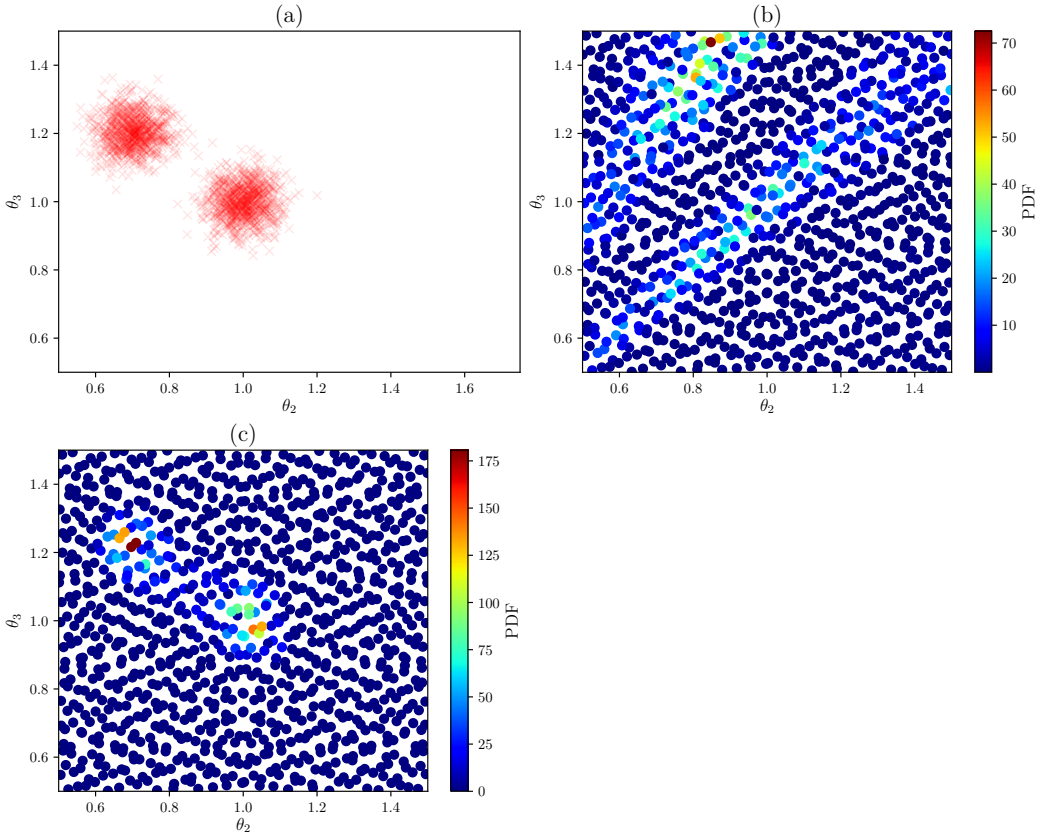

Figure 4.17: Point-wise visualization of the estimated PDF using the observable moment matching method. The visualization is made in a cuboid of the parameter space defined by $0.9 \leq \theta_1 \leq 1.1$ to observe the (θ_2,θ_3) dependence.
(a): parameters samples used to generate the synthetic measurements. (b): estimated PDF using the whole signal. (c): estimated PDF using the numerical biomarkers.

Observable	whole signal			numerical biomarkers			**true parameters**		
Parameter	μ_1	μ_2	μ_3	μ_1	μ_2	μ_3	$\boldsymbol{\mu_1}$	$\boldsymbol{\mu_2}$	$\boldsymbol{\mu_3}$
g_{fi}	1.00	1.00	1.01	1.03	1.06	1.10	**1.00**	**1.00**	**1.01**
g_{so}	0.90	0.87	0.91	0.86	0.76	0.70	**0.85**	**0.75**	**0.68**
g_{si}	1.14	1.36	1.68	1.11	1.24	1.40	**1.10**	**1.22**	**1.38**

Table 4.2: OMM results: statistics summary of the estimated parameters of the MEA model using the whole signal as the observable and using the numerical biomarkers.

exploiting the results in order to define biomarkers which are maximally correlated to the parameters they are meant to monitor and minimally correlated with respect to all the others. Such an objective is translated into an optimization problem and the biomarkers are sought as the solution of its discretized version. The biomarkers are, by construction, linear combinations of dictionary entries that comprise relevant features found in the literature and additional quantities computed from the observable signal. Furthermore, a sparsity-promoting penalization ensures that the obtained biomarker representation on the dictionary entries are sparse and, often, easily interpretable. As a by-product, a metric in the space of the observable is obtained which is equivalent, up to a small perturbation, to the $2-$distance in the space of parameters. The method can be exploited in order to enhance the robustness of the biomarkers which are used in biology and medicine by using numerical simulations. Furthermore, it can be used to regularize inverse problems and make them less ill-conditioned.

We propose three realistic scenarios in biology: two in electrophysiology and one in hemodynamics. In the first example, we show that using the numerical biomarkers makes the inverse problems associated with parameter estimation easier to solve. In the second example, we propose a numerical biomarker associated to monitor arterial stiffness that is independent other quantities that naturally fluctuate. In the last example, we propose numerical biomarkers associated with MEA measurements that improve the PDF estimation carried out using the OMM method (see Chapter 2).

Chapter 5

Optimal Biomarkers Design for Drug Safety Evaluation Using Microelectrode Array Measurements

---

This chapter is based on [TRLG17]

The Micro-Electrode Array device enables high-throughput electrophysiology measurements that are less labour-intensive than patch-clamp based techniques. Combined with human-induced pluripotent stem cells (hiPSC), it represents a new and promising paradigm for automated and accurate in-vitro drug safety evaluation. In this chapter, the following question is addressed: which features of the MEA signals should be measured to better classify the effects of drugs? A framework for the classification of drugs using MEA measurements is proposed. It relies on an in silico electrophysiology model of the MEA, a feature selection algorithm and automatic classification tools. An in silico model of the MEA is developed and is used to generate synthetic measurements. An algorithm that extracts MEA measurements features designed to perform well in a classification context is described. These features are called numerical biomarkers. A state-of-the-art machine learning program is used to carry out the classification of drugs using MEA measurements. We show that the numerical biomarkers outperform the classical ones in different classification scenarios. We show that using both synthetic and experimental MEA measurements improves the robustness of the numerical biomarkers and that the classification scores are increased.

Contents

5.1 Introduction 121
5.2 Methods 122
5.2.1 Equations 122
5.2.2 Biomarkers 125
5.2.3 Experimental data set 128
5.2.4 Classification 129
5.3 Results 130
5.3.1 Comparison between classical and numerical biomarkers . . . 130
5.3.2 Using combined experimental and synthetic measurements for the numerical biomarkers computation 131
5.4 Discussion 132
5.5 Tables and Figures 135
5.6 Supplementary Material 142
5.6.1 Imperfect electrode model 142
5.6.2 Biomarker computation 142
5.6.3 Classification metrics 143

5.1 Introduction

One of the main goals of safety pharmacology studies is to anticipate the effect of drugs on cardiomyocytes. Among other adverse effects, it focuses on predicting arrhythmic behaviors which may lead to torsades de pointes (TdP). The most common risk factors under consideration are QT prolongation and hERG block. However these risk factors are now considered insufficient and the guidelines need to be improved. Several advances in technology and computational modeling may favor the emergence of new methods for more efficient drug safety evaluation. On the hardware side, the Micro-Electrode Array (MEA) technology [Sys , MBGF04] enables high-throughput electrophysiology measurements that are less labour-intensive than patch-clamp based techniques. On the biological side, the use of human-induced pluripotent stem cells (hiPSC) has developed [SPD13] and their recent large-scale production makes it a viable human model replacement. The combined use of the MEA technology and hiPSC represents a new and promising paradigm for automated and accurate in-vitro drug safety evaluation [CT14, CGB+16]. In parallel of these technological breakthroughs, several efforts have been recently made towards promoting the use of computational tools in drug safety evaluation [DWM+16, LS16]. In this context, a framework for drug safety evaluation using *in silico* models and experimental measurements using a MEA device is hereby presented.

The framework aims at predicting the effect of a drug onto the cardiomyocytes ionic channels activities from the knowledge of MEA experimental recordings. More precisely, the goal is to determine which ionic channels are affected by a given drug. The approach is based on an *in silico* model of the MEA and the cardiomyocytes tissue, a feature selection algorithm and a classification model. The *in silico* model is based on a simple ionic model [BOCF08] for the cardiomyocytes electrical activity and on the bidomain equations [Tun78] for the spatial propagation of the electrical potentials. The ionic model counts three different currents (fast inward, slow inward, slow outward), each being associated with an ionic species (respectively sodium, calcium, potassium). The activity of each current is controlled by a scaling parameter that is referred to as conductance in the following. In the present work, the drugs considered are assumed to affect one of these currents. Thus, the inactivation of a current caused by a drug is modeled by a diminution of the corresponding conductance in the ionic model. The conductances and some other parameters of the model can be varied in order to replicate the variability observed in the experimental measurements. The *in silico* model is used to generate what is later referred to as synthetic MEA measurements. The experimental data set itself consists of MEA electrode recordings which come in the form of time series. Each recording is done in control conditions (no drug) and with different drug concentrations levels. The experimental data is also labelled, meaning the affected ionic channels are known for each drug.

As explained above, the MEA measurements, whether synthetic or experimental, come in the form of time series. For classification purposes, it is more efficient to

extract features from these time series. Some features, also called biomarkers, are already widely used in the community such as the field potential duration which may be associated with the QT segment in ECGs. These common features are referred to as classical biomarkers. We propose a way to automatically extract features from the MEA measurements that are designed to perform well in a classification context. These new features, referred to as numerical biomarkers in the following, are defined as linear combinations of dictionary entries whose weights are solution of a sparse optimization problem. The weights are computed using MEA features coming from experimental measurements, synthetic ones or a composite set of both. To predict the effect of drugs, the idea developed in this work is to train a classification model, or classifier, to associate MEA measurements with a type of affected ionic channel, or label. Then, the classifier is tested with new MEA measurements for which it predicts labels. Provided that the true labels are known, it is possible to measure the precision of the classification and therefore evaluate a given classifier. In the present work, a state-of-the-art machine learning classification tool, Support Vector Classification (SVC), is used.
The paper is organized as follows. First, the methods are described. The *in silico* model is presented and the generation of synthetic data is explained. The algorithm that computes the numerical biomarkers is described and the classification tools are presented. Second, the performance of the numerical biomarkers and of the classification tools are studied in different drug classification scenarios. The numerical biomarkers are compared to the classical ones using two different classification strategies. Finally, numerical biomarkers computed with experimental data only and with a composite set of experimental and synthetic data are compared.

5.2 Methods

5.2.1 Equations

5.2.1.1 Bidomain equations and ionic model

Let Ω be the domain representing a MEA's well. The thickness of the layer of cells being small compared to the size of the well, the problem is assumed to be two-dimensional. The activation is assumed to be triggered by a current I_{app} that is applied in an arbitrary region of the well. We denote by A_{m}, C_{m}, z_{thick} the surface area of membrane per unit volume of tissue, the membrane capacitance, and the thickness of the cell layer, respectively. The intra and extra-cellular conductivity tensors σ_{i} and σ_{e} are assumed to be scalar. The propagation of the transmembrane potential V_{m} and the extracellular potential ϕ_{e} are modeled in Ω with the bidomain model [Tun78]:

$$\begin{cases} A_{\text{m}}C_{\text{m}}\dfrac{\partial V_{\text{m}}}{\partial t} + A_{\text{m}}I_{\text{ion}}(V_m, w) - \nabla\cdot(\sigma_{\text{i}}\nabla V_{\text{m}}) - \nabla\cdot(\sigma_{\text{i}}\nabla\phi_{\text{e}}) = A_{\text{m}}I_{\text{app}}, \\ -\nabla\cdot((\sigma_{\text{i}}+\sigma_{\text{e}})\nabla\phi_{\text{e}}) - \nabla\cdot(\sigma_{\text{i}}\nabla V_{\text{m}}) = \frac{1}{z_{thick}}\displaystyle\sum_{e_k}\frac{I_{\text{el}}^k}{|e_k|}\chi_{e_k}. \end{cases} \tag{5.1}$$

In the second equation, I_{el}^k is the electric current which goes through the electrode located at e_k, $|e_k|$ is the electrode surface and χ_{e_k} is the characteristic function of e_k (which takes the value 1 on the electrode and 0 elsewhere). An imperfect model for the electrode is used to compute I_{el}^k and described in the Supplementary Material. Let $\boldsymbol{n}$ be the outward normal to the boundary of the domain Ω. Equations (5.1) are completed with the following boundary conditions: $\sigma_{\text{i}} \nabla \phi_{\text{i}} \cdot \boldsymbol{n} = 0$ (where $\phi_{\text{i}} = V_{\text{m}} + \phi_{\text{e}}$), and either $\phi_e = 0$ on the region connected to the ground or $\sigma_{\text{e}} \nabla \phi_{\text{e}} \cdot \boldsymbol{n} = 0$ elsewhere.

The transmembrane ionic current I_{ion} is described with the Minimal Ventricular (MV) model [BOCF08] which includes three currents: fast inward (fi), slow inward (si) and outward (so) currents. The reader is referred to the original publications for more details. Schematically, I_{ion} depends on V_{m} and on gating variables $w = (w_j)_{1 \leq j \leq 3}$, solution of a system of three nonlinear ordinary differential equations. A conductance coefficient g_s, with $s = fi, so$ or si, controls the activity of the idealized channels associated with each of three currents of the model.

The partial differential equations are discretized in space by means of P1 finite elements, and in time by using backward differentiation formula (BDF) schemes with adaptive time steps and order provided by the Sundials library [HBG+05]. The quantity of interest is the extra-cellular potentiel, also referred to as field potential (FP). It is a function of time and recorded at the electrodes locations.

Synthetic measurements In the present work, the computational model is used to generate synthetic MEA measurements. For a given set of conductances, the model is evaluated and the electrodes FPs are recorded. The conductances are chosen as to represent meaningful scenarios, as explained later in the Results section. To mimic experimental measurements, a zero-mean Gaussian noise of standard deviation 10 μV is added to the FPs (see Figure 5.3). A heterogeneity model of some ionic parameters is also considered to replicate the variability exhibited by the experimental measurements. This model is described later in this section.

Steady-state regime Because the initial conditions of the ionic model do not correspond to those of a steady-state regime, several beats may need to be simulated before reaching a regime where there is negligible beat-to-beat variations. A numerical experiment was carried out to determine when this regime is reached. Figure 5.2 shows super-imposed consecutive simulated FPs and the normalized beat-to-beat variations in the FP. When considering noisy synthetic measurements as described above, the steady-state is assumed to be reached when the beat-to-beat variations is comparable to variations induced by noise only. The beat-to-beat variability observed after this beat may be imputed to the coarseness of the mesh, the time discretization errors and the fluctuations of the ionic model itself. In the present work, the steady-state is assumed to be reached at the second beat. Therefore, the simulations are run for two cardiac cycles and the second beat is recorded to be used as a synthetic measurement.

5.2.1.2 Drug modeling

We chose to model the action of drugs on the ion channels by the conductance-block formulation of the pore block model [MCS+11, ZBS+13, BPS+06]. This simple approach, which relies on a small number of parameters, was shown in [ABC+17] to be able to reproduce the expected effects of several drugs on MEA signals. The conductance of a given channel s is given by:

$$g_s = g_{control,s}\left[1 + \left(\frac{[D]}{IC_{50}}\right)^n\right]^{-1}, \tag{5.2}$$

where $g_{control,s}$ is the drug-free maximal conductance, $[D]$ is the drug concentration, IC_{50} is the value of the drug concentration at which the peak current is reduced of 50%, n is the Hill coefficient. In this work, n will be assumed to be equal to 1.

5.2.1.3 Heterogeneity modeling

A typical experimental MEA FP measurement exhibits both a depolarization spike and a repolarization wave (see Figure 5.3). Using the computational model described above, the repolarization wave is usually too small compared to what is observed in experiments. As noted in [ABC+17], the repolarization wave provided by this model is larger when the domain includes cells with different APDs. In [ABC+17], the cell heterogeneity was defined on a checkerboard arbitrarily chosen in the MEA's well. We propose here a different approach, based on a probabilistic description of the heterogeneity. The tissue is supposed to be a continuous mixture characterized by a space dependent coefficient:

$$\theta_w(x,y) = (1 - c(x,y))\theta_w^{(A)} + c(x,y)\theta_w^{(B)}, \tag{5.3}$$

where c is a random process with values in $[0,1]$, $\theta_w^{(A)}$ and $\theta_w^{(B)}$ are coefficients of the MV model characterizing two kinds of cells, called "type A" and "type B". In our simulations, we took $\theta_w^{(A)} = 0.1$, $\theta_w^{(B)} = 0.8$. The AP corresponding to different homogeneous realizations of c is shown in Figure 5.4. We make the hypothesis that the spatial variations of c are structured by a normal correlation function f_c:

$$f_c\left[\begin{pmatrix}x\\y\end{pmatrix}, \begin{pmatrix}x'\\y'\end{pmatrix}\right] = \exp\left[-\frac{(x-x')^2 + (y-y')^2}{2l_c^2}\right], \tag{5.4}$$

where l_c is the correlation length, set to $l_c = 0.25$ mm in the present work. To discretize the random process c, we compute the correlation matrix on the finite element mesh used for the discretization of the bidomain equations. The correlation matrix $\mathbf{C} = [C_{i,j}] \in \mathbb{R}^{N_{\text{mesh}} \times N_{\text{mesh}}}$ reads:

$$C_{i,j} = f_c\left[\begin{pmatrix}\hat{x}_i\\\hat{y}_i\end{pmatrix}, \begin{pmatrix}\hat{x}_j\\\hat{y}_j\end{pmatrix}\right], \tag{5.5}$$

where N_{mesh} is the total number of mesh nodes and $(\hat{x}_i, \hat{y}_i)$ are the coordinates of the i^{th} node. The eigenpairs of $\mathbf{C}$ are denoted by (λ_i, Φ_i), and ordered by decreasing order of the eigenvalues λ_i. By a convenient abuse of notation, we denote by $(\hat{x}, \hat{y}) \to \Phi_i(\hat{x}, \hat{y})$ the function of the finite element space associated with the eigenmode Φ_i. Finally, the discretized heterogeneity field is approximated by the following truncated expansion:

$$c(\hat{x}, \hat{y}, \boldsymbol{\xi}) = \sum_{i=1}^{n_c} \xi_i \Phi_i(\hat{x}, \hat{y}) \tag{5.6}$$

where $\boldsymbol{\xi} = (\xi_i)_{i=1\dots n_c}$ is a random vector and n_c a truncation index chosen so that the truncation explains at least 99% of the variance. In other words, n_c is the smallest index n such that the following criterion is verified:

$$\frac{\sum_{i=1}^{n} \lambda_i}{\sum_{i=1}^{N_{\text{mesh}}} \lambda_i} > 0.99 \ . \tag{5.7}$$

Heterogeneity fields can now be generated simply by sampling the random variable $\boldsymbol{\xi}$. In the present work, $N_h = 128$ heterogeneity fields were generated by sampling $\boldsymbol{\xi}$ from an uncorrelated uniform distribution over $[-1, 1]^{n_c}$, and each sample is rescaled to range between 0 and 1. An example of heterogeneity field is presented in Figure 5.5.

5.2.2 Biomarkers

Biomarkers may be defined as quantities extracted from a signal that convey information about hidden quantities of interest. In our case, the biomarkers are features extracted from the MEA FP which would ideally provide information about the conductances of interest: g_{fi}, g_{so}, g_{si}. In this section, we present different choices of biomarkers to be used in a classification context.

5.2.2.1 "Classical" biomarkers

The MEA FP can be split into two regions of interest: the depolarization and the repolarization. The depolarization observed at one electrode corresponds to the local depolarization of the cardiomyocytes. The depolarization amplitude (DA) may be qualitatively linked to the AP upstroke velocity. This biomarker is commonly associated with the activity of the fast sodium channel (g_{fi} for the MV model). The repolarization amplitude (RA) may be qualitatively linked to some extent to the AP repolarization slope and to a bigger extent to spatial heterogeneities in AP durations. Once the depolarization and repolarization have been detected, it is possible to measure the FP duration (FPD), simply as the difference between the repolarization and depolarization times. Both biomarkers RA and FPD are associated with the activity of the potassium and calcium currents (g_{so} and g_{si} in the MV model). In Figure 5.3, a sample of FP with the corresponding classical biomarkers is shown. As explained above, each (real or numerical) experiment is performed both in a

drug-block condition and in control condition. Because of the significant variability of measurements in MEA, it is important to consider the variations observed in the FP in drug block conditions with respect to the control conditions to isolate the effect of the drug from other sources of variability: tissue variability, stimulation protocol, *etc.* Therefore, as proposed in [RBZ+17], the features of interest are the biomarkers in drug block condition divided by the biomarkers in control conditions. For instance, the depolarization amplitude is actually the following ratio:

$$\mathrm{DA}_{\mathrm{ratio}} = \frac{\mathrm{DA}_{\mathrm{drug}}}{\mathrm{DA}_{\mathrm{control}}} \tag{5.8}$$

For the sake of clarity in the notation, the subscript "ratio" is omitted in the following and any biomarker actually refers to a ratio with the control value. For each MEA measurement, the FP is recorded at each of the nine electrodes. Again, the important variability in the measurements motivates the use of robust features. Since the behavior of the FP may greatly vary from one electrode to another, the median of the biomarkers over all electrodes is in practice a good choice of features. In the following, the set of biomarkers $\{\tilde{\mathrm{DA}}, \tilde{\mathrm{RA}}, \tilde{\mathrm{FPD}}\}$ is referred to as the classical biomarkers, where the $\tilde{}$ operator denotes the median over all nine electrodes.

5.2.2.2 Numerical biomarkers

The rationale behind the choice of biomarkers described above is only qualitative and oftentimes does not represent the best set of features in a classification context. Here, we adopt a more automatic strategy to select the best set of biomarkers for a given experimental scenario, as described in Chapter 4. First, the set of features to be extracted from a given FP is enriched to build a dictionary of features. It is indeed possible to extract additional quantities from the FP other than DA, RA and FPD. We propose to compute also, for each electrode of the MEA, the following features: the area under curve of the repolarization wave (AUCr), the repolarization center (RC), the repolarization width (RW) and the FP notch (FPN). The details on how to compute these additional biomarkers are described in the Supplementary Material. Ratios of these quantities are also added to the dictionary of features: RA/DA, DA/RA, RA/FPD, FPD/RA, DA/FPD, FPD/DA, RA/RW, RW/RA. Each feature is actually a ratio with its control counterpart as described in (5.8). To include the information of all nine electrodes, the median (denoted by the $\tilde{}$ operator), mean (denoted by the $<>$ operator) and maximum values (denoted by a max subscript) over the electrodes are retained in the dictionary. This amounts to a total of $N_b = 38$ dictionary entries.

The purpose of the method described below is to associate each conductance with a numerical biomarker obtained by weighting the entries of the dictionary of features. The weights of such a combination are solution of an optimization problem. First, let us introduce some notation.

We denote by y_1 (resp. y_2, y_3) the numerical biomarker (to be determined) associated with g_{fi} (resp. g_{so}, g_{si}). From now on, the conductances (g_{fi}, g_{so}, g_{si})

are denoted by $\boldsymbol{\theta} = (\theta_1, \theta_2, \theta_3)$. Each dictionary entry is considered as a function of $\boldsymbol{\theta}$. The numerical biomarkers are sought as a linear combination of the dictionary entries:

$$y_h(\boldsymbol{\theta}) = \sum_{j=1}^{N_b} w_j^{(h)} b_j(\boldsymbol{\theta}), \quad 1 \leq h \leq 3, \tag{5.9}$$

where the weights $\boldsymbol{w}^{(h)} = (w_j^{(h)}) \in \mathbb{R}^{N_b}$ are the unknowns of the problem. These weights are sought so that $y_h(\boldsymbol{\theta})$ is maximally correlated with θ_h and minimally correlated with θ_k, $\forall k \neq h$. This may be stated as follows:

$$\forall h \in \{1, \ldots, 3\}, \quad \begin{cases} \max\limits_{y_h} & \operatorname{cov}\left(y_h(\boldsymbol{\theta}), \theta_h\right) & \text{(5.10a)} \\ \min\limits_{y_h} & \left|\operatorname{cov}\left(y_h(\boldsymbol{\theta}), \theta_k\right)\right|, \quad \forall k \neq h & \text{(5.10b)} \\ \text{s.t.} & \operatorname{var}\left(y_h(\boldsymbol{\theta})\right) = 1 & \text{(5.10c)} \end{cases}$$

where $\operatorname{cov}(\cdot, \cdot)$ and $\operatorname{var}(\cdot)$ are respectively the covariance and variance operators. In the following, we assume that each component of $\boldsymbol{\theta}$ is a zero-mean unit-variance random variable. This is achieved in practice by a simple rescaling of the conductances samples. We also adopt the following notation:

$$\tilde{b}_j(\boldsymbol{\theta}) = b_j(\boldsymbol{\theta}) - \mathbb{E}\left[b_j(\boldsymbol{\theta})\right], \tag{5.11}$$

where $\mathbb{E}[\cdot]$ is the expectation operator. The problem may now be recast into an optimization problem where the cost function to be minimized reads:

$$\mathcal{J}(\boldsymbol{w}^{(h)}) = \mathcal{J}_C(\boldsymbol{w}^{(h)}) + \mathcal{J}_N(\boldsymbol{w}^{(h)}) + \mathcal{J}_P(\boldsymbol{w}^{(h)}), \tag{5.12}$$

where

$$\mathcal{J}_C(\boldsymbol{w}^{(h)}) = \frac{1}{2}\|\mathbf{C}\boldsymbol{w}^{(h)} - \mathbf{e}^{(h)}\|^2 \quad \text{where} \quad C_{kj} := \mathbb{E}(\theta_k \tilde{b}_j),\ e_k^{(h)} := \delta_{kh}, \tag{5.13a}$$

$$\mathcal{J}_N(\boldsymbol{w}^{(h)}) = \frac{\xi}{2}\left(\boldsymbol{w}^{(h)T}\mathbf{G}\boldsymbol{w}^{(h)} - 1\right)^2 \quad \text{where} \quad G_{ij} := \mathbb{E}(\tilde{b}_i \tilde{b}_j), \tag{5.13b}$$

$$\mathcal{J}_P(\boldsymbol{w}^{(h)}) = \frac{\lambda_h}{N_g}\|\boldsymbol{w}^{(h)}\|_1. \tag{5.13c}$$

Let us now explain each term of (5.13). $\mathcal{J}_C(\boldsymbol{w}^{(h)})$ corresponds to (5.10a) and (5.10b). It measures the discrepancy to the situation where $\operatorname{cov}\left(y_h(\boldsymbol{\theta}), \theta_h\right) = 1$ and $\operatorname{cov}\left(y_h(\boldsymbol{\theta}), \theta_k\right) = 0$, $\forall k \neq h$.
$\mathcal{J}_N(\boldsymbol{w}^{(h)})$ is a relaxation of the constraint in (5.10c). ξ is a regularization parameter that is set to 1 in practice.
$\mathcal{J}_P(\boldsymbol{w}^{(h)})$ is a regularization term by penalization of the 1–norm of $\boldsymbol{w}^{(h)}$. ℓ_1 penalized cost functions tend to promote sparse solutions [Tib96]. Sparse solutions for $\boldsymbol{w}^{(h)}$ are interesting in that they offer a more interpretable decomposition onto the dictionary entries (since most weights are zero) than what an ℓ_2 penalization would

yield.

We now discretize the problem by considering N samples of the parameters $\boldsymbol{\theta}$ drawn over a parameter space $\Theta \subset \mathbb{R}^3$. The expectation operator is approximated using a quasi-Monte-Carlo quadrature rule and the cost function in (5.12) is minimized using a Nesterov accelerated gradient descent [OC15]. The Monte-Carlo samples may come from synthetic or experimental measurements. For synthetic measurements, the conductances are known, but this is not the case for experimental measurements. In that case, an approximation of these conductances is computed using Equation (5.2). Note that the solution weights depend strongly on the choice of samples used for the Monte-Carlo approximations.

An example of the obtained weights is shown in Figure 5.7. Interestingly, the classical biomarkers are still among the most weighted features. The correlation between the conductances of interest and the numerical biomarkers is compared to the correlation with the classical biomarkers in Figure 5.8. The correlation between two quantities u and v is defined as follows:

$$\mathrm{cor}(u, v) = \frac{\mathrm{cov}(u, v)}{\sqrt{\mathrm{var}(u)\mathrm{var}(v)}}. \tag{5.14}$$

As expected, each numerical biomarker is well correlated with its associated conductance whereas uncorrelated with the others. This is not the case for the classical biomarkers. The results in the next section show that such a choice of features improves the classification performance.

5.2.3 Experimental data set

The MEA considered in the present work is a 6-well MEA with nine electrodes per well. Its geometry as well as the corresponding finite element mesh is shown in Figure 5.1. The MEA measurements come in the form of FP recordings corresponding to the different electrodes of the different wells of the MEA.The MEA used is a 6-well MEA with nine electrodes per well. These recordings come in the form of time series where several cardiac cycles, or beats, are recorded. We extracted several beats on each electrode from each well of the MEA. Data were provided by Janssen Pharmaceutica NV using MC_Rack (Multi Channel Systems GmbH) and post-processed by NOTOCORD Systems (NOTOCORD-FPS 3.0 software). Cells cultures were developped by the CDI company (iCell Cardiomyocytes). As explained earlier the recordings were made in control conditions (no drug) and with different drugs at different concentrations levels. The drugs used for the present study are summarized in Table 5.2. Note that the diltiazem was recorded in two different wells (A and B) to compensate the scarcity of calcium-antagonist drugs. The experimental process consists in adding five times a compound at increasing concentrations in a given well. Thus, including the control condition record, we finally obtain field potentials for six contexts in each well. Equation (5.2) was used to obtain an approximation of the conductances values associated with the experimental measurements which are needed for the numerical biomarkers calculations. The Hill

coefficients and IC_{50} values are given in the Supplementary Material of [KOPM+13] and in [MCS+11]. Concerning the dictionary of features, a few adjustments need to be made in some cases. Indeed, it appears that at some high concentration levels of mexiletine, there is simply no action potential (because the sodium channels are too blocked) and therefore the field potential is a flat line. To take this into account, the values of dictionary entries are set to the ones at the last concentration where an action potential was observed. In addition, all features where DA is in the numerator position in a ratio are set to zero for this concentration.

5.2.4 Classification

5.2.4.1 Support Vector Classification

Support vector classification [BGV92] (SVC) is an adaptation of the support vector machine (SVM) method in a classification setting. Classification generally consists in attributing labels to inputs. The available data set, comprising both inputs and labels, is generally split into a training set used to build the classifier and a validation set to test the classifier. The inputs are often multi-dimensional and in our case correspond to the biomarkers, whether classical or numerical. The labels are integers that represent the classes to which the inputs are assigned. These classes are mutually exclusive, meaning one sample can only belong to a single class. SVC belongs to the so-called supervised methods since the labels are known, at least for the training set. The main idea behind SVC is to maximize the margin between the inputs and the decision boundary [BGV92]. In the linear case, the decision boundary is a hyperplane of the input space. In general however, this is not sufficient to properly separate the samples according to their classes. A common way to obtain more complex boundary decisions is to use a so-called "kernel trick" [SS02] which is based on a mapping from the input space to a higher-dimensional space where the existence of a separating hyperplane is more likely. In the present case, the labels are "sodium antagonist", "calcium antagonist" and "potassium antagonist", respectively associated with labels 0, 1 and 2. Among various possible choices of kernels, a Gaussian kernel is employed in this work.
We used a Python implementation of SVC through the Scikit-learn [PVG+11] machine learning library which itself uses the LIBSVM library [CL11]. For a given training set, a so-called classifier is built. The classifier is then called to predict the labels of the validation set samples. The predictions are finally compared to the true labels. There exist several metrics to quantify the prediction quality. Two different metrics are considered here: the Cohen's kappa and the receiver operating characteristic area under curve (AUC). The Cohen's kappa is a single scalar designed to measure the performance of multi-class classifiers. Its value ranges from -1 (worst possible classifier) to 1 (perfect classifier), 0 corresponding to a coin-flip classifier. The AUC is defined for each class and measures how a classifier performs with respect to a given class. Its value ranges from 0 (worst) to 1 (best), 0.5 being a coin-flip. Because the classification is repeated several times with different data set

splittings, the classification metrics are summarized using their means and standard deviations (see Table 5.3 for instance). The "averaged AUC" corresponds to the average of all AUCs (one AUC per class).

Both metrics are described in detail in the Supplementary Material. We now present two different strategies to employ SVC in the context of drug classification.

3-versus-3 classification Since there are three distinct classes in the experimental set, those three classes need to be included in the training set, preferably in equal proportions. The strategy of 3-versus-3 (3v3) classification consists in dividing the experimental set into a training set and validation set that both include samples from the three classes. Each class is divided into two sub-classes. This is naturally done for the sodium and potassium antagonist classes since they are each comprised of data from two different drugs. For the calcium antagonist class, the diltiazem data is artificially split into two drugs "diltiazem A" and "diltiazem B" (see Table 5.2). Each sub-class is associated with an identification number (ID) from 0 to 5. Therefore, there are 8 possible choices for the training and validation set combinations as summarized in Table 5.1.

One-versus-All classification The One-versus-All (OvA) classification strategy consists in training one classifier for each class. For each class j, the training set labels are modified to take the value 1 for samples in class j and 0 otherwise and a classifier is trained on this relabeled training set. In other words, the classifier for class j is only trained to recognize whether or not a sample belongs to class j. For the validation step, the classifiers do not predict a class label but a probability for a given sample to be in their respective class. Each sample of the validation step goes through each of the three classifiers and the predicted class corresponds to the classifier returning the highest probability. The splitting between training and validation sets is done in the same way as in the 3-vs-3 classification strategy.

5.3 Results

5.3.1 Comparison between classical and numerical biomarkers

Here the performance of the numerical biomarkers in a classification context is compared to that of the classical biomarkers for two different classification strategies. The data set is composed of 880 experiments, each counting one control measurement and 5 measurements at different drug concentration levels. For each experiment, the conductances values and FP features are computed as explained in the Methods section and the labels are defined according to Table 5.2.

5.3.1.1 3v3 classification

The performance of the numerical biomarkers compared to the classical ones is evaluated using the 3v3 classification strategy. The classification procedure is carried

out for each different splitting of the data set as summarized in Table 5.1. First, the classification inputs are the 3 classical biomarkers for each drug concentration level:

$$\left\{\tilde{\mathrm{DA}}_{c1}, \tilde{\mathrm{RA}}_{c1}, \tilde{\mathrm{FPD}}_{c1}, \ldots, \tilde{\mathrm{DA}}_{c5}, \tilde{\mathrm{RA}}_{c5}, \tilde{\mathrm{FPD}}_{c5}\right\}, \tag{5.15}$$

where c_k is the k-th concentration level. The inputs are therefore of dimension 15. Then, the classification inputs are the numerical biomarkers for each concentration, computed as explained in the Methods section using the classification training set as samples for the Monte-Carlo approximations. The inputs now read:

$$\left\{y_{1,c1}, y_{2,c1}, y_{3,c_1}, \ldots, y_{1,c5}, y_{2,c5}, y_{3,c_5}\right\}. \tag{5.16}$$

Note that for each splitting of the data set, new weights for the numerical biomarkers are computed. The classification procedure is carried out in both cases and the results are summarized in Table 5.3. Regardless of the chosen classification score, the results are better using the numerical biomarkers as inputs.

5.3.1.2 OvA classification

The same procedure as in the 3v3 case is applied to the OvA strategy. The classification procedure is carried out with both classical and numerical biomarkers as inputs and the results are summarized in Table 5.4. Again, the classification results are better using the numerical biomarkers as input, regardless of the classification score considered. Furthermore, the results are overall better when using the OvA approach rather than the 3v3 one.

5.3.2 Using combined experimental and synthetic measurements for the numerical biomarkers computation

Having established that numerical biomarkers outperform classical ones in two different classification scenarios, we now investigate the addition of synthetic measurements for the computation of the numerical biomarkers weights. To enrich the set of experimental samples used to compute the numerical biomarkers, a set of synthetic measurements is built. First, conductances samples are chosen to mimic the effect of drugs as shown in Figure 5.6. Depending on the most affected conductance, these samples are associated to a synthetic sodium (resp. calcium and potassium) antagonist drug called "synth A" (resp. B and C). 775 samples per drug are chosen which amounts to 155 experiments per drug. and their repartition is summarized in Table 5.2. This approximately corresponds to a 50%/50% split between experimental and synthetic measurements. For each conductances sample, the computational model described in the Methods section is evaluated and the dictionary features are computed from the simulated FPs. For each experiment, the computational model is also evaluated in the control conditions, *i.e.* with $g_{fi} = g_{si} = g_{so} = 1$ in order to compute the ratios as defined in (5.8). The features are incorporated in the experimental set to create a composite set. This composite set is then used to compute the

numerical biomarkers weights. The same data set splitting procedure as described before is carried out. Note that the synthetic measurements are only used for the numerical biomarkers computation and are not included neither in the training set nor in the validation set. Again, two classification strategies are explored.

5.3.2.1 Classification results

The classification is carried out using both 3v3 and OvA approaches. The results are summarized in Tables 5.5 and 5.6. The addition of synthetic measurements to compute the numerical biomarkers improves the classifier predictions in both cases. In the 3v3 case, the improvement is more important than in the OvA case.

5.4 Discussion

In this study, a framework for an automatic classification of drugs from MEA measurements has been presented. The framework relies on an *in silico* model of a MEA device, on a feature selection algorithm and on state-of-the-art machine learning tools. The *in silico* model is a PDE model (the bidomain equations) coupled with a ionic model that describes the transmembrane current of the cardiomyocytes. The ionic model is a phenomenological model consisting of a set of coupled non-linear ODEs. The feature selection algorithm proposes a way to compute a so-called numerical biomarker for each conductance of interest, designed to perform better in a classification context than classical biomarkers. The numerical biomarkers are linear combinations of the entries of a dictionary of features which is given. The calculation of the weights involves Monte-Carlo approximations which use experimental or synthetic (or both) conductances and FP samples. It has been applied to drug classification problems using experimental MEA recordings. The classification was carried out using the Scikit-Learn Python library [PVG+11] which includes several classification tools. In the present work a Support Vector Classification was used. The data used for the classification consist in FP features extracted from experimental measurements and their associated labels corresponding to the type of drug that is considered.

The purpose of the present work is twofold. First, it intends to establish that the classically used biomarkers may be improved, at least in a classification context, by using numerical biomarkers instead. Second, it intends to show that the classification performance may benefit from the addition of synthetic measurements in the calculation of the numerical biomarkers. More generally, the authors intend to show that numerical simulations are useful to cardiac electrophysiology in general, beyond the sole scope of drug classification.

First, a comparison between classical and numerical biomarkers was carried out. The comparison consists in classifying drugs from experimental measurements using two different strategies: 3v3 and OvA. For each strategy, the classification is performed using classical or numerical biomarkers as inputs. As expected, the classification results in both cases are improved when using the numerical biomarkers.

The latter were indeed designed to be maximally correlated to their associated conductance and minimally correlated to the others. As a consequence, they are more revealing of the underlying conductances than the classical biomarkers. In the 3v3 case, the mean AUCs are increased when using the numerical biomarkers as inputs and the standard deviations remain similar. The mean Cohen's kappa also significantly increases. However, its standard deviation is also higher but not enough to compromise the improvement of its mean. The same observations can be made for the OvA case except for the g_{fi} AUC which is reduced when using numerical biomarkers.

Second, the use of combined experimental synthetic measurements to compute numerical biomarkers is investigated. The numerical biomarkers are computed using Monte-Carlo approximations that require conductances and FP features samples. In the previous case, these samples are experimental. The idea is to improve the robustness of the numerical biomarkers by incorporating synthetic measurements that span better the parameters (*i.e.* conductances) space. This approach is meant to compensate the scarcity of experimental data and more generally the fact that experiments do not cover every possible drug block scenario. Conductances samples were drawn and the computational model was evaluated to generate noisy FPs. From these FPs, the entries of the dictionary of features were computed. The numerical biomarkers weights are then computed using a composite set of experimental and synthetic samples. These numerical biomarkers are compared to the ones computed using only experimental data. The same two classification strategies as before are used to compare both approaches. In the 3v3 case, the improvement is not significant, both for the AUCs and the Cohen's kappa. This relatively low improvement needs to be mitigated by the fact that the classification scores were already high when using experimentally derived numerical biomarkers, especially for the AUCs. The improvements for the OvA case are however important. These results suggest that, for the classification scenarios envisioned here, the addition of synthetic measurements is always beneficial. Note also that the OvA strategy clearly outperforms 3v3 when using composite numerical biomarkers whereas it is not clear which strategy is the best when using numerical biomarkers computed from experimental measurements only.

The use of FP features in a classification context is now discussed. In classification problems, and in machine learning in general, a large number of inputs tend to provoke an over-fitting of the model. This means that the classifier tends to have satisfactory training scores but generalizes poorly on a validation test. This is in part solved by the regularization used but the number of inputs still remains important. When dealing with experimentally recorded FPs, the different signals are often not perfectly synchronized, making timestep-wise comparisons meaningless. Furthermore, an important variability of the signal amplitudes is observed in practice, making even perfectly synchronized signals difficult to compare. Using features extracted from the FP that are do not depend on time shifts and amplitude variations are therefore more robust in a classification context.

The limitations of the proposed approach are now discussed. First, the conduc-

tances values associated with the experimental measurements are not knwown and are therefore approximated using Equation (5.2). This approximation is however subject to several sources of uncertainty such as the IC_{50} whose value for a given drug may vary according to the source considered [KOPM+13, MCS+11]. The uncertainties also come from the Hill's equation which is an imperfect model. Knowing the exact values for the conductances is however not critical since those values are only needed to derive the numerical biomarkers and are not directly used dusing the classification procedure. Another limitation comes from the computational model used in the present work. The sources of error are multiple: ionic model error, space and time dicretizations, conductivities errors, etc. These errors are not critical either since the computational model is only used to compute the numerical biomarkers weights. This study shows that, despite the modeling errors, adding synthetic measurements simulated by the computational model leads to better classification results. Other limitations come from the classification strategies. Both classification strategies are non-exhaustive in that they do not explore every possible way of splitting the data set. Furthermore, the classification metrics used to compare the different approaches are not flawless. In some cases comparing AUCs for instance is not the best way to compare classifiers [AH00]. Other metrics exist, such as the mean squared error, but were not investigated in this work. Finally, the numerical biomarkers derived in the present work are not optimal in the sense that their correlation with their associated conductances is not one, as seen in Figure 5.8. We now discuss some perspectives that could lead to interesting future works. Other classification methods than SVC exist, such as neural networks or random forests for instance. It would be interesting to assess whether the findings of this work are still valid when considering other classification tools. It would also be interesting to evaluate which classification tool generally performs best in the present drug classification context. Other perspectives concern the numerical biomarkers computed using a composite set of synthetic and experimental measurements. In the present work, the composite set is roughly composed of half synthetic and half experimental measurements. However, other proportions could be investigated and an optimal proportion with respect to the classification score could be found. In the present work, only sodium, potassium and calcium antagonists drugs are considered but other types of drugs exist. Drugs that affect other ionic channels or even simultaneously several of them could be investigated. In parallel, more sophisticated ionic models including more current types would need to be used to model these new drugs. This would of course come at the expense or more computationally intensive simulations. Finally, training classifiers with only synthetic measurements instead of experimental ones could be considered. This would be very useful when experimental data are insufficient or even not available. The classifiers could also be trained with a composite set of synthetic and experimental data just like it is done in this work for the computation of numerical biomarkers.

5.5 Tables and Figures

Splitting index	0	1	2	3	4	5	6	7
training set IDs	{0,2,4}	{0,2,5}	{0,3,4}	{0,3,5}	{1,2,4}	{1,2,5}	{1,3,4}	{1,3,5}
validation set IDs	{1,3,5}	{1,3,4}	{1,2,5}	{1,2,4}	{0,3,5}	{0,3,4}	{0,2,5}	{0,2,4}

Table 5.1: Different possible splittings of the experimental data set.

Drug name	Blocked ionic channel	Associated conductance	ID	SVC class label	#experiments
Mexiletine	sodium	g_{fi}	0	0	160
Flecainide	sodium	g_{fi}	1	0	120
Diltiazem A	calcium	g_{si}	2	1	160
Diltiazem B	calcium	g_{si}	3	1	160
Moxifloxacin	potassium	g_{so}	4	2	120
Dofetilide	potassium	g_{so}	5	2	160
synth. A	sodium	g_{fi}	6	0	155
synth. B	calcium	g_{si}	7	1	155
synth. C	potassium	g_{so}	8	2	155

Table 5.2: Repartition of the available (experimental and synthetic) data set.

	classical biomarkers		numerical biomarkers	
Score	mean	std.	mean	std.
Cohen's kappa	0.18	0.15	0.51	0.27
g_{fi} AUC	0.65	0.10	0.86	0.11
g_{si} AUC	0.92	0.09	1.00	0.00
g_{so} AUC	0.36	0.11	0.82	0.10
averaged AUC	0.65	-	0.89	-

Table 5.3: Comparison between classical and numerical biomarkers with the 3v3 classification strategy.

	classical biomarkers		numerical biomarkers	
Score	mean	std.	mean	std.
Cohen's kappa	0.18	0.14	0.53	0.25
g_{fi} AUC	0.66	0.11	0.59	0.41
g_{si} AUC	0.92	0.11	0.96	0.06
g_{so} AUC	0.43	0.11	0.85	0.13
averaged AUC	0.67	-	0.80	-

Table 5.4: Comparison between classical and numerical biomarkers. Classification scores in the one-vs-all scenario.

	experiments only		experiments + synthetic	
Score	mean	std.	mean	std.
Cohen's kappa	0.51	0.27	0.54	0.06
g_{fi} AUC	0.86	0.11	0.87	0.13
g_{si} AUC	1.00	0.00	1.00	0.00
g_{so} AUC	0.82	0.10	0.84	0.08
averaged AUC	0.89	-	0.91	-

Table 5.5: Comparison between numerical biomarkers computed from experiments only and combined experiments and synthetic measurements. 3v3 classification strategy.

	experiments only		experiments + synthetic	
Score	mean	std.	mean	std.
Cohen's kappa	0.53	0.25	0.69	0.28
g_{fi} AUC	0.59	0.41	0.87	0.32
g_{si} AUC	0.96	0.06	1.00	0.01
g_{so} AUC	0.85	0.13	0.89	0.15
averaged AUC	0.80	-	0.92	-

Table 5.6: Comparison between numerical biomarkers computed from experiments only and combined experiments and synthetic measurements. OvA classification strategy

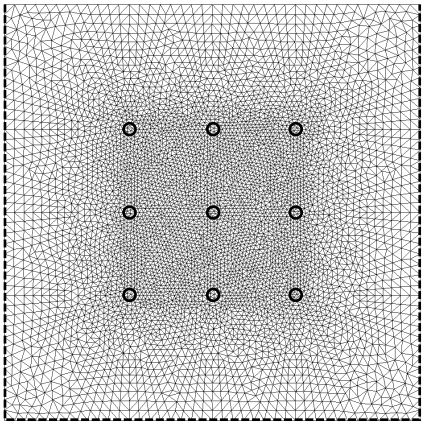

Figure 5.1: MEA geometry and its corresponding finite element mesh. The circles represent the locations of the nine electrodes.

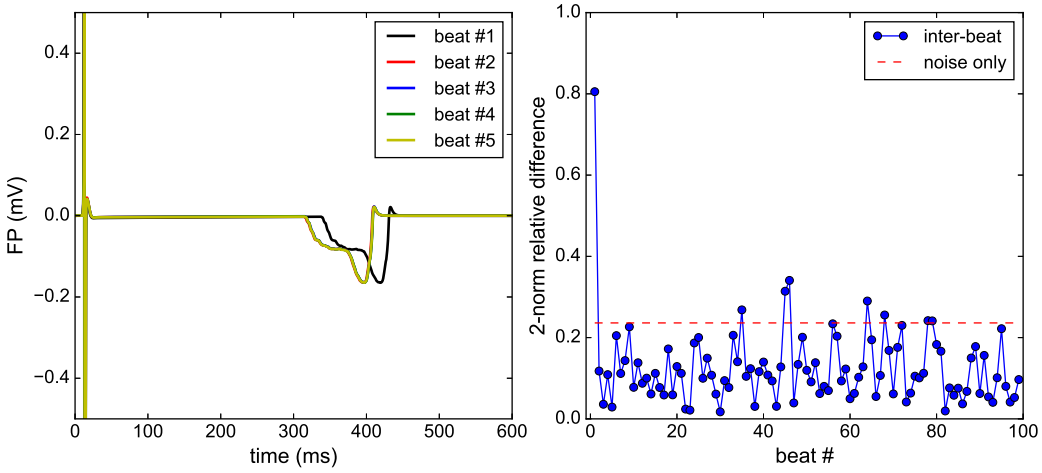

Figure 5.2: Steady-state analysis: the Bidomain equations are solved for 100 consecutive beats. Qualitatively, a satisfactory steady state is reached at the second beat (left). The beat-to-beat relative difference of the FP is monitored (right) and is to be compared to the relative difference between two identical solutions, each polluted by an independent noise (right).

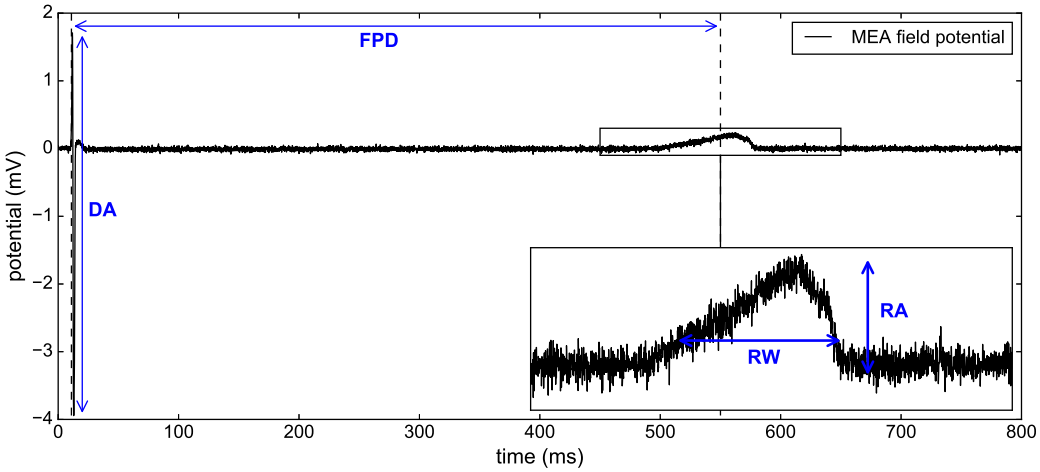

Figure 5.3: Synthetic MEA field potential and some associated biomarkers.

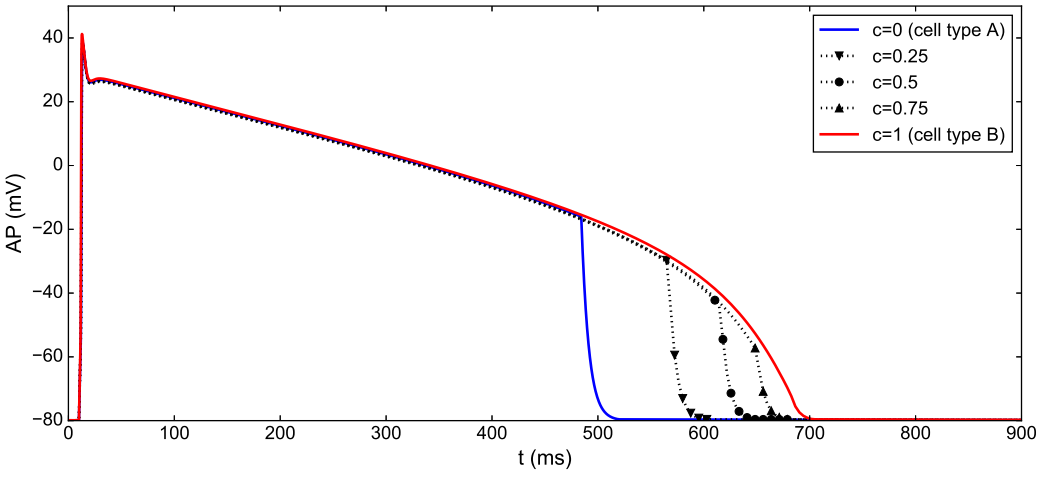

Figure 5.4: Heterogeneity modeling: different APs obtained by simulating the MV model with different values of the heterogeneity parameter c.

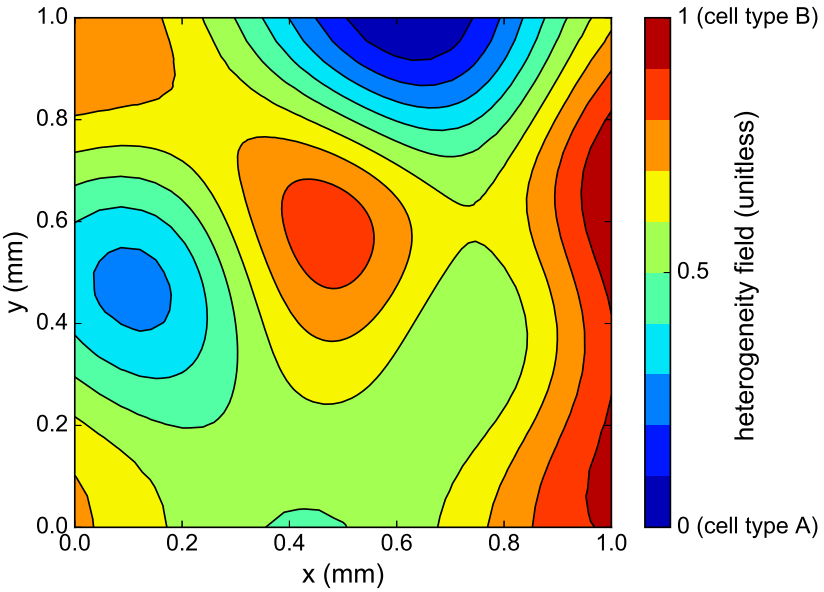

Figure 5.5: One sample of cell heterogeneity field generated using the correlation matrix method.

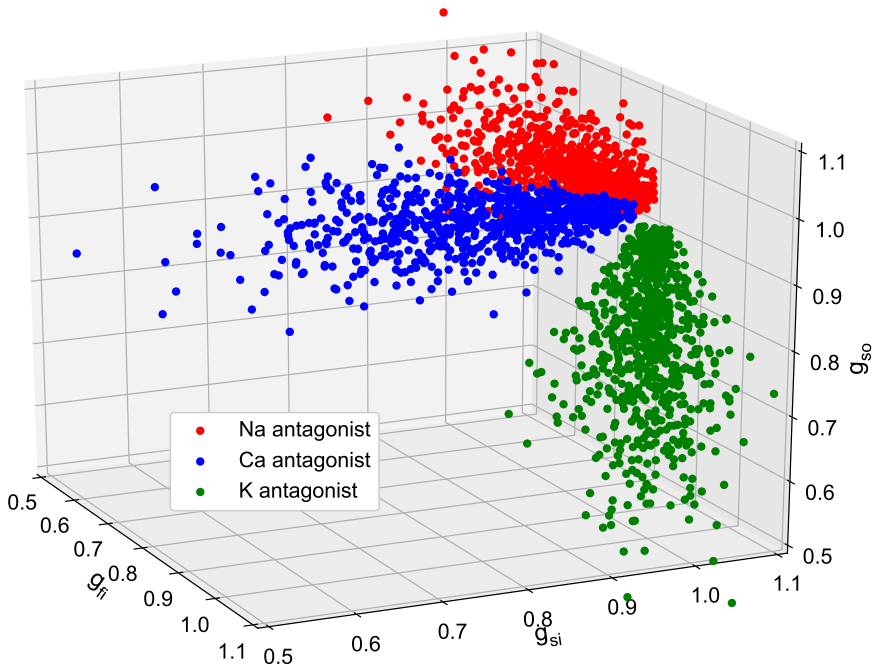

Figure 5.6: Conductances samples used to build the simulation set.

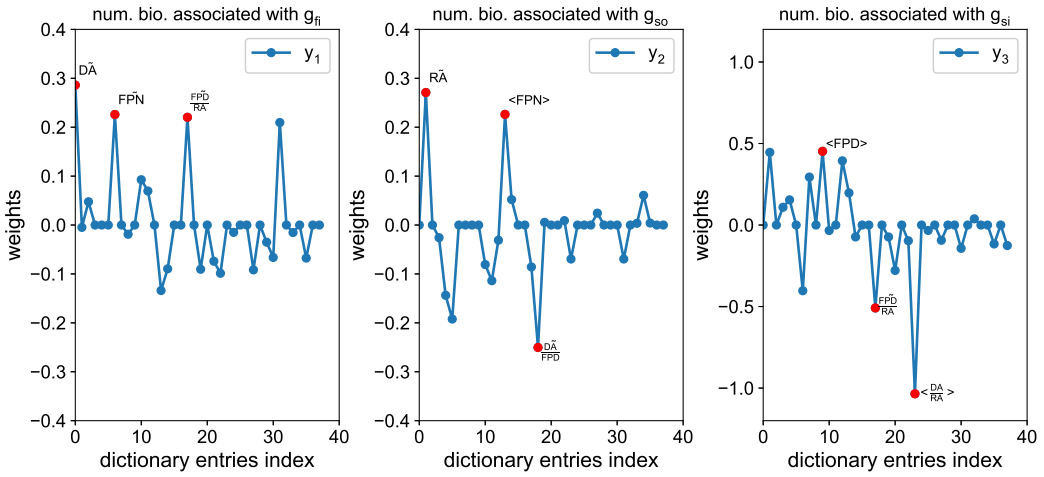

Figure 5.7: Example of numerical biomarkers weights.

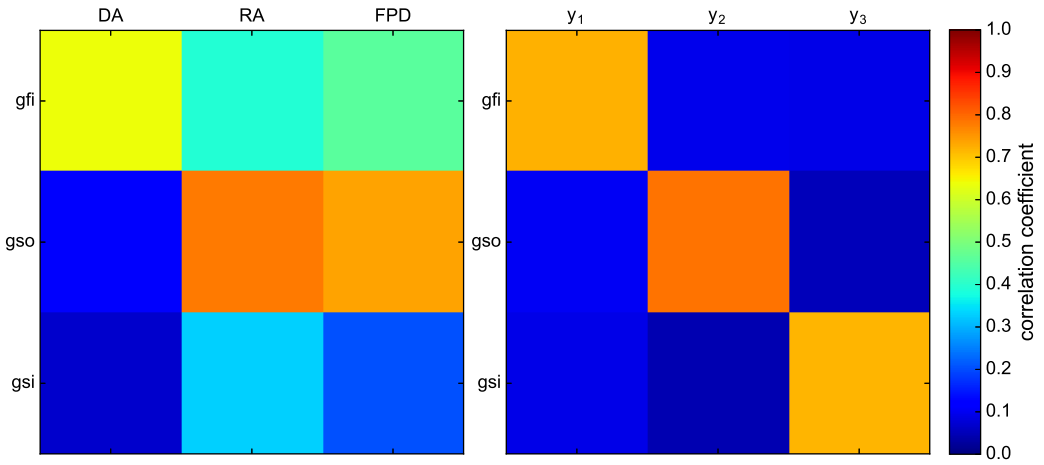

Figure 5.8: Correlation matrix of the conductances of interest with the "classical" biomarkers (left) and with the numerical biomarkers (right)

C_{el}	R_i	R_{el}
$1\mu F$	$2M\Omega$	$10M\Omega$

Table 5.7: table
Parameters used for the imperfect electrode model.

5.6 Supplementary Material

5.6.1 Imperfect electrode model

The bidomain model describes the evolution of the transmembrane potential V_m and the extracellular potential ϕ_e in a domain Ω. We denote by R_i, R_{el} and C_{el}, the internal resistance of the measurement device, the electrode resistance and the electrode capacitance respectively. The field potential ϕ_f^k measured on an electrode e_k is given by $\phi_f^k = R_i I_{el}^k$, where I_{el}^k is linked to the averaged extracellular potential $\phi_{e,mean}^k$ at the electrode e_k by the equation:

$$\frac{dI_{el}^k}{dt} + \frac{I_{el}^k}{\tau} = \frac{C_{el}}{\tau}\frac{d\phi_{e,mean}^k}{dt}, \tag{5.17}$$

where $\tau = (R_i + R_{el})C_{el}$.

For the present study the parameters values are summarized in Table 5.7.

5.6.2 Biomarker computation

In this section, we provide details on how to compute the biomarkers from FP time series. For a given signal, we denote by t the time vector and y the FP. Each signal is divided in two parts: the depolarization region (t_1, y_1) and the repolarization region (t_2, y_2) as shown in Figure 5.9.

Depolarization amplitude (DA) The DA is simply defined as the difference between the maximum and minimum values of the potential during the depolarization:

$$\mathrm{DA} = \max(y_1) - \min(y_1). \tag{5.18}$$

Repolarization amplitude (RA) The RA is defined as the maximum (in absolute value) of the repolarization.

$$\mathrm{RA} = \max(|y_2|). \tag{5.19}$$

Field potential duration (FPD) The FPD is defined as the time difference between the maximum (in absolute value) of the depolarization and the maximum (in absolute value) of the repolarization. Let $t_d = t\left[\underset{t}{\mathrm{argmax}}(|y_2(t)|)\right]$ and $t_r =$

$t\left[\underset{t}{\text{argmax}}(|y_1(t)|)\right]$. Then,

$$\text{FPD} = t_r - t_d. \tag{5.20}$$

Area under the curve of the repolarization wave (AUC) The AUC is defined as the area under the curve of y_2 truncated around $\pm\Delta t$ of t_r. We used $\Delta t =$ 100ms. The integral is approximated using the trapezoidal rule.

$$\text{AUC} = \left| \int_{t_r-\Delta t}^{t_r+\Delta t} y_2(t)\mathrm{d}t \right| \tag{5.21}$$

Repolarization center (RC) The RC is defined as the offset of the barycenter (with respect to time) of the repolarization wave.

$$\text{RC} = \frac{1}{\text{AUC}} \int_{t_r-\Delta t}^{t_r+\Delta t} t y_2(t)\mathrm{d}t - t_r \tag{5.22}$$

Repolarization width (RW) The RW is defined as the normalized standard deviation of the repolarization wave.

$$\text{RW} = \frac{1}{\text{AUC}} \left[\int_{t_r-\Delta t}^{t_r+\Delta t} t^2 y_2(t)\mathrm{d}t - \left(\int_{t_r-\Delta t}^{t_r+\Delta t} t y_2(t)\mathrm{d}t \right)^2 \right]^{1/2}. \tag{5.23}$$

Field potential notch (FPN) The FPN is defined as the potential value 4ms after t_d. The FPN value is smoothed out by multiplying the signal with a test function and then integrat the product. This proves to be less sensitive to noise than just a point-wise evaluation. Let $\phi(t_1) = \exp\left[-\frac{(t_1-(t_d+4))^2}{.04}\right]$. Then,

$$\text{FPN} = \int_{t_1} y_1(t_1)\phi(t_1)\mathrm{d}t_1. \tag{5.24}$$

5.6.3 Classification metrics

We now present the two different classification metrics used in this work.

Cohen's kappa Cohen's kappa, denoted by κ, is particularly suited for multi-class and/or imbalanced classification problems. The main idea is that it measures the labeling dicrepancy between two annotators (or classifiers). It is simply adapted to our case by considering one of the annotators as the ground truth (true labels). Its formula reads:

$$\kappa = \frac{p_o - p_e}{1 - p_e}, \tag{5.25}$$

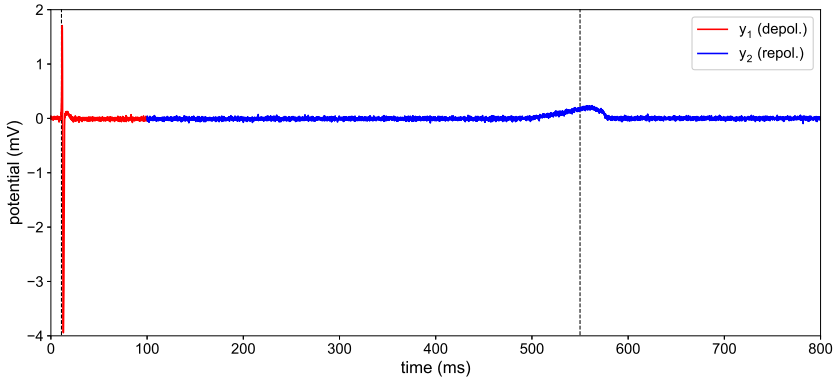

Figure 5.9: FP depolarization and repolarization regions.

where p_o is the observed agreement between the two annotators and p_e is the probability of an agreement between two random annotators. For further details, the reader is referred to Scikit-learn's implementation [1] of Cohen's kappa.

ROC The receiver operating characteristic area under curve (ROC AUC, later referred to as AUC for the sake of clarity) is basically associated with binary classification problems. In our case, one can define a AUC for each class k by considering all the other classes as only one class. With SVC it is possible to evaluate, in addition to the predicted class, the probability of belonging to each class. Given a threshold parameter (that varies between 0 and 1), it is possible to decide if a sample belongs to a given class when the SVC probability returned for this class is greater than the threshold parameter. The predicted class therefore depends on this parameter. When all samples of the validation set have been tested, the following quantities are computed, for each class k and for a given threshold parameter:

- true positives (TP): number of samples affected to class k which are actually in class k.
- false positives (FP): number of samples affected to class k which are actually *not* in class k.
- true negatives (TN): number of samples affected to another class than k which are actually in class k.
- false negatives (FN): number of samples affected to another class than k which are actually *not* in class k.
- true positive rate (TPR): $\frac{TP}{TP+FN}$.
- false positive rate (FPR): $\frac{FP}{FP+TN}$.

[1] https://github.com/scikit-learn/scikit-learn/blob/ab93d65/sklearn/metrics/classification.py#L278

The ROC is the curve of TPR against FPR as the threshold parameter varies between 0 and 1. The AUC is simply the area under this curve.

Chapter 6

Computing Numerical Biomarkers for Electrocardiograms

Contents

6.1 Introduction 149
6.2 Methods 149
6.2.1 ECG computational model 149
6.2.2 The ECG 155
6.2.3 ECG biomarkers 156
6.3 Results 156
6.3.1 Numerical biomarkers in healthy conditions 156
6.3.2 Numerical biomarkers in pathological conditions 159
6.4 Conclusions and perspectives 162
6.5 Appendix 163
6.5.1 Figures and tables 163
6.5.2 ECG leads definition 169
6.5.3 Definition of the biomarkers dictionary entries 169

6.1 Introduction

This chapter builds on previous works, extensively described in the PhD theses of Elisa Schenone [Sch14] and Annabelle Collin [Col14]. This chapter is a preliminary work where we try to derive numerical biomarkers (see Chapter 4) for electrocardiogram (ECG) signals. This is a first step towards the identification of optimal features in order to solve, in a reliable and computationally inexpensive way, inverse electrocardiography problems [NCL07] (*i.e.* restituting the electrical activity of the heart from the knowledge of ECG recordings).

The ECG [GGb81] is the recording, by means of electrodes located on the skin surface, of the heart electrical activity. Its wide use in cardiology, and in medicine in general, can be explained by the fact that it is non invasive, easy to interpret by a trained physician and relatively inexpensive. In the present work, we focus on the 12-lead ECG which is the most commonly used kind. For a detailed history and description of this essential medical tool, the interested reader is referred to the very informative introduction of [Sch14]. Numerous attempts at numerically modelling ECG recordings may be found in the literature [TDP+04, KSW+07, BCF+10]. On the contrary, to the authors knowledge, models based on a full and realistic geometry of the heart and body are scarce [SCG16]. The present work uses the same models and numerical methods as in [SCG16]. The applications of numerical biomarkers associated with cardiac quantities of interest are numerous, ranging from the calibration of *in silico* patient-specific models to the monitoring or diagnosis of pathological conditions.

The chapter is organised as follows. First, the computational model of the ECG is described. The bidomain equations are used to model the heart electrical activity and the rest of the body is simply modeled as a passive conductor. The resulting PDEs are solved using the FELiScE[1] finite element library. The parameters of interest are presented and their physiological roles explained. Second, the dictionary of features used to compute the numerical biomarkers is presented. Then, the numerical biomarkers procedure is applied to synthetic test cases in different healthy scenarios to validate the method in the context of ECG studies. The approach is then illustrated with synthetic pathological cases for which a qualitative analysis of the results is provided. Finally, conclusions are drawn and future research objectives are presented.

6.2 Methods

6.2.1 ECG computational model

6.2.1.1 Geometry

To simulate realistic ECGs, a full body geometry is used. Both the geometries of the heart and the body are the same as in [SCG16]. The heart is modeled by

[1] https://gforge.inria.fr/projects/felisce

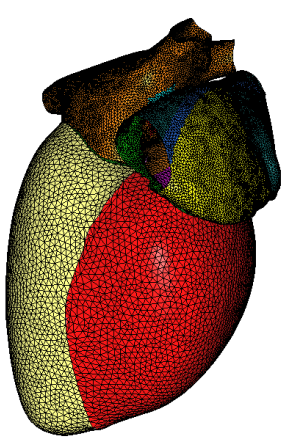

(a) Complete heart: ventricles and atria

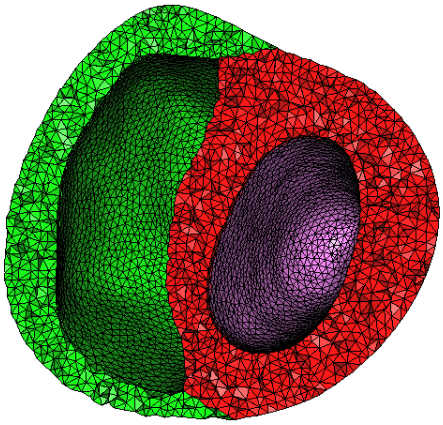

(b) Horizontal cut of the heart: left ventricle in red and right ventricle in green.

Figure 6.1: Geometry of the Zygote (http://www.3dscience.com) human heart.

a 3-D mesh following a realistic geometry (see Figure 6.1). It is comprised of the ventricles (left and right) and the atria (left and right). The heart is immersed in a 3-D mesh of a human body (see Fig. 6.3). A more thorough description of the problem geometry is available in [SCG16, Sch14].
In the following, we denote by Ω_H the heart domain, Ω_T the rest of the body domain and Σ the interface between the heart and the rest of the body.

6.2.1.2 Electrophysiology of the heart: the bidomain equations

The electrical activity in the heart is modeled by the so-called bidomain equations [Tun78]. Except for the electrodes model and the dimension (3-D instead of 2-D), it is identical to the bidomain model of the MEA presented in Chapter 5. The bidomain equations read:

$$\begin{cases} A_{\mathrm{m}} C_{\mathrm{m}} \dfrac{\partial V_{\mathrm{m}}}{\partial t} + A_{\mathrm{m}} I_{\mathrm{ion}}(V_m, \mathbf{x}) - \nabla \cdot (\sigma_{\mathrm{i}} \nabla V_{\mathrm{m}}) - \nabla \cdot (\sigma_{\mathrm{i}} \nabla u_H) = A_{\mathrm{m}} I_{\mathrm{app}}, & \text{in } \Omega_H \\ -\nabla \cdot ((\sigma_{\mathrm{i}} + \sigma_{\mathrm{e}}) \nabla u_H) - \nabla \cdot (\sigma_{\mathrm{i}} \nabla V_{\mathrm{m}}) = 0, & \text{in } \Omega_H, \end{cases} \tag{6.1}$$

where V_m is the transmembrane potential, u_H the extracellular potential, σ_i and σ_e the conductivity sensors, A_{m} the cells surface area per unit volume and C_{m} the cells electrical capacitance. I_{app} is a function of time and space and corresponds to the external electrical stimulation of the atria and ventricles as explained in [Col14, Sch14]. The term $I_{\mathrm{ion}}(V_m, \mathbf{x})$ corresponds to the electrical activity at the cell scale and is explained later. For the atria, the model in (6.1) has been transformed into a 2-D model to take into account the small thickness of this region. The surface model is presented in [CCG13]. The variational formulation and the finite element discretization associated with this problem may be found in [BCF+10, Col14, Sch14]. The conductivity in the ventricular tissues is actually heterogeneous and is associ-

ated with an architecture of fibers in the cardiac muscle. The conductivity tensors are defined as follows:

$$\sigma_{\mathrm{i}} = \sigma_i^t I + (\sigma_i^l - \sigma_i^t)\tau \otimes \tau, \tag{6.2}$$

$$\sigma_{\mathrm{e}} = \sigma_e^t I + (\sigma_e^l - \sigma_e^t)\tau \otimes \tau, \tag{6.3}$$

where I is the identity tensor and τ is a local unit-norm vector that is parallel to the fibers direction. The quantities σ_i^t, σ_i^l, σ_e^t and σ_e^l are uniform across the ventricles and belong to the set of parameters that are studied in the present work. For more information about how the fibers directions are determined, the interested reader is referred to [BCF+10] and to Figure 1.15 of [Sch14].

6.2.1.3 Full cardiac cycle

The electrical activity in the heart takes place in two regions: the atria and the ventricles (see Figure 6.2). In the present work, we will only focus on the electrical activity of the ventricles. The initial electrical stimulation starts from the sinus node in the atria. The depolarization front propagates through the atria until it reaches the atrioventricular node where it triggers the depolarization of the ventricles. The stimulus first travels through a fast conduction network called the Hiss bundle (see Figure 6.2) where it goes much faster than through other cardiac tissues. This stimulus corresponds to the term I_{app} in (6.1). This enables the formation of a uniform depolarization front in the inside of the ventricles (endocardium) which can then travel outwards through the thickness of the ventricles. In healthy conditions, both ventricles are stimulated at the same time. We introduce the delay parameter $\delta_{\mathrm{stim}}^{\mathrm{LV}}$ which controls the delay of the stimulation between the left and right ventricles. When this delay is important, it is called a left or right bundle branch block whether the left or right ventricle is late with respect to the other.

6.2.1.4 Ionic models

The ionic models are used to approximate the term $I_{\mathrm{ion}}(V_m, \mathbf{w})$ in the model in (6.1). At the cell scale it corresponds to the I_{ion} term in the governing equations of the action potential AP (see Chapters 2 and 3). Due to profound differences between atrial and ventricular cells, two different models are used for these regions.

Ventricular ionic models In the ventricles, we use the so-called "minimal ventricular model" [BOCF08] (referred to as MV model in the following). It belongs to the category of phenomenological models (as opposed to the physiological ones) in the sense that each term in the ODE does not correspond to an actual membrane ionic channel. It is however computationally less demanding than physiological models while being able to reproduce a wide variety of realistic signals, which justifies its use in our context. The ionic current I_{ion} in the MV model consists in the sum

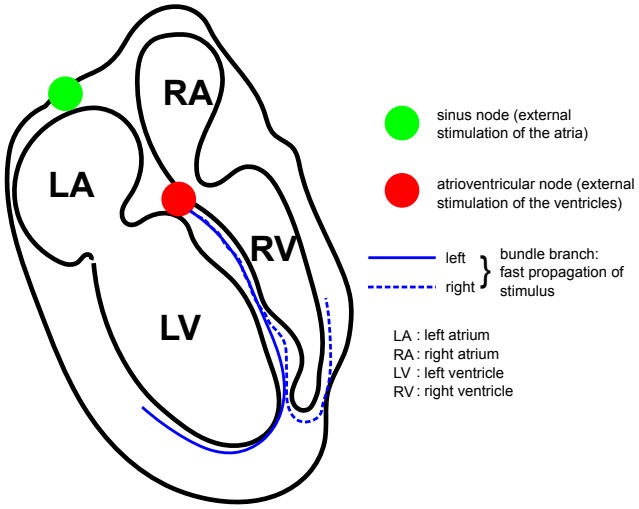

Figure 6.2: Schematic of the heart conduction system. The electrical stimulation of the ventricles starts from the atrioventricular node and follows the bundle branches.

of three currents:

$$I_{\text{ion}}(V_m, \mathbf{x}) = g_{fi} J_{\text{fi}}(V_m, \mathbf{x}) + g_{so} J_{\text{so}}(V_m, \mathbf{x}) + J_{\text{si}}(V_m, \mathbf{x}), \tag{6.4}$$

where J_{fi} is the fast inward current and controls the depolarization phase of the AP, J_{so} is the slow outward current and controls the duration of the AP plateau and J_{si} is the slow inward current and controls the height of the AP plateau. We added two parameters (referred to as conductances in the following): g_{fi} and g_{so} which modulate the activity of J_{fi} and J_{so}, respectively. Even though it is a simplified model, these currents may be qualitatively associated with the activity of, respectively and in the same order, the sodium, potassium and calcium ionic currents. The currents are defined as follows:

$$\begin{aligned} J_{\text{fi}}(V_m, \mathbf{x}) &= -H(u-\theta_v)(u-\theta_v)(u_u-u)\frac{v}{\tau_{\text{fi}}}, \\ J_{\text{so}}(V_m, \mathbf{x}) &= (1-H(u-\theta_w))\frac{u-u_{\text{o}}}{\tau_{\text{o}}} + \frac{H(u-\theta_w)}{\tau_{\text{so}}}, \\ J_{\text{si}}(V_m, \mathbf{x}) &= -H(u-\theta_w)\frac{ws}{\tau_{\text{si}}}, \end{aligned} \tag{6.5}$$

where $u = aV_m + b$ is the non-dimensional transmembrane potential, rescaled to take values between 0 and 1. $H(x)$ is the Heaviside function and $\mathbf{x} = (s, v, w)$ is a vector of state variables which are solution of coupled non-linear ODEs. The detailed ODEs, as well as the other parameters in (6.5), are available in [BOCF08]. In the present work, we focus on the following set of ionic parameters: $\{g_{fi}, g_{so}, \tau_{so}\}$. The cardiomyocytes properties are actually not uniform across the ventricles. The latter may be divided into four zones: right ventricle (RV), endocardium (endo), midmyocardium (MCell) and epicardium (epi) as shown in Figure 6.4. For each of these zones, a different set of parameters is chosen so that the simulated AP resembles the typical AP in the zone. These parameters values may be found in Table

1 of [BOCF08]. One may therefore consider that there are four different models in the ventricles and the ionic parameters of interest are now: g_{fi}^{RV}, g_{fi}^{MCell}, g_{fi}^{endo}, g_{fi}^{epi}, $g_{so}^{\text{RV}}, \ldots, \tau_{so}^{\text{epi}}$ which amounts to a total of 12 ionic parameters of interest. With the addition of the conductivity tensors and the stimulation delay, this represents 17 parameters of interest.

Atrial ionic model Even though the electrical activity in the atria is not studied in this work, some information about this region is given for the sake of completeness. As explained earlier, the bidomain equations in the atria are actually modified so as to become a 2-D model. Furthermore, the ionic model in this region is different from that of the ventricles. The atrial cardiomyocytes are modeled with the Courtemanche model [CRN98]. Note that it is the same model as the one studied in Chapter 3. The interested reader is referred to [CCG13] for more information about the atrial region.

6.2.1.5 Coupling with the body

The rest of the body is considered as a passive conductor and therefore a simple diffusion problem is solved for the electrical potential u_T in this region:

$$-\operatorname{div}(\sigma_T \nabla u_T) = 0 \quad \text{in } \Omega_T \tag{6.6}$$

where σ_T takes different values in the lungs, the ribs and the rest of the body to take into account the conductivity differences in these three regions.

To reduce the computational cost of the model, the isolated heart assumption [CNLH04] is used. It consists in assuming there is continuity of the electrical potential at the interface between the heart and the torso but that there is no electrical current flowing through it. Using this assumption, it is possible to decouple the problem in the heart and in the rest of the body and therefore to obtain two smaller problems. This assumption does not induce major modifications in the resulting ECG as shown in [BCF+10]. The full problem now reads:

$$\begin{cases} (6.1) & \text{in } \Omega_H \\ -\operatorname{div}(\sigma_T \nabla u_T) = 0, & \text{in } \Omega_T \\ u_T = u_H, & \text{on } \Sigma \\ \sigma_T \nabla u_T \cdot n_T = 0, & \text{on } \partial\Omega_T \backslash \Sigma \end{cases} \tag{6.7}$$

Furthermore, it is shown in [BCF+10] that, due to the linearity of the operator that maps the solution on the heart surface to the ECG, the latter is simply a product between the heart surface solution and a pre-computed transfer matrix. Solving the electrical problem in the rest of the body can now be seen as a post-processing step.

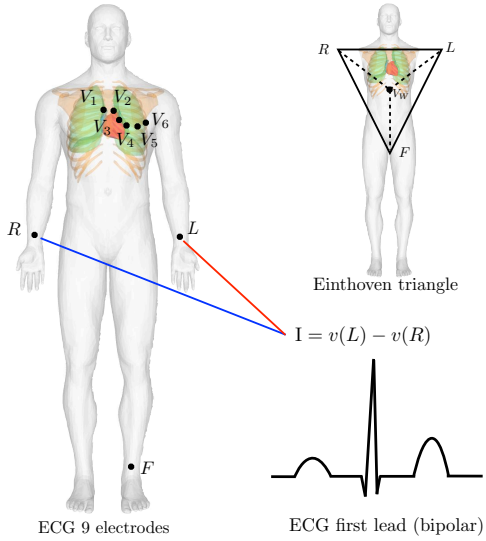

Figure 6.3: Position of the nine electrodes of the ECG at the surface of the body. Reproduced from Elisa Schenone's PhD thesis [Sch14]

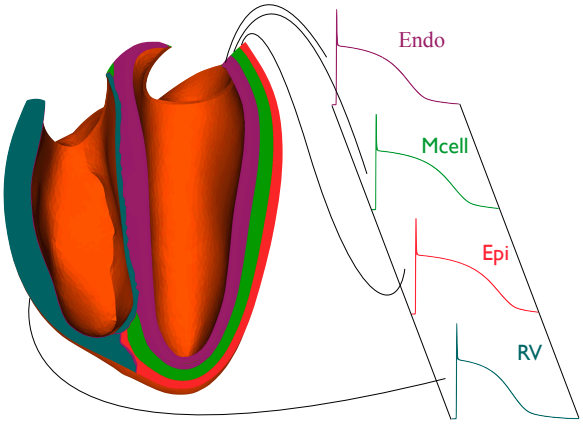

Figure 6.4: Longitudinal clip of the ventricles showing the regions associated with the four different cell types considered: right ventricle (RV), endocardium (endo), midmyocardium (MCell) and epicardium (Epi). Reproduced from Elisa Schenone's PhD thesis [Sch14].

6.2.2 The ECG

The ECG is the observation at the surface of the body of the electrical activity in the heart. The observation is made by recording the electrical potential on the patient's skin with nine electrodes denoted by V_1, V_2, V_3, V_4, V_5, V_6, R, L and F. Their locations is shown in Figure 6.3. Using these nine electrodes, 12 leads are computed. With a slight abuse of notations, these leads are denoted by: I, II, III, aVR, aVL, aVF, V_1, V_2, V_3, V_4, V_5, V_6. The formulas needed to derive these leads are found in the Appendix.
Each lead is a time series of an electrical potential and provides insight into the different phases of the cardiac cycle. A typical lead may be divided into 5 segments (or waves) denoted by P, Q, R, S and T (see Figure 6.5). The P wave corresponds to the depolarization of the atria. The Q, R and S waves, also referred to as the QRS segment, correspond to the depolarization of the ventricles. The Q and S waves (not always both visible on every lead) are by definition negative deflections of the potential while the R wave (not visible on every lead) is by definition positive. In a healthy ECG, at least one of these three waves should be visible in each lead. Finally, the T wave corresponds to the repolarization of the ventricles. Note that we did not mention the repolarization of the atria as it is usually buried in the QRS complex and therefore invisible (in the ECG). The T wave can be either positive or negative and can sometimes be bipolar. As explained earlier, the present work focuses on the ventricles electrical activity and therefore the ECGs presented hereafter start from the Q wave.

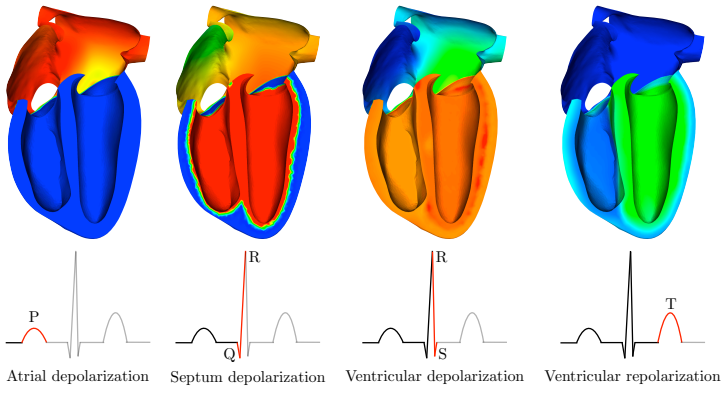

Figure 6.5: Top: Simulation of a cardiac cycle: positive extracellular potential in red and negative in blue.
Bottom: P,Q,R,S,T waves of a standard ECG lead. Each wave corresponds to the depolarization or repolarization of a region of the heart. Reproduced from Elisa Schenone's PhD thesis [Sch14].

6.2.3 ECG biomarkers

Analogously to what has been done for MEA field potentials (see Chapter 5) or cardiomyocytes action potentials (see Chapter 4), a set of features (referred to as biomarkers) is computed for each of the 12 ECG leads. For each lead, we extract 13 biomarkers which capture important features of the Q,R,S and T waves. The first four biomarkers are related to the QRS complex, the next three to the ST segment (or plateau) and the last six to the T wave. To compute numerical biomarkers, one needs a dictionary of features as explained in Chapter 4. In our case, the entries of the dictionaries are the 13 biomarkers of each of the 12 leads, which amounts to a total of 156 entries. The entries are sorted biomarker by biomarker, as follows:

$$b_1^{\text{lead 1}}, b_1^{\text{lead 2}}, \ldots, b_{13}^{\text{lead 11}}, b_{13}^{\text{lead 12}}$$

This allows for a better visualization of the weights since they can be divided in three segments whether they correspond to the QRS complex, the ST segment or the T wave (see Figure 6.6).

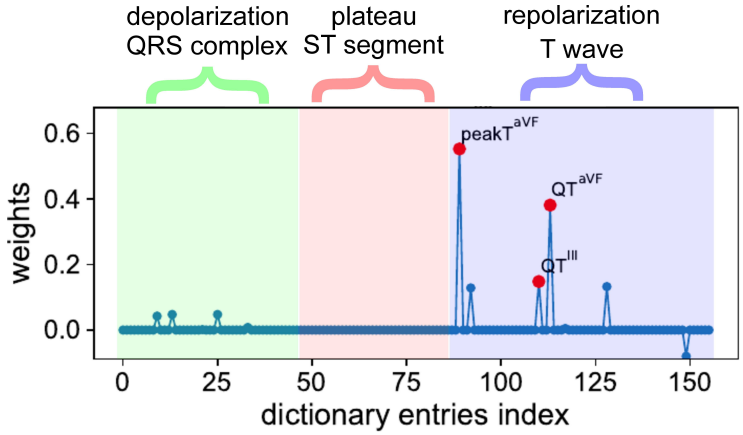

Figure 6.6: The biomarker dictionary entries are sorted so that they are visually divided into three regions: QRS complex (left), ST segment (middle) and T wave (right).

6.3 Results

The numerical biomarker procedure as described in Chapter 4 is now applied to synthetic ECGs generated by solving the model in (6.1) and (6.6) with the FELiScE finite element library.

6.3.1 Numerical biomarkers in healthy conditions

To illustrate the use of numerical biomarkers in ECG measurements, we propose three different scenarios of healthy conditions. We study the variations of some

parameters associated with sodium and potassium dynamics around their reference (*i.e.* healthy) values. Unless stated otherwise, the following procedure is adopted when deriving the numerical biomarkers. The dictionary of features is the same as described in 6.2.3 and is comprised of 156 entries. To avoid any inverse crime, the synthetic ECG signals are polluted with a zero-mean Gaussian noise of standard deviation 5 μV. This corresponds to a signal-to-noise ratio of around 40-50 dB depending on the test case considered. The ℓ^1 penalization parameters are calibrated using the threshold method with a threshold value of 10^{-1}. In the figure representing the obtained numerical biomarkers weights, the three highest weights are materialized by a red dot and their names are displayed for a better visualization of the results.

6.3.1.1 Healthy test case 1

In this test case, 7 parameters of interest are retained: τ_{so}^{RV}, τ_{so}^{endo}, τ_{so}^{Mcell}, τ_{so}^{epi}, g_{fi}^{RV}, g_{fi}^{endo}, g_{fi}^{epi}. The τ_{so} parameters control the duration of the AP plateau while the g_{fi} parameters control the fast sodium channel associated with the upstroke velocity during the depolarization phase.

Numerical settings The training set is generated with $N = 568$ samples drawn from a uniform distribution over the hypercube $[0.5, 1.5]^7$. The ℓ^1 regularization parameters values $\lambda_1, \ldots, \lambda_7$ are summarized in Table 6.1.

Results The numerical biomarkers weights are shown in Figure 6.8. The numerical biomarkers associated with the τ_{so} parameters (with the exception of τ_{so}^{Mcell}) all include the QT biomarker which measures the duration of the QT segment of the ECG and is linked to the plateau duration in the cardiomyocyte AP. The fact that most weights are non-zero for τ_{so}^{Mcell} is due to the fact that its associated ℓ^1 penalization parameter needed to obtain the presribed cost function threshold is relatively low compared to the others. This is usually a sign that the parameter is in fact poorly identifiable and the numerical biomarker is probably over-fitting the training set. More generally, these numerical biomarkers mostly include, as expected, biomarkers related to the ST segment and T wave (see Figure 6.6).
The numerical biomarkers associated with the g_{fi} parameters have non-zero weights mostly for biomarkers related to the QRS complex. Interestingly, the numerical biomarkers associated with the endocardium g_{fi} include mostly biomarkers corresponding to the positive peak of the QRS complex while the ones associated with the epicardium g_{fi} include mostly biomarkers corresponding to the negative peak.

6.3.1.2 Healthy test case 2

In this test case, 8 parameters of interest are retained: δ_{stim}^{LV}, σ_i^t, σ_e^t, σ_i^l, σ_e^l, g_{so}^{RV}, g_{so}^{endo}, g_{so}^{epi}. As explained earlier, the δ_{stim}^{LV} parameter represents the delay after which the left ventricle receives the stimulus compared to the right ventricle.

The σ parameters model how the electrical potential diffuse inside the myocardium tissues. The g_{so} parameters control the opening of the slow outward current in the cardiomyocytes and therefore have mostly an effect onto the T wave.

Numerical settings The training set is generated with $N = 576$ samples drawn from a uniform distribution over Θ, where

$$\Theta = [-5, 5]\times[10^{-4}, 2.10^{-4}]\times[4.10^{-3}, 8.10^{-3}]\times[10^{-3}, 2.10^{-3}]\times[10^{-3}, 2.10^{-3}]\times[.5, 1.5]^3$$

The ℓ^1 regularization parameters values $\lambda_1, \ldots, \lambda_8$ are summarized in Table 6.2.

Results The numerical biomarkers weights are shown in Figure 6.9. Akin the the τ_{so} parameters of the previous test case, the numerical biomarkers associated with the g_{so} parameters all include one QT biomarker in their non-zero weights.
The conductivity parameters biomarkers are overall more difficult to interpret since there are more non-zero weights for the prescribed cost function threshold than for the other parameters. It is however possible to note that the non-zero weights are mostly localized in the QRS complex biomarkers, suggesting that these parameters are more identifiable during this phase of the ECG. The conductivity parameters potentially have an effect onto the whole ECG duration since there are not involved in the cardiomyocytes ionic dynamics but rather in the passive diffusion of the whole tissue. However, the signal amplitude is higher during the QRS complex which may explain why their effect is more visible during this phase.
Finally, the numerical biomarker associated with the delay parameter δ_{stim}^{LV} is characterized by non-zero weights in the QRS complex and the ST segment. Note that this parameter is allowed to vary inside a small range (+/- 5ms) which one could consider healthy. Beyond this range, it corresponds to a pathology called bundle branch block which is investigated later in the present work.

6.3.1.3 Healthy test case 3

In this test case, a new strategy is adopted to model the ECG variability. In addition to varying six parameters of interest, other parameters, which we are not trying to identify, are allowed to vary. Here, the six parameters of interest are: g_{fi}^{RV}, g_{fi}^{endo}, g_{fi}^{epi}, g_{so}^{RV}, g_{so}^{endo} and g_{so}^{epi}. The other varying parameters are the four conductivity parameters σ_i^t, σ_e^t, σ_i^l, σ_e^l and stimulation delay $\delta_{\text{stim}}^{RV}$. Small variations of these parameters induce small perturbations of the resulting ECGs which may be seen as an additional noise and increase the robustness of the numerical biomarkers associated with the parameters of interest.

Numerical settings The training set is generated with $N = 1024$ samples drawn from a uniform distribution over the hypercube $[0.7, 1.3]^6$ for the six parameters of interest. For the other parameters, the samples are drawn from a uniform distribution over the hypercube $[1.96 \cdot 10^{-4}, 2.04 \cdot 10^{-4}] \times [5.88 \cdot 10^{-3}, 6.12 \cdot 10^{-3}] \times [1.96 \cdot$

$10^{-3}, 2.04 \cdot 10^{-3}] \times [1.96 \cdot 10^{-3}, 2.04 \cdot 10^{-3}] \times [-2, 2]$. The ℓ^1 regularization parameters values $\lambda_1, \ldots, \lambda_6$ are summarized in Table 6.3.

Results The numerical biomarkers weights are shown in Figure 6.10. As in the previous two test cases, the same observations can be made about the localization of the non-zero weights. Note however that, for each parameter, the weights found in this test case are different than those found in previous test cases. This highlights the fact that the numerical biomarkers strongly depend on the chosen set of varying parameters as well as on the bounding box of the parameters samples.

6.3.2 Numerical biomarkers in pathological conditions

We now focus on pathological conditions and aim at determining numerical biomarkers that are associated with these conditions.

6.3.2.1 Pathological test case 1: left or right ventricle infarction

The first pathological cases considered in this work are left and right ventricle infarction. A myocardial infarction is a zone where the cardiac tissue is not electrically active because of a lack of vascularization for instance. We choose to model this phenomenon in the infarcted zone by replacing in (6.1) the ionic current term I_{ion} by the following:

$$I'_{\text{ion}}(V_m, \mathbf{x}) = G_{\text{infarct}} I_{\text{ion}}(V_m, \mathbf{x}), \tag{6.8}$$

where G_{infarct} is a parameter controlling the degree of infarction, 1 being the healthy condition and 0 being a complete infarction. The infarcted zones considered in our case are spherical of radius 2cm and are located in the left ventricle in the first case and in the right ventricle in the second case as shown in Figure 6.7. In both cases, 5 parameters of interest are retained: g_{fi}^{RV}, g_{fi}^{endo}, g_{fi}^{MCell}, g_{fi}^{epi} and G_{infarct}. The idea is to build a numerical biomarker that is able to capture a left (or right) ventricle infarction regardless of natural variations of the activity of the sodium channels in the different regions of the heart.

Numerical settings The training set is generated with $N = 512$ samples drawn from a uniform distribution over Θ, where

$$\Theta = [0.8, 1.1]^4 \times [0, 1].$$

Note that the parameters samples are the same in both cases, the only difference in the simulated ECGs being the localization of the infarction.

Left ventricle Infarction For the left ventricle infarction, the ℓ^1 regularization parameters values $\lambda_1, \ldots, \lambda_5$ are summarized in Table 6.4. The weights are shown in Figure 6.11. The numerical biomarker associated with the G_{infarct} parameter has

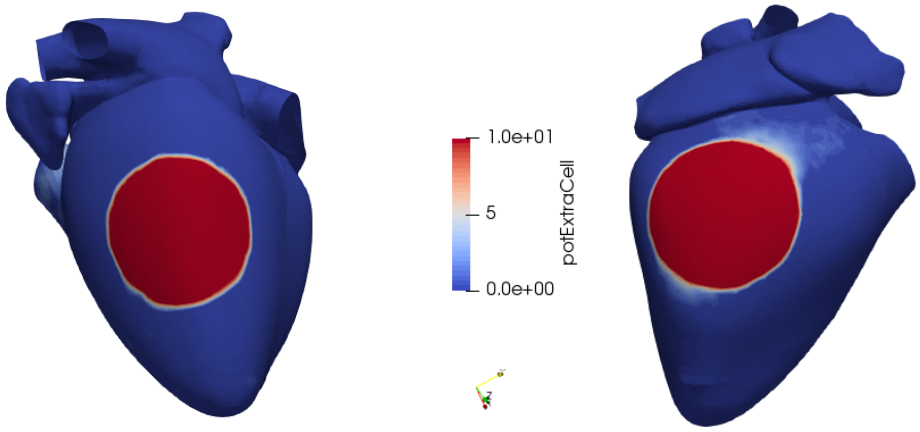

(a) Left ventricle infarction (b) Right ventricle infarction

Figure 6.7: Visualization of infarcted regions: healthy region in blue, infarcted region in red.

only three non-zero weights. These weights are associated with, in descending order of magnitude, the Q/S peak value of the aVL lead ($\text{QSPeak}^{\text{aVL}}$), the ST segment (plateau) height of the II and aVF leads (Qp200^{II} and $\text{Qp200}^{\text{aVF}}$). Interestingly, the elevation of the ST segment is clinically associated with an infarction [OKA+13, Dub84]. Furthermore, an infarction is also clinically revealed by modifications of the Q waves in the ECG [Dub84], which is also captured in the obtained numerical biomarkers. In practice, the leads where the abnormal Q waves are observed give an indication about the localization of the infarction. According to [Dub84], an abnormal Q wave in the aVL lead corresponds to a lateral infarction, which is the case in our synthetic model.

Right ventricle infarction For the right ventricle infarction, the ℓ^1 regularization parameters values $\lambda_1, \ldots, \lambda_5$ are summarized in Table 6.5. The weights are shown in Figure 6.12. Similarly to the left case, the non-zero weights are associated with the Q/S peak and the ST elevation. Another non-zero weight is present for the T wave (signed) amplitude of the third derivation. An inversion of the T wave (*i.e.* a change of its sign) or exaggerated amplitudes of the T wave may be the sign of an infarction in general, but not a sign of right ventricle infarction in particular. Note that right ventricular infarction happen less often than left ones [Dub84] which is why the position of the electrodes in the standard 12-lead ECG may not be suited to the detection of right ventricular infarction [GD01]. To obtain a more accurate diagnosis for the right ventricle infarction, practitioners use additional leads called right precordial leads [ZKK+93]. These extra leads require the use of more electrodes positioned at different locations on the torso, there are not discussed in the present work.

6.3.2.2 Pathological test case 2: left or right bundle branch block

The last pathological cases considered in this work are left and right bundle branch blocks (BBB). As explained in 6.2.1.3, this pathology corresponds to a delay of the electrical stimulation in either one of the ventricles. The pathology is modeled by increasing the delay parameter $\delta^{\text{LV}}_{\text{stim}}$. The left (resp. right) BBB is modeled by a positive (resp. negative) value of $\delta^{\text{LV}}_{\text{stim}}$. In both cases, 5 parameters of interest are retained: g^{RV}_{fi}, g^{endo}_{fi}, g^{MCell}_{fi}, g^{epi}_{fi} and $\delta^{\text{LV}}_{\text{stim}}$. Analogously to the infarction cases, the idea is to build a numerical biomarker that is able to capture a BBB regardless of natural variations of the activity of the sodium channels.

Numerical settings The training set is generated with $N = 512$ samples drawn from a uniform distribution over Θ_l for the left BBB and Θ_r for the right BBB, where

$$\Theta_l = [0.8, 1.1]^4 \times [0, 40]$$
$$\Theta_r = [0.8, 1.1]^4 \times [-40, 0].$$

Note that the parameter $\delta^{\text{LV}}_{\text{stim}}$ is a time, measured in ms.

Left bundle branch block For the left BBB, the ℓ^1 regularization parameters values $\lambda_1, \ldots, \lambda_5$ are summarized in Table 6.6. The weights are shown in Figure 6.13. The numerical biomarker associated with the left ventricle delay parameter has non-zero weights for the peak values of the QRS complex of lead II (RPeak^{II} and $\text{absPeak}^{\text{II}}$) and for the ST segment elevation (Qp100^{V1}). The QRS complex is affected by a left BBB since the left ventricle (being bigger and thicker than the right one) represents the highest electrical contribution to the ventricles depolarization. The left BBB is clinically associated with an elongation (in time) of the QRS complex [Dub84] which is not captured in this numerical experiment. One explanation would be that the non-zero weighted biomarkers are sufficient to reveal the BBB phenomenon in a synthetic case but that the QRS elongation biomarker is preferred in practice. A change of amplitude might be harder to visualize by a physician than a change of duration of the QRS complex. Note finally that the Qp100^{V1} biomarker measures the plateau height but can also capture a QRS elongation. Indeed, what is interpreted as a plateau might be in fact the end of the QRS complex in case the latter is pathologically elongated. This has to do with the way the biomarkers are extracted from the ECG signals and some modifications my be needed so that the QRS elongation appears in the numerical biomarker non-zero weights.

Right bundle branch block For the right BBB, the ℓ^1 regularization parameters values $\lambda_1, \ldots, \lambda_5$ are summarized in Table 6.7. The weights are shown in Figure 6.14. Contrary to the left BBB, this time the $\delta^{\text{LV}}_{\text{stim}}$ numerical biomarker does not include weight related to the QRS complex. This can be explained by the fact that, as explained earlier, the left ventricle is the major contributor to the QRS complex.

Delaying the right ventricle may not affect much the QRS amplitude. However, the same observation as before can be made about the biomarker $\mathrm{Qp200}^{\mathrm{V3}}$ which has a non-zero weight in the numerical biomarker associated with $\delta^{\mathrm{LV}}_{\mathrm{stim}}$. Though it measures an elevation of the ST segment, it might in fact be associated with an elongation of the QRS segment.

6.4 Conclusions and perspectives

In this work, we have presented a way to define numerical biomarkers for ECG signals. The computational model has been described. It consists of PDEs that model the electrical propagation at the tissue level and ODEs that describe the electrical dynamics at the cell scale. The ECG medical tool is presented and its *in silico* approximation is described. It consists of the bidomain equations for the heart, the passive conductor model for the rest of the body and the isolated heart assumption for the coupling between both regions. The parameters of interest in the context of the study are highlighted and the entries of the dictionary of features are described. Synthetic ECGs are generated by evaluating the computational model many times with different parameters values, with the addition of noise to the simulation outputs.
The method is first illustrated in healthy conditions. For each test case, a set of meaningful uncertain parameters is chosen. The obtained numerical biomarkers associated with these parameters of interest are described and their relevance discussed.
Finally, the method is applied to pathological conditions. We describe a model of the cardiac muscle infarction, which corresponds to a region where the tissue is so damaged that it is no longer electrically active. We consider two different locations for the infarction and compute the numerical biomarkers associated with the degree of infarction as well as other parameters that are susceptible to vary independently of the infarction. Interestingly, the non-zero weights obtained for the numerical biomarkers correspond to quantities that are actually used in a clinical context to diagnose infarctions. Second, we model bundle branch blocks in the left and right ventricles. The results are less clear than for the infarction cases in that the quantities clinically associated with bundle branch blocks are not visible in the non-zero weights. This is explained by the fact that the biomarkers extracted from the ECGs are well suited to the study of healthy signals but that they are more difficult to interpret in certain pathological cases.

As explained in the Introduction section, this work is a preliminary step towards the development of an inverse electrocardiography framework. The next step is to use the obtained numerical biomarkers to perform inverse problems (more specifically parameters estimations) with synthetic ECGs. As shown in Chapter 4, the use of such features (as opposed to the whole time series for instance) generally helps making the inverse problems less ill-posed and easier to solve in practice. The ultimate goal is to perform such inverse problems with real clinical data. Many chal-

lenges remain, such as how to deal with the modeling errors (and the inescapable gaps between real data and simulation outputs) and with natural variability not taken into account in our models. The use of biomarkers (instead of the raw time series) may help circumvent some of these issues. Furthermore, additional features may be defined to better reveal the effects of some parameters which remain difficult to observe.

Besides these forecasted additions to the inverse electrocardiography framework, other possible improvements to the overall model are presented in the following. First, the isolated heart assumption, despite not having much influence in certain scenarios, might prove to be insufficient in some cases where the electrical coupling between the heart and torso becomes essential (*e.g.* in the modeling of epicarditis and defibrillation). A domain decomposition approach using a Robin-Robin coupling between the heart and the body has been implemented in the FELiScE library but was not discussed in the present work. Second, the way the cardiac muscle is stimulated (both in the atria and ventricles) appears to be much influential in the ECG shape in practice. Beyond the possible delay in the ventricles stimulation (as seen in the bundle branch block examples), accurate modeling of the time and space evolution of the electrical stimulus is paramount.

6.5 Appendix

6.5.1 Figures and tables

N	λ_1	λ_2	λ_3	λ_4	λ_5	λ_6	λ_7
568	6.1	4.6	0.037	8.8	3.3	2.8	0.34

Table 6.1: Healthy test case 1: numerical biomarkers hyper-parameters.

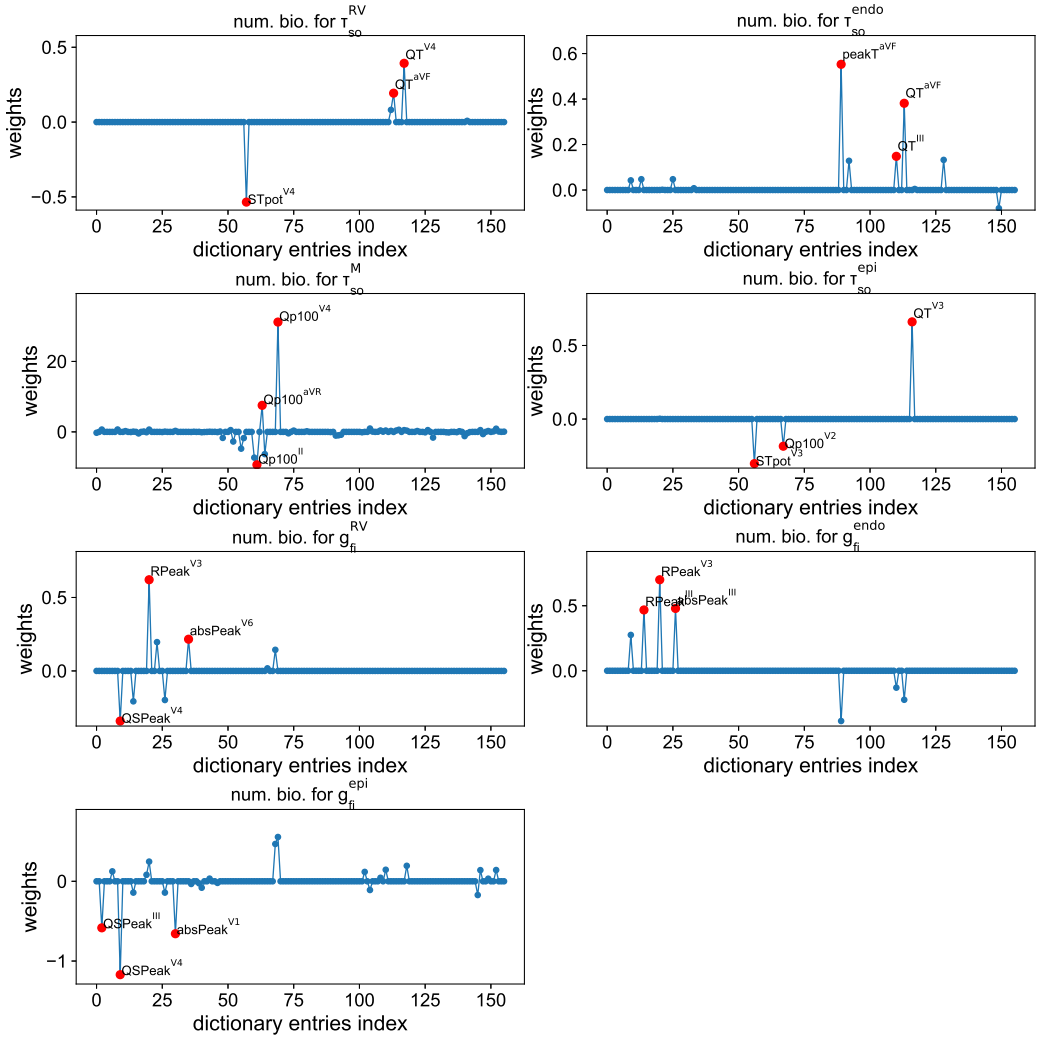

Figure 6.8: Healthy test case 1. Numerical biomarkers associated with: τ_{so}^{RV}, $\tau_{so}^{\mathrm{endo}}$, $\tau_{so}^{\mathrm{Mcell}}$, τ_{so}^{epi}, g_{fi}^{RV}, g_{fi}^{endo} and g_{fi}^{epi}.

N	λ_1	λ_2	λ_3	λ_4	λ_5	λ_6	λ_7	λ_8
576	2.2	0.17	0.34	0.41	0.076	4.56	4.5	10

Table 6.2: Healthy test case 2: numerical biomarkers hyper-parameters.

N	λ_1	λ_2	λ_3	λ_4	λ_5	λ_6
1024	0.78	0.29	0.12	7.6	5.6	10

Table 6.3: Healthy test case 3: numerical biomarkers hyper-parameters.

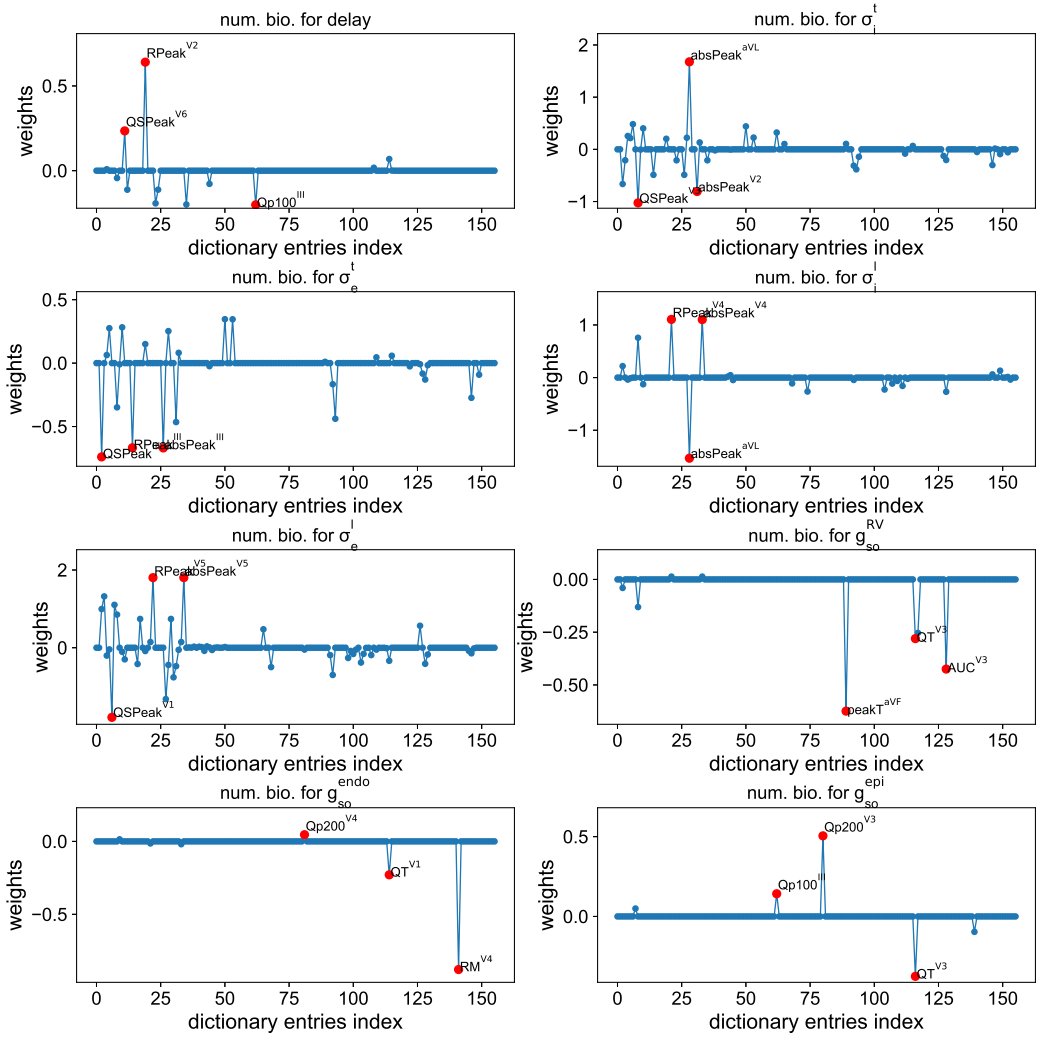

Figure 6.9: Healthy test case 2. Numerical biomarkers associated with: $\delta_{\text{stim}}^{RV}$, σ_i^t, σ_e^t, σ_i^l, σ_e^l, g_{so}^{RV}, g_{so}^{endo}, g_{so}^{epi}

N	λ_1	λ_2	λ_3	λ_4	λ_5
512	8.1	8.2	0.0027	17	13

Table 6.4: Pathological case 1a: left ventricle infarction. Numerical biomarkers hyper-parameters.

N	λ_1	λ_2	λ_3	λ_4	λ_5
512	11	0.73	0.0045	12	7.5

Table 6.5: Pathological case 1b: right ventricle infarction. Numerical biomarkers hyper-parameters.

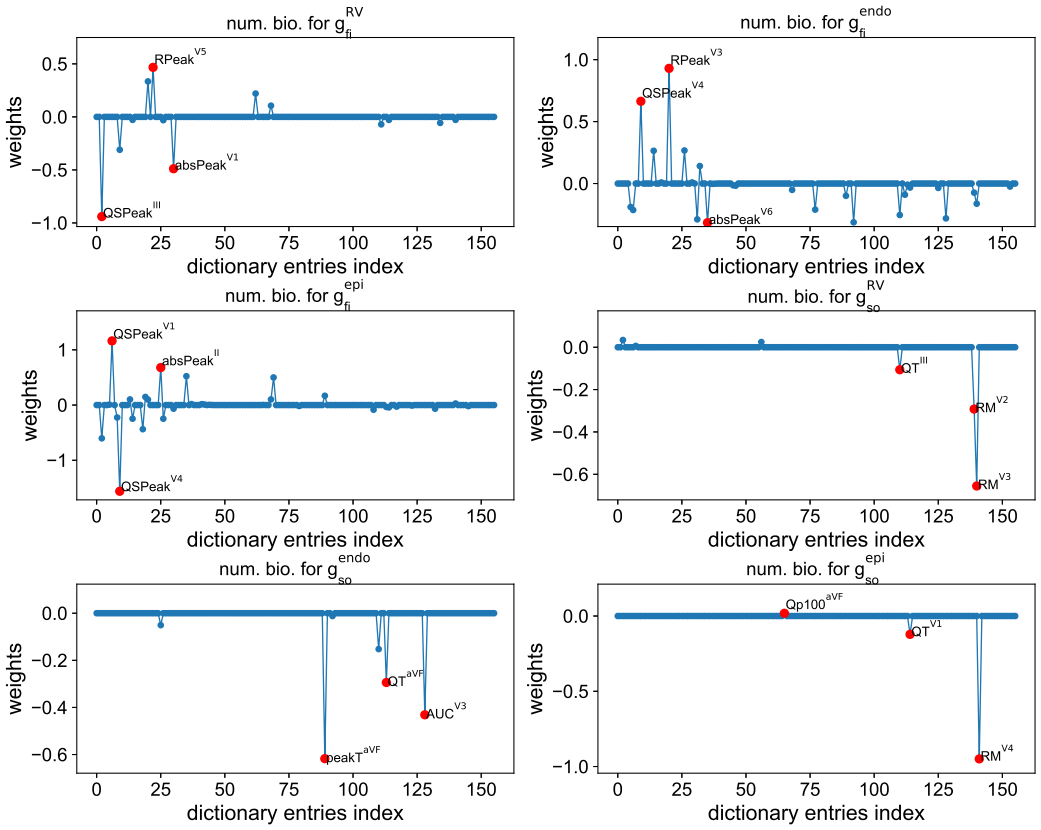

Figure 6.10: Healthy test case 3: Numerical biomarkers associated with: g_{fi}^{RV}, g_{fi}^{endo}, g_{fi}^{epi}, g_{so}^{RV}, g_{so}^{endo}, g_{so}^{epi}.

N	λ_1	λ_2	λ_3	λ_4	λ_5
512	0.94	0.091	0.001	1.7	12

Table 6.6: Pathological case 2a: left bundle branch block. Numerical biomarkers hyper-parameters.

N	λ_1	λ_2	λ_3	λ_4	λ_5
512	0.73	0.44	0.0016	18	24

Table 6.7: Pathological case 2b: right bundle branch block. Numerical biomarkers hyper-parameters.

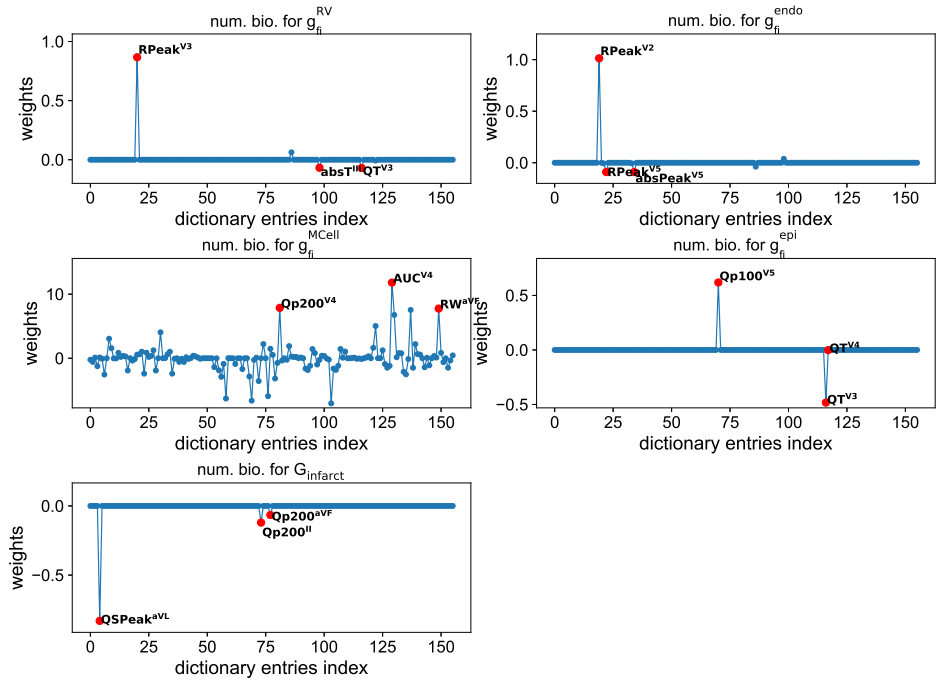

Figure 6.11: Pathological case 1a: left ventricle infarction. Numerical biomarkers associated with g_{fi}^{RV}, g_{fi}^{endo}, g_{fi}^{MCell}, g_{fi}^{epi} and G_{infarct}

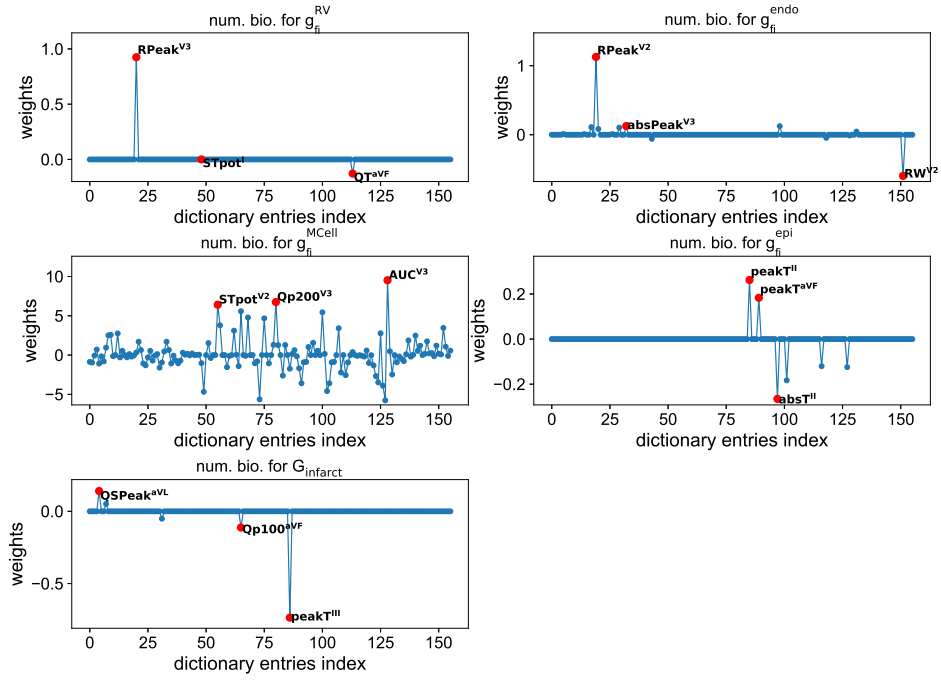

Figure 6.12: Pathological case 1b: right ventricle infarction. Numerical biomarkers associated with g_{fi}^{RV}, g_{fi}^{endo}, g_{fi}^{MCell}, g_{fi}^{epi} and G_{infarct}

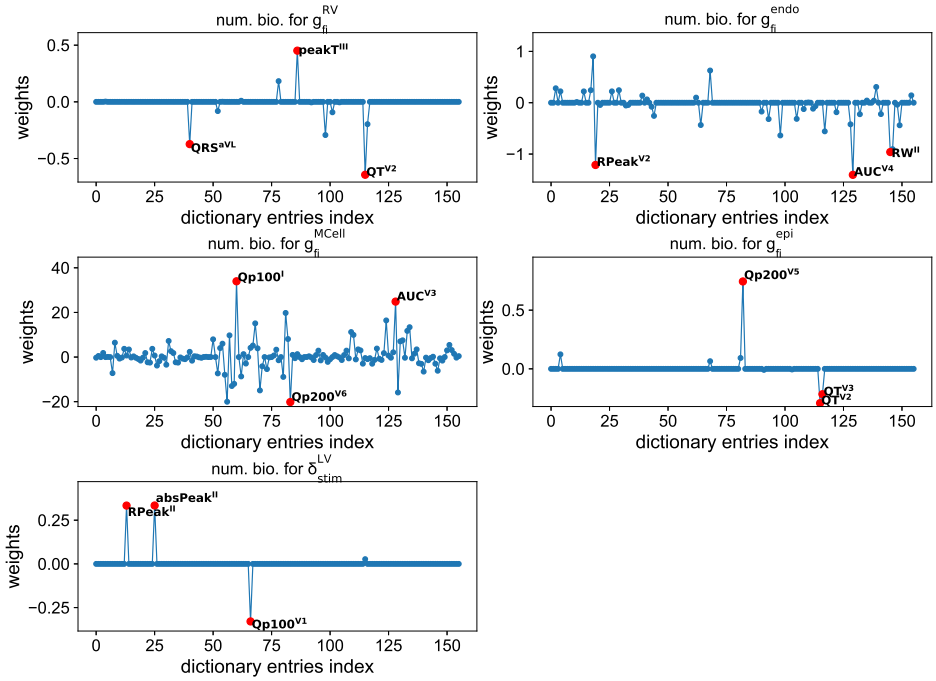

Figure 6.13: Pathological case 2a: left bundle branch block. Numerical biomarkers associated with g_{fi}^{RV}, g_{fi}^{endo}, g_{fi}^{MCell}, g_{fi}^{epi} and $\delta_{\text{stim}}^{\text{LV}}$

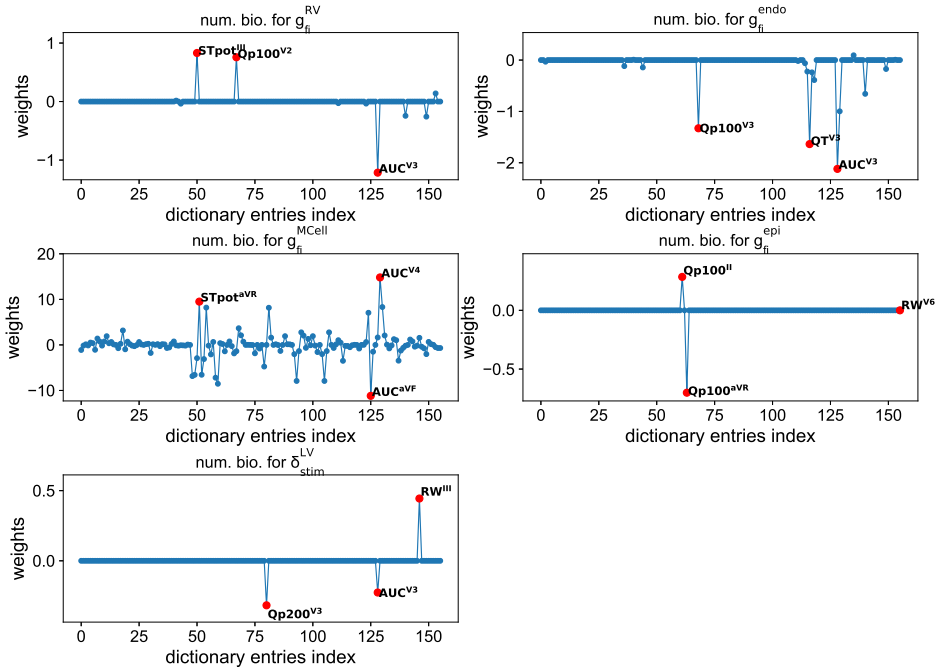

Figure 6.14: Pathological case 2b: right bundle branch block. Numerical biomarkers associated with g_{fi}^{RV}, g_{fi}^{endo}, g_{fi}^{MCell}, g_{fi}^{epi} and $\delta_{\text{stim}}^{\text{LV}}$

6.5.2 ECG leads definition

The 12 ECG leads are defined as follows:

$$\begin{array}{ll} \mathrm{I} = u_T(L) - u_T(R) & aVR = 1.5(u_T(R) - u_w) \\ \mathrm{II} = u_T(F) - u_T(R) & aVL = 1.5(u_T(L) - u_w) \\ \mathrm{III} = u_T(F) - u_T(L) & aVF = 1.5(u_T(F) - u_w) \\ V1 = u_T(V_1) - u_w & V4 = u_T(V_4) - u_w \\ V2 = u_T(V_2) - u_w & V5 = u_T(V_5) - u_w \\ V3 = u_T(V_3) - u_w & V6 = u_T(V_6) - u_w \end{array} \tag{6.9}$$

where $u_w = \frac{1}{3}(u_T(L) + u_T(R) + u_T(F))$ is the Wilson potential.

6.5.3 Definition of the biomarkers dictionary entries

Biomarkers abbreviations (subscript is added in the plots for corresponding lead):

- QSPeak: negative extremum of QRS complex (either Q or S wave depending on who's the highest in magnitude).
- RPeak: positive extremum of QRS.
- absPeak: max of QSPeak and RPeak.
- QRS: duration of the QRS complex.
- STPot: average lead potential between end of QRS complex and beginning of T wave.
- Qp100: lead potential 100ms after Q wave.
- Qp200: lead potential 200ms after Q wave.
- peakT: extremum value of T wave.
- absT: absolute value of peakT.
- QT: duration between beginning of Q wave and maximum of T wave.
- AUC: area under curve of T wave.
- RM: barycenter of T wave.
- RW: width of T wave.

Conclusions and Perspectives

This work was dedicated to the study of the variability in cardiac electrophysiology measurements and to the design of numerical biomarkers. We have presented original contributions to the development of numerical tools in order to solve the following questions that go beyond the scope of electrophysiology: Given a set of measurements and an associated computational model, what is the PDF of the model uncertain parameters that replicate the observed variability in the measurements? What are the best features to extract in order to perform specific tasks such as classification or solving parameter estimation problems? The numerical tools developed to address these issues have been validated with simple models, tested with realistic synthetic data and finally applied to real experimental measurements, both in healthy and pathological conditions.

In Chapter 2, we proposed a procedure to estimate the PDF of uncertain parameters from the knowledge of experimental moments of an observable. The procedure relies on two different algorithms. The first one finds the uncertain parameters PDF using the maximum entropy principle and the matching of observable moments on a set of model DOFs. The second one selects the subset of DOFs for which the moments constraints are to be matched to alleviate the first algorithm's computational cost. This approach has been compared to existing techniques on an ODE test case and illustrated with PDE models.

In Chapter 3, the proposed method is applied to electrophysiology data, and more precisely measurements at the cell scale. We have presented four different test cases where a variety of models and uncertain parameters are studied. For two of these test cases, the approach is successfully applied to experimental data coming from canine and human action potential measurements.

In Chapter 4, we proposed a method to compute numerical biomarkers. Given a dictionary of biomarkers, the numerical biomarkers are sought as linear combinations of their entries. Finding the numerical biomarkers boils down to finding the weights for each dictionary entry. The weights are found by solving a sparse optimization problem. We apply the method to simple models and to more complex biological systems, including synthetic MEA measurements. In Chapter 5, we address a practical drug safety pharmacology problem: classifying drugs with respect to their effect onto cardiomyocytes. The classification is made from experimental MEA measurements. We show that using the numerical biomarkers presented in the previous chapter, as opposed to classically used features, actually improves the classification results. In Chapter 6, we apply the numerical biomarkers method to ECG measurements. In different scenarios using synthetic measurements, we derive numerical biomarkers associated with key parameters of the heart electrical activity. We also apply the method to four pathological cases for which we obtain meaningful

numerical biomarkers.

Some promising extensions to the present work are now presented. Concerning the MEA (micro-electrode array) study, it has recently been proposed to add other types of measurements to increase the amount of information available in field potential measurements. The impedance [ZGZ+16] (the global resistance of the tissue) may for instance be measured as a function of time as well as the calcium ionic concentration which may be extracted using fluorescence recordings [GGS11]. Using *ad hoc* models of these different types of measurements, it would be possible to develop a multi-physics framework which could be applied, for instance, to drug safety pharmacology.

As for the ECG computational model, several additions could be made. First, a better understanding and modeling of the electrical stimulation in the atria and in the ventricles is necessary since it has much effect onto the simulated ECGs. Second, a first step towards the strong coupling between the heart and torso has been made by using a domain decomposition approach. However, the numerical method related to the Robin-Robin coupling should be improved in order to reduce its computational cost which should ideally be lower than solving the heart and torso monolithically.

Bibliography

[AA13] Aravind Alwan and Narayan R Aluru. Improved statistical models for limited datasets in uncertainty quantification using stochastic collocation. *Journal of Computational Physics*, 255:521–539, 2013.

[ABB+16] Chloe Audebert, Petru Bucur, Mohamed Bekheit, Eric Vibert, Irene E Vignon-Clementel, and Jean-Frédéric Gerbeau. Kinetic scheme for arterial and venous blood flow, and application to partial hepatectomy modeling. *Computer Methods in Applied Mechanics and Engineering*, 2016.

[ABC+17] E. Abbate, M. Boulakia, Y. Coudière, J-F. Gerbeau, P. Zitoun, and N. Zemzemi. In silico assessment of the effects of various compounds in MEA/hiPSC-CM assays: Modelling and numerical simulations. Research report, Inria, https://hal.inria.fr/hal-01562673, July 2017.

[AH00] Niall M. Adams and David J. Hand. Improving the practice of classifier performance assessment. *Neural computation*, 12(2):305–311, 2000.

[AM87] Didier G Arquès and Christian J Michel. Study of a perturbation in the coding periodicity. *Mathematical biosciences*, 86(1):1–14, 1987.

[AXL+12] Yama A Abassi, Biao Xi, Nan Li, Wei Ouyang, Alexander Seiler, Manfred Watzele, Ralf Kettenhofen, Heribert Bohlen, Andreas Ehlich, Eugen Kolossov, et al. Dynamic monitoring of beating periodicity of stem cell-derived cardiomyocytes as a predictive tool for preclinical safety assessment. *British journal of pharmacology*, 165(5):1424–1441, 2012.

[BBOVA+13] Oliver J Britton, Alfonso Bueno-Orovio, Karel Van Ammel, Hua Rong Lu, Rob Towart, David J Gallacher, and Blanca Rodriguez. Experimentally calibrated population of models predicts and explains intersubject variability in cardiac cellular electrophysiology. *Proceedings of the National Academy of Sciences*, 110(23):E2098–E2105, 2013.

[BCF+10] Muriel Boulakia, Serge Cazeau, Miguel A Fernández, Jean-Frédéric Gerbeau, and Nejib Zemzemi. Mathematical modeling of electrocardiograms: a numerical study. *Annals of biomedical engineering*, 38(3):1071–1097, 2010.

[BG04] Hans-Joachim Bungartz and Michael Griebel. Sparse grids. *Acta numerica*, 13:147–269, 2004.

[BGV92] Bernhard E Boser, Isabelle M Guyon, and Vladimir N Vapnik. A training algorithm for optimal margin classifiers. In *Proceedings of the fifth annual workshop on Computational learning theory*, pages 144–152. ACM, 1992.

[BJM+11] Francis Bach, Rodolphe Jenatton, Julien Mairal, Guillaume Obozinski, et al. Convex optimization with sparsity-inducing norms. *Optimization for Machine Learning*, 5:19–53, 2011.

[BNT07] Ivo Babuška, Fabio Nobile, and Raul Tempone. A stochastic collocation method for elliptic partial differential equations with random input data. *SIAM Journal on Numerical Analysis*, 45(3):1005–1034, 2007.

[BOCF08] Alfonso Bueno-Orovio, Elizabeth M Cherry, and Flavio H Fenton. Minimal model for human ventricular action potentials in tissue. *Journal of theoretical biology*, 253(3):544–560, 2008.

[BPS+06] D. Bottino, R. C. Penland, A. Stamps, M. Traebert, B. Dumotier, A. Georgieva, G. Helmlinger, and G. S. Lett. Preclinical cardiac safety assessment of pharmaceutical compounds using an integrated systems-based computer model of the heart. *Progress in biophysics and molecular biology*, 90(1):414–443, 2006.

[BVW+15] Stuart Barber, Jochen Voss, Mark Webster, et al. The rate of convergence for approximate bayesian computation. *Electronic Journal of Statistics*, 9(1):80–105, 2015.

[CABCL09] Ariel Cintrón-Arias, HT Banks, Alex Capaldi, and Alun L Lloyd. A sensitivity matrix based methodology for inverse problem formulation. *Journal of Inverse and Ill-Posed Problems*, 17(6):545–564, 2009.

[CBC+11] RH Clayton, Olivier Bernus, EM Cherry, Hans Dierckx, FH Fenton, L Mirabella, AV Panfilov, Frank B Sachse, G Seemann, and H Zhang. Models of cardiac tissue electrophysiology: progress, challenges and open questions. *Progress in biophysics and molecular biology*, 104(1):22–48, 2011.

[CCG13] Dominique Chapelle, Annabelle Collin, and Jean-Frédéric Gerbeau. A surface-based electrophysiology model relying on asymptotic analysis and motivated by cardiac atria modeling. *Mathematical Models and Methods in Applied Sciences*, 23(14):2749–2776, 2013.

[CCY+12] Fulong Chen, Angdi Chu, Xuefei Yang, Yao Lei, and Jizheng Chu. Identification of the parameters of the beeler–reuter ionic equation with a partially perturbed particle swarm optimization. *IEEE Transactions on Biomedical Engineering*, 59(12):3412–3421, 2012.

[CDE06] Mike Christie, Vasily Demyanov, and Demet Erbas. Uncertainty quantification for porous media flows. *Journal of Computational Physics*, 217(1):143–158, 2006.

[CDW14] Paul G Constantine, Eric Dow, and Qiqi Wang. Active subspace methods in theory and practice: Applications to kriging surfaces. *SIAM Journal on Scientific Computing*, 36(4):A1500–A1524, 2014.

[CELI15] Paul G Constantine, Michael Emory, Johan Larsson, and Gianluca Iaccarino. Exploiting active subspaces to quantify uncertainty in the numerical simulation of the hyshot ii scramjet. *Journal of Computational Physics*, 302:1–20, 2015.

[CGB+16] I. Cavero, J-M. Guillon, V. Ballet, M. Clements, J-F. Gerbeau, and H. Holzgrefe. Comprehensive in vitro proarrhythmia assay (cipa): Pending issues for successful validation and implementation. *Journal of pharmacological and toxicological methods*, 81:21–36, 2016.

[CH96] Scott D Cohen and Alan C Hindmarsh. Cvode, a stiff/nonstiff ode solver in c. *Computers in physics*, 10(2):138–143, 1996.

[CL11] Chih-Chung Chang and Chih-Jen Lin. Libsvm: a library for support vector machines. *ACM transactions on intelligent systems and technology (TIST)*, 2(3):27, 2011.

[CLN+03] Autumn A Cuellar, Catherine M Lloyd, Poul F Nielsen, David P Bullivant, David P Nickerson, and Peter J Hunter. An overview of cellml 1.1, a biological model description language. *Simulation*, 79(12):740–747, 2003.

[CLPS03] Yang Cao, Shengtai Li, Linda Petzold, and Radu Serban. Adjoint sensitivity analysis for differential-algebraic equations: The adjoint dae system and its numerical solution. *SIAM Journal on Scientific Computing*, 24(3):1076–1089, 2003.

[CNLH04] John C Clements, Jukka Nenonen, PKJ Li, and B Milan Horáček. Activation dynamics in anisotropic cardiac tissue via decoupling. *Annals of biomedical engineering*, 32(7):984–990, 2004.

[Col14] Annabelle Collin. *Analyse asymptotique en électrophysiologie cardiaque: applications à la modélisation et à l'assimilation de données.* PhD thesis, Paris 6, 2014.

[Con15] Paul G Constantine. *Active Subspaces: Emerging Ideas for Dimension Reduction in Parameter Studies.* SIAM, 2015.

[CRN98] Marc Courtemanche, Rafael J Ramirez, and Stanley Nattel. Ionic mechanisms underlying human atrial action potential properties: insights from a mathematical model. *American Journal of Physiology-Heart and Circulatory Physiology*, 275(1):H301–H321, 1998.

[CT14] Mike Clements and Nick Thomas. High-throughput multi-parameter profiling of electrophysiological drug effects in human embryonic stem cell derived cardiomyocytes using multi-electrode arrays. *Toxicological Sciences*, 140(2):445–461, 2014.

[CWV+08] T Christ, E Wettwer, N Voigt, O Hala, S Radicke, K Matschke, A Varro, D Dobrev, and U Ravens. Pathology-specific effects of the ikur/ito/ik, ach blocker ave0118 on ion channels in human chronic atrial fibrillation. *British journal of pharmacology*, 154(8):1619–1630, 2008.

[DCP+16] C. C. Drovandi, N. Cusimano, S. Psaltis, B. A. J. Lawson, A. N. Pettitt, P. Burrage, and K. Burrage. Sampling methods for exploring between-subject variability in cardiac electrophysiology experiments. *Journal of The Royal Society Interface*, 13(121), 2016.

[DDM17] Shaun M Davidson, Paul D Docherty, and Rua Murray. The dimensional reduction method for identification of parameters that trade-off due to similar model roles. *Mathematical Biosciences*, 285:119–127, 2017.

[DHS+09] Keith F Decker, Jordi Heijman, Jonathan R Silva, Thomas J Hund, and Yoram Rudy. Properties and ionic mechanisms of action potential adaptation, restitution, and accommodation in canine epicardium. *American Journal of Physiology-Heart and Circulatory Physiology*, 296(4):H1017–H1026, 2009.

[DL04] Socrates Dokos and Nigel H Lovell. Parameter estimation in cardiac ionic models. *Progress in biophysics and molecular biology*, 85(2):407–431, 2004.

[DLR77] Arthur P Dempster, Nan M Laird, and Donald B Rubin. Maximum likelihood from incomplete data via the em algorithm. *Journal of the royal statistical society. Series B (methodological)*, pages 1–38, 1977.

[DMH+11] Mark Richard Davies, Hitesh Balvanta Mistry, Leyla Hussein, Chris E Pollard, Jean-Pierre Valentin, Jonathan Swinton, and Najah Abi-Gerges. An in silico canine cardiac midmyocardial action potential duration model as a tool for early drug safety assessment. *American Journal of Physiology-Heart and Circulatory Physiology*, 2011.

[DR03] Dobromir Dobrev and Ursula Ravens. Remodeling of cardiomyocyte ion channels in human atrial fibrillation. *Basic research in cardiology*, 98(3):137–148, 2003.

[Dub84] Dale Dubin. *Lecture accélérée de l'ECG: un enseignement programmé pour une interprétation systématique des électrocardiogrammes*. Maloine, 1984.

[DWM+16] Mark R Davies, Ken Wang, Gary R Mirams, Antonello Caruso, Denis Noble, Antje Walz, Thierry Lavé, Franz Schuler, Thomas Singer, and Liudmila Polonchuk. Recent developments in using mechanistic cardiac modelling for drug safety evaluation. *Drug Discovery Today*, 2016.

[Fis30] Ronald Aylmer Fisher. *The genetical theory of natural selection: a complete variorum edition*. Oxford University Press, 1930.

[FQV10] Luca Formaggia, Alfio Quarteroni, and Alessandro Veneziani. *Cardiovascular Mathematics: Modeling and simulation of the circulatory system*, volume 1. Springer Science & Business Media, 2010.

[GB15] R Gul and S Bernhard. Parametric uncertainty and global sensitivity analysis in a model of the carotid bifurcation: Identification and ranking of most sensitive model parameters. *Mathematical Biosciences*, 269:104–116, 2015.

[GBRQ14] Philip Gemmell, Kevin Burrage, Blanca Rodriguez, and T Alexander Quinn. Population of computational rabbit-specific ventricular action potential models for investigating sources of variability in cellular repolarisation. *PLoS One*, 9(2):e90112, 2014.

[GD01] D Luke Glancy and Waleed Doghmi. Use of indicative and reciprocal electrocardiographic changes to help localize the site of coronary occlusion. *Proceedings (Baylor University. Medical Center)*, 14(1):104, 2001.

[GE03] Isabelle Guyon and André Elisseeff. An introduction to variable and feature selection. *Journal of machine learning research*, 3(Mar):1157–1182, 2003.

[GGb81] Ary Louis Goldberger and Emanuel Gold-berger. Clinical electrocardiography, a simplified approach. *Critical Care Medicine*, 9(12):891–892, 1981.

[GGS11] Silvia Guatimosim, Cristina Guatimosim, and Long-Sheng Song. Imaging calcium sparks in cardiac myocytes. *Light Microscopy: Methods and Protocols*, pages 205–214, 2011.

[GLMG06] P Gokulakrishnan, AD Lawrence, PJ McLellan, and EW Grandmaison. A functional-pca approach for analyzing and reducing complex chemical mechanisms. *Computers & chemical engineering*, 30(6):1093–1101, 2006.

[GLT16] Jean-Frédéric Gerbeau, Damiano Lombardi, and Eliott Tixier. A moment-matching method to study the variability of phenomena described by partial differential equations. https://hal.archives-ouvertes.fr/hal-01391254, 2016.

[GLT17] J-F. Gerbeau, D. Lombardi, and E. Tixier. How to choose biomarkers in view of parameter estimation. submitted for publication, 2017.

[GLV14] Emmanuel Grenier, Violaine Louvet, and Paul Vigneaux. Parameter estimation in non-linear mixed effects models with saem algorithm: extension from ode to pde. *ESAIM: Mathematical Modelling and Numerical Analysis*, 48(5):1303–1329, 2014.

[GNSG11] J Guilleminot, A Noshadravan, C Soize, and RG Ghanem. A probabilistic model for bounded elasticity tensor random fields with application to polycrystalline microstructures. *Computer Methods in Applied Mechanics and Engineering*, 200(17):1637–1648, 2011.

[GS13] Johann Guilleminot and Christian Soize. On the statistical dependence for the components of random elasticity tensors exhibiting material symmetry properties. *Journal of elasticity*, 111(2):109–130, 2013.

[GW08] Andreas Griewank and Andrea Walther. *Evaluating derivatives: principles and techniques of algorithmic differentiation*. Siam, 2008.

[GZ07] Baskar Ganapathysubramanian and Nicholas Zabaras. Sparse grid collocation schemes for stochastic natural convection problems. *Journal of Computational Physics*, 225(1):652–685, 2007.

[Han06] Nikolaus Hansen. The cma evolution strategy: a comparing review. In *Towards a new evolutionary computation*, pages 75–102. Springer, 2006.

[HBG+05] Alan C Hindmarsh, Peter N Brown, Keith E Grant, Steven L Lee, Radu Serban, Dan E Shumaker, and Carol S Woodward. Sundials: Suite of nonlinear and differential/algebraic equation solvers. *ACM Transactions on Mathematical Software (TOMS)*, 31(3):363–396, 2005.

[HDL07] Ben BCB Hui, Socrates Dokos, and Nigel H Lovell. Parameter identifiability of cardiac ionic models using a novel cellml least squares optimization tool. In *2007 29th Annual International Conference of*

the IEEE Engineering in Medicine and Biology Society, pages 5307–5310. IEEE, 2007.

[Hec12] F. Hecht. New development in freefem++. *J. Numer. Math.*, 20(3-4):251–265, 2012.

[HLM14] Didier Henrion, Jean B Lasserre, and Martin Mevissen. Mean squared error minimization for inverse moment problems. *Applied Mathematics & Optimization*, 70(1):83–110, 2014.

[HMN+81] Owen P Hamill, A Marty, Erwin Neher, Bert Sakmann, and FJ Sigworth. Improved patch-clamp techniques for high-resolution current recording from cells and cell-free membrane patches. *Pflügers Archiv European journal of physiology*, 391(2):85–100, 1981.

[HNGK09] Nikolaus Hansen, André SP Niederberger, Lino Guzzella, and Petros Koumoutsakos. A method for handling uncertainty in evolutionary optimization with an application to feedback control of combustion. *Evolutionary Computation, IEEE Transactions on*, 13(1):180–197, 2009.

[HO14] Christian Himpe and Mario Ohlberger. Cross-gramian-based combined state and parameter reduction for large-scale control systems. *Mathematical Problems in Engineering*, 2014, 2014.

[HR04] Thomas J Hund and Yoram Rudy. Rate dependence and regulation of action potential and calcium transient in a canine cardiac ventricular cell model. *Circulation*, 110(20):3168–3174, 2004.

[HW08] Florian Heiss and Viktor Winschel. Likelihood approximation by numerical integration on sparse grids. *Journal of Econometrics*, 144(1):62–80, 2008.

[Jay57] Edwin T Jaynes. Information theory and statistical mechanics. *Physical review*, 106(4):620, 1957.

[JCB+15] Ross H Johnstone, Eugene TY Chang, Rémi Bardenet, Teun P De Boer, David J Gavaghan, Pras Pathmanathan, Richard H Clayton, and Gary R Mirams. Uncertainty and variability in models of the cardiac action potential: Can we build trustworthy models? *Journal of molecular and cellular cardiology*, 2015.

[JG00] Peter R Johnston and Ramesh M Gulrajani. Selecting the corner in the l-curve approach to tikhonov regularization. *IEEE Transactions on biomedical engineering*, 47(9):1293–1296, 2000.

[KFWV06] C Krier, D Francois, V Wertz, and M Verleysen. Feature scoring by mutual information for classification of mass spectra. In *7th International FLINS Conference on Applied Artificial Intelligence (FLINS 06)*, pages –, 2006.

[KL05] Estelle Kuhn and Marc Lavielle. Maximum likelihood estimation in nonlinear mixed effects models. *Computational Statistics & Data Analysis*, 49(4):1020–1038, 2005.

[KNV14] Jaspreet Kaur, Anders Nygren, and Edward J Vigmond. Fitting membrane resistance in single cardiac myocytes reduces variability in parameters. In *Computing in Cardiology 2014*, pages 209–212. IEEE, 2014.

[Kog09] Boris Ja Kogan. *Introduction to computational cardiology: mathematical modeling and computer simulation*. Springer Science & Business Media, 2009.

[KOPM+13] James Kramer, Carlos A Obejero-Paz, Glenn Myatt, Yuri A Kuryshev, Andrew Bruening-Wright, Joseph S Verducci, and Arthur M Brown. Mice models: superior to the herg model in predicting torsade de pointes. *Scientific reports*, 3, 2013.

[Kou09] Phaedon-Stelios Koutsourelakis. A multi-resolution, non-parametric, bayesian framework for identification of spatially-varying model parameters. *Journal of computational physics*, 228(17):6184–6211, 2009.

[KS06] Jari Kaipio and Erkki Somersalo. *Statistical and computational inverse problems*, volume 160. Springer Science & Business Media, 2006.

[KSMT14] Jussi T Koivumäki, Gunnar Seemann, Mary M Maleckar, and Pasi Tavi. In silico screening of the key cellular remodeling targets in chronic atrial fibrillation. *PLoS Comput Biol*, 10(5):e1003620, 2014.

[KSW+07] David UJ Keller, Gunnar Seemann, Daniel L Weiss, Dimitry Farina, Jorg Zehelein, and Olaf Dossel. Computer based modeling of the congenital long-qt 2 syndrome in the visible man torso: From genes to ecg. In *Engineering in Medicine and Biology Society, 2007. EMBS 2007. 29th Annual International Conference of the IEEE*, pages 1410–1413. IEEE, 2007.

[Lem09] Christiane Lemieux. *Monte carlo and quasi-monte carlo sampling*. Springer Science & Business Media, 2009.

[LFNR16] Daniel M Lombardo, Flavio H Fenton, Sanjiv M Narayan, and Wouter-Jan Rappel. Comparison of detailed and simplified models of human atrial myocytes to recapitulate patient specific properties. *PLOS Comput Biol*, 12(8):e1005060, 2016.

[LHS+16] Young-Seon Lee, Minki Hwang, Jun-Seop Song, Changyong Li, Boyoung Joung, Eric A Sobie, and Hui-Nam Pak. The contribution of ionic currents to rate-dependent action potential duration and pattern of reentry in a mathematical model of human atrial fibrillation. *PloS one*, 11(3):e0150779, 2016.

[Lix14] Lixoft. *Monolix Software, Version 4.3.2*. Orsay, France, 2014.

[LR94] Ching-hsing Luo and Yoram Rudy. A dynamic model of the cardiac ventricular action potential. i. simulations of ionic currents and concentration changes. *Circulation research*, 74(6):1071–1096, 1994.

[LS16] M Cummins Lancaster and EA Sobie. Improved prediction of drug-induced torsades de pointes through simulations of dynamics and machine learning algorithms. *Clinical Pharmacology & Therapeutics*, 100(4):371–379, 2016.

[LW67] GN Lance and WT Williams. A general theory of classificatory sorting strategies. 1 hierarchical systems. *Computer Journal*, 9:373–380, 1967.

[MAP+07] Koen S Matthys, Jordi Alastruey, Joaquim Peiró, Ashraf W Khir, Patrick Segers, Pascal R Verdonck, Kim H Parker, and Spencer J Sherwin. Pulse wave propagation in a model human arterial network: assessment of 1-d numerical simulations against in vitro measurements. *Journal of biomechanics*, 40(15):3476–3486, 2007.

[MBG+16] Anna Muszkiewicz, Oliver J Britton, Philip Gemmell, Elisa Passini, Carlos Sánchez, Xin Zhou, Annamaria Carusi, T Alexander Quinn, Kevin Burrage, Alfonso Bueno-Orovio, et al. Variability in cardiac electrophysiology: using experimentally-calibrated populations of models to move beyond the single virtual physiological human paradigm. *Progress in biophysics and molecular biology*, 120(1):115–127, 2016.

[MBGF04] Thomas Meyer, Karl-Heinz Boven, Elke Günther, and Michael Fejtl. Micro-electrode arrays in cardiac safety pharmacology. *Drug Safety*, 27(11):763–772, 2004.

[MCS+11] G. Mirams, Y. Cui, A. Sher, M. Fink, J. Cooper, B. Heath, N. McMahon, D. Gavaghan, and D. Noble. Simulation of multiple ion channel block provides improved early prediction of compounds clinical torsadogenic risk. *Cardiovascular research*, 91(1):53–61, 2011.

[MLKDC10] Marc Massot, Frédérique Laurent, Damien Kah, and Stephane De Chaisemartin. A robust moment method for evaluation of the disappearance rate of evaporating sprays. *SIAM Journal on Applied Mathematics*, 70(8):3203–3234, 2010.

[MP84] L. R. Mead and N. Papanicolaou. Maximum entropy in the problem of moments. *Journal of Mathematical Physics*, 25(8):2404–2417, 1984.

[MT11] Eve Marder and Adam L Taylor. Multiple models to capture the variability in biological neurons and networks. *Nature neuroscience*, 14(2):133–138, 2011.

[NCL07] Bjørn Fredrik Nielsen, Xing Cai, and Marius Lysaker. On the possibility for computing the transmembrane potential in the heart with a one shot method: An inverse problem. *Mathematical biosciences*, 210(2):523–553, 2007.

[Nes83] Yurii Nesterov. A method of solving a convex programming problem with convergence rate o (1/k2). In *Soviet Mathematics Doklady*, volume 27, pages 372–376, 1983.

[OC15] Brendan O'Donoghue and Emmanuel Candes. Adaptive restart for accelerated gradient schemes. *Foundations of computational mathematics*, 15(3):715–732, 2015.

[OKA+13] Patrick T O'Gara, Frederick G Kushner, Deborah D Ascheim, Donald E Casey, Mina K Chung, James A De Lemos, Steven M Ettinger, James C Fang, Francis M Fesmire, Barry A Franklin, et al. 2013 accf/aha guideline for the management of st-elevation myocardial infarction. *Journal of the American College of Cardiology*, 61(4):e78–e140, 2013.

[OMO14] Johnny T Ottesen, Jesper Mehlsen, and Mette S Olufsen. Structural correlation method for model reduction and practical estimation of patient specific parameters illustrated on heart rate regulation. *Mathematical biosciences*, 257:50–59, 2014.

[PDB+16] E Pueyo, CE Dangerfield, OJ Britton, L Virág, K Kistamás, N Szentandrássy, N Jost, A Varró, PP Nánási, K Burrage, et al. Experimentally-based computational investigation into beat-to-beat variability in ventricular repolarization and its response to ionic current inhibition. *PloS one*, 11(3):e0151461, 2016.

[PL15] Sanjay Pant and Damiano Lombardi. An information-theoretic approach to assess practical identifiability of parametric dynamical systems. *Mathematical biosciences*, 268:66–79, 2015.

[Pow09] Michael JD Powell. The bobyqa algorithm for bound constrained optimization without derivatives. *Cambridge NA Report NA2009/06, University of Cambridge, Cambridge*, 2009.

[PS09] Edoardo Patelli and Gerhart Schuëller. On optimization techniques to reconstruct microstructures of random heterogeneous media. *Computational Materials Science*, 45(2):536–549, 2009.

[PVG+11] F. Pedregosa, G. Varoquaux, A. Gramfort, V. Michel, B. Thirion, O. Grisel, M. Blondel, P. Prettenhofer, R. Weiss, V. Dubourg, J. Vanderplas, A. Passos, D. Cournapeau, M. Brucher, M. Perrot, and E. Duchesnay. Scikit-learn: Machine learning in Python. *Journal of Machine Learning Research*, 12:2825–2830, 2011.

[RBZ+17] F. Raphel, M. Boulakia, C. Zemzemi, Y. Coudière, J-M. Guillon, P. Zitoun, and J-F. Gerbeau. Identification of ion currents components generating field potential recorded in MEA from hiPSC-CM. Preprint available at https://hal.inria.fr/hal-01570341, 2017.

[RKÖW+15] Ursula Ravens, Deniz Katircioglu-Öztürk, Erich Wettwer, Torsten Christ, Dobromir Dobrev, Niels Voigt, Claire Poulet, Simone Loose, Jana Simon, Agnes Stein, et al. Application of the rimarc algorithm to a large data set of action potentials and clinical parameters for risk prediction of atrial fibrillation. *Medical & biological engineering & computing*, 53(3):263–273, 2015.

[RMP+09] Philippe Reymond, Fabrice Merenda, Fabienne Perren, Daniel Rüfenacht, and Nikos Stergiopulos. Validation of a one-dimensional model of the systemic arterial tree. *American Journal of Physiology-Heart and Circulatory Physiology*, 297(1):H208–H222, 2009.

[Ros95] Jeffrey S Rosenthal. Minorization conditions and convergence rates for markov chain monte carlo. *Journal of the American Statistical Association*, 90(430):558–566, 1995.

[RPFR09] Lucía Romero, Esther Pueyo, Martin Fink, and Blanca Rodríguez. Impact of ionic current variability on human ventricular cellular electrophysiology. *American Journal of Physiology-Heart and Circulatory Physiology*, 297(4):H1436–H1445, 2009.

[Rus10] Trent Michael Russi. Uncertainty quantification with experimental data and complex system models. *Ph.D. Thesis*, 2010.

[SBOW+14] Carlos Sánchez, Alfonso Bueno-Orovio, Erich Wettwer, Simone Loose, Jana Simon, Ursula Ravens, Esther Pueyo, and Blanca Rodriguez. Inter-subject variability in human atrial action potential in sinus rhythm versus chronic atrial fibrillation. *PloS one*, 9(8):e105897, 2014.

[SCG16] Elisa Schenone, Annabelle Collin, and Jean-Frédéric Gerbeau. Numerical simulation of electrocardiograms for full cardiac cycles in healthy and pathological conditions. *International journal for numerical methods in biomedical engineering*, 32(5), 2016.

[Sch14] Elisa Schenone. *Reduced order models, forward and inverse problems in cardiac electrophysiology.* PhD thesis, Université Pierre et Marie Curie-Paris VI, 2014.

[SFB06] Stefan Streif, Rolf Findeisen, and Eric Bullinger. Relating cross gramians and sensitivity analysis in systems biology. In *Proceedings of the 17th International Symposium on Mathematical Theory of Networks and Systems*, pages 437–441, Kyoto, Japan, July 2006.

[Sha48] C E Shannon. A mathematical theory of distribution. *Bell System Technical Journal*, 27:623, 1948.

[SHM+15] Rami Shinnawi, Irit Huber, Leonid Maizels, Naim Shaheen, Amira Gepstein, Gil Arbel, Anke J Tijsen, and Lior Gepstein. Monitoring human-induced pluripotent stem cell-derived cardiomyocytes with genetically encoded calcium and voltage fluorescent reporters. *Stem cell reports*, 5(4):582–596, 2015.

[SLT05] Joakim Sundnes, Glenn Terje Lines, and Aslak Tveito. An operator splitting method for solving the bidomain equations coupled to a volume conductor model for the torso. *Mathematical biosciences*, 194(2):233–248, 2005.

[Sob76] Ilya M Sobol. Uniformly distributed sequences with an additional uniform property. *USSR Computational Mathematics and Mathematical Physics*, 16(5):236–242, 1976.

[SPD13] Clay W Scott, Matthew F Peters, and Yvonne P Dragan. Human induced pluripotent stem cells and their use in drug discovery for toxicity testing. *Toxicology letters*, 219(1):49–58, 2013.

[SS02] Bernhard Schölkopf and Alexander J Smola. *Learning with kernels: support vector machines, regularization, optimization, and beyond.* MIT press, 2002.

[SS10] Amrita X Sarkar and Eric A Sobie. Regression analysis for constraining free parameters in electrophysiological models of cardiac cells. *PLoS Comput Biol*, 6(9):e1000914, 2010.

[ST43] James Alexander Shohat and Jacob David Tamarkin. *The problem of moments.* American Mathematical Society, 1943.

[Str68] Gilbert Strang. On the construction and comparison of difference schemes. *SIAM Journal on Numerical Analysis*, 5(3):506–517, 1968.

[SVNL05] Z Syed, E Vigmond, S Nattel, and LJ Leon. Atrial cell action potential parameter fitting using genetic algorithms. *Medical and Biological Engineering and Computing*, 43(5):561–571, 2005.

[Sys] Multichannel Systems. Microelectrode array (mea) manual. http://www.multichannelsystems.com/sites/multichannelsystems.com/files/documents/manuals/MEA_Manual.pdf, -.

[SZ06] S. Sankaran and N. Zabaras. A maximum entropy approach for property prediction of random microstructures. *Acta Materialia*, 54(8):2265–2276, 2006.

[TDP+04] M-C Trudel, Bruno Dubé, Mark Potse, Ramesh M Gulrajani, and L Joshua Leon. Simulation of qrst integral maps with a membrane-based computer heart model employing parallel processing. *IEEE Transactions on Biomedical Engineering*, 51(8):1319–1329, 2004.

[Tib96] Robert Tibshirani. Regression shrinkage and selection via the lasso. *Journal of the Royal Statistical Society. Series B (Methodological)*, pages 267–288, 1996.

[TLRG17] Eliott Tixier, Damiano Lombardi, Blanca Rodriguez, and Jean-Frédéric Gerbeau. Modelling variability in cardiac electrophysiology: a moment-matching approach. *Journal of the Royal Society Interface*, 14(133), 2017.

[TRLG17] Eliott Tixier, Fabien Raphel, Damiano Lombardi, and Jean-Frédéric Gerbeau. Optimal Biomarkers Design for Drug Safety Evaluation Using Microelectrode Array Measurements. working paper or preprint, July 2017.

[Tun78] L. Tung. *A bi-domain model for describing ischemic myocardial D–C potentials*. PhD thesis, MIT, 1978.

[VdSB08] Erik Van der Straeten and Christian Beck. Superstatistical distributions from a maximum entropy principle. *Physical Review E*, 78(5):051101, 2008.

[VWPL+99] David R Van Wagoner, Amber L Pond, Michelle Lamorgese, Sandra S Rossie, Patrick M McCarthy, and Jeanne M Nerbonne. Atrial l-type ca2+ currents and human atrial fibrillation. *Circulation research*, 85(5):428–436, 1999.

[WG69] John C Wheeler and RG Gordon. Rigorous bounds for thermodynamic properties of harmonic solids. *The Journal of Chemical Physics*, 51(12):5566–5583, 1969.

[WHC+04] Erich Wettwer, Ottó Hála, Torsten Christ, Jürgen F Heubach, Dobromir Dobrev, Michael Knaut, András Varró, and Ursula Ravens. Role of ikur in controlling action potential shape and contractility in the human atrium influence of chronic atrial fibrillation. *Circulation*, 110(16):2299–2306, 2004.

[WHM+13] Mathias Wilhelms, Hanne Hettmann, Mary M Maleckar, Jussi T Koivumäki, Olaf Dössel, and Gunnar Seemann. Benchmarking electrophysiological models of human atrial myocytes. *Front Physiol*, 3:487, 2013.

[WRWD84] Svante Wold, Arnold Ruhe, Herman Wold, and WJ Dunn, III. The collinearity problem in linear regression. the partial least squares (pls) approach to generalized inverses. *SIAM Journal on Scientific and Statistical Computing*, 5(3):735–743, 1984.

[WZ04] Jingbo Wang and Nicholas Zabaras. A bayesian inference approach to the inverse heat conduction problem. *International Journal of Heat and Mass Transfer*, 47(17):3927–3941, 2004.

[YFLN96] LIXIA Yue, JIANLIN Feng, GR Li, and STANLEY Nattel. Transient outward and delayed rectifier currents in canine atrium: properties and role of isolation methods. *American Journal of Physiology-Heart and Circulatory Physiology*, 270(6):H2157–H2168, 1996.

[YGPD13] Sylvia Young, Michael E Goddard, Jennie E Pryce, and Guang Deng. Kernel methods and haplotypes used in selection of sparse dna markers for protein yield in dairy cattle. *Mathematical biosciences*, 243(1):57–66, 2013.

[ZBOO+16] Xin Zhou, Alfonso Bueno-Orovio, Michele Orini, Ben Hanson, Martin Hayward, Peter Taggart, Pier D Lambiase, Kevin Burrage, and Blanca Rodriguez. In vivo and in silico investigation into mechanisms of frequency dependence of repolarization alternans in human ventricular cardiomyocytes. *Circulation research*, 118(2):266–278, 2016.

[ZBS+13] N. Zemzemi, M. Bernabeu, J. Saiz, J. Cooper, P. Pathmanathan, G. Mirams, J. Pitt-Francis, and B. Rodriguez. Computational assessment of drug-induced effects on the electrocardiogram: from ion channel to body surface potentials. *British journal of pharmacology*, 168(3):718–733, 2013.

[ZG08] N. Zabaras and B. Ganapathysubramanian. A scalable framework for the solution of stochastic inverse problems using a sparse grid collocation approach. *Journal of Computational Physics*, 227(9):4697–4735, 2008.

[ZGZ+16] Xiaoyu Zhang, Liang Guo, Haoyu Zeng, Stephen L White, Michael Furniss, Bharathi Balasubramanian, Edward Lis, Armando Lagrutta, Frederick Sannajust, Li Leyna Zhao, et al. Multi-parametric assessment of cardiomyocyte excitation-contraction coupling using impedance and field potential recording: A tool for cardiac safety

assessment. *Journal of pharmacological and toxicological methods*, 81:201–216, 2016.

[ZKK+93] Manfred Zehender, Wolfgang Kasper, Elisabeth Kauder, Martin Schonthaler, Annette Geibel, Manfred Olschewski, and Hanjorg Just. Right ventricular infarction as an independent predictor of prognosis after acute inferior myocardial infarction. *New England Journal of Medicine*, 328(14):981–988, 1993.